School of Civil and Mechanical Engineering
Department of Mechanical Engineering

Experimental Investigation of Fluid Dynamics and Heat Transfer Characteristics of a Turbulent Jet Impinging on an Oscillating Target Surface

Vishal Chaugule

This thesis is presented for the Degree of
Doctor of Philosophy
of
Curtin University

October 2017

Declaration

To the best of my knowledge and belief this thesis contains no material previously published by any other person except where due acknowledgment has been made.

This thesis contains no material which has been accepted for the award of any other degree or diploma in any university.

Signature:……

Date:18th October 2017

Acknowledgments

I want to express my deepest gratitude to Dr. Ramesh Narayanaswamy for his support and guidance throughout the course of my research work. He was a constant source of encouragement, and his advice, both on academic and personal fronts, was remarkably helpful in navigating through testing times. His support and assistance was instrumental in the establishment of the Particle Image Velocimetry Laboratory, in the Department of Mechanical Engineering at Curtin University, where all the experiments in this study were conducted.

I am grateful to Dr. Anthony D Lucey for his support and guidance. His brilliant research acumen has been an inspiration for me and his insightful suggestions have immensely helped enhance the standard of this work. I also thank Dr. Vinod Narayanan for his astute observations and critical comments on experimental work.

The support of the Australian Research Council (ARC) Discovery Project Grant - DP 130103271 and the Curtin International Postgraduate Research Scholarship (CIPRS) for this study has been vital and is gratefully acknowledged.

I appreciate the assistance provided by Mr. David Collier, and his team of Technical Staff, in the design and fabrication of components and sub-systems required for conducting the experiments. Their expertise and workmanship were noteworthy. The discussions I had with Mr. Collier on practical aspects of engineering design, and sometimes on the game of cricket, were enlightening and interesting.

A special thanks to Dr. Rodney Entwistle for employing me as a tutor for the Engineering Foundation Year, and to Naomi Mockford for all the related administrative assistance. I also thank Sucy Leong, Frankie Sia, Sharon Quek, Margaret Brown, and Ying Hong Lin. The prompt help and support they always provided made life easier as a research student.

Thangam Natarajan was a fantastic peer. The numerous talks and discussions I have had with him in the past 4 years have been really fruitful and have helped me grow as a researcher. I am grateful to him for his help in securing accommodation for me and my family.

I am indebted to my parents without whom I would not have been where I am today, and who have worked so hard to help me achieve my goals. Their support in all my endeavours, their encouragement to pursue my dreams, and their endless love and care has always give me strength and belief.

I had to commence my studies soon after my daughter was born, and staying away from my first born child and her mother was emotionally devastating. The sacrifices my wife made for me to be able to complete my studies, the struggles she had to endure alone while bringing up our child, and the precious moments we lost as a family were unfathomable. I hope I can make it up to them as I dedicate this thesis to my wife Virginia and my 3 year old daughter Shaina Prisha.

- Vishal Chaugule

Abstract

An impinging-jet flow involves a fluid-jet issuing from a nozzle and impinging on a target surface placed at some distance downstream of the nozzle. This simple geometric configuration of jet and target surface produces high transfer rates of mass, momentum and energy, thus resulting in impinging jets being used in a wide range of applications spanning both industry and everyday life. While the fluid dynamics and heat transfer in jet impingement on a static target surface have been studied extensively to date, the nature of these characteristics in jet impingement on a moving target surface is relatively unknown.

Studies reported on jet impingement on a moving target surface categorize the motion of target surface considering two directions; one in a direction perpendicular to the jet axis and the other in a direction parallel to the jet axis. The focus of the present work is to study the effect of the second kind of moving target surface on an impinging-jet flow. Physically, such a moving target surface undergoes oscillation about a mean nozzle-to-surface separation distance from the jet nozzle exit.

Published work on this topic shows that an oscillating target surface gives rise to higher jet impingement heat transfer rates than those present in the case of a static target surface, but the reasons for this enhancement are not exactly known. A detailed examination of the fluid dynamics in jet impingement on an oscillating target surface is carried out in this thesis, in order to understand how the changes in the flow due to target-surface oscillation affect the heat transfer characteristics.

The present study has been carried out in two parts using two different experimental systems. In the first part, the experimental system comprises an axisymmetric turbulent jet impinging on unheated static and oscillating target surfaces. In the second, it comprises an axisymmetric turbulent jet impinging on heated static and oscillating target surfaces. The jet-nozzle exit diameter in the two systems is equal to 12.6 mm and the jet Reynolds numbers, based on the jet-nozzle exit diameter, are equal to 5200 and 5000 respectively. The mean nozzle-to-surface separation distances about which the target surface oscillates are equal to 2.1 and 1.95 times the jet-nozzle exit diameters, respectively. These nozzle-to-surface separation distances are also the positions where the static target surface is placed in the corresponding systems. Target-surface oscillation in the first experimental system is at frequencies of 20 Hz and 80

Hz with a peak-to-peak displacement amplitude of 0.16 times the nozzle diameter, while in the second it is at 20 Hz and 50 Hz with 0.2 times the nozzle diameter.

Particle Image Velocimetry and Infrared Thermography are used to measure the flow quantities and surface temperatures respectively. The flow-field measurements are analysed at 6 different phases of target-surface motion during oscillation, whereas the temperature measurements are acquired at phase-averaged steady-state conditions. Three of the phases are during motion of target surface away from the jet exit, while the other three are during the opposite motion. The measurements obtained for jet impingement on an oscillating target surface are compared with corresponding measurements for jet impingement on a static target surface.

The flow characteristics of the free-jet, in the absence of the target surface, and the validation of the experimental system are presented. The fluid dynamics results for jet impingement on static and oscillating target surfaces include the presentation of the instantaneous velocity vectors, mean-flow velocities, wall-shear stress, normal- and shear-strain rates. A proper orthogonal decomposition analysis has been carried out to examine large-scale coherent structures and the effect of target-surface oscillation on them. The fluid-dynamics results also include the rms axial and radial velocity fluctuations, Reynolds stress and turbulence kinetic energies. The heat transfer results presented are of the steady-state time-averaged surface temperature distributions, and the estimation of convective heat transfer coefficients in the form of non-dimensional Nusselt numbers for jet impingement on heated static and oscillating target surfaces.

The fluid-dynamics results show that the mean velocities in the impinging jet are significantly affected by target-surface oscillation, and these effects vary depending on the velocity magnitudes in different flow regions, the spatial location from the wall, and the frequency of target-surface oscillation. The mean axial velocities increase during target surface motion away from the jet exit, and decrease during the opposite motion. The variations of mean radial velocities are opposite to those of the mean axial velocities.

There is an increase in the entrainment of the ambient fluid into the jet, as compared with a static target surface, during target-surface motion away from the jet exit at 80 Hz and 50 Hz frequencies of oscillation. The entrained fluid is decelerated

due to target-surface motion towards the jet exit at these frequencies. The oscillatory motion of the target surface at these frequencies generates higher turbulence intensities and velocity fluctuations in both the free-jet and wall-jet regions compared to those for a static target surface, in addition to an increase in the Reynolds stress and turbulence kinetic energies.

A heated target surface is found to induce buoyancy in the ambient fluid, which leads to lower entrainment of the ambient fluid into the jet, compared to a heated target surface. This gives rise to higher mean velocities and turbulence intensities in jet impingement on a heated target surface than in jet impingement on an unheated target surface, and it occurs for both static and oscillating target surfaces.

It is shown that there is an increase in surface temperatures caused by target-surface oscillation. However, the convective heat transfer rate at the surface also increases in the presence of target-surface oscillation, as compared with jet impingement on a static target surface. This enhancement is greater in the impingement region than in the wall-jet region. The primary reason for this increase is the interaction between the axial velocity of the jet and the target surface velocity during oscillation which gives rise to higher rms axial velocity fluctuations that affect the heat transfer rate. Although there is an enhancement of heat transfer, it is found that this increase is small, as expressed by the stagnation-point Nusselt number for target-surface oscillation at 50 Hz which is only 5.6% higher than that for a static target surface.

In summary, the findings from this study show that although target-surface oscillation produces significant changes in the mean flow and generates higher turbulence intensities in the impinging jet, the increase in the heat transfer rate, from that in the case of jet impingement on a static target surface, is far less pronounced for the range of parameters considered in this study.

Publications originating from this work

Peer reviewed conference proceedings

Chaugule V, Narayanaswamy R, Lucey AD, Narayanan V, Jewkes J. The Effect of Target Surface Oscillations on a Turbulent Impinging-Jet Flow. *Proceedings of the 20th Australasian Fluid Mechanics Conference*, Perth, Australia 5-8 December 2016

Chaugule V, Narayanaswamy R, Lucey AD, Narayanan V, Jewkes J. Turbulent Impinging Jet on an Oscillating Surface. *Proceedings of the 7th Australian Conference on Laser Diagnostics in Fluid Mechanics and Combustion*, Melbourne, Australia 9-11 December 2015

Chaugule V, Narayanaswamy R, Narayanan V, Jewkes J, Lucey AD. A Novel Flow Control Valve for Pulsating Flows. *Proceedings of the 19th Australasian Fluid Mechanics Conference*, Melbourne, Australia 8-11 December 2014

Table of Contents

Part I: Jet Impingement on Unheated Static and Oscillating Target Surfaces

Part II: Jet Impingement on Heated Static and Oscillating Target Surfaces

Nomenclature

Latin alphabetical symbols

A	foil area (mm^2)
a_s	peak target-surface acceleration (m/s^2)
A_s	peak-to-peak target-surface displacement amplitude (mm)
b	jet nozzle-exit width (mm)
C_p	specific heat of air at constant pressure (kJ/kg.K)
d	jet nozzle-exit diameter (mm)
E	hot-wire sensor voltage (Volts)
f_j	frequency of formation of vortex structures in free-jet (Hz)
f_s	target-surface oscillation frequency (Hz)
g	acceleration due to Earth's gravity (m/s^2) = 9.81
h	nozzle-to-surface separation distance (mm)
h_{conv}	convective heat transfer coefficient = $Q_{fconv}/(T_w - T_{aw})$ (W/m^{2}K)
I	current supplied to the foil (A)
k	thermal conductivity of air (W/m-K) = 0.02514
k_f	thermal conductivity of Inconel 600 alloy foil (W/m-K) = 14.8
P	foil perimeter (mm)
Q_{cond}	tangential conduction heat flux (W/m^2)
Q_{fconv}	forced convective heat flux (W/m^2)
Q_j	Joule heat flux (W/m^2)
Q_{nconv}	natural convection heat flux (W/m^2)
Q_{rad}	radiative heat flux (W/m^2)
s_f	thickness of foil (μm)
t_l	integral time-scale of the flow (s) = d/U
T_a	ambient temperature (K)
T_j	jet temperature at nozzle exit (K)
T_w	local wall temperature (K)
T_{aw}	local adiabatic wall temperature (K)
u	axial velocity (m/s)
u_{rms}	root-mean-square axial velocity fluctuation (m/s)
U	jet bulk-flow speed (m/s)

U_{cal} hot-wire sensor calibration velocity (m/s)

$\overline{u'v'}$ Reynolds stress (m/s)^2

v radial velocity (m/s)

v_{rms} root-mean-square radial velocity fluctuation (m/s)

v_s peak target-surface velocity (m/s)

v_{srms} root-mean-square target-surface speed (m/s)

V electrical potential difference across the foil (Volts)

x axial direction

y radial direction

z lateral direction

Greek alphabetical symbols

β volumetric thermal expansion coefficient of air = $1/T_a$ (K^{-1})

ε emissivity of the black-paint coated foil = 0.88

μ dynamic viscosity of air (kg/m-s) = 1.82×10^{-5}

ν kinematic viscosity of air (m^2/s) = μ/ρ

ρ density of air (kg/m^3) = 1.2047

σ Stefan-Boltzmann constant = 5.67×10^{-8} (W/m^{2}K^4)

ϕ phase (displacement position) of target surface during oscillation

Non-dimensional quantities

Bi Biot number = $h_{conv}s_f/k_f$

Gr Grashof number, based on a length scale A/P, = $\frac{(A/P)^3 g\beta(T_w-T_a)}{\nu^2}$

$(h/d)_m$ mean nozzle-to-surface separation distance

h/d nozzle-to-surface separation distance

Nu Nusselt number = $h_{conv}d/k$

Pr Prandtl number of air = 0.71

Ra Rayleigh number = $GrPr$

Re Reynolds number = $\rho Ud/\mu$

St Strouhal number of free jet = $f_j d/U$

St_s Strouhal number of target surface oscillation = $f_s A_s/U$

Wo Womersely number = $\sqrt{2\pi(Re)(St_s)}$

Subscripts and Superscripts

cj	centerline of the jet
max	maximum
rms	root-mean-square
w	wall
s	target surface
–	mean
′	fluctuation

Abbreviations

HWA	Hot-Wire Anemometry
IRT	Infra-Red Thermography
LCT	Liquid Crystal Thermography
LDV	Laser Doppler Velocimetry
LIF	Laser Induced Fluorescence
MDF	Medium-Density Fiberboard
PVC	Poly-Vinyl Chloride
PIV	Particle Image Velocimetry
PTV	Particle Tracking Velocimetry

List of Figures

List of Tables

Chapter 1

Introduction

An impinging-jet flow typically involves a fluid originating as a jet from a nozzle and impinging normally upon a target surface. This flow configuration is illustrated in Fig. 1.1, where upon impingement the fluid flows along the surface, outwards from the point of impingement, with the formation of a thin boundary layer over the surface. An important feature of impinging jets is the effective transfer of mass, momentum and energy between the fluid and the target surface. It is this characteristic which is responsible for jet impingement techniques to be extensively used for surface drying, heating, cooling, and particle removal. Another advantage is the simple geometrical arrangement that exists between the jet and the target surface that facilitates an uncomplicated design and operation of this technique for practical use.

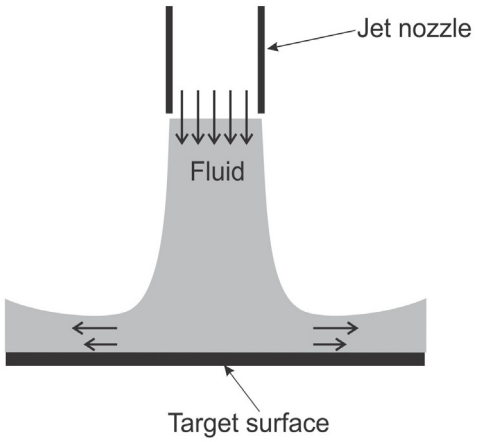

Fig 1.1 Impinging-jet flow configuration

1.1 Applications of impinging jets

Applications of impinging jets are widespread both in industry and everyday life. Impinging jets are used in tempering of glass (Cirillo and Isopi 2009; Sozbir and Yao 2004) and cooling of hot metals (Mozumder et al. 2005; Wang et al. 2012). An illustration of the tempering process is shown in Fig. 1.2, wherein glass is first heated to reach very high temperatures, of about 650 $^{\circ}$C, and is then rapidly cooled. The cooling process is called quenching, where high-velocity air jets from an array of nozzles impinge on the hot glass. This cools outer surfaces of the glass at a much

faster rate than its center, resulting in the center of the glass being in a state of tension while its outer surfaces are in a state of compression. Tempered glass is about 5 times stronger than annealed glass and is less likely to suffer thermal damage. It is also safe upon breakage due to its disintegration into small blunt pieces of glass, reducing chances of injury due to cutting or piercing.

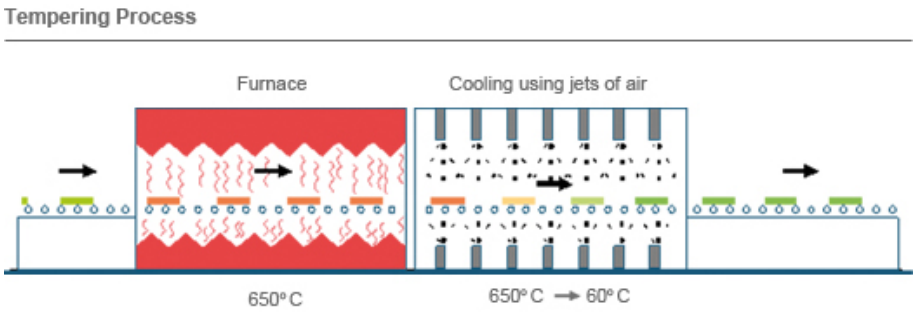

Fig. 1.2 Tempering of glass[1]

Fig. 1.3 Jet-impingement cooling of hot metal sheets[2]

Cooling of hot metals is performed by water jets impinging on sheets of hot metals or alloys after they undergo rolling, a snapshot of which is shown in Fig. 1.3. The heat transfer mechanisms in this cooling process involves internal and external conduction, stagnation forced convection, forced boiling convection, air convection and radiation, and heat generation from material phase transformation (Wang et al. 2012). The velocity and temperature of the jets, the jet geometry and arrangement, and the speed and temperature of the metal sheets moving on the conveyor affect the heat transfer rates, and hence the properties of the metal sheets. A proper control of these parameters can produce cooling effects that minimizes thermally induced stresses in the metal sheets thereby extending their roll life and preserving the quality of their shape (Chen and Tseng 1992).

[1] http://bearglass.info/tempering.php

[2] http://www.voestalpine.com/blog/wp-content/uploads/2014/08/donau-voestalpine-kuehlstrecke.jpg

In the application of gas turbine cooling, jet impingement technology is used to cool gas turbine blades, which reach operating temperatures in excess of 1300 °C (Han et al. 2012). The structural strength and operating life of these blades not only depend on the material characteristics but also on effective cooling schemes. Effective cooling of gas turbine blades allows higher inlet temperatures, which improve engine efficiency and output power density (Han and Goldstein 2001). Jet impingement cooling is performed using air supplied from the compressor of the gas turbine, which flows through narrow cavities within the blade and impinges on its internal surfaces as shown in Fig. 1.4. Depending on a higher requirement of cooling, in locations such as near the stagnation region, the number and spacing of these jets can be modified in the structural design of the turbine blade. Additionally, jet impingement can be combined with film cooling in order to enhance cooling rates.

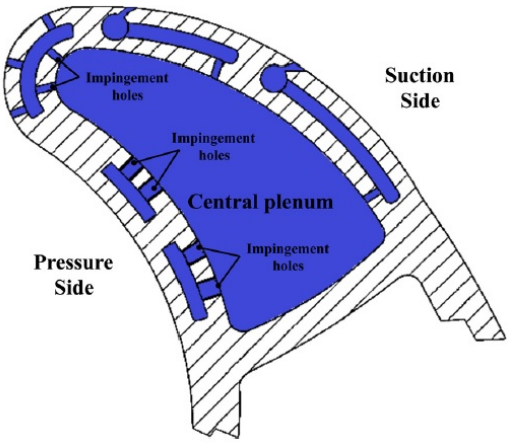

Fig. 1.4 Jet-impingement cooling of gas turbine blade (adapted from Terzis et al. 2014)

Anti-icing and de-icing processes in aircraft applications also employ impinging jets. The formation of ice on aircraft wings and control surfaces, during flight as well as on the ground, is detrimental to aircraft performance and safety. During flight, ice formation near the wing leading edge disrupts air flow over the wing which leads to a loss in lift. This is prevented by directing hot-air jets on the internal surface of the wing leading edge, as shown in Fig. 1.5. These jets are supplied from engine bleed flow and designed to issue from holes in a manifold integrated within the wing structure (McLaren and Orr 1991). When on the ground, de-icing is carried out by impingement spraying of heated ethylene glycol on aircraft surfaces to remove frozen contaminants (Volkner and Schmedemann 1977), a snapshot of which is shown in Fig. 1.6.

[3] http://substance-en.etsmtl.ca/impinging-spray-technique-for-ground-deicing

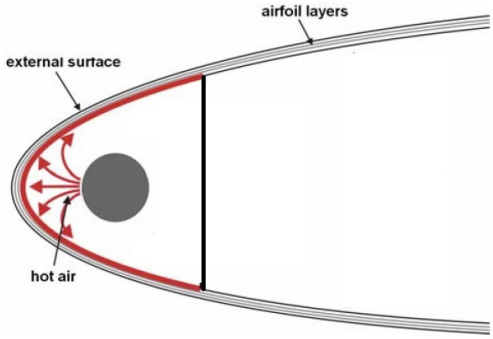

Fig. 1.5 Anti-icing of wing leading edge (adapted from Donatti et al. 2007)

Fig. 1.6 De-icing of aircraft surfaces[3]

Synthetic impinging air jets are presently utilized in electronic equipment that have closely packed components (Pavlova and Amitay 2006) and require efficient cooling. These jets do not require any piped supply of air as they are created by periodic suction and ejection of ambient air due to the action of an oscillating diaphragm inside a walled cavity with an orifice. Synthetic jets have zero-net mass flux and are unsteady due to reciprocating motion of the diaphragm, which is commonly generated using piezoelectric or electromagnetic mechanisms. The ejection part of the oscillation cycle produces vortices near the orifice, which enhance mixing and turbulence responsible for dissipation of heat from the target surface (Persoons et al. 2011). Advantages of synthetic impinging jets over conventional cooling fans are in the reduction of acoustic noise, local and uniform cooling of heat sinks, and greater thermal efficiency.

[3] http://substance-en.etsmtl.ca/impinging-spray-technique-for-ground-deicing

Removal of particles adhering to a surface can be carried out using impinging jets (Smedley et al. 1999; Young et al. 2013), wherein the action of jet impingement imparts sufficient aerodynamic force to overcome the adhesion force between the particle and the surface. The efficiency of particle removal is found to increase with increasing jet pressure and decreasing separation distance of the jet from the surface. An innovative approach to clean the internal surfaces of a tank, without the need to access or open it, is to use impinging water jets from nozzles that rotate and revolve, as shown in Fig. 1.7. These articulated nozzles are driven by fluid motion and allow a complete and quick clean-up of the inside of the tank. On the other hand, impinging jets are also used to deposit particles on surfaces in the form of impingement spray coating (Shukla et al. 2000; Liu et al. 2010). This includes deposition of both solid particles as well as liquid droplets.

Fig. 1.7 Jet-impingement removal of particles from internal surfaces of a tank[4]

Jet impingement heat transfer applications in the food industry are used in processes such as baking, freezing, toasting and drying (Sarkar et al. 2004), to enable faster processing rates and reduced cooking times compared to conventional food processing mechanisms. Baking and toasting are done using impingement ovens, wherein hot air jets, created by heating fresh air using a heat exchanger, impinge on food materials in the baking chamber. The advantages of such ovens are control of the heating process to produce uniform baking across the surface and absence of combustion by-products in the baking chamber. An illustration of an impingement oven and a snapshot of the baking process are shown in Figs. 1.8(a) and 1.8(b).

[4] http://www.gamajet.com

(a)

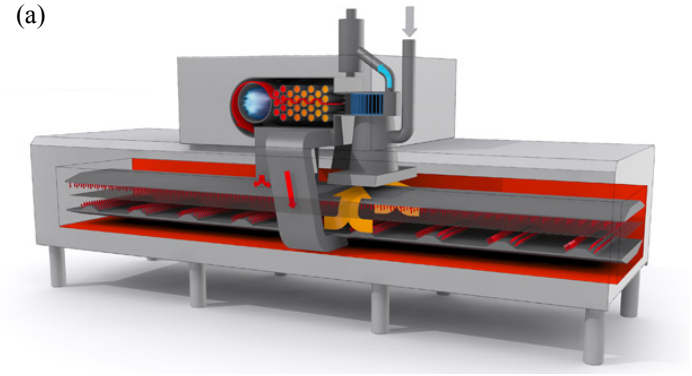

(b)

Fig. 1.8 Jet impingement applications in food processing: (a) impingement oven[5] (b) snapshot of baking process[6]

Freezing or chilling is performed by directing high velocity refrigerated-air jets on top and bottom surfaces of food products as they move along a conveyor. Refrigerated-air jet impingement removes the insulating thermal boundary layer on the material and freezes it faster than conventional refrigeration techniques (Salvadori and Mascheroni 2002). An impingement freezer designed by Lee and Sahm (1998) had different zones in the freezing chamber with independent temperature control. In addition, velocities of the refrigerated-air jets could also be controlled to produce maximum cooling efficiency. Freezing of tissue and organs for purposes of medical and veterinary transplantation is also done using similar jet impingement technique that preserves integrity of the cell structure even after the material is thawed (Morris and Acton 2001).

[5] http://naegele-inc.com/bakery-equipment/ovens/impingement-ovens-2/

[6] http://www.wolverineproctor.com/en-us/equipment/impingement-oven/

Drying application of jet impingement involves directing hot-air jets to remove moisture from food products and other materials such as textiles, paper, and wood veneer. A cut-away picture of a hot-air impingement dryer used for drying textiles is shown in Fig. 1.9, in which hot-air jets arising from arrays of nozzles, impinge upon a sheet of fabric as it moves horizontally over cylindrical rollers. The drying process involves physical mechanisms of capillary transport of moisture trapped in small pores to the surface, liquid mass transfer, and gas phase diffusion (Polat 1993). Hot-air jet impingement over a porous material evaporates water from the liquid, causing the water vapor to diffuse through the boundary layer. This moisture removal rate can be controlled by changing the jet temperature and velocity. An experimental study by De Bonis and Ruocco (2011) on jet impingement drying of moist substrates showed that the drying process was non-uniform over the surface and it reduced in effect as the distance of the jet exit from the surface increased.

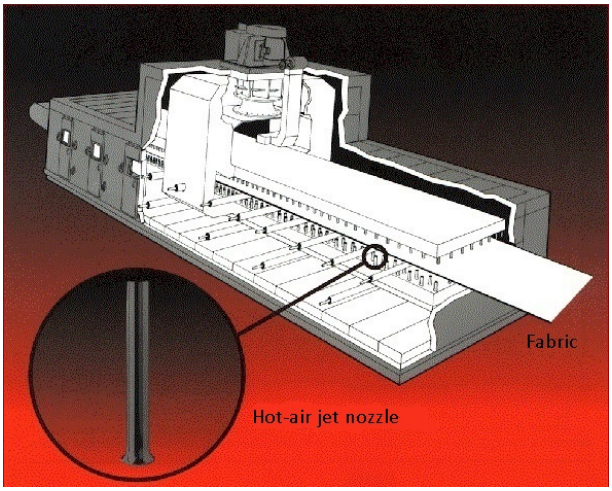

Fig. 1.9 Hot-air jet impingement dryer[7]

Nuclear power-plants rely on safe and controlled production of nuclear energy to run fusion power systems. These systems have high temperature components which need to be cooled to temperatures at which their structural strength limit is not exceeded. This is performed by using helium coolant impinging jets which arise from small holes placed at short interspacing distances (Norajitra et al. 2008; Ihli and Ilić 2009; Amini and Hassan 2009).

[7] http://lanly.com/wp-content/uploads/2014/03/dryer_cutaway.gif

Impinging jets can also be employed in drying images generated from inkjet printers (Meyers et al. 2002), in order to prevent smudging of ink after printing and avoid ink transfer onto other objects that come in contact with the recording medium. Large scale processing of photographic films requires rapid and efficient drying of the coated films. This can be achieved through the use of impingement dryers that direct hot-air jets on films passing over rollers (Lin and Russell 1974). An everyday use of impinging jets occurs in hand dryers, as shown in Fig. 1.10. The present day hand dryers, for example those manufactured by Dyson^{TM}, incorporate design features such as precision nozzles, and compact and efficient motors that generate high velocity air jets for faster drying.

Fig. 1.10 Jet impingement drying – hand dryer[8]

Automotive applications of impinging jets include fuel spray impingement in direct injection diesel engines (Naber et al. 1988; Liu and Reitz 1995), hot-air impingement on windshields for de-fogging (Arnold and Owen 1958) and oil-jet impingement cooling of engine piston (Howe 1973; Yang et al. 1999). De-fogging of automotive windshields is performed by directing hot-air jets onto the windshield glass from ducts placed in the edge of the dashboard attached to the firewall, as shown in Fig. 1.11.

[8] http://www.dyson.com.au/hand-dryers/airblade-v.aspx

Internal combustion engine pistons reach operating temperatures that exceed the melting point of the alloy used in their construction, and hence have to be cooled in order to reduce thermal stresses and prevent structural deformation (Esfahanian et al. 2006). An illustrative example of engine piston cooling is shown in Fig. 1.12, where lubricating oil jets are directed on the internal surface of the piston crown, with supply and return of oil facilitated through hollow annular spaces inside the piston rod.

Fig. 1.11 De-fogging of automotive windshield[9]

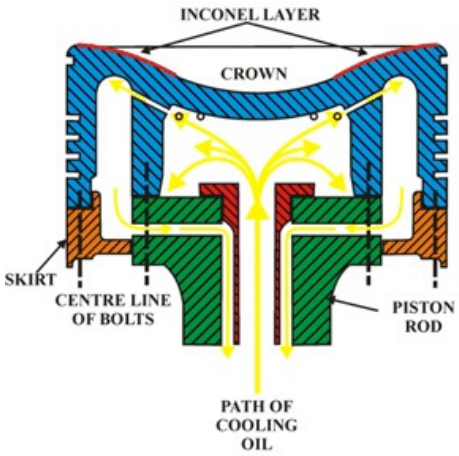

Fig. 1.12 Jet-impingement engine-piston cooling[10]

The applications presented here show the wide range of uses of impinging jets highlighting their efficiency in the transport of mass, momentum and energy. These applications include target surfaces either static or moving. Impinging jets are preferred over parallel flows for surface cooling because the heat transfer coefficients produced due to jet impingement are up to 3 times higher than those produced by parallel flows. This is primarily due to thinner boundary layers and higher turbulence intensities generated in impinging-jet flows (Zuckerman and Lior 2006).

[9] http://m.hyundai.com/WW/Showroom/Cars/Centennial/Safety/index.html

[10] http://www.marinediesels.info/2_stroke_engine_parts/piston.htm

1.2 Motivation

The fluid dynamics and heat transfer characteristics of jet impingement on a static target surface have been topics of extensive investigation. It has been shown that the transport phenomena in impinging jets is characterized by the velocity and turbulence intensity profiles in the jet flow, along with the interaction of large-scale structures, formed in the shear layer, with the target surface (wall) upon impingement. These play an important role in affecting jet impingement heat transfer performance which is dependent on the advection of momentum and turbulence from the jet to the flow over the target surface.

Although knowledge of flow and heat transfer in jet impingement on a static target surface is well-established, the effect of an oscillating target surface on the impinging-jet flow remains largely unknown. A target surface which oscillates in a direction perpendicular to the jet axis can affect the fluid dynamic features of the jet, and hence its heat transfer. Specifically, the oscillatory motion of the target surface can modify the turbulence levels in an impinging-jet flow, which in turn could alter the convective heat transfer coefficients at the surface. The motivation for the present work arises from the need to investigate the flow characteristics that occur in jet impingement on an oscillating target surface, in order to gain further understanding of the inter-relationship between the fluid-dynamics effects and the convective heat transfer rate.

1.3 Research aim and objectives

The aim of the present work is to experimentally study the fluid-dynamics and heat transfer characteristics of a turbulent jet impinging on an oscillating target surface. This is done with a view to explore the flow characteristics and its relevance to heat transfer. This study is conducted in two parts.

The objective of the first part is to investigate the fluid-dynamics characteristics of a jet impinging on an unheated oscillating target surface. This study serves to understand the characteristics of the flow due to target-surface oscillation, from the fluid dynamics point of view.

There are two objectives for the second part:

- The first objective is to examine the fluid-dynamics characteristics of an impinging-jet flow on unheated and heated static target surfaces, and unheated and heated oscillating target surfaces. This serves to determine the effects of surface heating on the impinging-jet flow on both static and oscillating target surfaces.
- The second objective is to investigate both the fluid dynamics and heat transfer characteristics of a jet impinging on a heated oscillating target surface. This serves to understand how the changes in flow features due to target-surface oscillation alter the convective heat transfer rate on the oscillating target surface.

1.4 Research methods

The two parts of this study are conducted using two different experimental systems and parameters. The experimental system for the first part involves an axisymmetric jet impinging on unheated, static and oscillating target surfaces, whereas for the second part it involves an axisymmetric jet impinging on heated, static and oscillating target surfaces. These systems differ in the design of the impingement target surfaces. The impingement target surface in the first system is an unheated aluminum sheet, whereas in the second system it is a heated thin Inconel 600 alloy foil. In each of two experimental systems, the static target surface is placed at the mean position of the oscillating target surface from the jet nozzle exit.

The experimental methods of hot-wire anemometry (HWA), particle image velocimetry (PIV) and infrared thermography (IRT) are used to conduct flow and temperature measurements in the above mentioned systems. The flow velocities are measured for jet impingement on a static target surface and for jet impingement on an oscillating target surface at various phases of the target surface during oscillation. These measurements are then used to determine various statistical flow quantities. The determination of jet impingement convective heat transfer coefficient at the surface is performed by measuring steady-state time-averaged temperatures of the static and oscillating target surfaces.

In the first part of the study, the fluid-dynamics measurements for jet impingement on an unheated oscillating target surface are analyzed and compared with those of jet impingement on an unheated static target surface.

In the second part of the study, the fluid-dynamics measurements for jet impingement on unheated static and oscillating target surfaces are analyzed and compared with those of jet impingement on heated static and oscillating target surfaces. Later, the fluid dynamics and heat transfer measurements for jet impingement on a heated oscillating target surface are analyzed and compared with those of jet impingement on a heated static target surface. This comparative analysis enables the understanding of the effect an oscillating target surface produces on an impinging jet-flow, and thereby on the convective heat transfer rate.

An overview of the above mentioned research methods, highlighting the two parts of this study and their respective experimental systems, impingement target surfaces, and measurements and analysis carried out, is provided in Table 1.1.

Table 1.1 Overview of research methods

Part of study	**Experimental system**	**Impingement target surface**	**Measurements and analysis**
Part I	Jet impingement on unheated, static and oscillating target surfaces	Aluminum sheet	Fluid-dynamics of a jet impinging on unheated, static and oscillating target surfaces
Part II	Jet impingement on heated, static and oscillating target surfaces	Inconel 600 alloy foil	Fluid-dynamics of a jet impinging on unheated and heated, static and oscillating target surfaces
			Fluid-dynamics and heat transfer of a jet impinging on heated, static and oscillating target surfaces

1.5 Summary

An introduction to impinging jet and its practical applications has been presented. The wide-range of applications of jet impingement in both industry and everyday life span the operations of complex machinery of gas turbines to simple hand-dryers. The motivation for the present study has stemmed from the need to study the effect an oscillating target surface has on the flow and heat transfer characteristics of an impinging jet. This study is conducted in two parts using two different experimental systems of jet impingement on unheated and heated, static and oscillating target surfaces. The techniques of HWA, PIV, and IRT have been chosen to measure and study the fluid-dynamics and heat transfer characteristics of a jet impinging on an oscillating target surface and to compare with those of a jet impinging on a static target surface.

1.6 Thesis layout

Chapter 1 briefly introduces an impinging jet and its applications. It also explains the motivation for the present study, identifying its aims and objectives, and providing an overview of the methods used.

Chapter 2 describes the flow regions and characteristics that occur in a typical impinging jet. It also provides a review of studies reported on jet impingement on static and oscillating target surfaces.

In Chapter 3, details of the two experimental systems studied in the present work are provided, along with the description of relevant experimental methods and parameters, and the uncertainties in the measured fluid dynamics and heat transfer quantities.

In Chapter 4, the results and discussion from the first part of the study are presented, which comprise the fluid-dynamics characteristics of jet impingement on unheated, static and oscillating target surfaces. The results include the instantaneous flow vector fields, mean velocities, turbulence statistics, wall-shear stress, and proper orthogonal decomposition analysis, and are presented for jet impingement on static target surface and various phases of the oscillating target surface.

In Chapter 5, the results and discussion from the second part of the study have been presented. The mean velocities of impinging-jet flow on unheated and heated, static and oscillating target surfaces are presented first. Then, the fluid dynamics and heat transfer characteristics of jet impingement on heated, static and oscillating target surfaces are presented. The fluid-dynamics results are of the same quantities as those presented in the first part of this study. The heat transfer results include estimation of heat transfer coefficients obtained from steady-state time-averaged temperature measurements of heated, static and oscillating target surfaces during jet impingement.

Chapter 6 presents the conclusions from the two parts of this study and provides suggestions for future work.

An Appendix to this thesis includes a dimensional analysis of the system of jet impingement on an oscillating target surface. The details of PIV image processing and the computations of uncertainties in the measurements of fluid dynamics and heat transfer quantities are also presented in the Appendix.

Chapter 2
Literature Review

2.1 Impinging-jet flow characteristics

A schematic of the typical flow geometry in the canonical case of a jet impinging perpendicularly onto a static target surface, with its various flow regions, is shown in Fig. 2.1. The nozzle, from which the jet issues, usually has a rectangular or a circular cross-section. As the present study involves an axisymmetric jet impingement, the nozzle has a circular cross-section with an exit diameter *d*. The *x* and *y* axes represent the axial and radial flow directions respectively, with the origin located on the jet axis at the jet-nozzle exit. A uniform temperature jet with an exit velocity profile and turbulence intensity, dependent on the upstream flow conditions and the nozzle geometry, impinges on a target surface kept at a distance *h* downstream to the jet nozzle exit. Upon impingement, the jet deflects from the stagnation point axi-symmetrically in all azimuthal directions, and flows radially outwards along the target surface. This flow configuration has different flow regions as labelled in Fig. 2.1 and complex flow patterns within these.

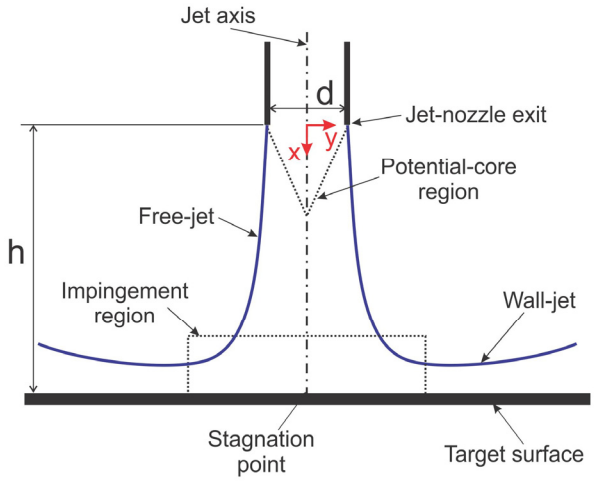

Fig. 2.1 Impinging-jet flow regions

After the jet exits the nozzle it takes the form of a free-jet, being far enough from the target surface, which interacts with the ambient fluid. This interaction causes a shear between the faster moving free-jet and the surrounding ambient fluid giving rise to entrainment of mass into the jet. In this free-jet region the axial

velocity of the jet gradually decreases and the jet expands linearly with downstream distance, owing to the increasing effect of mixing with the ambient fluid that generates high shear stresses at the jet boundaries. Further downstream, the jet attains a velocity profile which closely resembles a Gaussian distribution. Within the free-jet region is a potential-core region, unaffected by the shear layer turbulence, where the local velocity of the jet is almost equal to its velocity at the jet-nozzle exit. The length of the potential-core region depends on the jet velocity profile and turbulence intensity at the nozzle exit, and is determined to be the axial distance from the nozzle exit where the centerline flow dynamic pressure retains 95% of its initial value (Martin 1977). In the case of circular jets, the potential-core is found to extend up to a non-dimensional nozzle-to-surface separation distance h/d = 6 to 7 (Livingood and Hrycak 1973).

As the free-jet progresses downstream, the presence of the target surface further reduces the axial velocity of the jet. The impingement creates a stagnation point at the intersection of the jet axis and the target surface plane, causing the jet to deflect in the radial direction. This region of high axial velocity deceleration and streamline curvature is called the impingement region, which is marked by large pressure gradients (Bradshaw and Love 1959) and high normal and shear strain rates. In the impingement region the thickness of the boundary layer on the target surface is found to be approximately constant (Martin 1977).

Upon impingement, there is a constricted region in which the flow accelerates as it deflects. This later takes the form of a wall-jet that progresses radially outwards along the target surface. The velocity profile in the wall-jet attains a maximum close to the wall and decreases further away from the wall. The boundary layer thickness at a given radial position is equal to the distance of the maximum radial velocity point from the wall. Typically, the maximum radial velocity occurs near a radial location of 1 nozzle diameter from the stagnation point. The wall-jet is bounded by the target surface on the bottom and the ambient fluid on the top. As the wall-jet travels downstream, it is increasingly affected by skin-friction from the target surface, and shear from the top ambient fluid. This decelerates the wall-jet, causing entrainment from the ambient fluid and expands in thickness, shifting the location of maximum radial velocity further away from the wall (Zuckerman and Lior 2006). It is in this

deceleration region that the boundary layer generally undergoes transition from laminar to turbulent.

There are several conditions and variables that govern the flow characteristics of jet impingement and its effect on convective heat transfer. These include: the jet exit flow conditions; the Reynolds number *Re* of the jet, which is based on the jet nozzle exit diameter *d*; the non-dimensional nozzle-to-surface separation distance *h*/*d*; and the type of the jet configuration, whether confined or unconfined. The above mentioned factors affect mixing between the jet and the ambient fluid, which in turn affects the jet turbulence intensity on which the heat transfer rate is strongly dependent. For a fully-developed laminar flow coming out of a straight pipe nozzle, the velocity profile at the nozzle exit is parabolic, whereas for a flow coming out of a contoured nozzle or an orifice plate it is rectangular in profile. For practical purposes, an impinging jet with Reynolds numbers greater than 3000 is considered to be fully turbulent (Gauntner et al. 1970). The jet-nozzle exit flow characteristics, the nozzle-to-surface separation distance, and the condition of the jet being confined or unconfined determine whether a laminar free-jet remains laminar before impingement. Typical impinging jet applications for heat transfer span a *Re* range from 4000 to 80000, while *h*/*d* ranges from 2 to 12.

The jet turbulence intensity at nozzle exit is dependent on upstream flow conditions and nozzle geometry. A jet originating through an orifice plate or contoured nozzle has low initial turbulence. In addition, turbulence is generated at the jet boundaries as result of flow instabilities (Kelvin-Helmholtz type) being developed in the free-shear layer. These flow instabilities lead to spatial oscillation of the free-shear layer, called “jet flapping”, wherein the shear layer undergoes temporal swaying from side to side. The shear interaction between the wall-jet and the ambient fluid also generates turbulence. Turbulence thus generated in the impinging-jet flow field is eventually advected into the near-wall region, and has a strong effect on the heat transfer rate (Viskanta 1993). The stagnation point heat transfer coefficient attains a maximum when the target surface is placed at the apex of the potential core, i.e. at $h/d = 6$ to 7. This occurs due to the effect of turbulence which penetrates towards the jet axis, rather than the centerline velocity, which is constant in the potential-core region.

The following literature review is divided into 2 parts: (i) jet impingement on static target surfaces; and (ii) jet impingement on moving target surfaces. The focus of the review is to highlight the importance of the fluid-dynamics characteristics that affect the transport phenomena, and to position the need for conducting the existing work described in this thesis in the context of available research literature. Because of the nature of the work described in this thesis, the following literature review is restricted only to experimental studies of turbulent jet impingement.

2.2 Jet impingement on a static target surface

The influence of the aforementioned parameters on the flow and heat transfer characteristics of jet impingement has been studied analytically, numerically and experimentally, for a long time by many authors. There have been periodical surveys of the literature on jet impingement on a static target surface, in the form of reviews by Gauntner et al. (1970), Martin (1977), Hrycak (1981), Jambunathan et al. (1992), Viskanta (1993), Zuckerman and Lior (2006), Weigand and Spring (2011) and Carlomagno and Ianiro (2014).

One of the first experimental studies of a submerged, turbulent, circular, impinging air jet was conducted by Bradshaw and Love (1959) with the purpose of inspecting the flow deflection behavior in the impingement and wall-jet regions. The results presented in their study included the measurements of velocity, pressure and skin friction. The analysis of these results indicated large pressure gradients in the impingement region that were associated with streamline curvature, while the variation of the wall-shear stress showed a maximum at a non-dimensional radial distance of $y/d \approx 0.5$ from the stagnation point.

Gardon and Akfirat (1965, 1966) carried out extensive measurements of heat transfer coefficients generated by a submerged, single, and an array, of two-dimensional impinging air jets. They formulated correlations between the non-dimensional Nusselt number *Nu* and *Re* while examining the influence of turbulence on jet impingement heat transfer. The salient outcome of their work was to show that jet impingement heat transfer was not only determined by the boundary layer thickness on the wall, caused by varying velocities and nozzle-to-surface separation distances, but also by the influence of turbulence which could cause a transition of the boundary layer flow from laminar to turbulent. According to Gardon and Akfirat

(1965), this transition is responsible for the secondary peak in the radial distribution of local heat transfer coefficients at small h/d values. The radial distribution of local heat transfer coefficients at $h/d = 2$ and at various Reynolds numbers is shown in Fig. 2.2, which indicates that the formation of the secondary peak increases in prominence at higher Reynolds number. They also suggested that at small h/d values, the geometry of the nozzle and the upstream flow conditions may be important in the design of jet impingement heat transfer systems.

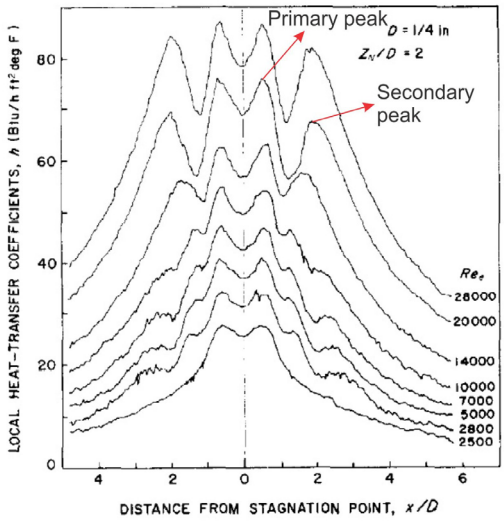

Fig. 2.2 Radial distribution of local heat transfer coefficients at $h/d = 2$ (adapted from Gardon and Akfirat 1965)

The effect of turbulence around the stagnation point in jet impingement was studied by Hoogendoorn (1977) using two different jet nozzles: one was similar to the exit of a long straight pipe, and the other had a smooth flow contraction at the exit, but both had same jet exit diameters. The straight jet-nozzle had an exit turbulence intensity of 3.2% while the contraction jet nozzle had only 0.5%. The resulting stagnation point Nu data for both nozzles was correlated with Re and turbulence intensity to describe the simultaneous effect of velocity and turbulence on the heat transfer. For the contraction jet nozzle, it was found that for $h/d < 5$, Nu attained a local maximum at a radial distance $y/d \approx 0.5$ from the stagnation point, which was caused by high radial acceleration of the jet.

Striegl and Diller (1984) studied the effect of thermal entrainment temperature on hot-air jet impingement heat transfer by proposing a non-dimensional entrainment factor that was equal to 0 if the ambient temperature was equal to the jet

temperature, and equal to 1 if the ambient temperature was equal to target surface temperature. They determined that higher thermal entrainment reduces *Nu* near the stagnation region, and this effect increases as the wall-jet grows and continues to entrain fluid. Goldstein et al. (1990) also investigated the effect of entrainment by proposing a different non-dimensional parameter called "effectiveness". This parameter was used to characterize the adiabatic wall temperature, as it depended on many parameters such as h/d, *Re*, the temperature of the jet T_j and the ambient temperature T_a. A higher value of effectiveness at lower values of h/d indicated reduced entrainment of ambient air into the free-jet region. However, in the wall-jet region, although the effectiveness was found to be independent of h/d, higher entrainment was observed at $h/d = 2$. In an earlier study by Goldstein et al. (1986), the radial distribution of jet impingement recovery factor was defined as, $(T_{aw} - T_j)/U^2\, C_p$, where T_{aw} is the local adiabatic wall temperature, U is jet exit mean-velocity, and C_p is the specific heat of air at constant pressure. The recovery factor was found to be dependent on h/d but not on *Re*, wherein it increased with h/d as a result of greater mixing of the ambient fluid with the jet.

The jet impingement heat transfer measurements conducted by Hrycak (1983) showed that the average *Nu* was independent of h/d, when the nozzle-to-surface separation distance was within the potential-core region. The correlation of the experimental data showed that for $h/d < 7$, the stagnation point *Nu* increased with h/d, whereas for $h/d > 7$ it decreased. The correlations also showed dependencies between *Nu* and *Re*, wherein *Nu* varied as function of $Re^{0.5}$ at the stagnation point, while the average *Nu* in the wall-jet region varied as a function of $Re^{0.7}$. The experimental data of Kataoka et al. (1987a) showed conclusively that the maximum stagnation point *Nu* occurred for optimal $h/d = 5$ to 8 and that the turbulence intensity of the flow reached a maximum for $h/d = 6$ to 8. The impingement of the jet with this high level of turbulence was determined to be responsible for enhancement of heat transfer in the stagnation region.

Baughn and Shimizu's (1989) jet impingement set-up used a fully-developed flow at the jet nozzle exit that originated from a long circular straight pipe. They found that the maximum stagnation point heat transfer occurred at $h/d \approx 6$ and that at $h/d = 2$, the local heat transfer attained a secondary maximum at $y/d \approx 1.8$, after the

primary peak at the stagnation point. Cooper et al. (1993), whose experimental jet impingement set-up produced flow conditions similar to those of Baughn and Shimizu (1989), carried out fluid dynamic measurements using hot-wire anemometry for a wide-range of h/d and Re values. It was shown that higher turbulence intensities occurred at larger values of h/d, due to increased mixing, and that Nu depended directly on the near-wall turbulence. They also stated that "Nusselt number provides the most sensitive indicator of the nature of viscous sub-layer", implying that ideally both fluid dynamic and heat transfer measurements should be conducted for, at least, the same experimental conditions, if not possible for the same experiment.

Stevens and Webb (1993) conducted flow measurements in the wall-jet region and found that for $y/d \leq 2.5$, the maximum radial velocity occurred very close to the wall and that it had a magnitude greater than the average jet exit velocity, sometimes being greater than 30% of U. Their results showed that the turbulence intensities increased near the wall at radial locations between $y/d = 1$ to 2.5, and then progressed radially outward and upward inside the wall-jet. Huang and El-Genk (1994) reported that for a given Re and radial distance from the stagnation point, the average Nu increased with h/d until it reached a maximum value at $h/d = 4.7$. It was found that the disappearance of a favorable pressure gradient led to a sharp increase in turbulence intensities which contributed to larger heat transfer coefficients.

Jet impingement heat transfer studies at low nozzle-to-surface separation distances were carried out by Lytle and Webb (1994) to investigate the occurrence of two distinct Nu peaks in the radial direction, one between $y/d = 0.5$ and 0.6 and the other between $y/d = 1.5$ and 2.5. The formation of the inner peak was argued to be due to increased convective heat transfer because of deflection and acceleration of the jet between the target surface and the jet exit; while that of the outer peak was due to increased boundary layer turbulence intensity because of very high shear between the wall-jet and the ambient fluid above. It was found that the radial location where the outer peak occurred moved closer to the stagnation point as h/d was decreased, as shown in Fig. 2.3. According to another study by Lee and Lee (1999), the occurrence of these peaks at $h/d = 2$ was due to the acceleration of the wall-jet at the radial location of the edge of the jet nozzle, and due to the transition of the wall boundary layer from laminar to turbulent. They also found that these peaks shifted radially outward as Re increased.

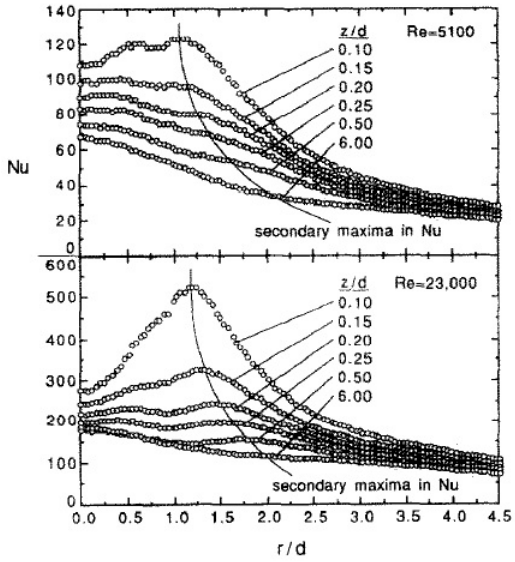

Fig. 2.3 Radial variation in *Nu* with nozzle-to-surface separation distance for two *Re* values (adapted from Lytle and Webb 1994)

Jet impingement heat transfer measurements were obtained by O'Donovan and Murray (2007) with the target surface maintained at a uniform wall temperature, instead of the typical constant heat-flux boundary condition on the target surface. They reported that the first *Nu* peak, situated within the free-jet shear-layer, was formed due to high turbulence in the wall-jet as a result of jet impingement, whereas the second peak was formed due to the wall-jet moving away from the influence of the free-jet. They concluded that heat transfer in jet impingement is dependent primarily on the magnitude of axial velocity fluctuations.

Confined impinging jets have been examined by many authors. In the study of a semi-confined slot jet impingement by Ashforth-Frost et al. (1997), it was found that confinement restricted entrainment and the spreading of the jet, which lead to longer potential-core regions than in the unconfined case. The reduced fluid entrainment contributed to lower levels of axial turbulence which decreased heat transfer rates. Fitzgerald and Garimella (1998) carried out flow-field measurements in a confined axisymmetric impinging jet, wherein the presence of confinement was found to create a toroidal recirculation zone between the target surface and the confinement plate. This caused the heated fluid from the target surface to recirculate and entrain into the impinging jet contributing to lower heat transfer coefficients when compared to unconfined impinging jets. This was also observed by Choo and

Kim (2010), who found that confined impinging jets have 20% to 30% lower heat transfer coefficients than unconfined impinging jets.

An experimental investigation into the dynamics of an impinging jet was conducted by Ho and Nosseir (1981) by carrying out measurements of pressure fluctuations on the target surface and in the free-jet region. They showed the existence of a feedback loop formed by downstream-convected coherent structures and upstream-propagating pressure waves. These waves were produced by impingement of coherent structures on the target surface. The pressure waves travelled at the speed of sound and were in-phase with shear-layer oscillations near the jet-nozzle exit. Small vortices in the oscillating shear-layer merged to form a large coherent structure, where the frequency of formation of these structures was phase-locked with the external forcing of the upstream-propagating pressure waves.

Landreth and Adrian (1990), who were the first to use the PIV technique for fluid dynamic measurements in impinging jets, reported that PIV measurements appeared to be "highly accurate and agreeing" with those of Laser Doppler Velocimetry (LDV). Their measurements of instantaneous velocities, vorticity and strain rates showed the presence of vortices in the free-jet shear layer and their interaction with the wall upon impingement, which caused instantaneous local flow separation from the wall and the formation of a secondary vortex. Although their ensemble average consisted of only 11 instantaneous measurements, the mean displacement thickness of the boundary layer was found to increase abruptly between y/d = 1.9 to 2.3 which suggested consistent breakaway of the secondary vortices.

Vortex-induced unsteady separation of the boundary layer was discovered by Didden and Ho (1985) using phase-averaged hot-wire measurements in a periodically forced impinging jet, and observed again later by Tummers et al. (2011) using high resolution PIV measurements in an unforced impinging jet. These studies showed that the boundary-layer separation was caused by the primary vortex. The near-wall measurements of Didden and Ho (1985) showed that the separation was due to an unsteady adverse pressure gradient produced by the primary vortex.

Tummers et al. (2011) determined the amount of flow reversal from the fraction of the total negative radial velocity components in the ensemble. They found that the instantaneous flow reversal occurred in a thin region very close to the

wall for $y/d > 1.2$ and it reached a maximum around $y/d = 1.5$ or 1.6, suggesting that flow reversal contributed to a local decrease of heat transfer. Detailed turbulence statistics and budget for the turbulence kinetic energy in an impinging jet flow were measured and reported by Nishino et al. (1996). They used measurement techniques of both two-dimensional and three-dimensional particle tracking velocimetry (PTV). The axial convection and turbulent normal stress were determined to be the major sources of momentum transport near the wall. The invariant map of the turbulent stress anisotropy revealed that turbulence in the stagnation region was isotropic. The examination of the turbulence kinetic energy budget showed that turbulence production occurred in the vicinity of the wall where higher radial turbulence intensity was observed.

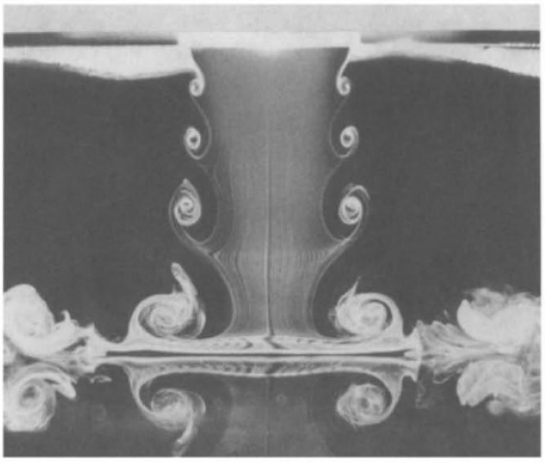

Fig. 2.4 Visualization of a circular impinging jet for $h/d = 2$ and $Re = 3500$ (adapted from Popiel and Trass 1991)

In a study conducted by Fairweather and Hargrave (2002), the instantaneous PIV measurements showed the presence of large-scale structures (eddies) in the wall-jet shear layer which caused the entrained fluid to penetrate the wall-jet and created a low-velocity recirculation zone above the wall-jet. These eddies were found to have a length scale of the same order of magnitude as the jet nozzle exit diameter. Popiel and Trass (1991) utilized the smoke-wire flow visualization technique to gain a deeper insight into these vortex structures. They suggested that the formation of these structures in well-defined shapes occur more prominently in jets issuing from convergent nozzles. The flow visualization images, one of which is shown in Fig. 2.4 for $h/d = 2$, showed that ring shaped wall-eddies were formed when toroidal vortices

impinged on the target surface. It was inferred that these wall-eddies further enhanced local momentum, heat and mass transfer. These structures were also observed in the flow visualization by Kataoka et al. (1987b), who ascertained that the impingement of these "strong turbulence carrying large-scale eddies" caused constant renewal of the thermal boundary layer in the impingement region, and this led to enhanced heat transfer in the vicinity of the stagnation point. Their analysis was based on the proposition of a surface-renewal parameter that was a product of the Strouhal number *St* and turbulent Reynolds number.

A study of the influence of shear-layer dynamics on jet impingement heat transfer by Meola et al. (1996), showed that at small nozzle-to-surface separation distances the formation of shear-layer instability structures was reduced, when compared to that at large distances, due to lower ambient fluid interference with the jet. They concluded that the impingement of vortex rings on the wall, which resulted in flow reattachment after flow separation, was responsible for the outer secondary *Nu* peak at a radial location y/d = 1.6. Hall and Ewing (2006) performed measurements of fluctuating wall-pressures in turbulent impinging jets. A modal decomposition of the pressure fluctuations indicated that large-scale ring structures formed in the jet shear-layer contributed significantly to pressure fluctuations in the wall-jet. The effect of large-scale motions increased in the stagnation region and decreased in the wall-jet region, as the nozzle-to-surface separation distance was increased. The characteristic frequency of large-scale structures in the wall-jet was found to be similar to the frequency of vortex rings in the stagnation region.

Pairing of counter-rotating shear layer vortices was observed at large nozzle-to-surface separation distances by Sakakibara et al. (1997), who performed simultaneous velocity and heat transfer measurements in a plane impinging jet. They found that the amplification of vorticity in these vortex pairs, due to vortex stretching, contributed to enhanced heat transfer in the stagnation region. The time-resolved stereoscopic PIV measurements conducted by Violato et al. (2012) demonstrated shedding and pairing of axisymmetric toroidal vortices in a circular jet impingement. Azimuthal flow instabilities and counter-rotating pairs of streamwise filaments were observed downstream of the region of pairing. The vortex ring interaction with the target surface was found to occur at a Strouhal number half that

of the vortex shedding. The increase in heat transfer for $h/d > 2$ was attributed to the penetration of turbulent mixing, induced by streamwise vortices, towards the jet axis.

El Hassan et al. (2012) performed simultaneous measurements of wall-shear stress and velocity field using electro-diffusion and PIV techniques. The radial distribution of wall-shear stress attained a peak value in the region where primary large-scale structures impinged on the wall, while an immediate trough corresponded to the detachment of these structures from the wall. Iso-contours of these vortex structures are shown in Fig. 2.5. The amplitudes of cross-correlation between the wall-shear stress and transverse vorticity fluctuations showed high values near the wall where transverse structures developed. Wall-shear stress measurements using Preston and Stanton tubes were carried out by Tu and Wood (1996). The findings showed that the maximum impingement pressure and the half-width of the pressure profile remained constant for $h/d \leq 6$. For greater h/d values, the pressure half-width was found to be linearly proportional to the nozzle-to-surface separation distance, while the maximum pressure was found to be inversely proportional.

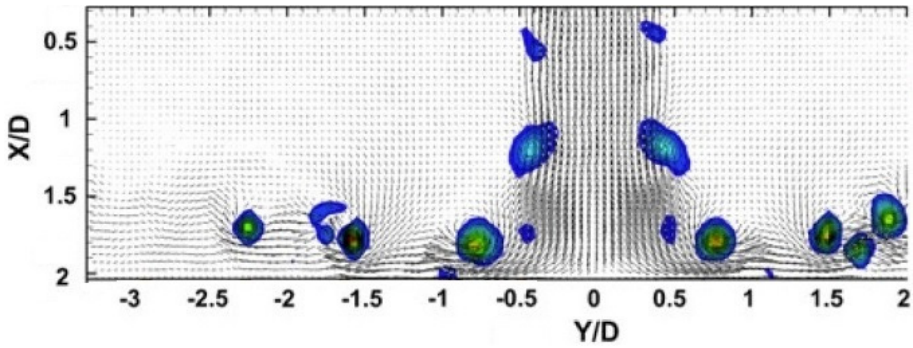

Fig. 2.5 Iso-contours of vortex structures for $h/d = 2.08$ and $Re = 2450$ (adapted from El Hassan et al. 2012)

An overview of the literature review presented on jet impingement on a static target surface suggests that jet-impingement heat transfer rate primarily depends on the impinging-jet flow characteristics. The main flow features that directly affect the heat transfer rate are the turbulence intensity of the jet and the large-scale flow structures formed in the free-jet and wall-jet shear-layers. The experimental techniques of 2D-PIV and stereoscopic PIV have been reported to be successfully applied for flow measurements in impinging jets. The findings demonstrate the capability of these techniques to produce velocity and turbulence intensity maps that

cover all the impinging-jet flow regions, and to clearly identify the vortex structures. In particular, the reviewed studies show that the heat transfer rate is influenced by advection of jet turbulence towards the wall and interaction of shear-layer vortices with the target surface.

A common finding from the aforementioned studies is that the stagnation region heat transfer rate is proportional to the jet Reynolds number, whereas it is non-monotonic in variation with the nozzle-to-surface separation. The stagnation region heat transfer rate increases with the nozzle-to-surface separation distance until the target surface is positioned within the potential-core region of the free-jet, after which it decreases. The local heat transfer rate in the wall-jet region shows a non-monotonic variation with the radial coordinate from the stagnation point. This occurs only at short nozzle-to-surface separation distances and is more pronounced at higher Reynolds numbers.

A consolidation of the studies reviewed in this section as well as other experimental works, carried out using axisymmetric circular jet impingement, is presented in Table 2.1, with information on important flow conditions, flow variables and experiment techniques used. The data presented in Table 2.1 shows that a wide range of experimental parameters have been used in axisymmetric impinging jet-flow studies. The literature on jet impingement is abundant with reports on studies in which researchers have not only varied the parameters mentioned in Table 2.1, but have also combined them with modified jet flows and target surface configurations, mostly with the primary goal of improving the jet-impingement heat transfer rate. To mention a few of these, jet impingement has been studied with: different jet nozzle exit geometries (Lee and Lee 2000; Koseoglu and Baskaya 2008); pulsating jets (Middelberg and Herwig 2009; Alimohammadi et al. 2015); excited jets (Hwang and Cho 2003; Roux et al. 2011); an array of jets (Geers et al. 2008; Wannassi and Monnoyer 2015); inclined angles of impingement and target surface (Naguib et al. 2012; Roy et al. 2002); swirling jets (Yang et al. 2010; Ahmed et al. 2017); different target surface profiles (Ekkad and Kontrovitz 2002; Gau and Chung 1991) and moving target surfaces (Zumbrunnen 1991; Harmand et al. 2013). In the context of the present work, the following section provides a brief review of jet impingement on moving target surfaces.

Table 2.1 Summary of experimental studies conducted on axisymmetric jet impingement on a static target surface

Authors	**Fluid**	**Flow configuration**	**Jet nozzle geometry**	**Jet exit diameter *d* (mm)**	**Reynolds number based on *d* *Re***	**Nozzle-to-surface separation distance *h*/*d***	**Experimental technique**
Ashforth-Frost et al. (1997)	Air	Unconfined and Semi-confined	Contraction	100	20000	1 to 8	HWA and LCT
Baughn et al (1991)	Air	Unconfined	Straight	26	23300 to 55000	2 to 10	LCT
Baydar and Ozmen (2005)	Air	Confined	Contraction	25	30000 to 50000	0.2 to 6	Thermocouple thermometry
Cooper et al. (1993)	Air	Unconfined	Straight	26 and 101.6	23000, 71000	2 to 10	HWA
El Hassan et al. (2012)	Electrolyte	Unconfined and submerged	Contraction	7.8	1260, 2450	2.08	PIV and Electro-diffusion
Fairweather and Hargrave (2002)	Air	Unconfined	Straight	13.3	18880	2	PIV
Fenot et al. (2015)	Air	Unconfined	Straight	56	23000 to 33000	1 to 6	PIV and IRT
Fitzgerald and Garimella (1998)	FC-77	Confined and submerged	Orifice plates	3.18 and 6.35	8500, 13000 and 23000	2, 3 and 4	LDV
Geers et al. (2004)	Air	Unconfined	Straight	36	23000	2	PIV and LDV
Goldstein et al (1990)	Air	Unconfined	Straight	40.9	61000 to 124000	2 to 12	Thermocouple thermometry
Hammad and Milanovic (2011)	Water	Unconfined and submerged	Straight	6.35	15895	1 to 8	PIV

Table 2.1 (continued)

Authors	**Fluid**	**Flow configuration**	**Jet nozzle geometry**	**Jet exit diameter *d* (mm)**	**Reynolds number based on *d* *Re***	**Nozzle-to-surface separation distance *h*/*d***	**Experimental technique**
Hollworth and Wilson (1984)	Water	Unconfined and unsubmerged	Orifice plate	2.5 and 10	7000 to 70000	1 to 30	Thermocouple thermometry
Huang and El-Genk (1994)	Air	Unconfined	Straight	6.2	6000 to 60000	1 to 12	Thermocouple thermometry
Hwang et al. (2005)	Water	Unconfined and submerged	Straight	20	33000	7	3D-PTV
Janiski et al. (2014)	Nitrogen	Unconfined and unsubmerged	Contraction	30	2000 to 10000	1	PIV and LIF
Jeffers et al. (2016)	Water	Confined and submerged	Straight	16 (square)	1350 to 17300	0.25 to 8.75	PIV
Kataoka et al. (1987)	Water	Unconfined and unsubmerged	Contraction	28	10000 to 30000	2 to 10	HWA
Katti and Prabhu (2008)	Air	Unconfined	Straight	7.3	12000 to 28000	0.5 to 8	IRT
Landreth and Adrian (1990)	Water	Unconfined and submerged	Contraction	26.9	6564	4	PIV
Lee and Lee (1999)	Air	Unconfined	Straight	25	5000 to 30000	2 to 10	LCT
Lytle and Webb (1994)	Air	Unconfined	Straight	7.8 and 10.9	3600 to 27600	0.1 to 1 and 6	LDV and IRT

Table 2.1 (continued)

Authors	**Fluid**	**Flow configuration**	**Jet nozzle geometry**	**Jet exit diameter *d* (mm)**	**Reynolds number based on *d* *Re***	**Nozzle-to-surface separation distance *h*/*d***	**Experimental technique**
Matsuda et al. (2010)	Air	Unconfined	Orifice	30	8900	1 to 6	PIV and IRT
Nishino et al. (1996)	Water	Unconfined and submerged	Contraction	40	10400 and 13100	5.63 and 5.86	2D and 3D PTV
O'Donovan and Murray (2007)	Air	Unconfined	Straight	13.5	10000 to 30000	0.5 to 8	LDV and Heat flux sensor
Sagot et al. (2008)	Air	Unconfined	Contraction	2.4 to 8	10000 to 30000	2 to 6	LDA
Stevens and Webb (1992)	Water	Unconfined and unsubmerged	Straight	2.1, 4.6 and 9.3	8500 to 47500	1, 2, 3 and 4	LDV
Tummers et al. (2011)	Air	Unconfined	Straight	37	23000	2	PIV and LDV
Violato et al. (2012)	Water	Unconfined and submerged	Contraction	10	5000	2 to 6	Tomo-PIV and IRT
Yao et al. (2015)	Air	Unconfined	Straight	7	10338	9	HWA

2.3 Jet impingement on a moving target surface

The literature on jet impingement on a moving target surface categorizes the motion of target surface into two directions, namely, motion in a direction that is perpendicular to the jet axis, and motion in a direction that is parallel to the jet axis, as shown in Figs. 2.6(a) and 2.6(b) respectively.

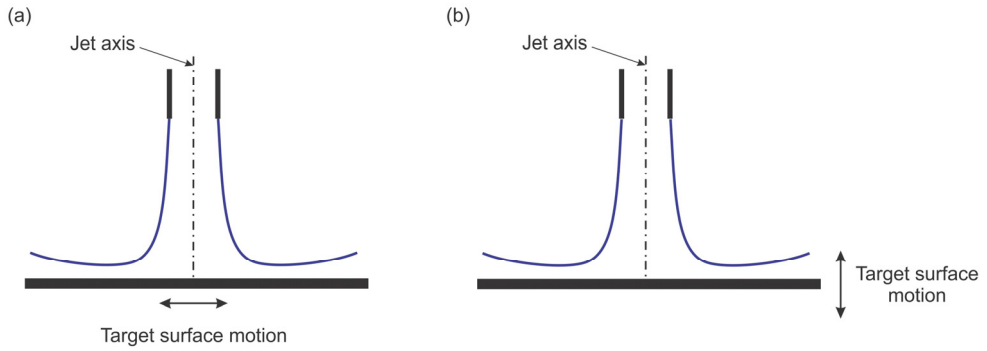

Fig. 2.6 Motion of target surface in jet impingement (a) direction perpendicular to the jet axis; (b) direction parallel to the jet axis

Application of jet impingement technology in areas such as food processing, drying of textiles, paper and film, and cooling of hot metal sheets, involves a target surface that has motion in a direction perpendicular to the jet axis as shown in Fig. 2.6(a). This physical system represents a target surface moving with a horizontal velocity, such as a conveyor belt/platform acted on by a vertical impinging jet. There are computational and experimental studies reported in literature that examine the fluid dynamics and heat transfer characteristics of jet impingement on such horizontally moving target surfaces. Recent among these are computational studies by Chattopadhyay and Saha (2003), Sharif and Banerjee (2009) and Aghahani et al. (2014); and experimental studies by Senter and Solliec (2007), Mobtil et al. (2014) and Jha et al. (2015).

The rotation of a target surface about the jet axis, in a plane perpendicular to the jet axis, also falls within the first kind of moving target surfaces. These rotating target surfaces in jet impingement exist in applications such as cooling of rotor-stator systems of turbines, bearings and gears, and large-size alternators on wind turbines. A considerable number of studies on jet impingement on such rotating target surfaces have also been carried out to date; a few of which are Metzger and

Grochowsky (1977), Popiel and Boguslawski (1986), Brodersen and Metzger (1992), Astarita and Cardone (2008), and Nguyen et al. (2012).

The purpose of the work presented in this thesis is, however, to study the second type of target surface motion, as shown in Fig. 2.6(b), wherein the target surface undergoes an oscillatory motion. Target surfaces which undergo reciprocation or even vibration in a direction parallel to the jet axis are also considered to have this type of target surface motion. There have been only few studies of jet impingement on a target surface which oscillates in a direction aligned with the jet axis; these are described in the following section.

2.3.1 Jet impingement on an oscillating target surface

Yang et al. (1999) experimentally studied the heat transfer of a confined impinging jet upon a reciprocating spherically concave target surface, for applications in engine piston cooling. The construction of the confined heat transfer module resembled a piston with a curved inner surface onto which the jet impinged. The nozzle-to-surface separation distance was fixed at h/d = 22.5, while the Reynolds number Re varied between 17500 and 43200 for target surface reciprocating frequencies f_s between 0.833 Hz to 2.08 Hz. The instantaneous Nusselt number Nu at a given spatial location on the target surface was found to be considerably different from the phase-averaged Nu at the same location, which was due to the unsteadiness of the reciprocation. The maximum heat transfer was clearly determined to be at the stagnation point, for both the reciprocating and non-reciprocating concave target surfaces, with an enhancement at this location observed for Re = 40000 and frequency f_s = 2.08 Hz, that was 3.2 times that of the non-reciprocating case. They concluded that the reciprocating action of the target surface contributed to the increase of spatially averaged Nusselt numbers over the target surface.

The heat transfer of a confined circular jet impinging upon a reciprocating target surface with ribs has been investigated by Chang et al. (2000), for parameters in the range of $10000 < Re < 25000$ and $0.83 < f_s < 1.67$. The reciprocation of the confined target surface arrangement was carried out using a crank-wheel mechanism, similar to the one used by Yang et al. (1999). The correlation between local Nu and Re for a static target surface suggested the presence of secondary flow effects, due to

vortices generated from the ribs, which reduced the convective heat transfer coefficients. They observed a 20% reduction in the convective heat transfer coefficients at the smallest target surface reciprocation frequency, and 240% improvement at the largest frequency, compared to that for the confined static target surface.

Wen (2005) investigated the flow structures and the heat transfer in swirling jet impingement on a heated vibrating target surface. The study was carried out at *Re* between 440 and 27000 and *h*/*d* values between 3 and 16. The target-surface oscillation was sinusoidal with frequencies and amplitudes in the range of 0.3 to 10.19 Hz and 0.5 to 8.1 mm. The flow structures were qualitatively identified using smoke visualization for *Re* = 440 and *h*/*d* = 3 and 8, at f_s = 2.53 Hz and a displacement amplitude A_s = 1.3 mm. The heat transfer investigations, and the presented correlations, showed that *Nu* was strongly dependent on the target surface vibrational parameters and *Re*, which suggested enhancement of heat transfer with increasing frequency and amplitude.

Ichimiya and Yoshida (2009) studied the effect of a confined slot impinging jet of width *b* on a heated oscillating target surface, and provided measurements of turbulence intensities in the flow-field and the heat transfer coefficients. The experimental parameters for this study varied over a range of *Re* between 1000 and 10000, *h/b* between 1 to 4, f_s in the range of 0-100 Hz, and A_s of 0.5 mm and 1 mm. They showed that the jet area from the nozzle exit expanded further outwards from that observed for the static target surface, and the turbulence intensity increased with increasing frequency of oscillation of the surface at *h/b* = 1. The heat transfer estimation showed enhancement, from that for the static target surface, at low *Re* and f_s values, for small nozzle-to-surface separation distances. However, at large separation distances, for higher *Re* and f_s values, the heat transfer was reduced.

A more recent study has been conducted by Klein and Hetsroni (2012) on the heat transfer from a heated vibrating silicon chip placed under a confined impinging micro-slot jet in the range of $756 < Re < 1260$. The slot width was 220 μm and the silicon chip was vibrated in the frequency range of 0-400 Hz and at micro-amplitudes of up to 150 μm using a piezoelectric actuator. A maximum increase of 34% in the heat transfer coefficients was measured for the case of *Re* = 1260 at 246

Hz vibration frequency of the chip at its highest displacement amplitude of 150 μm. They attributed this increase to the renewal of boundary layers caused by the vortices created by the vibration of the target surface.

Nasif et al. (2015) report a numerical investigation of the transient thermal effects in a circular jet impinging onto a reciprocating target surface using a volume-of-fluid (VOF) method. The jet had a Re = 3000 and the target surface oscillated at frequencies of 33 Hz and 100 Hz. They concluded that the cooling of the target surface was more effective at lower velocities of the target surface during its oscillation cycle, and that the maximum heat transfer occurred in the impingement region for the reciprocating target surface. They also found that the occurrence of the maximum Nu at the stagnation point lagged that of the maximum relative velocity between the jet and target surface by a short time.

2.4 Present work

In all of the aforementioned studies on jet impingement on an oscillating target surface, the emphasis was to obtain and examine the convective heat transfer coefficients that occurred in the presence of target-surface oscillation, rather than to study the flow-field characteristics of the impinging jet. Although Ichimiya and Yoshida (2009) reported measurements of turbulence intensities in the impinging-jet flow, the fluid dynamics of the jet interaction with the oscillating target surface has not been examined in detail.

The findings from existing published studies show that the heat transfer coefficients of the impinging jet are enhanced by target-surface oscillation but there is insufficient data to clearly understand and establish the relation between the heat transfer enhancement and the modification of the impinging-jet flow features due to an oscillating target surface. Furthermore, it is known that the mean-flow properties and the turbulence characteristics of the impinging jet are important in the heat removal process (Gardon and Akfirat 1965; Carlomagno and Ianiro 2014), and it is expected that these will change due to the effect of target-surface oscillation. Therefore, the emphasis of the present study is to thoroughly investigate the fluid-dynamics characteristics of a jet impinging on an oscillating target surface, and determine its effect on the resulting heat transfer characteristics.

2.5 Summary

The physics of impinging jet flows was presented with descriptions of the flow features in various regions, namely the free-jet, impingement and wall-jet regions. A literature review of experimental studies of jet impingement on a static target surface has been provided, along with a summary of the findings and a consolidation of the experimental techniques and main experimental parameters used in axisymmetric jet impingement on static target surfaces. Two kinds of moving target surfaces in jet impingement were described. Studies reported on jet impingement on moving target surfaces of the first kind were mentioned. The studies reported on the second kind of target surface motion, which involves an oscillation of the target surface, were reviewed in greater detail due to its relevance in the research described in this thesis.

In order to explore jet impingement on an oscillating target surface, the research was carried out in two parts using two different experimental systems. These systems and their parameters are explained in the next chapter along with the methods used to study them.

Chapter 3
Experimental Systems and Methods

This chapter describes the experimental systems and methods that have been developed and adopted in the present work. It begins with the description of the two experimental systems and the corresponding experimental parameters relevant to the two parts of this study. The specifications of various apparatus used in the system are also provided. This is followed by an elucidation of the experimental methods of hot-wire anemometry, particle image velocimetry, and infrared thermography techniques. The uncertainties in the measurements of the flow and heat transfer quantities are presented at the end of this chapter.

3.1 Experimental systems

One of the first objectives of this study was to establish the required experimental facilities. This establishment was based on an iterative design process that adopted the following steps:

1. Identification of requirements and conditions for the desired experimental system
2. Identification of system variables and constraints
3. Conceptual design of the experimental system
4. Identification and procurement of available equipment and components which meet the experimental requirements and functions
5. Design and fabrication of customized parts required for specific purposes
6. Installation and integration of the experimental sub-systems
7. Testing and evaluation of the experimental system
8. Modification and refinement of parts and sub-systems to achieve desired experimental capabilities

The experimental systems used in the two parts of this study on jet impingement on an oscillating target surface are:

1. Jet impingement on unheated, static and oscillating target surfaces
2. Jet impingement on heated, static and oscillating target surfaces

Experimental system No. 1 was developed primarily to study the fluid dynamics of a jet impinging on an oscillating target surface. Experimental system No. 2 was later developed to study the fluid dynamics of a jet impinging on unheated and heated, static and oscillating target surfaces, and to study both the fluid dynamics and heat transfer of a jet impinging on a heated oscillating target surface. Henceforth, these two systems will be referred to as *jet impingement on unheated target surfaces* and *jet impingement on heated target surfaces* respectively.

In each of these systems, the target surface is placed at a fixed nozzle-to-surface separation distance, or it undergoes oscillation about the same nozzle-to-surface separation distance. This nozzle-to-surface separation distance is called the mean nozzle-to-surface separation distance $(h/d)_m$. The flow characteristics of the impinging jet during its interaction with the oscillating target surface are obtained at various phases (displacement positions) during the oscillation cycle and compared with those obtained when the jet impinges on a static target surface. The jet impingement on a static target surface serves as a control against which to evaluate the effects of target-surface oscillation in the jet impingement system.

The difference between the two experimental systems is the design and construction of the impingement targets. The impingement target surface in the first system is an unheated aluminum sheet, whereas in the second system it is a thin Inconel 600 alloy foil, which is electrically heated. The differences between the two target surfaces are the materials they are made of, their dimensions, and their integration with the oscillation system. In addition, there is no heat supplied to the target surface in the first experimental system. Furthermore, the jet nozzles used in the two systems are distinct but have the same geometry and exit diameters. The details of these two impingement targets are provided in the descriptions of the two experimental systems that follow.

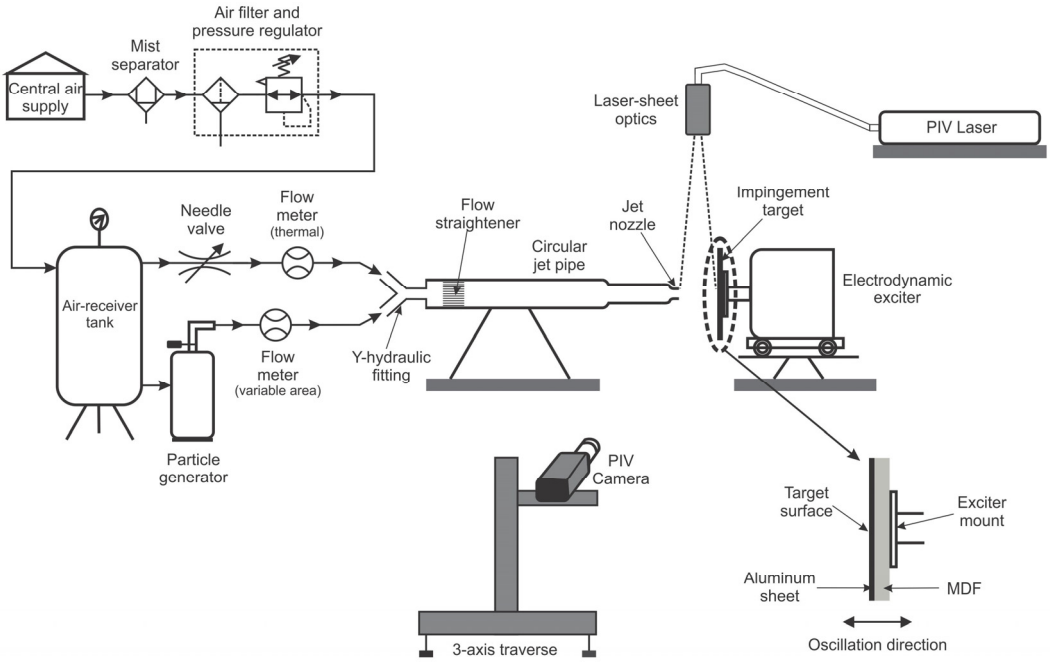

Fig. 3.1 Schematic of the experimental system for jet impingement on unheated target surfaces

A schematic of the experimental system for jet impingement on unheated target surfaces is shown in Fig. 3.1. Compressed air supplied from a central facility is first cleaned using a mist separator and then using an air filter installed within a pressure regulator. The filtered air is stored in an air-receiver tank that acts as a reservoir of continuous and stable supply of pressurized air for the experiments. There are two branches of outflow from the tank; one has a clean air-flow and the other has a flow seeded with particles from a particle generator. The provision of these two flow branches is for better control of the jet exit flow rate and to provide for the required particle seeding density for PIV measurements as will be explained later. The clean air-flow is regulated using a needle-valve fitted to an outlet port on the tank, and its flow rate is measured using a thermal-type flow-meter. Stainless steel nipples, 100 mm long, are attached to the inlet and outlet of this flow-meter to provide straight piping sections in order to reduce measurement inaccuracy.

Another outlet port on the tank provides pressurized air to the particle generator, which is a Laskin nozzle oil-droplet generator. Pressurized air is forced through tiny holes near the end of an inlet pipe that is submerged in the oil filled in the generator vessel. This produces bubbles containing atomized oil droplets because of the shearing action of the pressurized air on the oil. These bubbles then rise to the oil surface and

breakdown to release atomized oil droplets. Large atomized oil droplets are blocked from entering the particle-seeded outflow by an internal impactor plate. The particle volume in the seeded outflow can be controlled by regulating the inlet pressure using a valve installed outside on top of the pressure vessel. Olive oil is used as the seeding material and the seeded particles have an average optical diameter of 1 μm which is considered ideal for PIV measurements in air (Raffel et al. 2013). The seeded flow rate is measured using a variable area flow-meter.

The clean and the seeded air-flows are merged using a Y-hydraulic fitting at the entrance of the jet pipe. This fitting provides a smoother merging of the clean and seeded air-flows when compared to the traditional T-hydraulic fitting. A flow straightener is installed in the entrance of the jet pipe to eliminate any flow swirl generated by the Y-hydraulic fitting. The circular jet pipe is made up of three parts: at the flow entrance is a 400 mm long polyvinyl chloride (PVC) pipe with an inner diameter of 23.4 mm; this section is followed by a 100 mm long PVC pipe of 17.6 mm inner diameter and is attached to a copper reducer coupling that forms the jet nozzle. The jet nozzle has a wall thickness of 1.5 mm and an exit plane inner diameter of 12.6 mm that forms the jet exit diameter d. The nozzle has a straight section of length $0.87d$ downstream of the location where the contraction ends. The total length of the jet pipe ensures adequate mixing of the clean and seeded air-flows so that the jet exits with uniform particle seeding.

All the flow components and hydraulic fittings up to entrance of the jet pipe have a half-inch pipe size and all the flow connection lines are made up of high pressure flexible tubes. The components downstream of the needle valve and the particle generator, up to the jet nozzle exit are installed on a frame made of slotted steel angle sections. A Perspex square box (not shown in Fig. 3.1) with 300 mm sides is placed on this frame and around the jet exit, to increase the ambient particle seeding density. The dimensions of the box are large enough to ensure that the impinging jet is unconfined. The Y-hydraulic fitting is fixed on a rigid cantilever wooden frame to elevate the jet pipe to a position approximately along the center line of the box. As the cantilever arrangement causes the jet pipe to tilt down because of its weight, an alignment screw fixture is provided to align the jet pipe horizontally. The surfaces of the Perspex box and the outside of the jet nozzle are masked with a flat-black adhesive tape to reduce reflections from the laser light.

An expanded view of the unheated impingement target is included in Fig. 3.1. The target surface is a square aluminum sheet measuring 150 mm × 150 mm and 0.5 mm thick. A medium-density fiberboard (MDF), having the same area as the aluminum sheet, and a thickness of 3 mm, is attached to the underside of the aluminum sheet. This provides stiffness to the target surface during the oscillation and eliminates jet-induced vibrations of the target surface. The jet impingement surface of the aluminum sheet is painted with a black enamel to reduce reflections caused by the laser light. The opposite side of the MDF is fixed to the mount of an electrodynamic exciter.

The base of the electrodynamic exciter is fixed on top of a frame with wheels. This arrangement allows for variation of the mean nozzle-to-surface separation distance $(h/d)_m$. The electrodynamic exciter is powered using a power amplifier and the sinusoidal input signal to the exciter is provided via a function generator. The frequency of target-surface oscillation and its displacement amplitude are measured using a single axis accelerometer connected to a double-integrating signal conditioner. The signal conditioner is a battery-powered portable power source which supplies constant current to the accelerometer, and has a bias monitor meter to test the batteries and the operation of the accelerometer and its connecting cables. This unit also has two in-built integrating operational amplifiers with low-pass filtering to provide outputs for velocity and displacement from the acceleration signal. The output from the signal conditioner is read on a digital oscilloscope, with the desired frequencies and displacement amplitudes of the target-surface oscillation being achieved by controlling the corresponding settings of the function generator.

A schematic of the experimental system for jet impingement on heated target surfaces is shown in Fig. 3.2. The impingement target surface is an Inconel 600 alloy foil. The alloy has an electrical resistivity of 103×10^{-8} Ohm-m and its thermal conductivity is 14.8 W/m-K. The foil is 25 μm thick and 156 mm × 156 mm in area.

During the design of this experimental system it was found that the spatial temperature profile of the heated target surface under jet impingement could not be measured from the impingement surface of the foil using an infrared camera. This was because the jet nozzle, which is placed at a short nozzle-to-surface separation distance, hindered placement of the infrared camera close to the target surface at a 90° incidence angle. Moreover, the presence of the infrared camera near the jet nozzle exit would

have created unwanted flow disturbances. Hence the temperature of the foil was measured from its surface opposite to that of jet impingement.

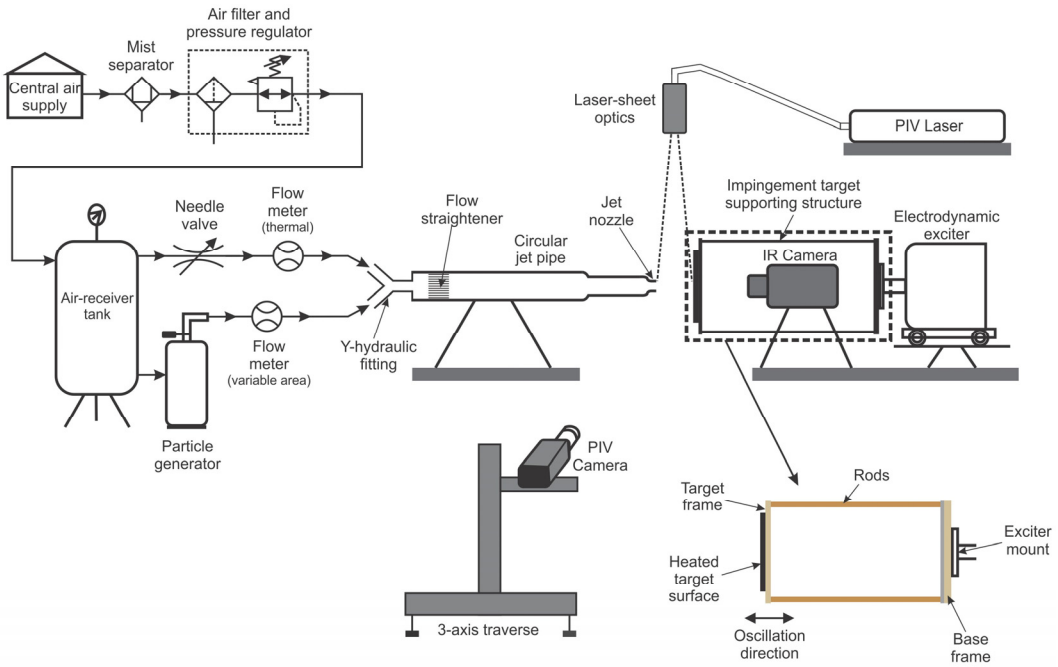

Fig. 3.2 Schematic of the experimental system for jet impingement on heated target surfaces

In order to provide the opposite surface of the foil at a 90° incidence angle to the infrared camera, and to simultaneously have the provision of a heated oscillating target surface, an impingement target supporting structure was fabricated. This structure facilitated the attachment of the heated target surface to the electrodynamic exciter, with the infrared camera placed stationary within the structure as shown in Fig. 3.2. The electrodynamic exciter and the infrared camera are placed on separate custom made scissor-jack platforms to facilitate alignment of the centres of the target surface and the infrared sensor with the jet axis.

An expanded view of the impingement target supporting structure is included in Fig. 3.2. The structure is made of 4 pine wood square rods, each measuring 12 mm × 12 mm and 500 mm in length, attached to the corners of a base frame at the bottom and a target frame at the top. The base frame, which is fixed to the exciter mount, is made of MDF, measuring 200 mm × 200 mm and 3 mm in thickness, reinforced by attaching 0.5 mm thick aluminum sheet of the same area to provide stiffness during

oscillation. Pine wood and MDF have been used in the construction of the supporting structure and its parts, to decrease the exciter payload to the lowest extent possible.

A photograph of the laboratory set-up of the experimental system for jet impingement on heated target surface is shown in Fig. 3.3. It shows the wooden-cantilever frame (2) on which the Y-hydraulic fitting (1) is fixed. The screw (3) for horizontal alignment of the jet pipe (4) is placed downstream of the Y-hydraulic fitting. The Perspex square box (5) placed around the jet pipe is shown in Fig. 3.3. The entire jet pipe sub-system is installed on a frame made of slotted-steel angle sections (6). The laser light-sheet optics (7) is connected to an articulated light guide arm (8) which delivers the laser beam from the PIV laser (9). The jet nozzle (10) is fixed at the end of the jet pipe and is painted black.

The heated target surface (11) is attached to one end of the impingement target supporting structure (12), while the other end consists of a base frame (14) which is attached to the electrodynamic exciter (15). The infrared camera (13) is placed stationary within the oscillating impingement target supporting structure. The infrared camera and the electrodynamic exciter are fixed to scissor-jacks platforms (16), with a DC power supply unit (17) stationed underneath.

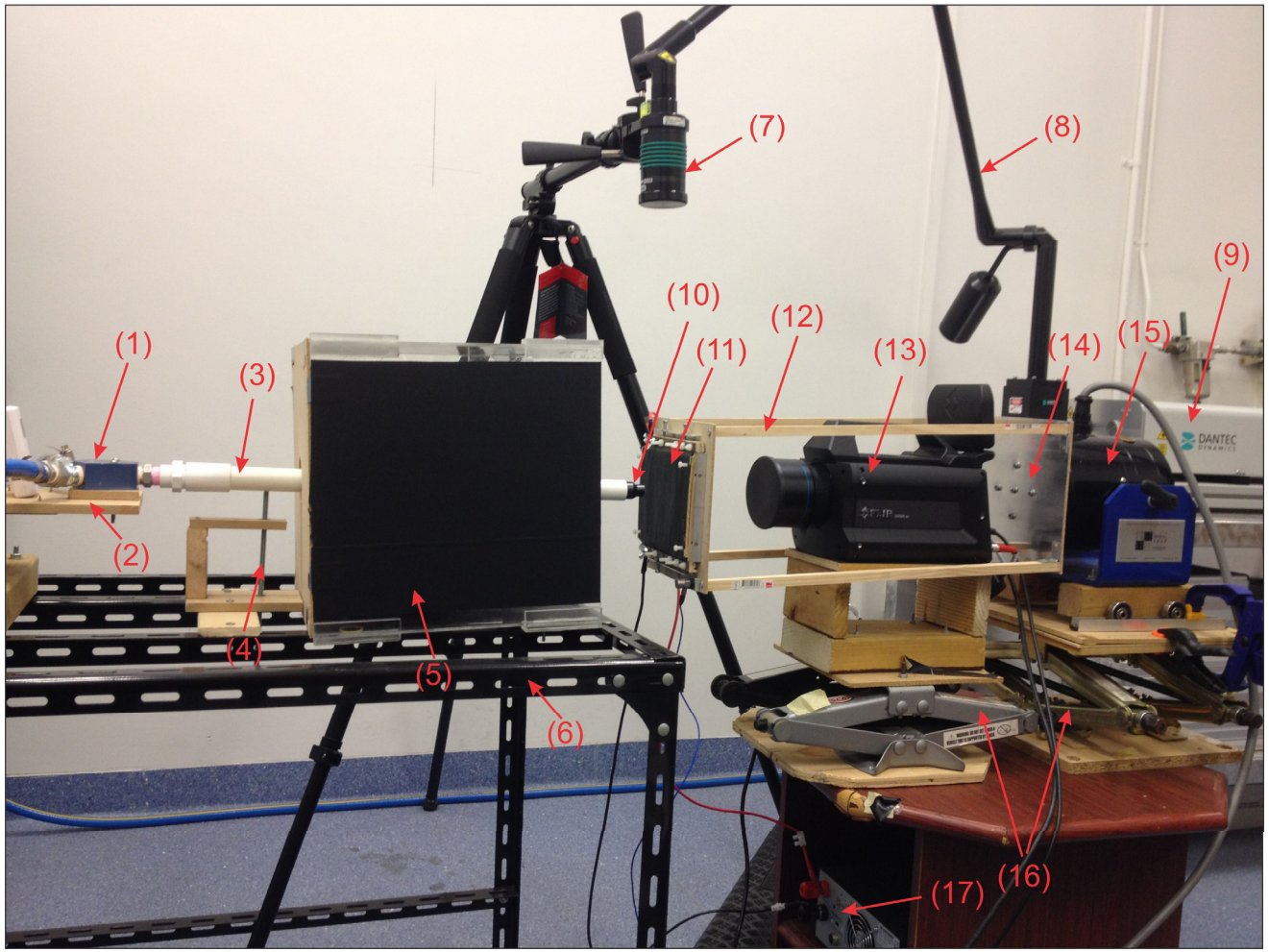

(1) Y-hydraulic fitting
(2) Cantilever frame for (1)
(3) Jet pipe
(4) Horizontal alignment screw for (3)
(5) Perspex square box
(6) Slotted-steel angle sections frame
(7) Laser sheet optics
(8) Articulated light guide arm
(9) PIV laser
(10) Jet-nozzle
(11) Heated target surface
(12) Impingement target supporting structure
(13) Infrared camera
(14) Base frame of (11)
(15) Electrodynamic exciter
(16) Scissor-jack platforms
(17) DC power supply unit

Fig. 3.3 Photograph of the laboratory set-up of experimental system for jet impingement on heated target surfaces

A detailed illustration of the target frame, which has the heated target surface mounted on it, is shown in Fig. 3.4. An isometric view of the target frame is shown in Fig. 3.4(a). The base of the target frame is made of MDF, which is attached to the wooden rods of the supporting structure. The Inconel foil is sandwiched between two copper bus-bars at each of the two sides parallel to the z axis as shown. The foil is sandwiched between the bus-bars using 4 nylon fasteners and 2 steel fasteners on each side to ensure proper electrical contact between the bus bars and the foil. The steel fasteners act as points for electrical connections and voltage measurements.

There are two spring loaded steel fasteners on each of these sides, as shown in Fig. 3.4(a), in order to keep the foil taut along the y direction. Each spring loaded fastener consists of a bolt that passes through a spring and screws into a hex nut. The spring lies in between the bolt hex head and the vertical side of an aluminum angle section, while the hex nut is rigidly fixed inside a wooden spacer which rests on the horizontal side of the aluminum angle section. This is shown in the exploded view of the target frame in Fig. 3.4(b). The bottom bus-bar on each side is attached to the top side of the wooden spacer to provide electrical and thermal insulation between the bus bars and the aluminum angle sections. The free sides of the foil, which are parallel to the y axis and not attached to the bus-bars, rest on wooden spacers to avoid flutter during oscillation.

During testing of the heated oscillating target surface, it was observed that the central area of the foil fluttered when the target-surface oscillation parameters were high. In order to delay this flutter to higher oscillation parameters, a 1 mm thick rubber sheet glued onto a 3 mm thick MDF sheet was inserted between the underside of the foil and top side of the wooden spacers parallel to the y axis; this is shown in Fig. 3.4(b) and also in the side view of the target frame in Fig. 3.4(c). Both the rubber and MDF sheets have dimensions of 156 mm × 120 mm in area and an 80 mm square cut-out at its center.

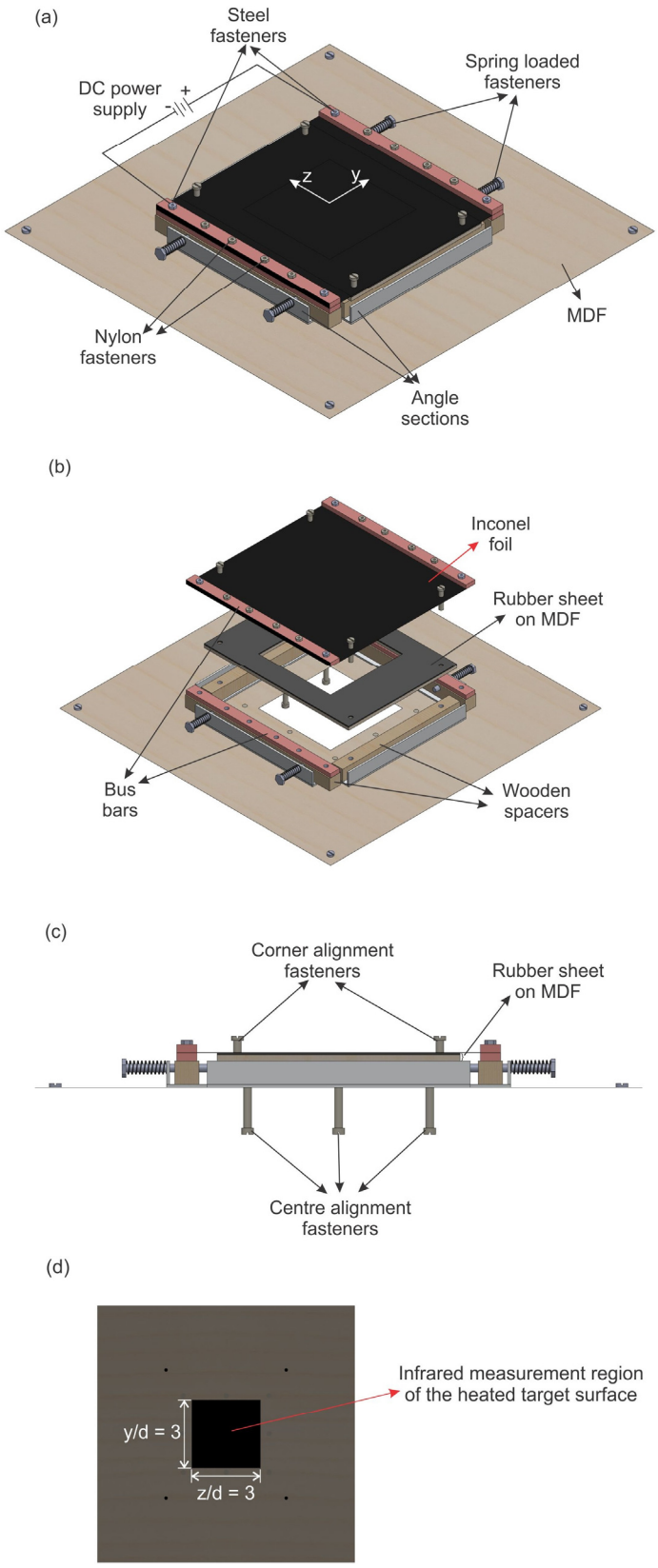

Fig. 3.4 Heated target surface on target frame (a) Isometric view (b) Exploded view (c) Side view (d) View of the surface opposite to jet impingement

To control the tension in the foil along both y and z directions as well as to reduce sag in the central area of the foil, 4 corner alignment fasteners are provided on the top and 8 central alignment fasteners are provided on the bottom, as shown in Figs. 3.4(b) and 3.4(c). All fasteners, except the spring loaded and those meant for electrical connections, are made of nylon to reduce the payload weight and to also provide electrical and thermal insulation. The alignment fasteners also contributed to the reduction of jet-induced vibrations of the foil.

As a result of the above mentioned modifications to the heated target surface arrangement, the measurement region of the foil on the surface opposite to jet impingement was restricted to 80 mm × 80 mm, as shown in Fig. 3.3(d) which shows the view of the target frame that faces the infrared camera. This measurement region covers a circular area within a radius of approximately $y/d = 3$ from the stagnation point. Both surfaces of the foil are painted with a black heat-resistant paint (White Knight Engine Enamel), in order to reduce reflections of the laser light from the target surface on the jet impingement surface, besides providing a constant high emissivity and diffuse reflective surface for radiation detection on the measurement surface. The foil is electrically heated using a direct-current (DC) power supply unit connected to the steel fasteners in the bus bars, as shown in Fig. 3.4(a). These also serve as terminals to measure the potential difference across the foil using a digital multi-meter. The current passing through the foil is measured using a clamp-meter placed around the wire which carries DC current from the power supply to the terminal on the bus bar.

Photographs of the heated target surface on the target frame are shown in Fig. 3.5. The various parts of the heated target surface, as explained in Fig. 3.4, are shown clearly in Fig. 3.5(a). The foil (2) is electrically heated using DC power (1) supplied through the steel fasteners with wing nuts. The black and red wires shown in the photograph carry current from the power supply unit located below. The central nylon fasteners (11) on either sides of heater were removed to prevent obstruction to the laser sheet during PIV measurements. An accelerometer is shown located on the right bottom side of the MDF target frame. The rear view of the heated target surface in Fig. 3.5(b) shows the region for infrared measurements (4), along with the centre alignment fasteners (2).

(a)

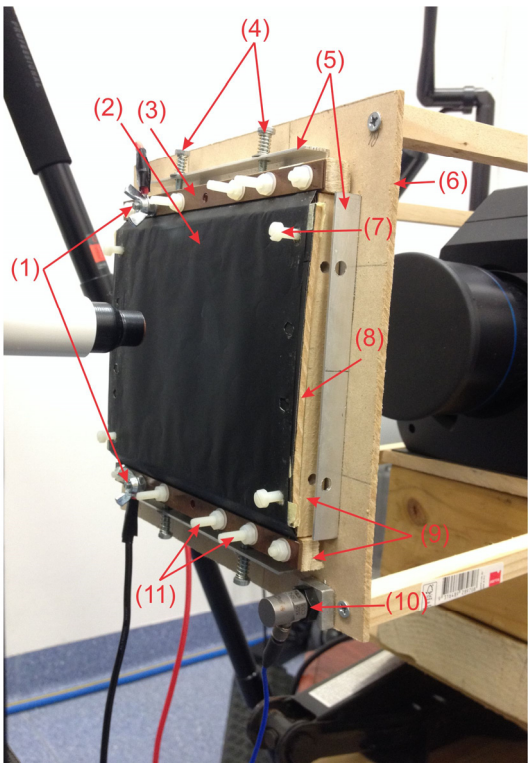

(1) DC power supply through steel fasteners with wing nuts
(2) Inconel foil
(3) Bus-bars
(4) Spring loaded fasteners
(5) Aluminum angle sections
(6) MDF target frame
(7) Corner alignment fasteners
(8) MDF with rubber sheet
(9) Wooden spacers
(10) Accelerometer
(11) Nylon fasteners

(b)

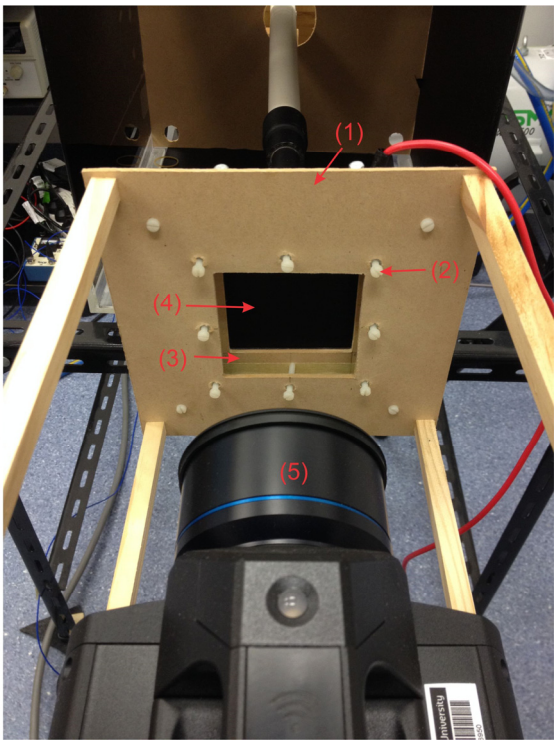

(1) MDF target frame
(2) Centre alignment fasteners
(3) MDF with rubber sheet
(4) Inconel foil (infrared measurement region)
(5) Infrared camera

Fig. 3.5 Photographs of the heated target surface on target frame (a) Isometric view (b) Rear view

3.2 Experimental parameters

The experimental parameters for jet impingement on unheated target surfaces and jet impingement on heated target surfaces are given in Table 3.1. The jet used for both the experimental systems (No. 1 and No. 2) is a single submerged air jet, originating from a circular nozzle of exit diameter d = 12.6 mm. The Reynolds number Re is based on the jet exit diameter d and jet bulk-flow speed U. A dimensional analysis of jet impingement on an oscillating target surface has been carried out to identify important parameters that control the physical system. This analysis is presented in Section I of the Appendix. As the aim of this study is to investigate to the effect of target-surface oscillation on the impinging-jet flow, only target-surface oscillation parameters have been varied while keeping Re and h/d values largely unchanged.

Table 3.1 Parameters for the experimental systems

Experimental system	d (mm)	U (m/s)	Re	$(h/d)_m$
1	12.6	6.21	5200	2.1
2	12.6	6.0	5000	1.95

The values of Re chosen is to ensure that a turbulent jet is studied. Short nozzle-to-surface separation distances have been chosen because:

(i) the surface lies within the range of jet development for which a potential (inviscid) core exists, where the mean axial velocity of the jet is uniform, and turbulence effects play a larger role in the transport process (Gauntner et al. 1970);

(ii) for heat transfer applications, a short nozzle-to-surface separation distance is preferred because, not only does the average heat transfer coefficient increase at this distance as compared to longer separation distances (Martin 1977), but there also exists a secondary annular peak in the heat transfer coefficient at a radial distance of about y/d = 1.5 to 2 from the jet axis (Gardon and Akfirat 1965), in addition to the primary peak at y/d = 0.5 within the stagnation region; the occurrence and locations of these peaks might change in the presence of target-surface oscillation; and,

(iii) the nozzle exit and thereby the jet flow can be influenced by high static pressure over the impingement region (Zuckerman and Lior 2006; Jeffers et al. 2016), and it is likely that the level of influence could change in the presence of an oscillating target surface.

In both the experimental systems, the target surface undergoes sinusoidal oscillation about the mean nozzle-to-surface separation distance $(h/d)_m$, as shown in Fig. 3.6. The position of the mean nozzle-to-surface separation distance, which is where the static target surface is placed in each of the experimental systems, is shown by the horizontal dashed line in Figs. 3.6(a) and 3.6(b). The target-surface oscillation parameters for the two systems are given in Table 3.2. The peak-to-peak displacement amplitudes of target-surface oscillation A_s in the two systems are 2 mm and 2.5 mm, which are approximately 0.16d and 0.2d. The values of (non-dimensional) target surface Strouhal number defined by $St_s = f_s A_s / U$, are also given in Table 3.2. This non-dimensional parameter characterizes the oscillatory motion of the target surface in the impinging-jet flow.

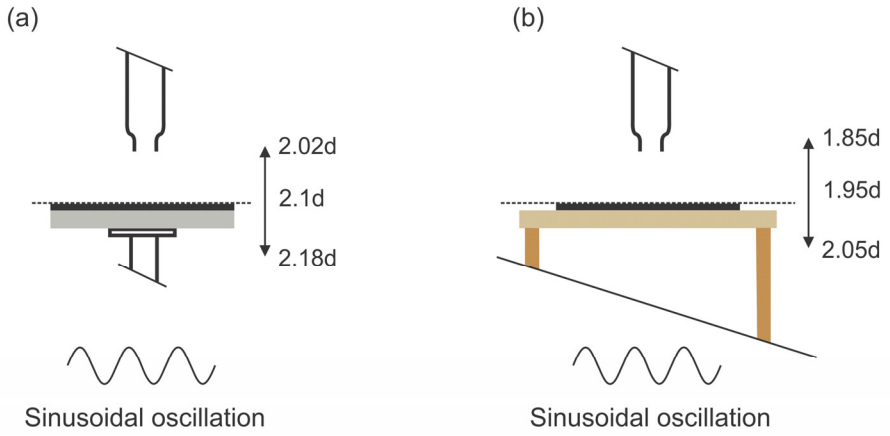

Fig. 3.6 Target-surface oscillation about the mean position (a) Jet impingement on unheated target surfaces (b) Jet impingement on heated target surfaces

Table 3.2 Target-surface oscillation parameters

Experimental system	f_s (Hz)	A_s (mm)	Peak acceleration a_s (m/s^2)	Peak velocity v_s (m/s)	St_s
1	20	2	15.8	0.126	0.0065
	80	2	252.7	0.503	0.0257
2	20	2.5	19.71	0.157	0.0083
	50	2.5	123.41	0.393	0.0208

The choice of target-surface oscillation parameters are based on the bulk jet-flow speed U, and the mean nozzle-to-surface separation distance $(h/d)_m$ such that:

(i) the peak velocities attained by the target surface during oscillation, which are 2.03% and 8.09% of U at the lowest and highest frequency of oscillation, are sufficient to influence the velocities of the impinging jet without causing any reverse flow effects near the jet exit and;

(ii) the peak to peak displacement of the target surface during oscillation, which are 7.62% and 10.25% of the mean nozzle-to-surface separation distances in the two experimental systems, are sufficient to perturb the wall-jet flow region without causing a considerable change in the nozzle-to-surface separation distance. For jet impingement on heated target surfaces, the higher frequency of oscillation was restricted to 50 Hz because of flutter of the Inconel foil above this frequency.

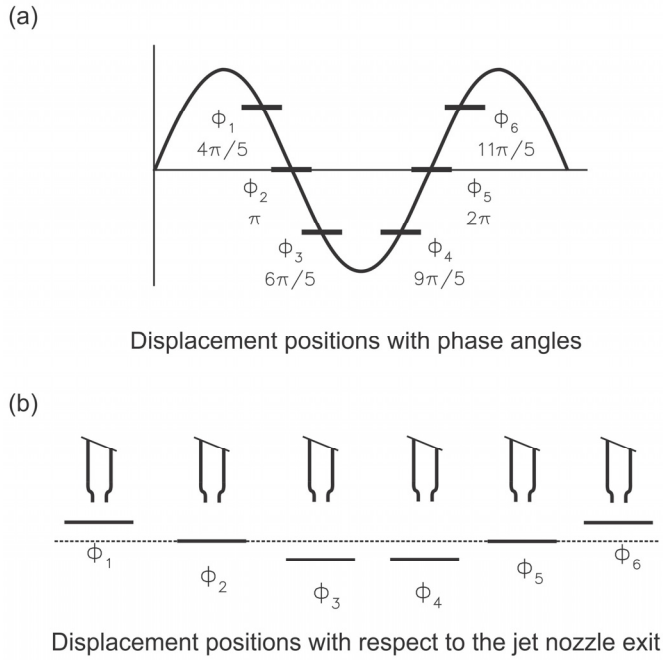

Fig. 3.7 Displacement positions (phases) of target-surface oscillation (a) Examined displacement positions of the oscillating target surface, based on which the results are presented (b) Displacement positions of the oscillating target surface with respect to the jet nozzle exit

In each of these experimental studies, the flow characteristics of jet impingement on an oscillating target surface are measured and analyzed at 6 phases of the target surface for an oscillation cycle, as shown in Fig. 3.7(a) along with the

corresponding phase angles. As illustrated in Fig. 3.7(b), three of these phases (ϕ_1, ϕ_2, ϕ_3) occur when the target surface moves away from the jet nozzle exit, while the other three (ϕ_4, ϕ_5, ϕ_6) occur when the surface moves towards the jet nozzle exit. The physical distance between two consecutive phases, for either of the target surface motions, is approximately 0.5 mm for jet impingement on unheated target surface, and 0.8 mm for jet impingement on heated target surface.

Many components have been used in the fabrication of the two experimental systems. Most of these components were procured, while some of them fabricated in-house to suit the desired requirements. Table 3.3 lists the specifications of these components.

Table 3.3 Specifications of components used in the experimental systems

Component	Make and model	Important specifications
Mist separator	SMC® AFM40	Rated flow 1100 L/min Nominal filtration rating 0.3 µm
Air filter cum pressure regulator	NORGREN® OLYMPIAN B13 M3	Range 0.04 to 1 MPa
Air-receiver tank	PILOTAIR® 100BR-V	Capacity 100 L; Maximum pressure 1.1 MPa
Needle valve	SWAGELOK® SS-26VF8	Stainless steel integral bonnet needle valve
Flow meter (thermal type)	SMC® PFMB7501	Range 5 to 500 L/min Accuracy ±3% of full scale
Flow meter (variable area)	DWYER® VISI-FLOAT	Range 10 to 100 L/min Accuracy of ±5% of full scale
Particle generator	TSI™ 9307	Aerosol flow rate 30 L/min Mean particle diameter 1 µm
Digital thermometer	OREGON SCIENTIFIC®	Temperature resolution of 0.1°C
Digital oscilloscope	RIGOL® DS4000	Sampling rate 4 GSa/s Bandwidth (-3 dB) 100 MHz
Electrodynamic exciter	MODAL SHOP® 2075E	Output force (sine peak) 178 N Stroke length (peak-to-peak) 25.4 mm Maximum acceleration (no payload) 735.75 m/s^2 Maximum payload 3.175 kg
Accelerometer	PCB® ICP® 352C03	Sensitivity 1.02 mV/(m/s^2) Measurement range ±4900 m/s^2 peak Broadband resolution 0.005 m/s^2 rms Frequency range (±5%) 0.5 to 10000 Hz
Signal conditioner for accelerometer	PCB® 480B10	Sensitivity-velocity 3.94 mV/(m/s) peak Sensitivity-displacement 0.79 V/mm peak-to-peak
Function generator	MATRIX® MFG-8216A	Frequency range 0.3 to 3 MHz Amplitude ≥ 10 V (peak-to-peak) Sine wave distortion ≤ 1%
Multi-meter	DIGITECH® QM1535	DC Voltage accuracy ±(0.8% +3 digits)
Clamp-meter	ISO-TECH® ICM A1	DC Current accuracy ±(1.5% +10 digits)
DC power supply	B&K PRECISION® 1693	Variable output voltage 1 to 15 V Maximum output current 60 A
Emissometer	D&S® Model AE	Infrared wavelength range 3 to 30 µm

3.3 Hot-Wire Anemometry (HWA)

A cross-wire hot-wire probe connected to a thermal anemometer was used to measure the frequency of vortices in the shear-layer of the free-jet in the absence of the impinging target. The sensing elements in the cross-wire probe were oriented 45° with respect to each other and made of platinum coated tungsten wires 3.8 μm in diameter and 1.27 mm in length. The thermal anemometer, supplied by TSI™, was an 8 channel IFA 300 Constant Temperature Anemometer (CTA) with a frequency response of up to 300 kHz. The anemometer was interfaced to a computer and all operations including setup, calibration and data-acquisition were software controlled.

Prior to obtaining flow measurements the hot-wire probe was calibrated over a velocity magnitude range of 0 to 20 m/s using a TSI™ 1127 Air Velocity Calibrator, which employed a differential-pressure based velocity determination. The calibration data was fitted using a 4th order polynomial equation given by

$$U_{cal} = a_0 + a_1 E + a_2 E^2 + a_3 E^3 + a_4 E^4 \tag{3.0}$$

where U_{cal} is the calibration velocity, E is the sensor voltage, and a_0 to a_4 are the calibration constants. The curves fitted to the calibration data points for the two cross-wire sensors are shown in Fig. 3.8. The calibration constants $(a_0, \ldots, a_4)$ for sensor 1 are (37.682, -158.522, 252.985, -188.454, 58.113), and for sensor 2 they are (30.581, -133.048, 218.026, -165.325, 51.246).

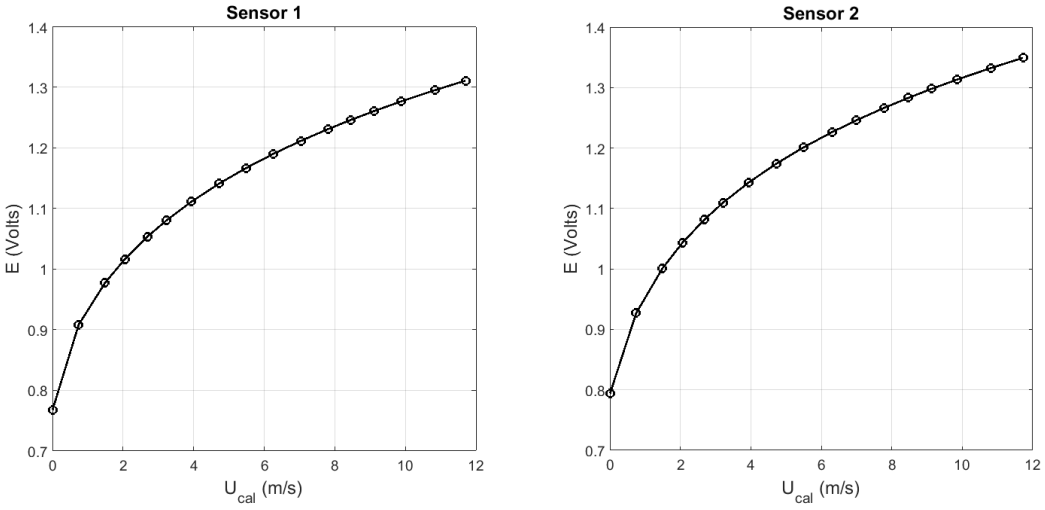

Fig. 3.8 Hot-wire probe calibration curves (a) Sensor 1 (b) Sensor 2

Velocity components in the free-jet were measured by placing the probe at various locations in the shear region, as will be shown in Chapter 4. The acquisition frequency and number of samples were set at 4 kHz and 64 kpt (1 kpt = 1024 samples) which resulted in a recording time of 16.384 s. The hot-wire signal was filtered through a low-pass filter of 1 kHz. The frequency of formation of shear-layer vortex structures was then determined from the spectral analysis of the radial velocity component measured by sensor 2 of the cross-wire probe. Single sample spectra with a sample size of 512 were computed with a spectral resolution of 4 Hz and an uncertainty of 4 Hz/sample.

3.4 Particle Image Velocimetry (PIV)

A time-resolved two-dimensional PIV system supplied by Dantec Dynamics® was used in this study. The PIV system has a Q-switched diode-pumped dual-cavity Nd:YLF laser, which is synchronized with a high speed camera to capture single-exposure double-frame images of the illuminated flow field. The PIV camera is equipped with a macro lens and is mounted on a 3-axis traverse as shown in Figs. 3.1 and 3.2. The specifications of the PIV system are listed in Table 3.4.

Table 3.4 PIV system specifications

Parameter	Value
PIV laser – LITRON® LDY304	
Repetition Frequency	10 kHz (per laser cavity)
Pulse energy	30 mJ at 1 kHz (per laser cavity)
Wavelength	527 nm
Pulse duration	~ 150 ns
Laser beam profile	Gaussian
Beam-quality-factor	$M_x^2 = 12$ $M_y^2 = 8$
PIV camera – Phantom® Miro 310 with AF Micro-Nikkor lens	
Sensor type and size	CMOS, 1200 × 800 pixels
Pixel size and depth	20 μm, 12-bit
Trigger rate	1600 Hz for double-frame acquisition
Internal memory	3 GB
Lens focal length	f = 200 mm
Lens aperture range	$f\#$ = 4 to 32

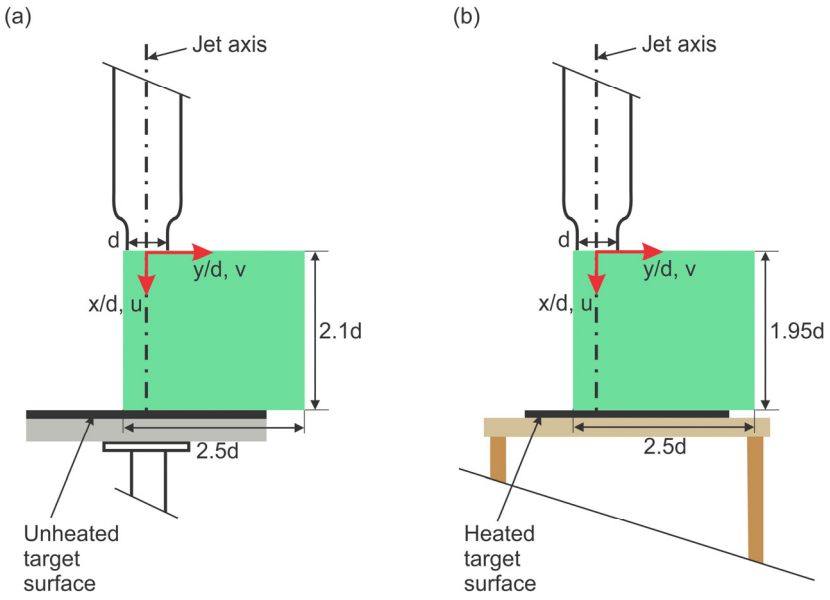

Fig. 3.9 PIV measurement areas (shown in green) and axes location: (a) Jet impingement on unheated target surfaces (b) Jet impingement on heated target surfaces

The laser sheet optics attached to the output arm of the laser illuminates a plane of symmetry that passes through the center of the jet exit, as shown in Figs. 3.1 and 3.2. The area of PIV measurements in the impinging jet are shown as the green shaded regions in Fig. 3.9 for the two experimental systems. As the circular-jet impingement flow is axisymmetric, this area was configured to cover only one-half of the illuminated flow regions. The *x*-axis in the PIV image frame is parallel to the jet axis while the *y*-axis is perpendicular to the jet axis. The measurement areas shown in Fig. 3.9 are for the static target surface of the corresponding experimental systems. During oscillation of the target surface, the *x* dimension of the measurement area changes as the nozzle-to-surface separation distance varies between the peak values shown in Fig. 3.6. The field of view of the camera is set in such a way that it always covers the area between the jet exit and these extrema of the target surface. Figure A1 in Section II of the Appendix shows a sample PIV image with the full field of view. The *y* dimension of the measurement area remains unchanged during the target-surface oscillation. The PIV recording parameters used in the two experimental systems are given in Table 3.5.

Table 3.5 PIV recording parameters for the two experimental systems

Parameter	Value
Lens aperture	$f\# = 8$
Magnification	≈ 0.4
Physical pixel size	0.05 mm
Field of view	≈ $5d \times 3d$ ($x \times y$)
Pulse delay:	
Jet impingement on unheated target surfaces	21 μs
Jet impingement on heated target surfaces	25 μs
Light sheet thickness	≈ 1 mm
Image interrogation area	16 ×16 pixels with 50% overlap
Physical interrogation area	0.8 × 0.8 mm^2
Depth-of-field	1.65 mm
Dynamic velocity range	28
Dynamic spatial range	442
Physical spatial resolution	0.031d (≈ 0.4 mm)
Frequency of PIV image acquisition:	
Static target surface (unheated and heated)	100 Hz
Target surface oscillating at 20 Hz (unheated and heated)	200 Hz
Target surface oscillating at 50 Hz (heated)	500 Hz
Target surface oscillating at 80 Hz (unheated)	800 Hz

The laser light-sheet plane was aligned to coincide with the center of the jet exit cross-section and perpendicular to the target surface plane. The orientation of the laser light sheet plane was set perpendicular to the camera lens plane to minimize image perspective errors. The seeding density was adjusted so that the PIV images have a high image density and have at least 5 particle images per interrogation area for the cross-correlation analysis. The loss-of-pairs in the double-frame images was reduced by the flow straightener installed at the entrance of the jet pipe that minimized out-of-plane particle displacements by eliminating swirl in the jet flow, and also by suitably adjusting the light sheet thickness.

A rigorous selection of lens f-number and magnification was carried out to ensure that all images of the seeding particles within the light sheet were focused, and that the size of the seeded particle images was at least 2 pixels in diameter to minimize the effect of pixel-locking (Fig. A4 in Section III of the Appendix). The optimal f-number was determined to be 8, such that the depth of field was greater than the light-

sheet thickness. The time between pulses was optimized to ensure that the maximum displacement of the particles was less than 4 pixels (one quarter rule) (Fig. A5(a) in Section III of the Appendix). The geometric calibration of the PIV image was done using a calibration target developed in-house. The calibration target consisted of laser etched dots in a 5 mm × 5 mm grid on a glass piece measuring 150 mm × 100 mm in area. The practical design rules for PIV measurements (Adrian and Westerweel 2011; Dantec Dynamics 2005) were followed in this study.

The frequency of acquisition of the double-frame images was based on the integral time scale of the flow, to ensure that each acquired image pair is statistically time independent of the other. The integral time-scale of the flow, given by $t_l = d/U$ is approximately 2 ms for both the experimental systems. For jet impingement on a static target surface in both the experiment systems, the frequency of acquisition was set at 100 Hz, so that the time between successive image pairs is 5 times the integral time scale. For jet impingement on an oscillating target surface in both the experimental systems, the double-frame images were captured at higher acquisition rates of 10 times the frequency of oscillation, as shown in Table 3.5. This was done in order to measure the transient flow characteristics at various phases of the target surface in an oscillation cycle.

In order to minimize the uncertainties in the measurements of the mean velocity components and the turbulent statistics, 1000 images were acquired for both the static and oscillating target surfaces in the two experimental systems. To evaluate the statistical quantities at various phases of the target surface during oscillation, 1000 images were extracted corresponding to a given phase of the target surface in an oscillation cycle. In other words, the phase-averaged statistics for jet impingement on an oscillating target surface in the two experimental systems were obtained by averaging over 1000 cycles at a given phase. 10 ensembles of 1000 double-frame images each were acquired for each of the oscillating target surface, and 100 images from each ensemble for a given phase were scanned and extracted to the pixel level precision of the displacement of the target surface. The time between successive image pairs in the acquisition at a particular phase is equal to the time period of target-surface oscillation, which when compared with integral time scale shows that the image pairs are statistically time-independent.

The images were acquired and analyzed using dedicated software (DynamicStudio) available with the PIV system. The undesirable image regions upstream of the nozzle exit and behind the target surface were masked. Sample images showing a raw PIV image and a masked PIV image are presented in Section II of the Appendix. The velocity vectors were calculated over the region of interest with an interrogation area of 16 × 16 pixels (50% overlap) using a multi-pass multi-grid digital cross-correlation method with deforming windows and sub-pixel refinement modules (Willert and Gharib 1991; Soria 1996; Scarano 2001). The initial interrogation area was 128 × 128 pixels with 2 passes per interrogation domain and a 3-step grid refinement. The raw velocity vectors were validated based on a minimum peak ratio (between the 1st and 2nd peak in the interrogation area) of 1.2 and a minimum peak width of 2 pixels, along with a local median validation in a neighborhood of 5 × 5 pixels. The resulting velocity vector maps were then scanned for any outliers (Westerweel and Scarano 2005) based on a detection threshold of 1.5 and the rejected vectors (if any) were substituted by a median vector. The maximum particle displacement was determined to be less than 3 pixels, and the spatial resolution between the resulting velocity vectors is 0.031*d*, i.e. approximately 0.4 mm.

3.5 Infrared Thermography (IRT)

The infrared camera used to measure temperature of the heated foil under jet impingement was a FLIR® X6540sc medium infrared wave (1.5 to 5.5 μm) camera, with specifications as listed in Table 3.6.

Table 3.6 Infrared camera specifications

Parameter	Value
Detector type	Indium Antimonide (InSb)
Sensor size	640 × 512 pixels
Pixel size and depth	15 μm, 14-bit
Frame rate	126 Hz at full resolution
Lens focal length and aperture	f = 12 mm, f/2
Angular field of view	Horizontal 43.6° Vertical 35.49°
Accuracy	±1 °C between 5 °C to 100 °C

The "heated thin-foil" technique proposed by Carlomagno and Cardone (2010) has been used to measure steady-state time-averaged local convective heat transfer coefficient between the heated target surface and the impinging jet. The foil is

uniformly Joule heated which provides a constant convective heat flux boundary condition. The foil is considered to be thermally thin as the total Biot number $Bi = h_{conv}s_{\mathrm{f}}/k_{\mathrm{f}} << 1$, where s_{f} and k_{f} are the Inconel foil thickness and thermal conductivity respectively. This means that the temperature can be assumed to be constant across the thickness of the foil, which allows measurement of the foil temperature from the surface opposite to jet impingement as is done in this study. The convective heat transfer coefficient is calculated by performing a steady state energy balance of the heated foil per unit area per unit time, as shown in Fig. 3.10 and given by

$$Q_{\mathrm{j}} = Q_{\mathrm{fconv}} + Q_{\mathrm{rad}} + Q_{\mathrm{nconv}} + Q_{\mathrm{cond}} \tag{3.1}$$

where Q_{j} is the input Joule heat flux, Q_{fconv} is the forced convective heat flux, Q_{rad} is the radiative heat flux from the two surfaces of the foil, Q_{nconv} is the natural convective heat flux from the surface of the foil opposite to jet impingement, and Q_{cond} is the conduction heat flux within the foil. The local convective heat transfer coefficient is defined as

$$h_{\mathrm{conv}} = \frac{Q_{\mathrm{fconv}}}{T_{\mathrm{w}} - T_{\mathrm{aw}}} = \frac{Q_{\mathrm{j}} - Q_{\mathrm{rad}} - Q_{\mathrm{nconv}} - Q_{\mathrm{cond}}}{T_{\mathrm{w}} - T_{\mathrm{aw}}} \tag{3.2}$$

where T_{w} is the local wall temperature and T_{aw} is the local adiabatic wall temperature.

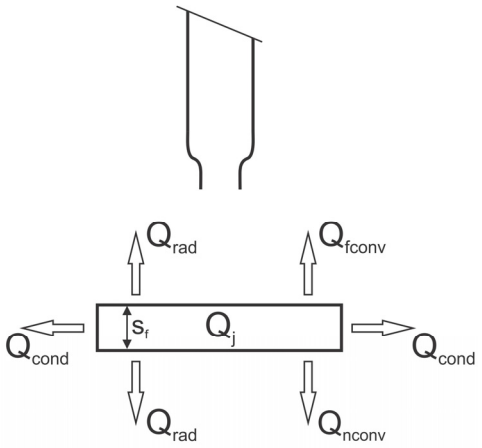

Fig. 3.10 Energy balance of the heated target surface

The input Joule heat flux is

$$Q_{\mathrm{j}} = \frac{VI}{A} \tag{3.3}$$

where V is the potential difference across the electrically heated foil, I is the current supplied, and A is the total heated area of the foil. The radiative heat flux is given by

$$Q_{\mathrm{rad}} = 2\varepsilon\sigma(T_{\mathrm{w}}^4 - T_{\mathrm{a}}^4) \tag{3.4}$$

where ε is the measurement surface emissivity coefficient, σ is the Stefan-Boltzmann constant, and T_{a} is the ambient temperature. The emissivity of the black-paint coated foil was measured using a suitable emissometer and was found to be 0.88. The laboratory ambient temperature during experiments was T_{a} = 21.7 $^{\circ}$C measured using a digital thermometer and was found to be

The natural convective heat flux is determined from the correlation between Nusselt number Nu and Rayleigh number Ra for a vertical flat plate provided by Fujii and Imura (1976). The natural convective heat flux is given by

$$Q_{\mathrm{nconv}} = \frac{0.56kRa^{1/4}(T_{\mathrm{w}} - T_{\mathrm{a}})}{(A/P)} \tag{3.5}$$

where $Ra = GrPr$ and $Gr = \frac{(A/P)^3 g\beta(T_w - T_a)}{\nu^2}$

In the above equation, the Grashof number Gr is based on a length scale A/P, which is the ratio of the foil area to its perimeter. The Prandtl number Pr of air is taken to be 0.71, β is the volumetric thermal expansion coefficient of air, which is taken to be $1/T_{\mathrm{a}}$, and ν is the kinematic viscosity of air at ambient temperature. The conduction heat flux within the foil is given by (Astarita and Carlomagno 2010)

$$Q_{\mathrm{cond}} = -s_{\mathrm{f}}k_{\mathrm{f}}\nabla^2 T_{\mathrm{w}} \tag{3.6}$$

The Laplacian operator is evaluated along the spatial coordinates of the target surface as given by

$$\nabla^2 T_{\mathrm{w}} = \frac{\partial^2 T_{\mathrm{w}}}{\partial y^2} + \frac{\partial^2 T_{\mathrm{w}}}{\partial z^2} \tag{3.7}$$

The Nusselt number Nu is then determined from

$$Nu = \frac{h_{\mathrm{conv}} d}{k} \tag{3.8}$$

The frequencies of acquisition of the thermal images for jet impingement on a heated static target surface is 10 Hz, while those for heated target surfaces oscillating at 20 Hz and 50 Hz, are 50 Hz and 125 Hz respectively, following the Nyquist criteria of sampling frequency. For each of these cases, the measurements consists of two parts. In the first, the adiabatic wall temperature T_{aw}, which is the temperature of the foil without supply of electrical power, i.e. when Q_{j} = 0, is measured with the jet impinging on the target surface. In the second, the wall temperature T_{w} is measured when the foil is electrically heated and with the jet impinging on the target surface. In each of these measurements, 2000 images are acquired upon reaching steady-state conditions, in order to reduce the effect of measurement noise in the time-averaged temperatures. The quantity (T_{w}-T_{aw}) in (3.2) is then obtained by subtracting the time-averaged target surface temperatures, obtained with and without the supply of electrical power, from each other.

The electrical power supplied yields a Joule heat flux value of Q_{j} = 682 W/m^2, which results in the average foil temperature in the measurement region to attain a value about 23 $^{\circ}$C higher than the ambient temperature. The geometrical calibration of the infrared thermal images is performed using an in-house calibration target that has circular holes of 2 mm diameter laser cut in a 10 mm × 10 mm grid into a Perspex sheet. The Perspex sheet measures 150 mm × 110 mm in area and is coated with a black paint. The convective heat transfer measurements are conducted separately from the PIV flow measurements.

3.6 Uncertainty analysis

The uncertainty in the velocity measurements obtained using hot-wire anemometry is ± 1.81%. The PIV measurement error in the estimation of a displacement vector is expressed as a sum of the bias and random errors. In addition, there is also a sampling error that arises due to ensemble averaging used for the determination of statistical quantities. The bias error is very small when compared to the PIV random error, and is usually negligible if the particle image diameter is about 2 pixel units, which minimizes the pixel-locking bias error as well (Raffel et al. 2013). The sample PIV images and pixel displacement histograms presented in Section III of the Appendix show that the PIV recordings are free from any pixel locking effects.

In flows having a high turbulent intensity, such as jet flows, the PIV random error is small when compared to the root-mean-square (rms) of the velocity fluctuations (Adrian and Westerweel 2011). In the present jet flow, the rms of the axial velocity fluctuations in the free-jet shear layer is *O*(10) larger than the PIV random error. Therefore, the uncertainties in the data presented here are only for the statistical sampling analysis averaged over 1000 image pairs. The uncertainties in the measurements of the mean velocity components and the determination of turbulence statistics are calculated based on the methods outlined by Benedict and Gould (1996) and Adrian and Westerweel (2011). The uncertainty values of the quantities reported in Table 3.7 are percentage relative uncertainty estimates with a 95% confidence interval. The details of their calculations have been provided in Section III of the Appendix.

Table 3.7 Uncertainty estimates for ensemble-average quantities obtained from PIV measurements

Quantity	Percentage relative uncertainty
Mean axial velocity $\overline{u}$	0.23
Mean axial velocity $\overline{v}$	1.20
RMS axial velocity fluctuation u_{rms}	3.94
RMS radial velocity fluctuation v_{rms}	4.61
Reynolds stress $\overline{u'v'}$	8.61
Turbulence kinetic energy TKE	5.90

The uncertainties in the computation of derived quantities such as the strain rates and the vorticity are reported in Table 3.8. These have been calculated using a

root-sum-square uncertainty analysis method (Moffat 1988) applied to the central finite difference formulas for the corresponding velocity gradients. These formulas and the uncertainty equations are presented in Section III of the Appendix.

Table 3.8 Uncertainty estimates for derived flow quantities obtained from PIV measurements

Quantity	Uncertainty (± s^{-1})
Mean axial strain rate	0.028
Mean radial strain rate	0.109
Mean shear strain rate	0.056
Vorticity	0.113

The relative uncertainties in the measurement of heat transfer quantities are calculated based on the methods outlined by Moffat (1988), and are reported in Table 3.9 with a 95% confidence interval. The details of these calculations are presented in Section IV of the Appendix. The uncertainties in the local wall temperature T_w and the local adiabatic wall temperature T_{aw} were measured at the stagnation point in jet impingement on a heated static target surface. The total uncertainty estimated in the determination of *Nu* is ± 3.02%. The maximum radiation heat flux Q_{rad}, Equ. (3.4), and the maximum natural convection heat flux Q_{nconv}, Eqn. (3.5), are estimated to be 11.30% and 6.00% of the Joule heat flux Q_j. The tangential conduction heat flux in the foil Q_{cond}, determined by Eqns. (3.6) and (3.7), shows that the maximum conduction loss in the foil due to tangential temperature variation in the measurement region is only 0.50% of Q_j, and hence has been neglected in the calculation of the heat transfer results.

Table 3.9 Uncertainty estimates for quantities obtained from IRT measurements

Quantity	Percentage relative uncertainty
Electrical potential difference across the foil *V*	0.43
Current supplied to the foil *I*	0.88
Local wall temperature T_w	0.39
Local adiabatic wall temperature T_{aw}	0.36
Ambient temperature T_a	0.46
Joule heat flux Q_j	0.97
Radiative heat flux Q_{rad}	3.29
Natural convection heat flux Q_{nconv}	3.29
Nusselt number *Nu*	3.02

3.7 Summary

A detailed description of the two experimental systems used in the present study, i.e., jet impingement on unheated static and oscillating target surfaces and jet impingement on heated static and oscillating target surfaces, has been provided. The experiment parameters for these two systems have been detailed and the examined displacement positions (phases) of the oscillating target surface have been illustrated. The experiment methods of PIV and IRT have been elucidated and the specifications and recording parameters of the PIV laser and camera as well as the infrared camera have been outlined. Finally, the relative uncertainties in the measurements obtained from PIV and IRT have been presented.

Part I

Jet Impingement on Unheated Static and Oscillating Target Surfaces

Chapter 4

Results and Discussion: Jet Impingement on Unheated Target Surfaces

The results of the first part of this study, which involves jet impingement on unheated static and oscillating target surfaces are presented in this chapter. The results commence with the characterization of the free-jet followed by a validation of the present methods by comparing results for jet impingement on a static target surface with available published work. The fluid-dynamics characteristics of a jet impinging on an unheated oscillating target surface are then presented in detail through a discussion of

i. Instantaneous flow fields;
ii. Mean flow characteristics and wall-shear stress;
iii. Proper Orthogonal Decomposition (POD) analysis;
iv. RMS axial and radial velocity fluctuations; and,
v. Reynolds stress and turbulence kinetic energy.

For each quantity the results obtained for an oscillating target surface are compared with a static target surface. The measured velocity field has been decomposed into its mean and fluctuating velocity parts. The details of this decomposition and the computation of rms velocity fluctuations and Reynolds stress are presented in Section III of the Appendix. A triple decomposition of the velocity field into its mean, phase-correlated, and, fluctuating velocity parts (Hussain and Reynolds 1970; Soria 2015) has not been performed in this comparative analysis as a triple decomposition of the velocity field for jet impingement on a static target surface results in a zero phase-correlated velocity.

Locations in the x-y plane are expressed non-dimensionally based upon the jet nozzle exit diameter d, with the origin located at the center of the nozzle exit, as shown in Fig. 3.8(a). The mean velocity components and the turbulence statistics are expressed non-dimensionally based on the mean-centerline jet exit velocity ($\overline{u}_{cj}$) of jet impingement on an unheated static target surface.

4.1 Characterization and validation

The characterization of a free-jet flow, and the validation of jet impingement on a static surface were performed with a view to establishing the quality of the jet flow created by the experimental system, and to confirm the integrity of the experimental procedure and analysis of results obtained using the PIV system.

4.1.1 Characterization of the free-jet

The flow characteristics of the free-jet (in the absence of the target surface) are shown in Figs. 4.1 and 4.2. The mean axial velocity and turbulence intensity profiles near the jet nozzle exit at $x/d = 0.2$ are shown in Fig. 4.1(a). The gradual drop in the axial velocity observed near the edges of the nozzle is due to the nozzle geometry; in particular, due to the length of the straight section after the contraction. This contributes to a larger boundary-layer displacement thickness of the flow within the nozzle when compared to a short axisymmetric nozzle that generates a rectangular jet-exit velocity profile (Tesar 2008). The turbulence intensity near the jet-nozzle exit at $x/d = 0.2$, in the region close to the center of the jet, is about 4%, and increases to about 17% near the jet edge.

The velocity profiles up to a downstream distance of $x/d = 2$ in Figs. 4.1(b) to 4.1(d) show that the flow is dominated by the potential-core region, in which the centerline jet exit velocity remains almost constant; this region corresponds to the red coloured contour in Fig. 4.2. As the downstream distance increases, disturbances in the flow begin to penetrate towards the jet axis from the adjacent free-shear layer as the jet mixes with the ambient fluid and expands radially. This increases the turbulence intensity near the jet centerline as seen in Figs. 4.1(b) to 4.1(d). The variation of the jet-centerline turbulence intensity with x/d is overlaid in Fig. 4.2. It shows that at a downstream distance of $x/d = 2$ the jet-centerline turbulence intensity is twice (8%) that at the jet nozzle exit. These results are found to be consistent with typical free-jet flows (Capone et al. 2013).

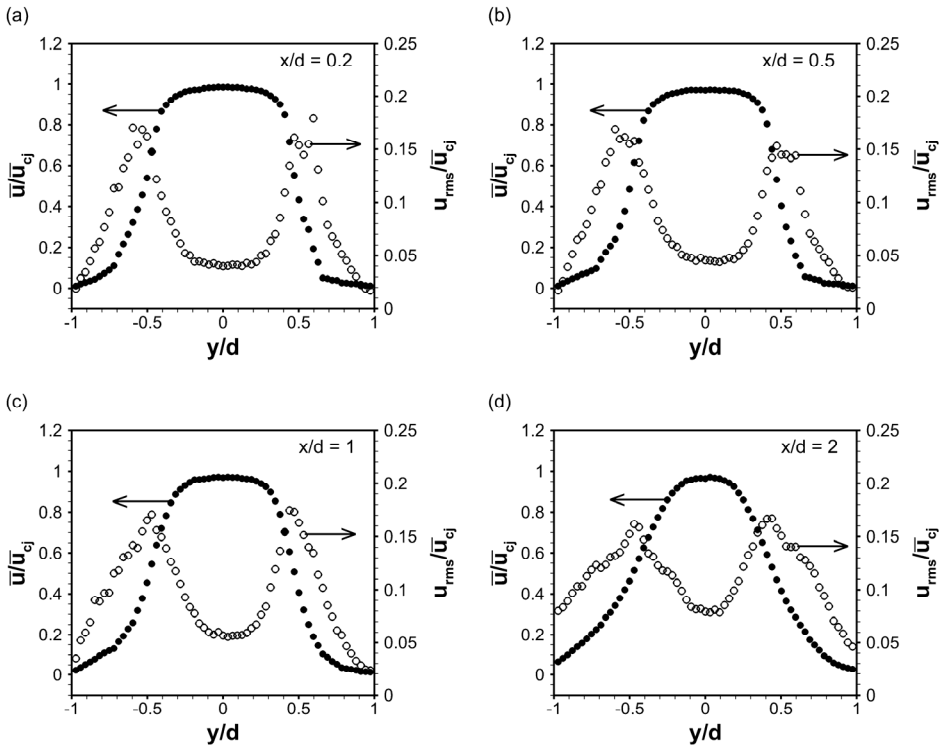

Fig. 4.1 Free-jet mean axial velocity and turbulence intensity profiles at various downstream locations: (a) $x/d = 0.2$; (b) $x/d = 0.5$; (c) $x/d = 1$; (d) $x/d = 2$. These results are obtained in the absence of the target surface.

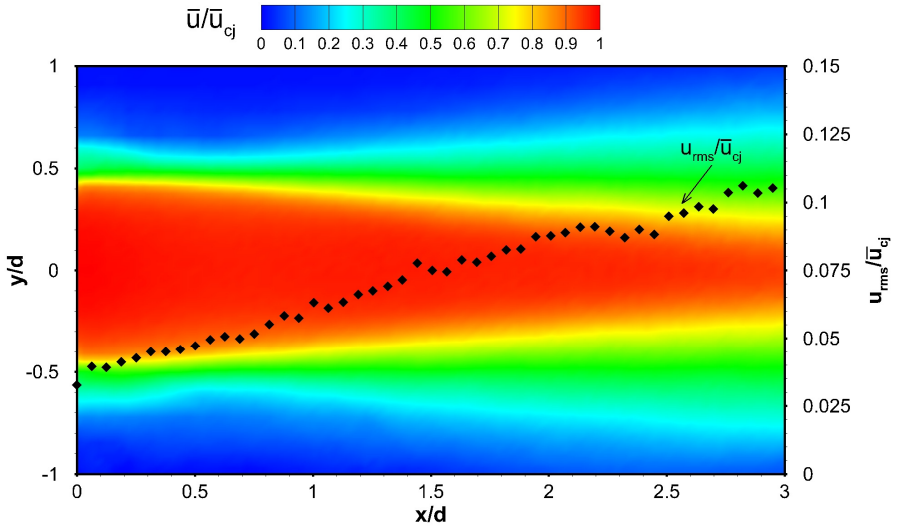

Fig. 4.2 Free-jet mean axial velocity contour and variation of jet-centerline turbulence intensity

The frequency of formation of vortex structures f_j in the free-jet shear layer was determined from spectral analysis of the radial velocity v. The radial velocity was measured using a cross-wire hot-wire probe connected to a thermal anemometry system, as explained in Section 3.3, and placed at various spatial locations in the shear layer. The power spectrum of radial velocity at three of those spatial locations (P1, P2, and P3) is shown in Fig. 4.3. The spatial locations of the probe with respect to the jet exit, marked as X in the corresponding colours, are shown in the inset of Fig. 4.3; these locations are in the vicinity of $x/d = 1$. The frequency of formation of vortex structures f_j is the dominant frequency in the spectrum, which is 230.5 Hz. This gives a Strouhal number for the free-jet, defined as $St = f_j d/U$, a value of 0.467.

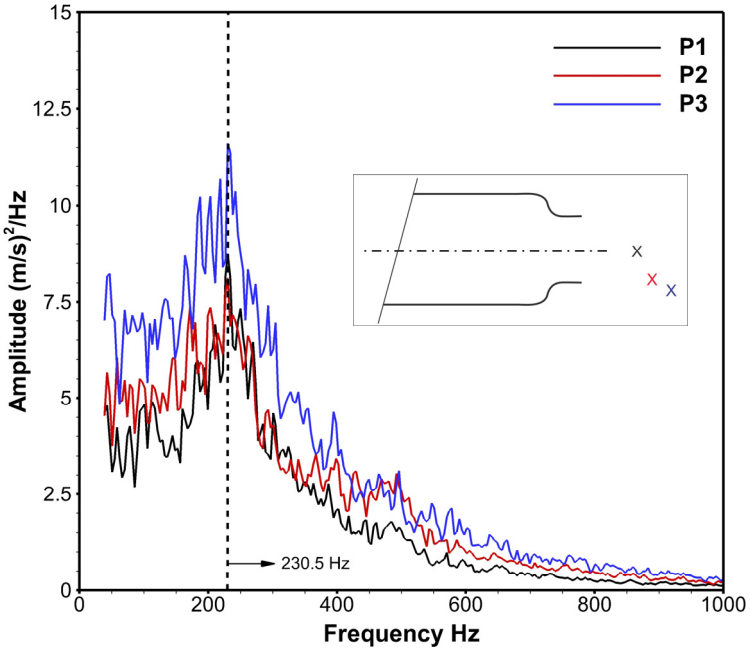

Fig. 4.3 Frequency of formation of vortex structures in the free-jet. Inset figure shows the corresponding spatial locations of the hot-wire probe with respect to the jet exit.

4.1.2 System validation

Figure 4.4 shows a comparison of the present experimental results of mean axial velocity profiles with published experimental work by Montagne et al. (2014), for jet impingement on a static target surface. The centerline mean axial velocities approaching the stagnation point from the exit of the jet are shown in Fig. 4.4(a), and the variation of the mean axial velocity with the radial direction at 2 axial locations (x/d = 0.5; x/d = 1.7) are shown in Fig. 4.4(b). The mean axial velocity profile near the jet nozzle exit at x/d = 0.5 obtained from the present experiment follows closely that of Montagne et al. (2014) across the free-shear layer, as seen from Fig. 4.4(b). However, the drop in the axial velocity is sharper in the results of Montagne et al. (2014). At a downstream distance closer to the target surface at x/d = 1.7, the velocity profiles deviate from each other.

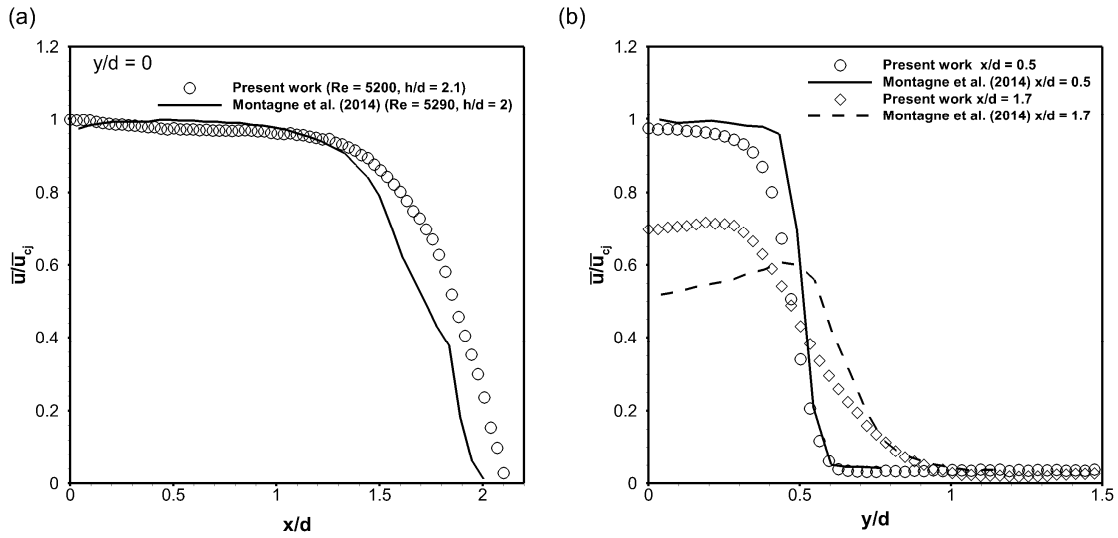

Fig. 4.4 Comparison of present experimental results of jet impingement on unheated static target surface with Montagne et al. (2014): (a) jet-centerline y/d = 0 mean axial velocity; (b) mean axial velocity profiles at x/d = 0.5 and x/d = 1

The differences seen in Fig. 4.4 are due to the following reasons: (i) a minor difference in the nozzle-to-target separation distance between that of the present work and of Montagne et al. (2014); and, (ii) the absence of a straight section in the sharp-edged convergent nozzle used by Montagne et al. (2014), leading to the generation of higher velocities near the jet shear layer due to absence of jet-nozzle wall interaction. While the results of the two studies could not be expected to be in exact agreement, the general features of the impinging jet flow are in good qualitative agreement.

4.2 Instantaneous flow characteristics

The instantaneous vector maps of the velocity field for jet impingement on the static and the oscillating target surfaces are shown in Fig. 4.5. The vector maps for jet impingement on oscillating target surface for the two frequencies, are presented for the 6 phases (ϕ_1 to ϕ_6) in Figs. 4.5(b) to 4.5(g) respectively, during one oscillation cycle as shown in Fig. 3.7(b). The vectors are overlaid on the contours of the magnitude of the velocity. As wall features are important, the vector maps show the region from the impingement target surface location up to a distance of x/d = 1.5.

For target-surface oscillation at 80 Hz, for phases ϕ_1 to ϕ_3 in Figs. 4.5(b) to 4.5(d), it can be seen that the motion of the target surface away from the jet exit increases the velocity magnitude of the flow not only in the impingement region but also in the ambient region, as compared to the static target surface shown in Fig. 4.5(a). For target-surface oscillation at 20 Hz, the velocity magnitude of only the ambient region is seen to be slightly higher than that for the static target surface. These occur due to the displacement of the target surface in the same direction as that of the axial velocity of the jet, where the target surface velocity is greater during oscillation at 80 Hz than at 20 Hz. The near-wall vectors for 80 Hz in the corresponding maps highlight the larger axial velocity components as compared to the static target surface case.

By contrast, motion of the target surface towards the jet exit reduces the velocity magnitude of the jet flow in the impingement region compared with the static target surface, as observed in the vector maps for phases ϕ_4 and ϕ_5, in Figs. 4.5(e) and 4.5(f), for target-surface oscillation at 80 Hz. This reduction of the velocity magnitude in the impingement region is lower for target-surface oscillation at 20 Hz. When the target surface moves closer to the jet exit at phase ϕ_6 in Fig. 4.5(g), the velocity magnitudes in the impingement region are similar to that of the static target surface for both the target-surface oscillation frequencies. This is because the velocity of the target surface approaches zero at this phase. Nevertheless, the near-wall vectors for 80 Hz in Figs. 4.5(f) and 4.5(g) show a greater axial component of the vectors in the negative axial direction when compared to the static target surface case.

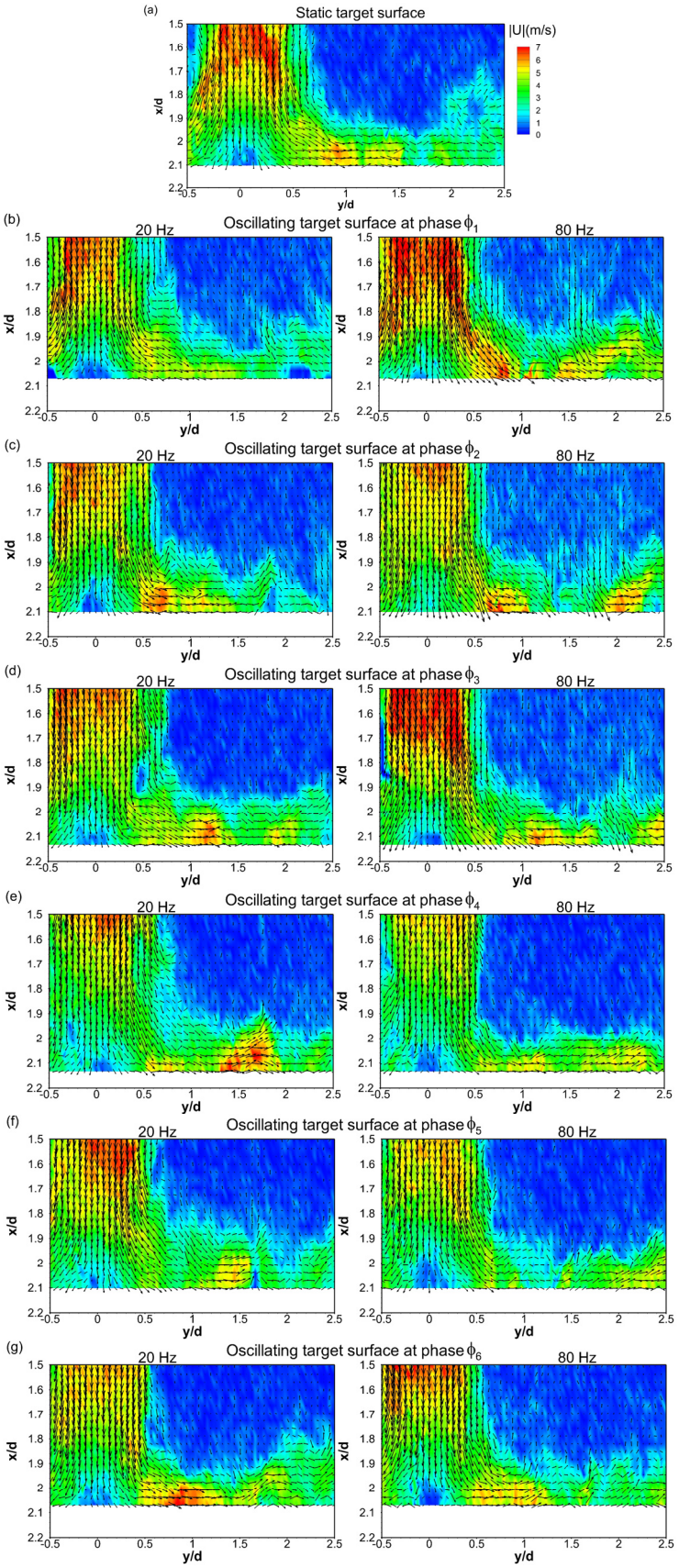

Fig. 4.5 Instantaneous velocity vector maps for jet impingement on unheated target surfaces: (a) static target surface; (b) to (g) oscillating target surface at 20 Hz and 80 Hz, at phases ϕ_1 to ϕ_6 respectively

The ambient regions for target-surface oscillation at 80 Hz for phases ϕ_4 to ϕ_6, in Figs. 4.5(e) to 4.5(g), contain lower velocity magnitudes when compared with those for phases ϕ_1 to ϕ_3, in Figs. 4.5(b) to 4.5(d), due to the motion of the target surface in the opposite direction to the issuing jet.

The instantaneous flow characteristics presented in Fig. 4.5 show that the oscillation of the target surface affects both the impingement and the wall-jet regions, with greater effect observed for target-surface oscillation at 80 Hz than at 20 Hz. This suggests that the fluid dynamics characteristics generated in these regions due to the oscillation of the target surface affect the transport phenomena when compared to jet impingement on a static target surface.

4.3 Mean flow characteristics

4.3.1 Mean velocities

The contours of the mean axial velocity $\overline{u}/\overline{u}_{cj}$ for jet impingement on a static target surface, and, for target-surface oscillation at 20 Hz and 80 Hz are presented in Fig. 4.6(a) and Figs. 4.6(b) to 4.6(g) respectively. It is seen in Fig. 4.6(a) that the jet retains most of its maximum mean axial velocity up to a distance of $x/d = 0.7$ from the jet exit, as shown by the marked contour level 0.97. Within this distance (potential-core region), the presence of the target surface does not affect the jet (Carlomagno and Ianiro 2014). As the jet approaches the target surface, the mean axial velocity reduces due to the presence of the wall (target surface). For phases ϕ_1 and ϕ_2, in Figs. 4.6(b) and 4.6(c), the axial extension of the potential-core region for target-surface oscillation at 80 Hz is larger than that observed for a static target surface, extending to about $x/d = 1.4$ from the nozzle exit plane. Whereas for phases ϕ_1 to ϕ_3, in Figs. 4.6(b) to 4.6(d), the axial extension of the potential-core region for target-surface oscillation at 20 Hz is similar to that for the static target surface.

When compared with results obtained for jet impingement on a static target surface, it is found that the mean axial velocities for phases ϕ_1 to ϕ_3, in the impingement region as well as in the ambient region, are higher for target-surface oscillation at 80 Hz, while the mean axial velocities in the impingement region for target-surface oscillation at 20 Hz, for phases ϕ_1 and ϕ_2, are similar to those observed for the static target surface.

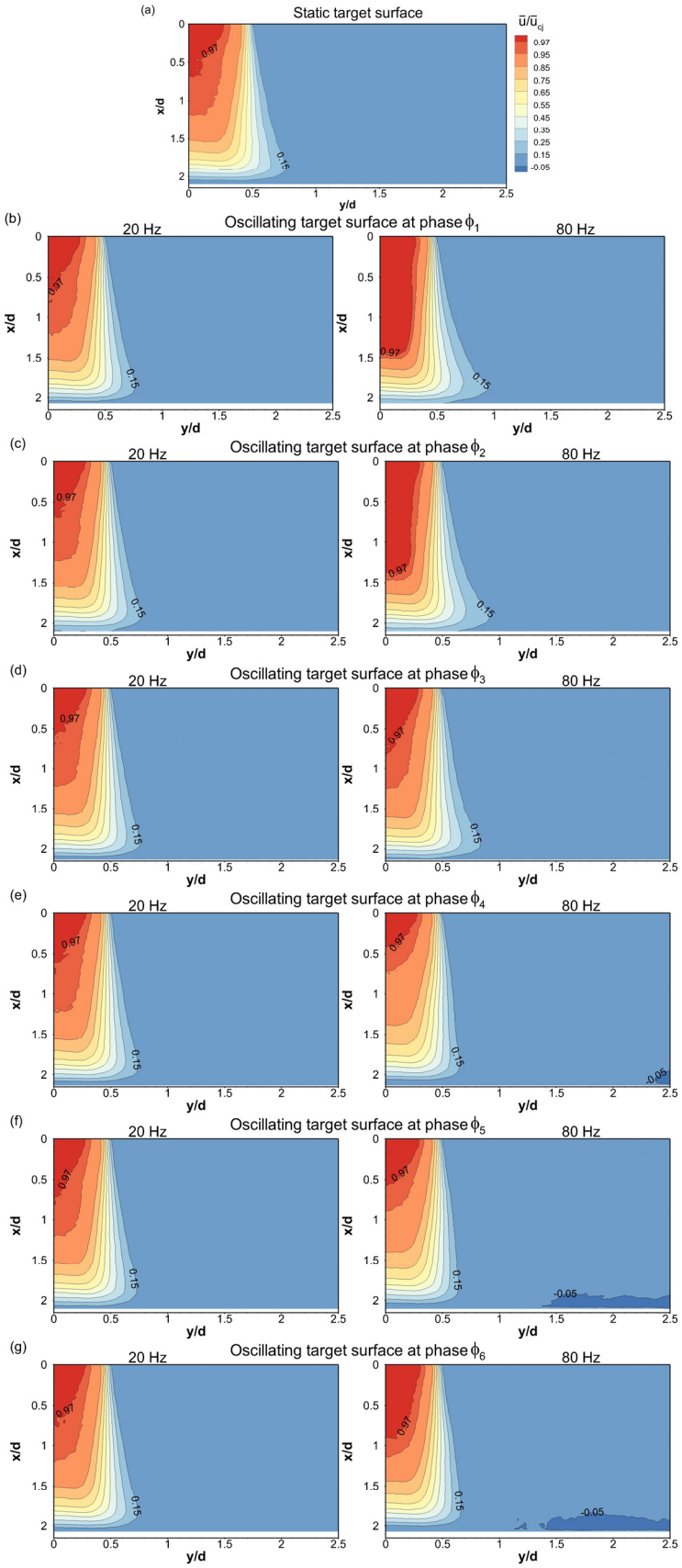

Fig. 4.6 Mean axial velocities for jet impingement on unheated target surfaces: (a) static target surface; (b) to (g) oscillating target surface at 20 Hz and 80 Hz, at phases ϕ_1 to ϕ_6 respectively

The axial extent of the potential-core region for target-surface oscillation at 80 Hz for phase ϕ_4 in Fig. 4.6(e) is up to x/d = 0.4, which is smaller than that observed for a static target surface, while for phases ϕ_5 and ϕ_6 in Figs. 4.6(f) and 4.6(g), the axial extent of the potential-core region is larger than that for phase ϕ_4, but smaller than that for the static target surface case. The axial extent of the potential-core region for target-surface oscillation at 20 Hz for phases ϕ_4 to ϕ_6, in Figs. 4.6(e) to 4.6(g), is again similar to that for the static target surface. For target-surface oscillation at 80 Hz, the radial extent of the marked contour level 0.15 for phases ϕ_1 to ϕ_3, indicate that the jet broadens for these phases from that seen for the static target surface, while the radial extent of the same contour level for phases ϕ_4 to ϕ_6, indicate a narrowing of the jet. The broadening of the jet was also observed by Ichimiya and Yoshida (2009), but with no information provided on when the broadening occurred in the oscillation cycle.

Furthermore, in the near-wall region for phases ϕ_4 to ϕ_6, the mean axial velocities for target-surface oscillation at 80 Hz have negative values, indicating a reverse component of axial velocity. This region of negative mean axial velocities is observed to increase in the wall-normal and radial directions from phase ϕ_4 to ϕ_6. The narrowing of the jet and the presence of negative mean axial velocities in the near-wall region imply that the ambient fluid region decelerates to give negative velocity levels at these three phases when compared to the static target surface. The broadening and narrowing of the jet, as well as the occurrence of negative mean axial velocities in the near-wall and ambient regions, are not observed when the target surface oscillates at a frequency of 20 Hz.

The mean radial velocity $\overline{v}/\overline{u}_{cj}$ contours in the wall-jet region for jet impingement on static target surface, and oscillating target surface at 20 Hz and 80 Hz are shown in Fig. 4.7. Upon impingement, the jet deflects radially and accelerates with increasing mean radial velocity to form a wall-jet along the target surface. For the static target surface shown in Fig. 4.7(a), the maximum mean radial velocity of 0.75 is found to occur at a radial location y/d = 0.8, which marks the end of the acceleration region. The wall-jet progresses beyond this radial location with decreasing mean radial velocity while increasing the thickness of the boundary layer.

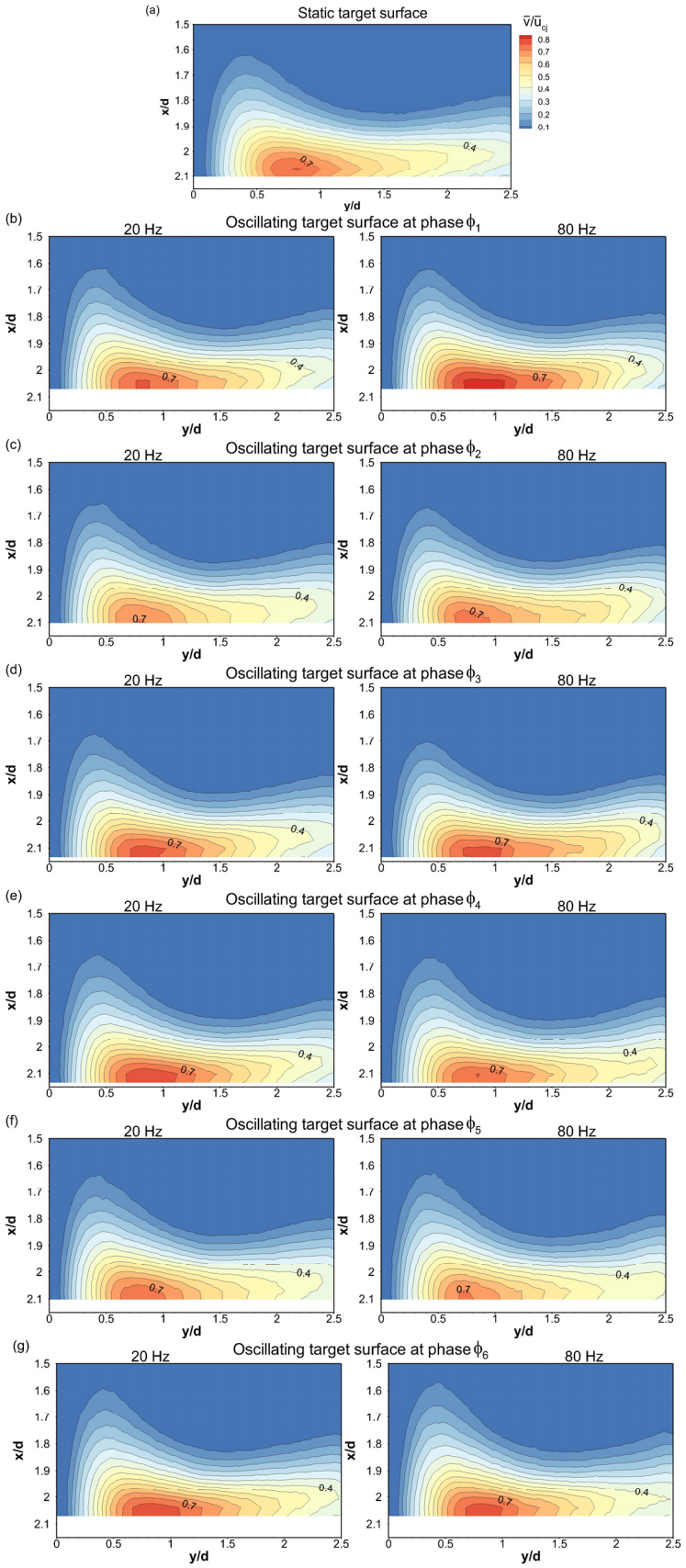

Fig. 4.7 Mean radial velocities for jet impingement on unheated target surfaces: (a) static target surface; (b) to (g) oscillating target surface at 20 Hz and 80 Hz, at phases ϕ_1 to ϕ_6 respectively

In the vicinity of $y/d = 0.8$, the mean radial velocities for phases ϕ_1 and ϕ_3, in Figs. 4.7(b) and 4.7(d), are higher than those for the static target surface, while for phase ϕ_2, in Fig. 4.7(c), the mean radial velocities are lower, with higher values at 80 Hz among the two target-surface oscillation frequencies for the corresponding phases. Similar behavior is seen when the target surface moves towards the jet exit, with phases ϕ_4 and ϕ_6 in Figs. 4.7(e) and 4.7(g) having higher mean radial velocities, and phase ϕ_5 in Fig. 4.7(f) having lower mean radial velocities than those for the static target surface, with higher values at 80 Hz.

In order to understand the aforementioned changes in the mean velocities due to target-surface oscillation, the variations of mean velocities with target surface phases at various spatial locations are provided. These variations are first shown for target-surface oscillation at 80 Hz in Fig. 4.8. A representative variation of the target surface velocity with phases, over two oscillation cycles, is shown at the bottom of each sub-figure. The oscillating target surface phases are marked on the horizontal axis within the range $\pi/2$ to $9\pi/2$. The variation of mean axial velocity at the jet-centerline $y/d = 0$ with oscillating target surface phases at various axial locations is shown in Fig. 4.8(a). The points marked red are the jet-centerline $y/d = 0$ mean axial velocities for static target surface at the corresponding axial locations.

During oscillation, while moving away from the jet exit, the target surface velocity is in the same direction as the axial velocity of the jet, as the target surface accelerates from phase ϕ_1 to ϕ_2 and decelerates from ϕ_2 to ϕ_3. While moving towards the jet exit, the target surface velocity is in the opposite direction to the axial velocity of the jet, as the target surface accelerates from phase ϕ_4 to ϕ_5 and decelerates from ϕ_5 to ϕ_6. The variation of stagnation point mean axial velocity with oscillating target surface phases, labelled ‘Stag’ in Fig. 4.8(a), shows that it follows the variation of the oscillating target surface speed, with a period approximately equal to the period of target-surface oscillation. The lower stagnation mean axial velocities for phases ϕ_4 to ϕ_6, as compared for phases ϕ_1 to ϕ_3, arise because the target surface moves against the jet at these phases.

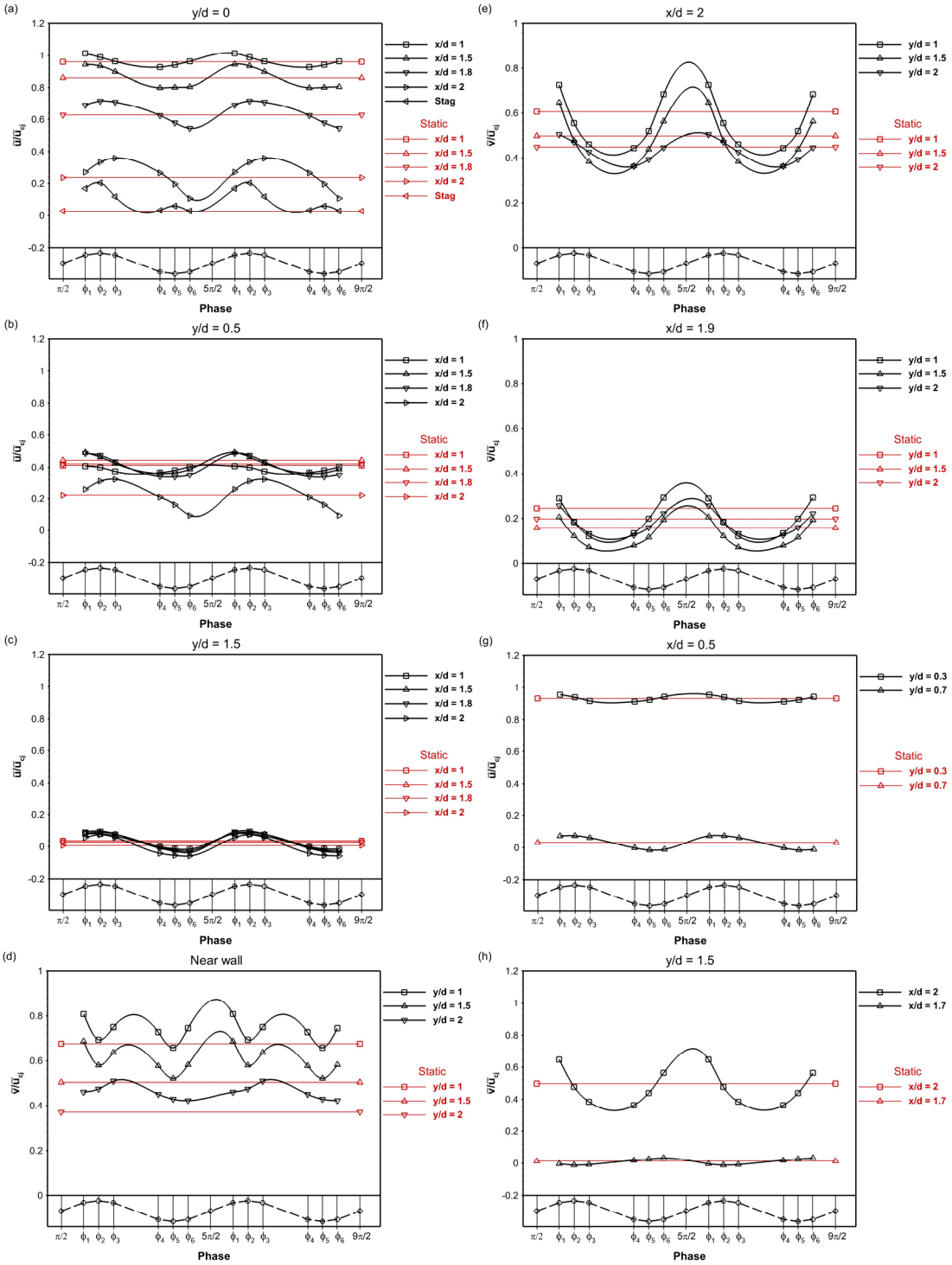

Fig. 4.8 Jet impingement on an unheated target surface oscillating at 80 Hz. Variation of mean velocities with phases ϕ_1 to ϕ_6 at various spatial locations: (a) mean axial velocity at y/d = 0, x/d = 1, 1.5, 1.8, 2 and stagnation point (Stag); (b) mean axial velocity at y/d = 0.5, x/d = 1, 1.5, 1.8 and 2; (c) mean axial velocity at y/d = 1.5, x/d = 1, 1.5, 1.8 and 2; (d) mean radial velocity at near-wall, y/d = 1, 1.5 and 2; (e) mean radial velocity at x/d = 2, y/d = 1, 1.5 and 2; (f) mean radial velocity at x/d = 1.9, y/d = 1, 1.5 and 2; (g) mean axial velocity at x/d = 0.5, y/d = 0.3 and 0.7; (h) mean radial velocity at y/d = 1.5, x/d = 2 and 1.7. The points marked in red in each of these figures denote the corresponding values for jet impingement on an unheated static target surface. At the bottom of each figure is the representative variation of the target surface velocity over 2 oscillation cycles (marked as –o–).

Moving towards the jet exit from the stagnation point, in Fig. 4.8(a), a time delay in the effect of target-surface oscillation on the flow is seen, and this increases as both the axial distance from the target surface and the flow speed increases. The variation of mean axial velocity at x/d = 1 lags the variation of that at x/d = 2 by 3 phases or π radians; this is reflected in the change of the axial extent of the potential-core region for target-surface oscillation at 80 Hz, as observed in Fig. 4.6. The smallest axial extent of the potential-core region found for phase ϕ_4 in Fig. 4.6(e) is because of the target surface motion that occurred at the earlier phase ϕ_1 in Fig. 4.6(b), when the target surface was closest to the jet exit and moving away from it. The largest axial extent of the potential-core region found for phase ϕ_1 can be similarly argued as the effect due to the target surface motion at phase ϕ_4, when it is farthest from the jet exit and moving towards it.

The variation of mean axial velocities with oscillating target surface phases at various axial locations at y/d = 0.5, are shown in Fig. 4.8(b). The variations of mean axial velocities with target surface phases at x/d = 1, 1.5 and 2 are in phase with the variations of jet-centerline y/d = 0 mean axial velocities at the same axial locations as shown in Fig. 4.8(a), while those at x/d = 1.8 are out of phase.

The variation of the mean axial velocities at a farther radial location y/d = 1.5 is shown in Fig. 4.8(c), wherein at x/d = 1, 1.5, points in the ambient region, phases ϕ_1 to ϕ_3 have higher mean axial velocities while phases ϕ_4 to ϕ_6 have lower mean axial velocities, when compared to those for the static target surface. This indicates increased entrainment from the ambient fluid into the impinging jet flow for phases ϕ_1 to ϕ_3, as compared to that for the static target surface. The mean axial velocities at these locations for phases ϕ_4 to ϕ_6 have small negative values which implies that although the entrained fluid is decelerated there is no removal or reduction of entrained fluid as compared with the static target surface case. The variations of mean axial velocities with target surface phases at locations x/d = 1.8, 2 at y/d = 1.5 in Fig. 4.8(c), points in the wall-jet region, are similar to those mentioned above, except that the mean axial velocities for phases ϕ_4 to ϕ_5 have lower negative values as we approach closer to the wall, which is due to the increased effect of the wall oscillatory motion.

The variations of mean radial velocities in the wall-jet with target surface phases, at three axial locations within the wall-jet: at the near-wall location, at $x/d = 2$, and at $x/d = 1.9$; at various radial locations are shown in Figs. 4.8(d), 4.8(e) and 4.8(f) respectively. The variation of near-wall mean radial velocities with target surface phases, at $y/d = 1$ and $y/d = 1.5$ in Fig. 4.8(d), show that their frequencies are approximately double those of their variations further away from the wall at $x/d = 2$ and $x/d = 1.9$ in Fig. 4.8(e) and Fig. 4.8(f), at the same radial locations. At a further radial location $y/d = 2$ in Fig. 4.8(d) the near-wall velocity variation with target surface has approximately the same frequency as that of the variations away from the wall at $x/d = 2$ and $x/d = 1.9$ in Fig. 4.8(e) and Fig. 4.8(f), but opposite phase (a phase lag of π radians). It is also observed that the mean radial velocities reduce more gradually from phases ϕ_1 to ϕ_3 at $x/d = 2$, $y/d = 2$ in Fig. 4.8(e) than that at $x/d = 1.9$, $y/d = 2$ in Fig. 4.8(f). The oscillatory motion of the target surface produces the aforementioned variations of mean radial velocities in the wall-jet region.

When the target surface is closer to the jet exit, higher mean radial velocities should exist in the wall-jet as a consequence of continuity. Clearly, this occurs everywhere in the wall-jet for phases ϕ_1 and ϕ_6, as seen in Figs. 4.8(d), 4.8(e) and 4.8(f), for all the radial locations, where the mean radial velocities are higher when compared to that for the static target surface. In Fig. 4.8(f), the increase in the mean radial velocities from those at $y/d = 1.5$ to those at $y/d = 2$, for both the static and oscillating target surfaces, is because the wall-jet grows in width with increasing radial distance. In Figs. 4.8(d) and 4.8(e) it is observed that as the mean radial velocities reduce with increasing radial distance from $y/d = 1.5$ to $y/d = 2$, their variation with the target surface phases increasingly lags that of the variation at a lower radial distance. Comparing the variation of the mean radial velocity at $x/d = 2$, $y/d = 1$ in Fig. 4.8(e), with the variation of the mean axial velocity at $x/d = 2$, $y/d = 0.5$ in Fig. 4.8(b), it is seen that they are opposite in phase to each other, indicating that mass conservation is satisfied during target-surface oscillation.

The variations of mean velocities at locations on either sides of the free-jet and wall-jet shear layers, with the target surface phases are shown in Fig. 4.8(g) and Fig. 4.8(h). The variation of the mean axial velocity inside the free-jet at $x/d = 0.5$, $y/d = 0.3$ in Fig. 4.8(g) shows that the mean axial velocity decreases until phase ϕ_3 and then increases until phase ϕ_6, whereas the variation of the mean axial velocity of the

ambient fluid at x/d = 0.5, y/d = 0.7 shows an increase from phase ϕ_1 to ϕ_2 then a decrease until phase ϕ_6. This is because the effect of target-surface oscillation is different for different magnitudes of mean axial velocities, which is evident in this case as there is a large difference between the mean axial velocities in these two regions. The variation of the mean radial velocity inside the wall-jet at x/d = 2, y/d = 1.5 in Fig. 4.8(h) is similar to that of the outside ambient fluid at x/d = 1.7, y/d = 1.5, except that the mean radial velocity at x/d = 2 decreases from phase ϕ_2 to ϕ_3 while that at x/d = 1.7 increases from phase ϕ_2 to ϕ_3. In addition at x/d = 1.7, y/d = 1.5 negative mean radial velocities occur for phases ϕ_1 to ϕ_3 because of the effect of higher entrainment.

The variations of mean velocities with target surface phases at various spatial locations for target-surface oscillation at 20 Hz are shown in Fig. 4.9. The variation of the stagnation point mean axial velocity in Fig. 4.9(a) is similar to that of the variation in Fig. 4.8(a), where the target surface oscillates at 80 Hz. However, the mean axial velocities for phases ϕ_1 to ϕ_3 are lower for 20 Hz because the target surface velocity is smaller while oscillating at this frequency.

The variations of mean axial velocities at locations x/d = 1.5, 1.8 and 2, show that they are in phase with each other, as the mean axial velocities increase from phase ϕ_1 to ϕ_3 and decrease from phase ϕ_4 to ϕ_6. Closer to the jet exit at x/d = 1, there is little effect of target surface motion on the mean axial velocity of the jet. A comparison between the variations shown in Fig. 4.8(a) and Fig. 4.9(a) shows that the mean axial velocities are higher for phases ϕ_1 to ϕ_3 and lower for phases ϕ_4 to ϕ_6 when the target surface oscillates at 80 Hz. This demonstrates a larger effect on the mean axial velocities in the jet at 80 Hz frequency of target-surface oscillation. The variation at x/d = 1.5 in Fig. 4.9(a) lags that of the variation at the same axial location in Fig. 4.8(a) by π radians.

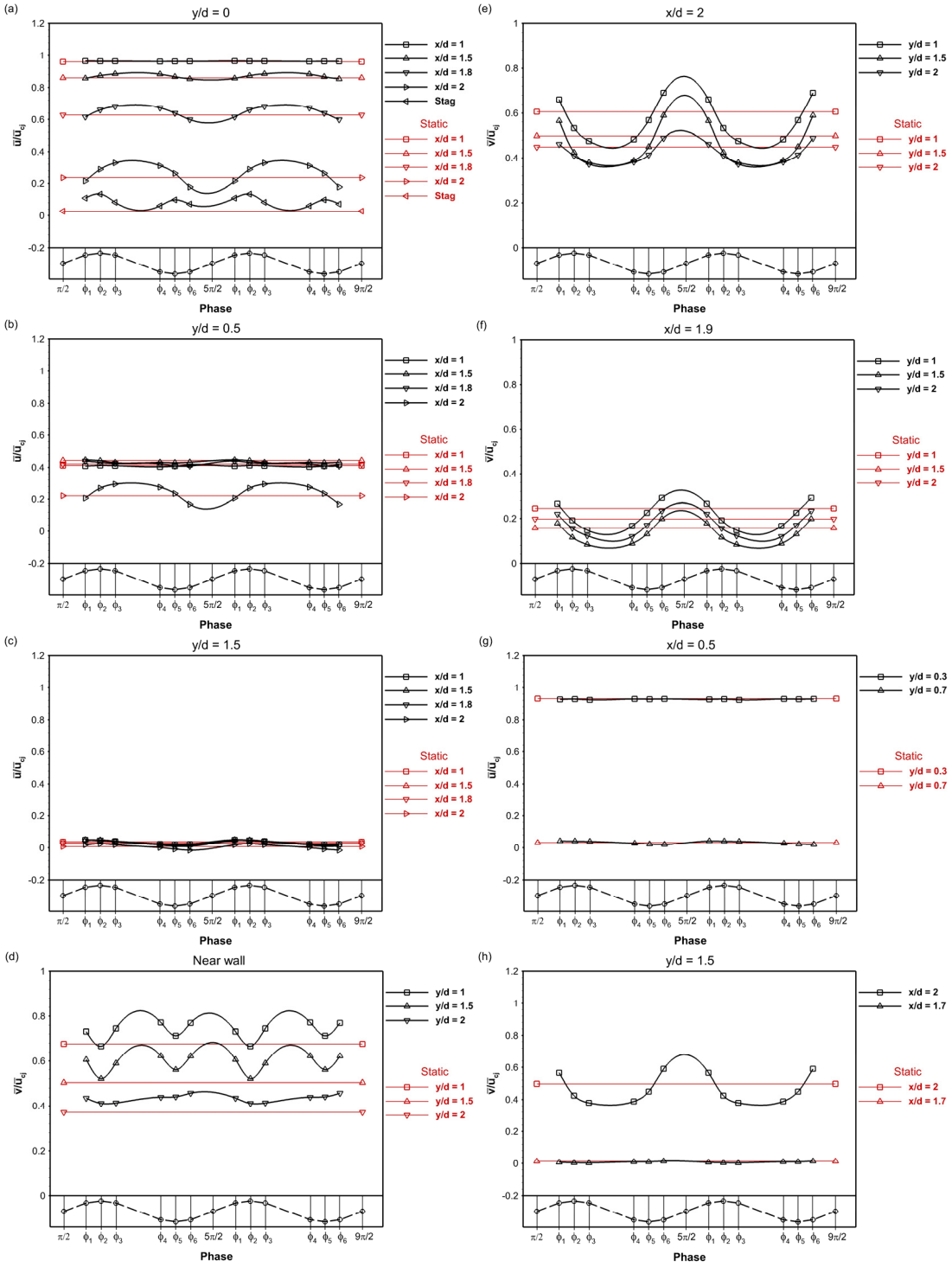

Fig. 4.9 Jet impingement on an unheated target surface oscillating at 20 Hz. Variation of mean velocities with phases ϕ_1 to ϕ_6 at various spatial locations: (a) mean axial velocity at y/d = 0, x/d = 1, 1.5, 1.8, 2 and stagnation point (Stag); (b) mean axial velocity at y/d = 0.5, x/d = 1, 1.5, 1.8 and 2; (c) mean axial velocity at y/d = 1.5, x/d = 1, 1.5, 1.8 and 2; (d) mean radial velocity at near-wall, y/d = 1, 1.5 and 2; (e) mean radial velocity at x/d = 2, y/d = 1, 1.5 and 2; (f) mean radial velocity at x/d = 1.9, y/d = 1, 1.5 and 2; (g) mean axial velocity at x/d = 0.5, y/d = 0.3 and 0.7; (h) mean radial velocity at y/d = 1.5, x/d = 2 and 1.7. The points marked in red in each of these figures denote the corresponding values for jet impingement on an unheated static target surface. At the bottom of each figure is the representative variation of the target surface velocity over 2 oscillation cycles (marked as –o–).

The variations of mean axial velocities at various axial locations at $y/d = 0.5$ in Fig. 4.9(b), and at $y/d = 1.5$ in Fig. 4.9(c), are similar to those in Figs. 4.8(b) and 4.8(c) respectively. However, the lower magnitudes in Figs. 4.9(b) and 4.9(c) show that the effect on the mean axial velocities due to target-surface oscillation at 20 Hz, is lower when compared to that during oscillation at 80 Hz. The variations shown in Figs. 4.9(c) and 4.8(c) indicate that entrainment of the ambient fluid into the jet is lower as a result of the effect of the target surface oscillating at 20 Hz frequency.

The variations of mean radial velocities with phases for target-surface oscillation at 20 Hz, at the near-wall location, $x/d = 2$ and $x/d = 1.9$, are shown in Figs. 4.9(d), 4.9(e) and 4.9(f) respectively. These variations are similar to the corresponding variations for target-surface oscillation at 80 Hz, as shown in Figs. 4.8(d), 4.8(e) and 4.8(f); apart from a phase lag of π radians in the variation of near-wall mean radial velocities at $y/d = 2$ for target-surface oscillation at 20 Hz. It is observed in Figs. 4.9(d) to 4.9(f), that largest mean radial velocities occur for phase ϕ_6, for target-surface oscillation at 20 Hz, whereas in Figs. 4.8(d) to 4.8(f) the largest mean radial velocities occur for phase ϕ_1, for target-surface oscillation at 80 Hz. This is because of the difference in the frequencies of target surface oscillation. For target-surface oscillation at 80 Hz frequency, the effect of target surface being closest to the jet exit (phase ϕ_6), which results in higher mean radial velocities, is observed later when the target surface moves away from the jet exit (phase ϕ_1).

The variations of mean axial velocities for target-surface oscillation at 20 Hz at locations on either sides of the free-jet shear layer, are shown in Fig. 4.9(g). These variations show a very small effect of target-surface oscillation on the mean axial velocities across the free-jet shear layer at $x/d = 0.5$. The variations of mean radial velocities across the wall-jet shear layer are shown in Fig. 4.9(h). At $y/d = 1.5$, $x/d = 1.7$ in Fig. 4.9(h), point in the ambient region, the variation shows that the entrainment of the ambient fluid into the wall-jet for phases ϕ_1 to ϕ_3 is not as high as observed for target-surface oscillation at 80 Hz in Fig. 4.8(h). The increased entrainment of ambient fluid into the wall-jet, as compared with the static target surface, reduces momentum of the wall-jet in locations away from the wall for target-surface oscillation at 80 Hz. This decreases the mean radial velocity at $y/d = 1.5$, $x/d = 1.7$ for phases ϕ_1 to ϕ_3, as shown in Fig. 4.8(h). A comparison of the variations of mean axial velocities for phases ϕ_4 to ϕ_6 in the ambient region at $x/d = 0.5$, $y/d = 0.7$, in Figs. 4.8(g) and 4.9(g),

show that the deceleration of ambient fluid in these phases is higher when target surface oscillates at a frequency of 80 Hz.

In summary, Figs. 4.8 and 4.9 show that the effects of target-surface oscillation on the free-jet, impingement region and wall-jet region are different. The mean axial velocities closer to the wall increase during target surface motion away from the jet exit and decrease during the opposite motion. There is a phase difference in the variations of mean axial velocities as the axial distance from the wall increases. The effect of target-surface motion on the mean axial velocities is higher for target-surface oscillation at 80 Hz. For the wall-jet flow, the effect of target-surface oscillation generates shorter time periods of variations of higher mean radial velocities at locations closer to the wall. The variation of mean radial velocities closer to the wall, for target-surface oscillation at 20 Hz, lags that of the variation for target-surface oscillation at 80 Hz. Finally the effect of target-surface oscillation is different across the free-jet and wall-jet shear layers, due to the difference in the velocity magnitudes across these layers. Furthermore, the entrainment of the ambient fluid into the jet is greater for target-surface oscillation at 80 Hz.

The variation of the maximum mean radial velocity with the radial coordinate for the static and oscillating target surfaces at 20 Hz and 80 Hz are shown in Fig. 4.10. The region bounded by the wall and the location of maximum mean radial velocity is considered the near-wall region where viscous forces dominate (Launder and Rodi 1983). The highest maximum mean radial velocities occur for phase ϕ_1 for target-surface oscillation at 80 Hz as shown in Fig. 4.10(a), with the largest of those values being 7.5% greater than that observed for the static target surface. Lower maximum mean radial velocities than that for the static target surface occur for phase ϕ_2, for target-surface oscillation at 20 Hz in Fig. 4.10(a), while they occur at a later phase ϕ_5, for target-surface oscillation at 80 Hz in Fig. 4.10(b).

The reason for this is the phase difference that exists between effect on the mean radial velocities by the two target-surface oscillation frequencies, as explained in Figs. 4.8(d) and 4.9(d). The radial location of the largest value of the maximum mean radial velocity marks the end of the acceleration region of the wall-jet. This location is found to be largest for phase ϕ_3 for target-surface oscillation at 80 Hz, and increases from that observed for the static target surface case by $y/d = 0.1$.

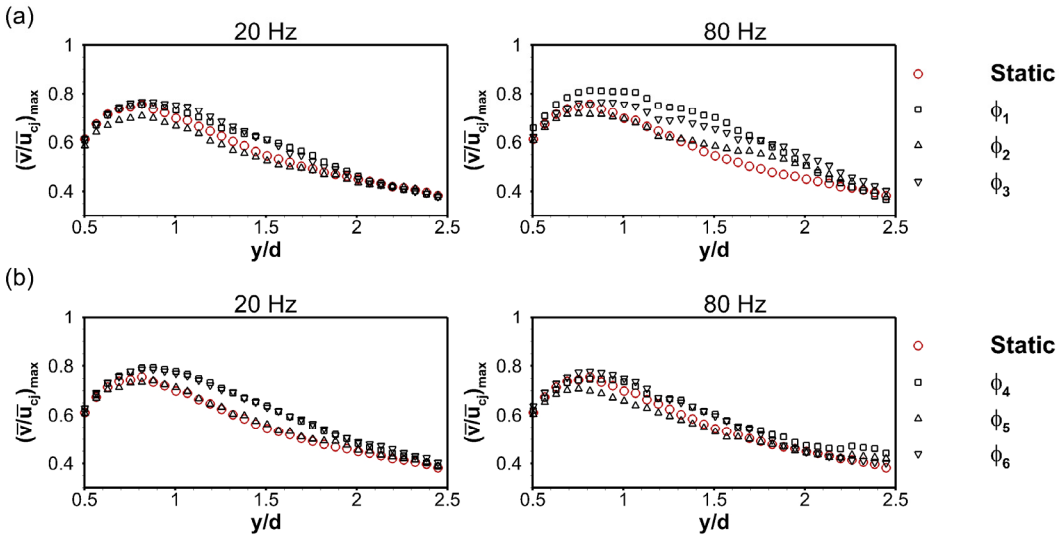

Fig. 4.10 Maximum mean radial velocity comparison for jet impingement on unheated static target surface and oscillating target surface at 20 Hz and 80 Hz, at (a) phases ϕ_1 to ϕ_3; (b) phases ϕ_4 to ϕ_6

4.3.2 Wall-shear stress

The variations of normalized wall-shear stress with radial position for jet impingement on unheated static and oscillating target surfaces are shown in Fig. 4.11. It is remarked that the determination of the velocity vectors very close to the wall is affected due to spatial averaging over the interrogation area in the PIV post-processing. This is due to the fact that the center of the interrogation area is at the wall and therefore the velocity vectors at the wall have magnitudes that represent an average value over a distance of 0.4 mm above the wall. Thus to calculate the wall-shear stress, given by $\tau_w = \mu(d\bar{v}/dx)_w$, the velocity components at the wall were taken to be zero. The Reynolds shear stress is not considered in the calculation of wall-shear stress as it is much lower in magnitude when compared to the viscous shear stress. The region of the maximum wall-shear stress for the static target surface and phases of the oscillating target surface in Fig. 4.11 corresponds with the maximum mean radial velocity in Fig. 4.10. A similar variation of the wall-shear stress with the radial coordinate has also been found by El Hassan et al. (2013).

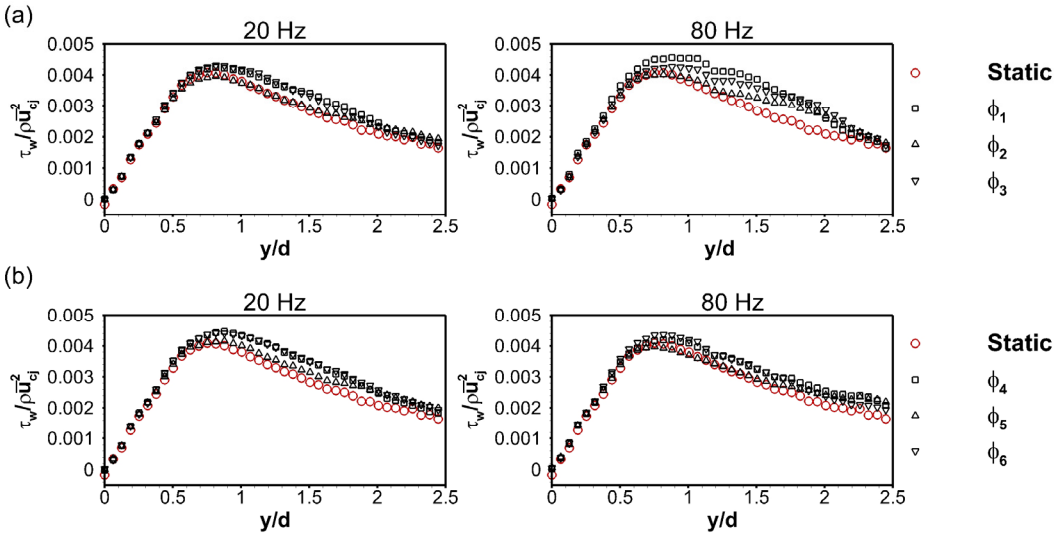

Fig. 4.11 Normalized wall-shear stress comparison for jet impingement on unheated static target surface and oscillating target surface at 20 Hz and 80 Hz, at (a) phases ϕ_1 to ϕ_3; (b) phases ϕ_4 to ϕ_6

The highest maximum wall-shear stress occurs at phase ϕ_1 for target-surface oscillation at 80 Hz in Fig. 4.11(a), which is 11.5% greater than that of the static target case, while also occurring at a larger radial distance. This reflects the higher near-wall radial velocities for phase ϕ_1 as seen in Figs. 4.8(d) and 4.10(a). For target-surface oscillation at both 20 Hz and 80 Hz, all phases, except ϕ_2 and ϕ_5, give rise to higher wall-shear stress than that for the static target surface, at radial distances $y/d \leq 1.5$.

In addition to the variation of near-wall mean radial velocities, in Figs. 4.8(d) and 4.9(d), being related to effect of oscillatory motion of the target surface, it is remarked that at phases ϕ_1, ϕ_3, ϕ_4, and ϕ_6, the target surface has high acceleration magnitudes while oscillating at 80 Hz which leads to high inertial forces acting on the impinging jet. The ratio of these inertial forces to the viscous forces can be quantified using the Womersely number, defined in terms of the Reynolds and Strouhal numbers as $Wo = \sqrt{2\pi(Re)(St_s)}$, that in the present study has values 29 and 14.6 for target-surface oscillation at 80 Hz and 20 Hz respectively. This indicates very high levels of transient inertial forces acting on the impinging-jet flow due to the target-surface oscillation at 80 Hz. And the action of these forces on the flow is higher where the effect of the impinging-jet is higher; as seen at radial locations $y/d \leq 1.5$ in the higher maximum mean radial velocities and the resulting higher wall-shear stress for these phases, in Figs. 4.10 and 4.11 respectively, when compared with the static target surface.

4.3.3 Mean strain rates

The mean axial strain rate $\partial\bar{u}/\partial x$ contours for jet impingement on static and oscillating target surfaces are shown in Fig. 4.12. Jet impingement produces high negative axial strain rates in the impingement region, as shown in Fig. 4.12(a) for the static target surface, due to the deceleration of the jet axial velocity. For target-surface oscillation at the two frequencies, the axial strain rates in the vicinity of the stagnation point for phases ϕ_1 and ϕ_2, in Fig. 4.12(b) and 4.12(c), have less negative values than those for the static target surface. At locations near y/d = 1, the axial strain rates for phases ϕ_1 to ϕ_3 for target-surface oscillation at 80 Hz have more negative values than those for the static target surface and target-surface oscillation at 20 Hz. This is because of higher mean axial velocities of the jet as the target surface moves away from the jet exit. When the target decelerates at phase ϕ_3, the axial strain rate increases from that at phase ϕ_2 as shown in Fig. 4.12(d).

For phases ϕ_4 to ϕ_6, in Figs. 4.12(e) to 4.12(g), during target-surface motion towards the jet exit, the axial strain rates beyond y/d = 1 and close to the wall, increasingly attains more positive values than those for the static target surface. And these values are greater for target-surface oscillation at 80 Hz than at 20 Hz. These occur due to negative mean axial velocities induced by the motion of target surface. Compared with other phases, the magnitudes of the axial strain rates within the impingement region are found to be lower for phases ϕ_2 and ϕ_5, when the target surface attains its maximum velocity during oscillation.

The mean radial strain rate $\partial\bar{v}/\partial y$ contours shown in Fig. 4.13 show positive values in the impingement region where the jet accelerates in the radial direction, and negative values in the wall-jet region as the mean radial velocities decrease. The mean radial strain rates for phases ϕ_1 to ϕ_3, in Figs. 4.13(b) to 4.13(d), for target-surface oscillation at 20 Hz, are similar to those observed for the static target surface. However, for target-surface oscillation at 80 Hz, the radial strain rates beyond y/d = 2, have marginally more negative values. The radial strain rate contours for target-surface oscillation at 20 Hz for phases ϕ_4 to ϕ_6, in Figs. 4.13(e) to 4.13(g), are similar to those for phases ϕ_1 to ϕ_3. While for these phases for target-surface oscillation at 80 Hz, the radial strain rates attain more positive values due to the increase in the mean radial velocities as the target surface moves towards the jet exit.

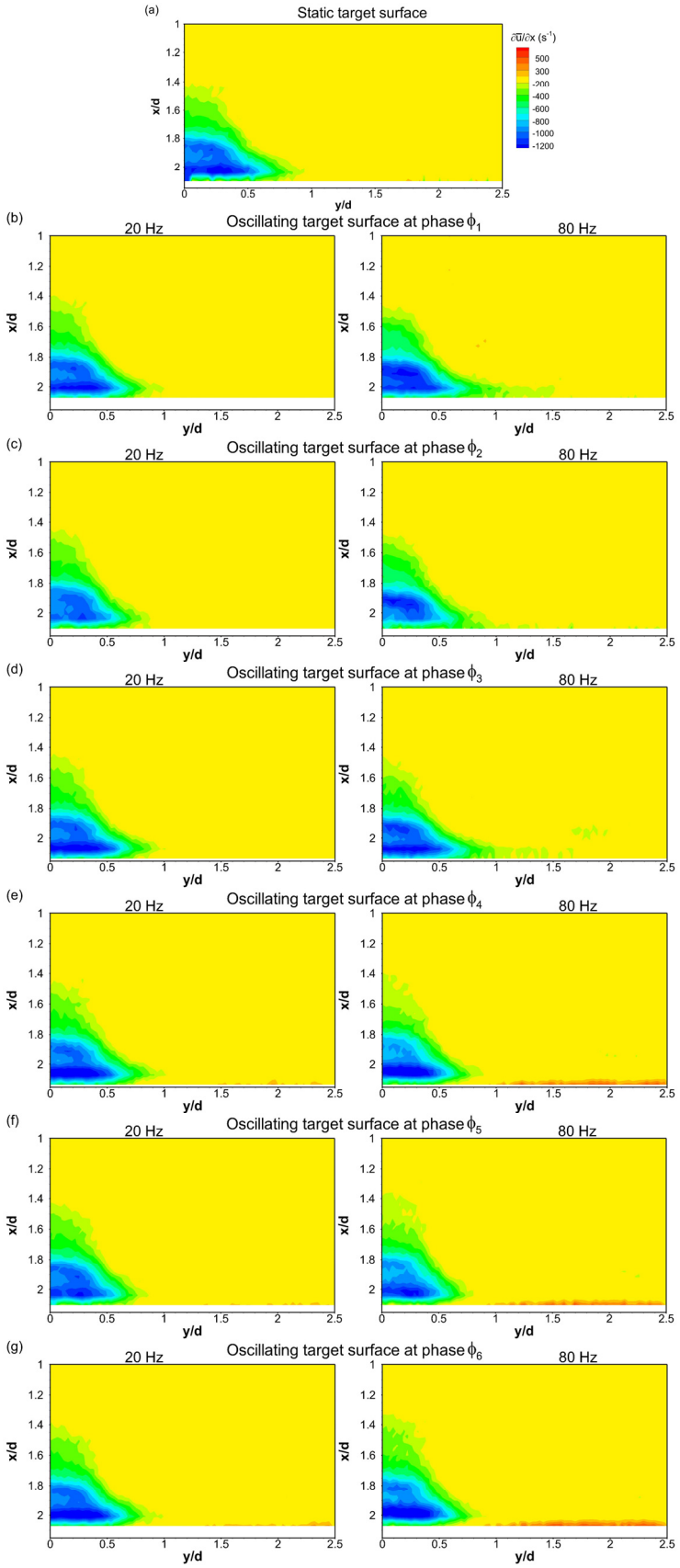

Fig. 4.12 Mean axial strain rate for jet impingement on unheated target surfaces: (a) static target surface; (b) to (g) oscillating target surface at 20 Hz and 80 Hz, at phases ϕ_1 to ϕ_6 respectively

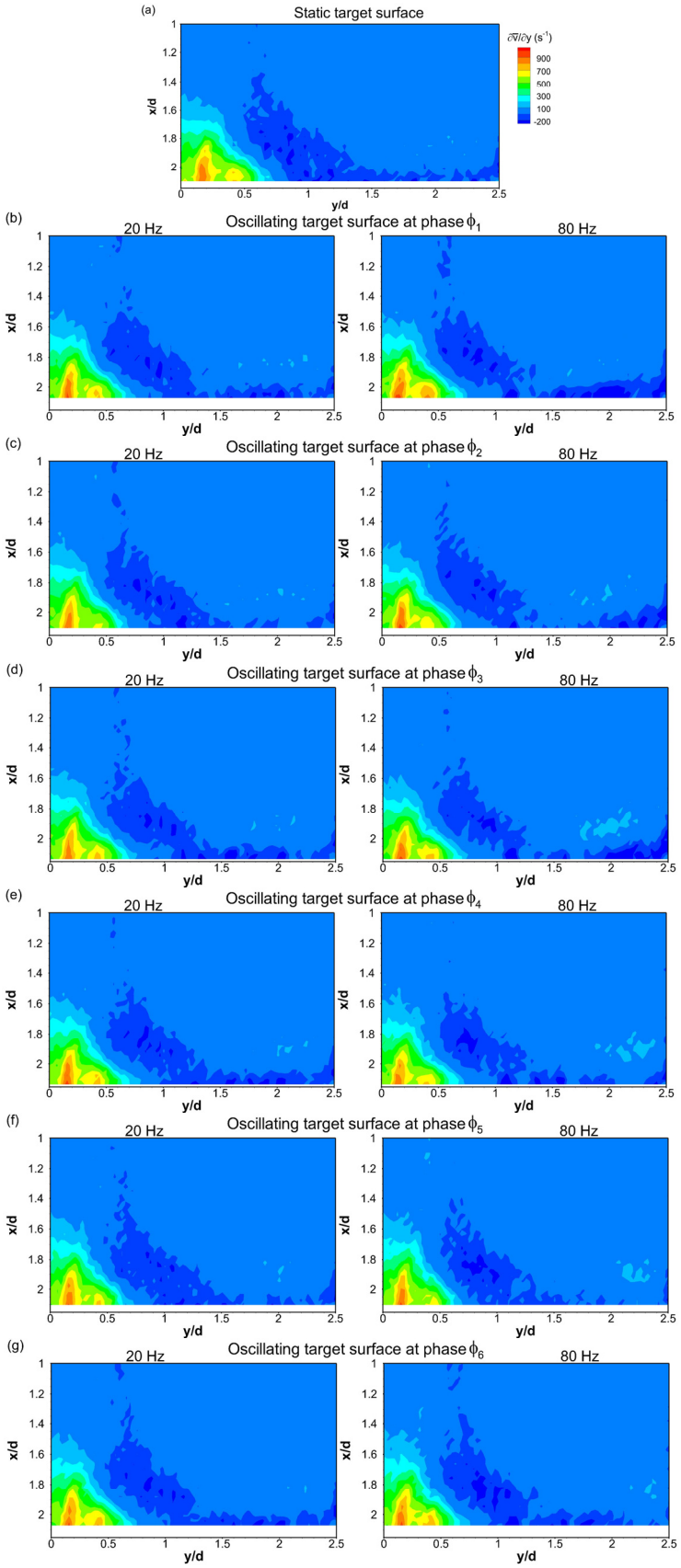

Fig. 4.13 Mean radial strain rate for jet impingement on unheated target surfaces: (a) static target surface; (b) to (g) oscillating target surface at 20 Hz and 80 Hz, at phases ϕ_1 to ϕ_6 respectively

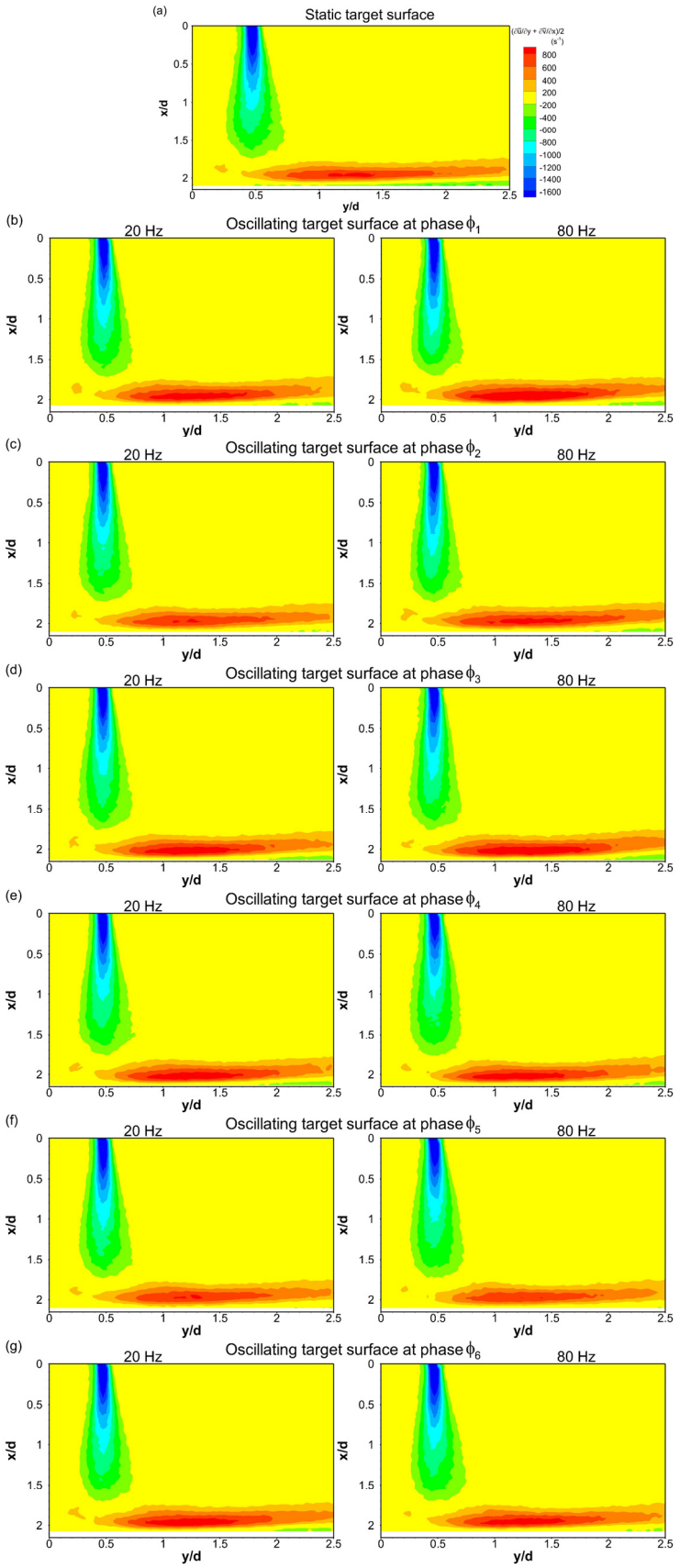

Fig. 4.14 Mean shear strain rate for jet impingement on unheated target surfaces: (a) static target surface; (b) to (g) oscillating target surface at 20 Hz and 80 Hz, at phases ϕ_1 to ϕ_6 respectively

The mean shear strain rates $(\partial\bar{u}/\partial y + \partial\bar{v}/\partial x)/2$ for jet impingement on static and oscillating target surfaces are shown in Fig. 4.14 being negative in the free-jet shear layer and positive in the wall-jet. For all phases for the two target surface oscillation frequencies, except ϕ_2 and ϕ_5, the shear strain rates in the wall-jet are higher than those for the static target surface. The free-jet shear layer for all phases of target-surface oscillation at 20 Hz has shear strain rates similar those for the static target surface. For phases ϕ_1 to ϕ_3 of target-surface oscillation at 80 Hz, the shear strain rates in the free-jet shear layer are lower than those for the static target surface. This is observed in the form of shear-layer thinning for these phases in Figs. 4.14(b) to 4.14(d), and it occurs because of the increase in the mean axial velocities of the ambient fluid as shown in Fig. 4.8(c). Whereas for phases ϕ_4 to ϕ_6, they are higher than those for the static target surface. This appears as a broadening of the shear-layer in Figs. 4.14(e) to 4.14(g), and is due to the deceleration of the ambient fluid as shown in Fig. 4.8(c).

4.4 Proper orthogonal decomposition analysis

Proper Orthogonal Decomposition (POD) is a statistical method to extract the main energetic flow features (Lumley 1967; Berkooz et al. 1993) by obtaining lower order approximations of the flow field. POD of an instantaneous velocity vector $u(\boldsymbol{x}, t)$ decomposes it into a linear combination of orthonormal spatial basis functions with temporal coefficients. The decomposition is given by

$$u(\boldsymbol{x}, t) = \sum_{k=0}^{M} a_k(t)\phi_k(\boldsymbol{x}) \tag{4.1}$$

where $\phi_k(\boldsymbol{x})$ is the k^{th} spatial basis function or mode and $a_k(t)$ is the k^{th} POD temporal coefficient. The POD analysis applied here uses the method of snapshots (Sirovich 1987) where each instantaneous PIV measurement is considered a snapshot of the flow field. The velocity field for a given PIV measurement can then either be reconstructed using a linear combination of the modes in (4.1) or the modes themselves can be individually extracted. The modes (Eigen-functions) are computed by solving an eigenvalue problem and are ordered based on decreasing eigenvalues. Each mode represents a typical flow feature and the associated eigenvalues represent the associated kinetic energy. The first mode ($k = 0$) represents the mean velocity field and is the most energetic, while the following modes represent the velocity fluctuations.

POD analysis on jet impingement on a static target surface have been performed in previous studies such as those by Geers et al. (2005), Dano and Liburdy (2007), Kim et al. (2007), and Meslem et al. (2013). In the present study a sample size of M = 500 snapshots is used for the POD analysis for jet impingement on unheated static and oscillating target surfaces. This sample size is based on a sensitivity analysis carried out on the effect of sample size on the POD modal energies and is determined to be adequate to capture all of the modal energies. The sensitivity analysis has been presented in the appendix. The first 50 modes for static target surface contains 48.19% of the total energy, while those for target-surface oscillation at 20 Hz and 80 Hz (mean of all the phases) contain 48.00% and 46.77% of the total energies respectively. A comparison of an instantaneous velocity vector field, shown in Fig. 4.15(a), with that of its POD reconstructed velocity vector field, shown in Fig. 4.15(b), is presented below. The reconstruction has been done using POD modes 1 to 30. The vectors in these two figures are shown overlaid on the contours of their non-dimensional vorticity $\omega d/\bar{u}_{cj}$, where vorticity is given by $\omega = (\partial v/\partial x - \partial u/\partial y)$. Figure 4.15(b) shows the capability of the present POD analysis to fully capture and represent the large-scale structures in the impinging jet-flow by increasing the signal to noise ratio present in the instantaneous vectors shown in Fig. 4.15(a).

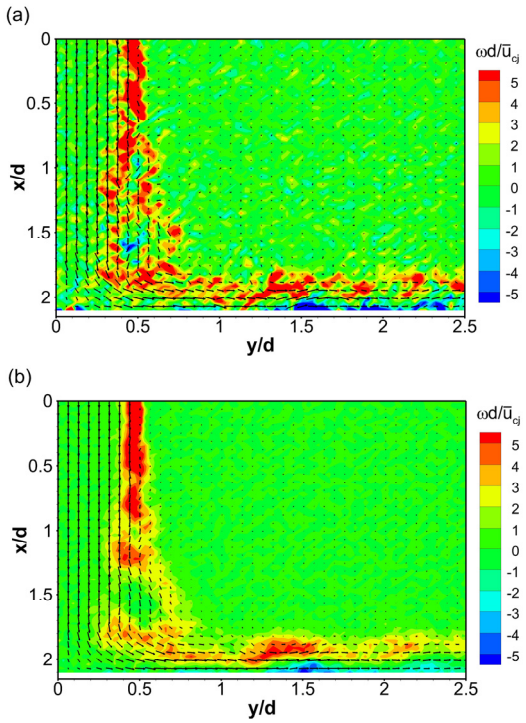

Fig. 4.15 POD of jet impingement on an unheated static target surface (a) Instantaneous velocity vector field (b) Reconstructed velocity vector field using POD modes 1 to 30. Contours shown are of non-dimensional vorticity $\omega d/\bar{u}_{cj}$.

To illustrate the effect of the target-surface oscillation on the main energetic features in the impinging-jet flow, POD modes 2, 3 and 4 for jet impingement on a static target surface and oscillating target surface at 80 Hz are shown in Fig. 4.16. Mode 1 has not been shown as it represents the mean flow-field presented in Figs. 4.6 and 4.7. The non-dimensional vorticity contour map for each mode with its proportion of system energy as a percentage is shown in Fig. 4.16(a) for the static target surface, and in Figs. 4.16(b) to 4.16(g) for oscillating target surface phases ϕ_1 to ϕ_6, where a negative vorticity region indicates a clockwise rotation.

The vorticity of the fluctuating velocity components in the free-jet shear layer and in the wall-jet region is shown for the static target surface in Mode 2 in Fig. 4.16(a). In the free-jet shear layer the velocity fluctuations are in the stream-wise direction and show higher vorticity magnitudes than those in the wall-jet flow, where the velocity fluctuations are in the opposite direction. The Mode 2 maps for the oscillating target surface show higher vorticity in the wall-jet than that for the static target surface, for phases ϕ_1 and ϕ_2 in Figs. 4.16(b) and 14.16(c). This indicates larger radial velocity fluctuations along the stream-wise direction in the wall-jet for these phases, which is because of the effect of target-surface motion at phases ϕ_6 and ϕ_1 respectively; these are phases where higher mean radial velocities occur in the wall-jet as shown in Fig. 4.8(d), 4.8(e) and 4.8(f).

The vorticity in the free-jet shear layer for phases ϕ_1 and ϕ_2 is lower than that for the static target surface and it also shows a change of sign. This indicates lower magnitudes of velocity fluctuations than that for the static target surface, where these fluctuations are now opposite to the stream-wise direction. The lower vorticity in the free-jet shear layer for phases ϕ_1 and ϕ_2 occurs as a result of reduced shear interaction between the free-jet and the ambient fluid for these phases due to an increase in the axial velocities of the ambient fluid as shown in Fig. 4.8(g), and also in Figs. 4.14(b) and 4.14(c). This increased entrainment of the ambient fluid into the wall-jet for phases ϕ_1 and ϕ_2 also contributes to the increase of vorticity magnitudes in the wall-jet shear layer. The Mode 2 vorticity map for phase ϕ_3 in Fig. 4.16(d) is similar to that for the static target surface, except for slightly lower levels of vorticity in the free-jet shear layer and higher in the wall-jet region.

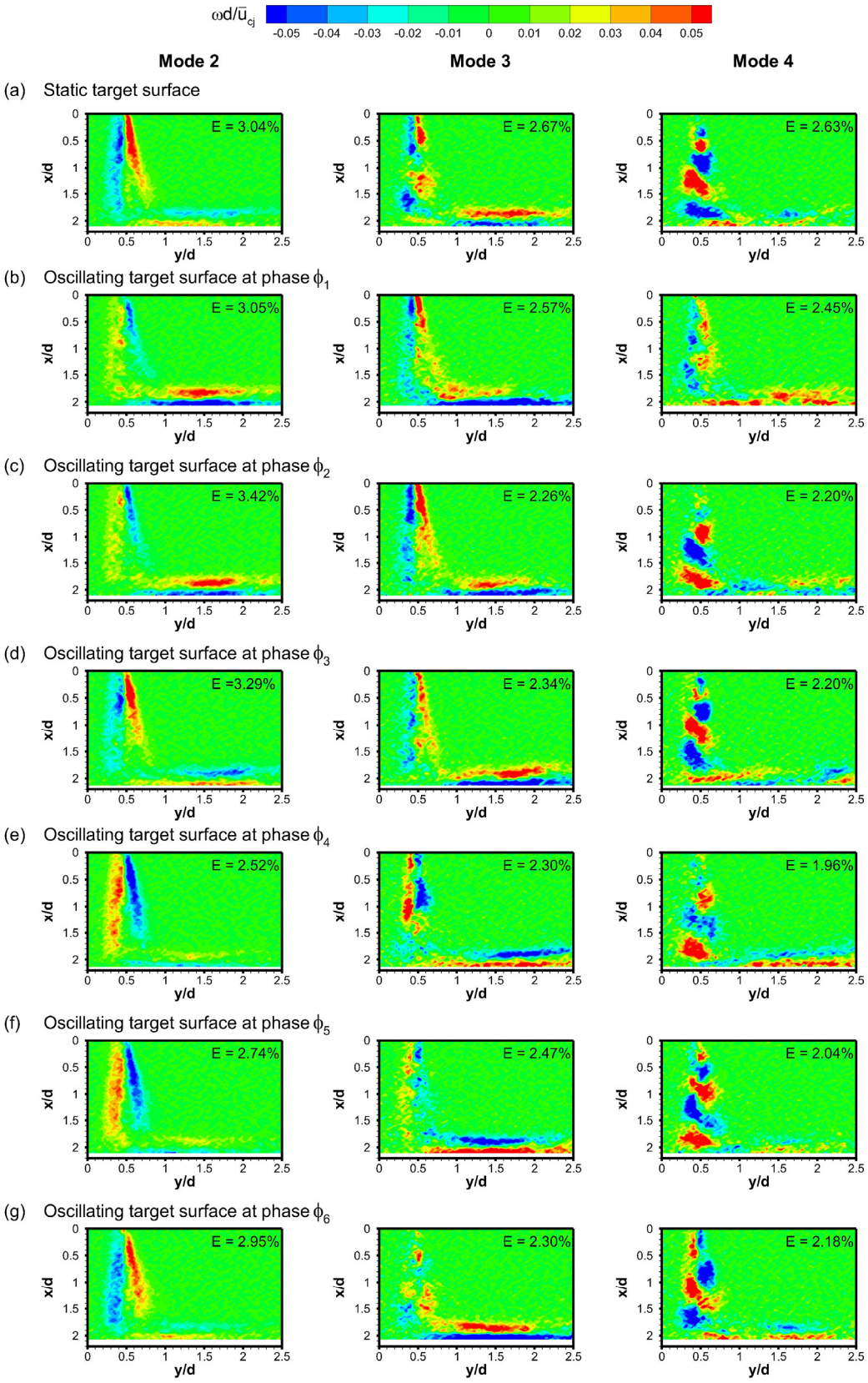

Fig. 4.16 Vorticity maps of POD modes 2 to 4 for jet impingement on unheated target surfaces: (a) static target surface, (b) to (g) oscillating target surface at 80 Hz, at phases ϕ_1 to ϕ_6 respectively

The Mode 2 maps for phases ϕ_4 and ϕ_5 in Fig. 4.16(e) and 4.16(f) show a change of sign in the vorticities in the free-jet shear layer from that observed for phase ϕ_3. When compared with phases ϕ_1 and ϕ_2, these vorticities are higher which are due to higher velocity fluctuations due to motion of the target surface towards the jet exit. It is observed that the Mode 2 vorticities for phase ϕ_6 in Fig. 4.16(g) are similar to those for the static target surface. The vorticity contours for Mode 3 for phases ϕ_1 and ϕ_6 show higher near-wall magnitudes than those for the static target surface implying larger near-wall fluctuations in the stream-wise direction. As seen in Mode 2, the Mode 3 vorticity maps for phases ϕ_4 and ϕ_5 are opposite in signs to the Mode 3 map for the static target surface.

The Mode 4 vorticity map in Fig. 4.16(a) for jet impingement on a static target surface clearly shows fluctuating coherent structures with alternating signs of vorticity. Phase ϕ_1 is observed to have higher positive vorticity structures in the wall-jet when compared to that for the static target surface, whereas in the free-jet shear layer the alternating structures are not well-formed and have lower vorticity magnitudes. This pattern of higher vorticity structures in the wall-jet and lower vorticity structures in the free-jet shear layer for phase ϕ_1, compared to that for the static target surface, is also observed in Mode 2 and 3. The signs of the Mode 4 alternating structures in the free-jet shear layer for phases ϕ_4 and ϕ_5 are found to be opposite for those for the static target surface – a similar behavior was present in the structures for these phases in Mode 2 and 3.

A comparison of Mode 4 maps for the oscillating target surface phases with that of the static target surface shows that target surface motion does not significantly alter the formation of alternating coherent structures in the impinging-jet flow. The exception to this occurs when the target surface is at phase ϕ_1, where the structures formed are actually due to the effect of target surface motion at an earlier phase ϕ_6, when the target surface is closest to the jet exit and moving towards it. It is observed that the vorticity maps for phases ϕ_3 and ϕ_6 are similar to those for the static target surface, in each of the corresponding modes. These similarities are found to occur when the target surface decelerates from phases ϕ_2 and ϕ_5 respectively, which are phases where it attains maximum velocity during oscillation.

The non-dimensional vorticity maps of POD modes 2 to 4 for jet impingement on an unheated static target surface and oscillating target surface at 20 Hz are shown in Fig. 4.17. The Mode 2 vorticity contours for phases ϕ_1 and ϕ_2, in Figs. 4.17(b) and 4.17(c), show that the vorticities in the free-jet shear layer are opposite in sign to those for the static target but similar in magnitude. However, when compared with the Mode 2 maps for these phases for target-surface oscillation at 80 Hz, as shown in Figs. 4.16(b) and 4.16(c), it is observed that the vorticities in the free-jet shear layer are higher. These observations indicate that there is no reduction in the magnitudes of velocity fluctuations in the free-jet shear layer for these phases, which is due to the minimal effect of target surface motion on the free-jet and the ambient fluid region while oscillating at a frequency of 20 Hz, as shown in Fig. 4.9(g) and also in Figs. 4.14(b) and 4.14(c).

The Mode 2 vorticities for phases ϕ_3 to ϕ_5, in Figs. 4.17(d) to 4.17(f), are observed to be similar to those for the static target surface, which means that the deceleration of the target surface and its ensuing motion towards the jet exit does not change the velocity fluctuations in the free-jet shear layer. The Mode 2 vorticities for phase ϕ_6 are found to be similar to those for phases ϕ_1 and ϕ_2. The vorticity magnitudes in the wall-jet region in the Mode 2 maps for all phases are similar to those for the static target surface indicating that target-surface oscillation at a frequency of 20 Hz does not significantly affect velocity fluctuation magnitudes in the wall-jet region.

The Mode 3 maps for phases ϕ_1 and ϕ_6 in Figs. 4.17(b) and 4.17(g), are similar to those for the static target surface, except that the structures in phase ϕ_6 have opposite vorticity signs when the target surface is closest to the jet exit but moving towards it. The Mode 3 vorticities in the wall-jet region for phases ϕ_1, ϕ_2 and ϕ_5 show the same signs as those for the static target, but the magnitudes are higher for phases ϕ_1 and ϕ_2. The lower magnitudes of vorticity in the wall-jet region for phase ϕ_5 occur due to motion of target surface towards the jet exit. This behavior was also observed at phase ϕ_5 in target surface oscillating at 80 Hz, as shown in Fig. 4.16(f), but in Mode 2.

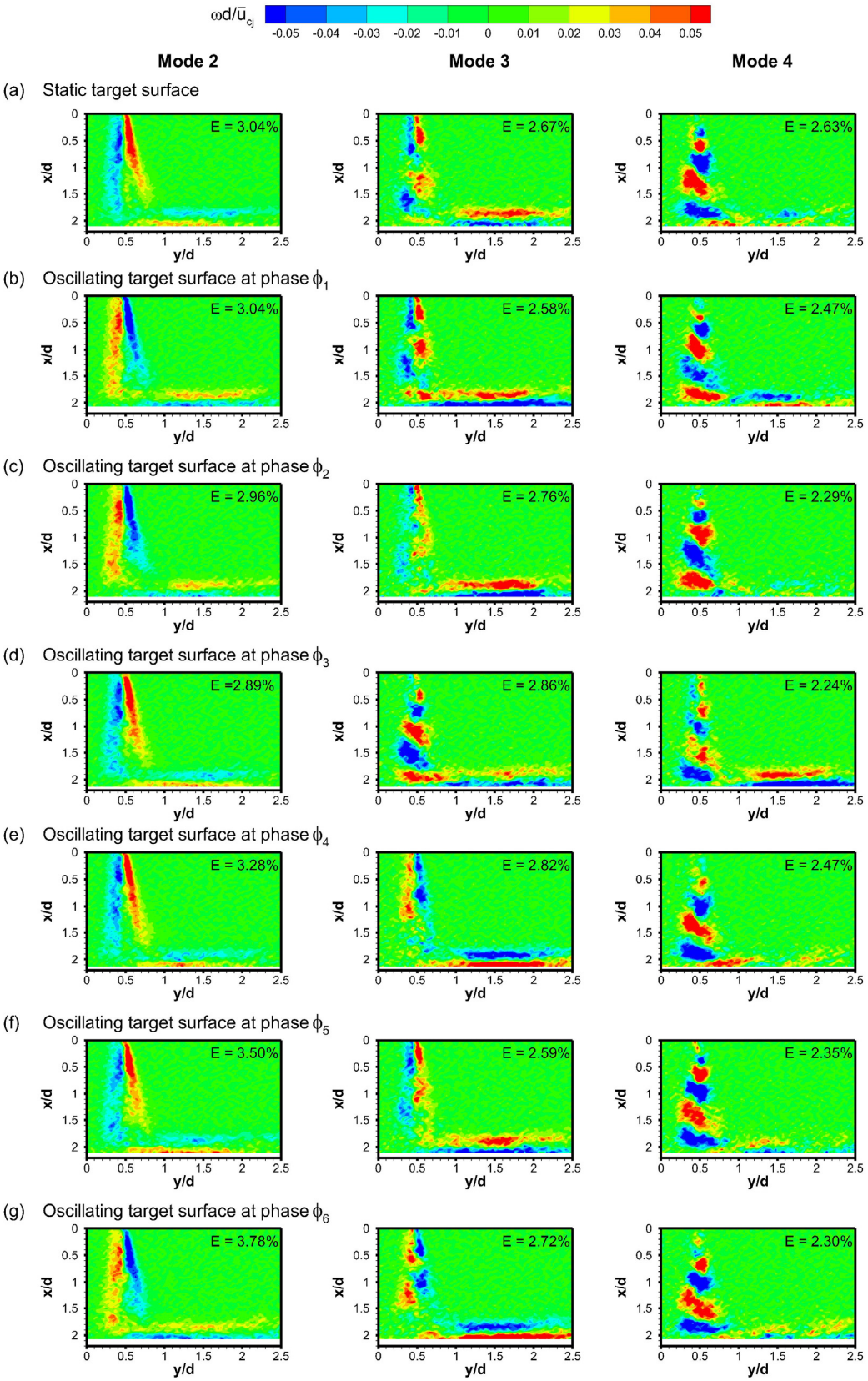

Fig. 4.17 Vorticity maps of POD modes 2 to 4 for jet impingement on unheated target surfaces: (a) static target surface, (b) to (g) oscillating target surface at 20 Hz, at phases ϕ_1 to ϕ_6 respectively

A comparison of the Mode 4 maps for the oscillating target surface with that for the static target surface shows that the alternating vorticity structures are present in all phases. It is also observed that phases ϕ_3 to ϕ_6 have structures with vorticity signs the same as those for the static target surface, while phases ϕ_1 and ϕ_2 have opposite signs. It is interesting to note that the vorticity structures in Mode 3 for phase ϕ_3 have the same signs as those in Mode 4 for phases ϕ_1 and ϕ_2, which suggests that the deceleration of the target surface while moving away from the jet exit gives rise to similar structures observed at the earlier phases but at a higher energy mode.

The POD modes shown in Figs. 4.16 and 4.17 elucidate the effect of target-surface oscillation on coherent structures in the impinging jet. It shows that for target surface oscillating at 80 Hz frequency, target-surface motion away from the jet exit increases stream-wise velocity fluctuations in the wall-jet shear layer, whereas motion towards the jet exit increases velocity fluctuations in the free-jet shear layer which are opposite to the stream-wise direction. Higher vorticity in the wall-jet during target-surface motion away from the jet exit indicates an increase in energy in this region from that for the static target surface. This is also reflected in Figs. 4.10(a) and 4.11(a), in the form of higher maximum mean radial velocities and wall-shear stress than those for the static target motion. In the case of target-surface oscillation at 20 Hz, the POD modes show that effect of target-surface motion on the velocity fluctuations in the free-jet shear layer and the wall-jet region is small and in some instances produces flow features which are similar to those found for the static target surface.

4.4.1 Instantaneous vortex structures

The formation of shear-layer vortices and their interaction with the target surface in the case of jet impingement on a static target surface are shown in Fig. 4.18. The instantaneous vectors in Fig. 4.18 have been reconstructed using POD modes 1 to 30 and are superimposed on their vorticity contours. The primary vortices (PV) generated in the free-jet shear layer, travel downstream and impinge on the surface. The interaction of primary vortices with the surface induces positive radial velocities in the flow and generates secondary vortices (SV) at the surface as a result of viscous retardation, as shown in Fig. 4.18(a). The secondary vortices are characterized by opposite sign of vorticity to that of the primary vortex and are formed at a radial location below and downstream of the primary vortex. These secondary vortices detach from the surface giving rise to an ejection of the fluid from the surface, as shown in Fig. 4.18(b), which is the zoomed-in representation of Fig. 4.18(a).

In some instances this fluid ejection due to the secondary vortex produces a local separation of the boundary layer. The vector map at such an instant is shown in Fig. 4.18(c) which shows the formation of a primary-secondary vortex pair. The flow separation region under the secondary vortex is shown marked in Fig. 4.18(d), which is a zoomed-in representation of Fig. 4.18(d). This instantaneous local flow reversal is a rare event that is found to occur only in 1% of the PIV images, which corroborates the findings of Tummers et al. (2011). The interaction of vortices with the target surface and the formation of primary-secondary vortex pairs in jet impingement on a static target surface have also been demonstrated in earlier studies by Didden and Ho (1985), Landreth and Adrian (1990), El Hassan et al. (2013) and Long and New (2016). The instantaneous flow structures in the following results are illustrated based on vorticity instead of quantities such as Q-criterion (Hunt et al. 1988; Chong et al. 1990) or λ_2-criterion (Jeong and Hussain 1995) because these criteria do not clearly capture and represent the phenomena of jet flapping in the free-jet shear layer and the shear-layer splitting in the wall-jet region.

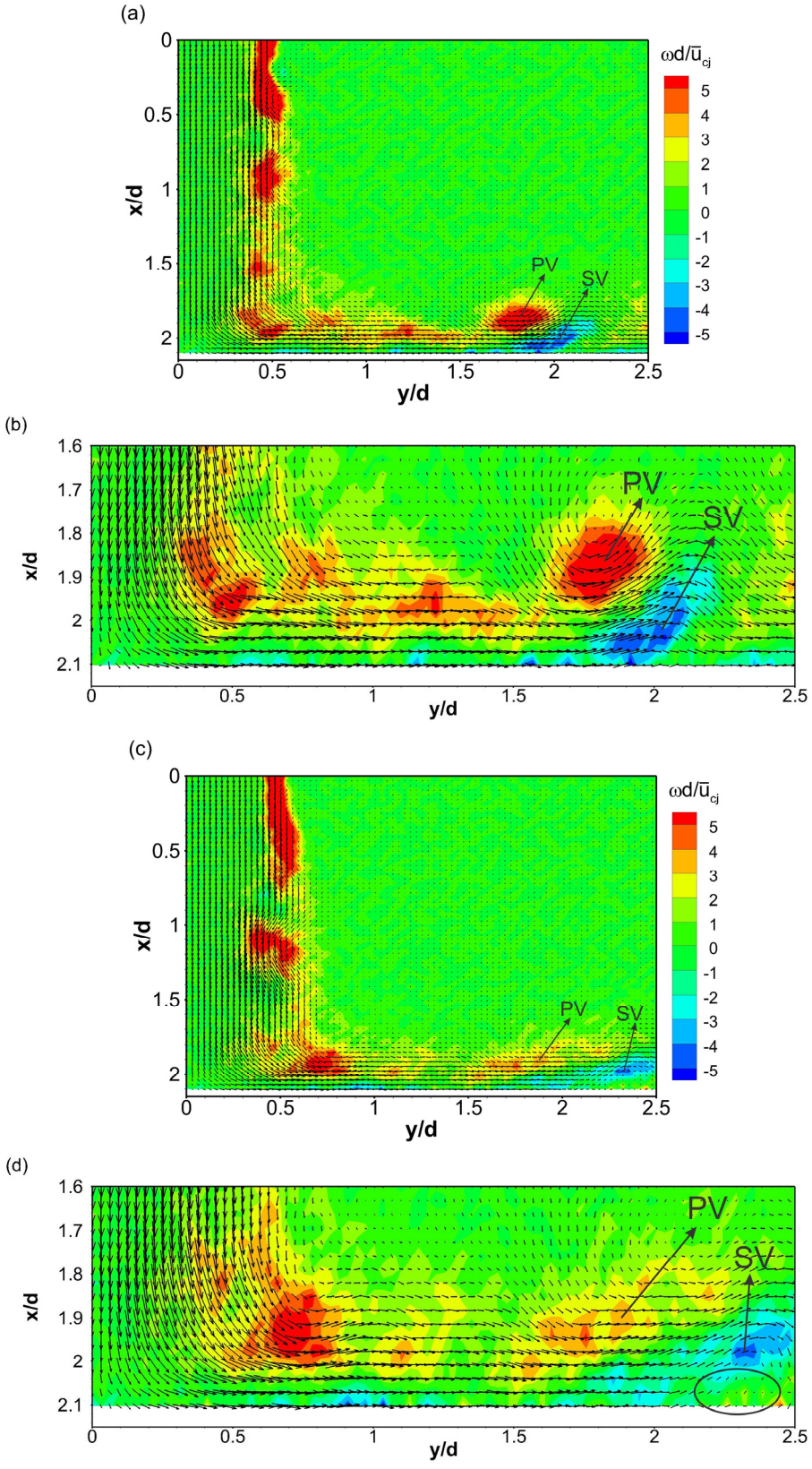

Fig. 4.18 Instantaneous vorticity maps of vectors reconstructed using POD modes 1 to 30 for jet impingement on an unheated static target surface: (a) Instantaneous map 1 (b) Zoomed-in view of Instantaneous map 1 (c) Instantaneous map 2 (d) Zoomed-in view of Instantaneous map 2

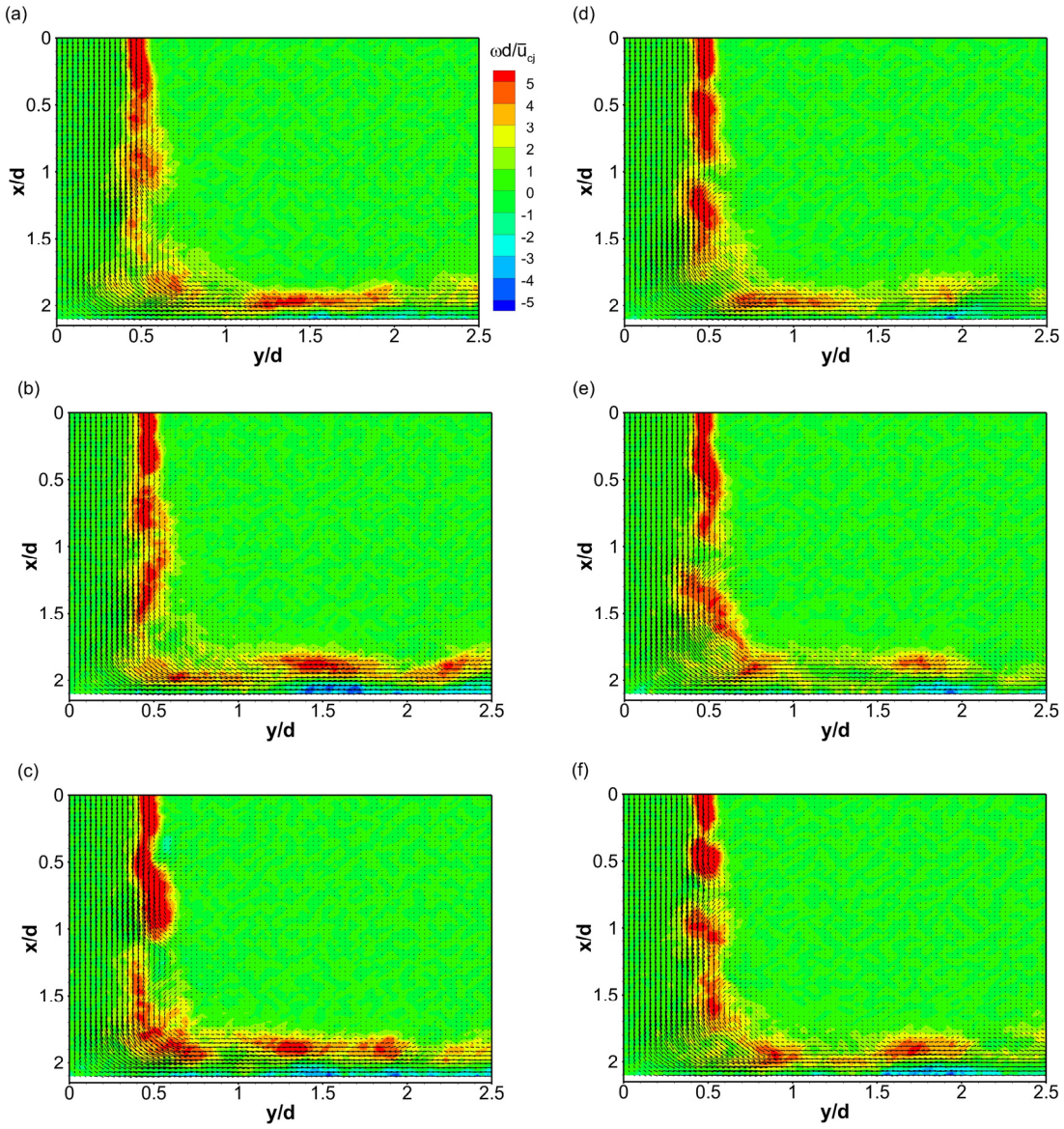

Fig. 4.19 Sequence of instantaneous vorticity maps of vectors reconstructed using POD modes 1 to 30 for jet impingement on an unheated static target surface. Time between each instantaneous map is 0.01s.

A sequence of instantaneous vorticity maps for jet impingement on a static target surface is shown in Fig. 4.19. These figures demonstrate the phenomenon of "jet flapping", which is associated with instabilities in the free-jet shear layer. The flapping instability is a low frequency lateral oscillation of the shear layer about its mean location in which the shear layer undergoes lateral oscillations as the primary vortices form and break-up downstream. This is shown in Figs. 4.19(a) and 4.19(b) and the process occurs repetitively as shown in Figs. 4.19(c) to 4.20(f). The flapping motion

is more pronounced in jets issuing from convergent nozzles and it contributes to a higher spreading rate and decay than in jets emerging from straight round nozzles (Donaldson and Snedeker 1971). The presence of a similar jet flapping motion has been examined in earlier studies by Ho and Nosseir (1981), Maurel and Solliec (2001) and Kim et al. (2007).

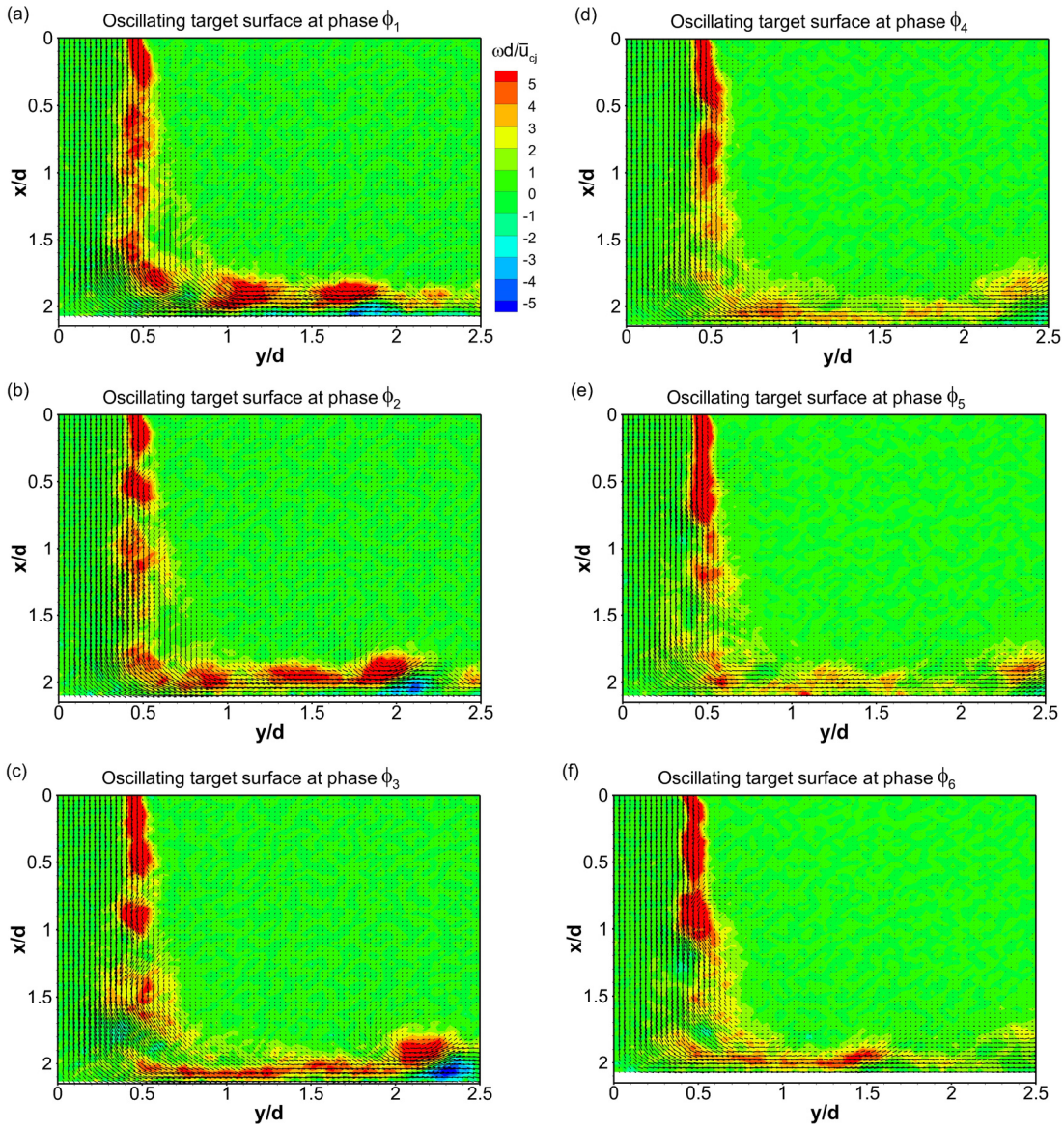

Fig. 4.20 Sequence (No. 1) of instantaneous vorticity maps of vectors reconstructed using POD modes 1 to 30 for one oscillation cycle in jet impingement on an unheated target surface oscillating at 80 Hz: (a) to (f) phases ϕ_1 to ϕ_6

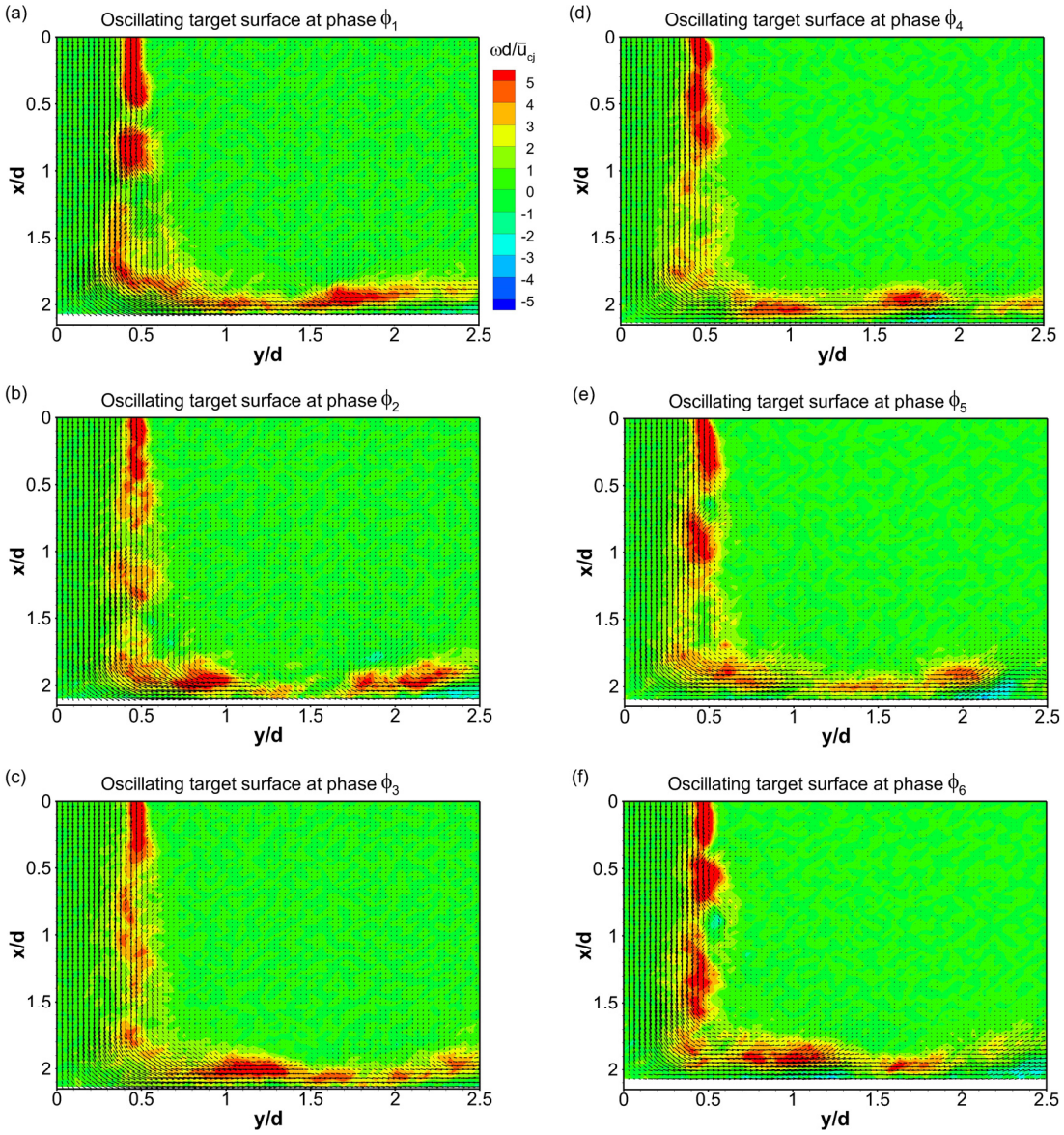

Fig. 4.21 Sequence (No. 2) of instantaneous vorticity maps of vectors reconstructed using POD modes 1 to 30 for one oscillation cycle in jet impingement on an unheated target surface oscillating at 80 Hz: (a) to (f) phases ϕ_1 to ϕ_6

The instantaneous vorticity maps in two different oscillation cycles for jet impingement on an unheated target surface oscillating at 80 Hz are shown in Figs. 4.20 and 4.21. As in the case of jet impingement on a static target surface, the instantaneous velocity vectors for each phase have been reconstructed using POD modes 1 to 30 and are overlaid on their non-dimensional vorticity contours. The time interval between successive instantaneous images for phases ϕ_1 to ϕ_3 and phases ϕ_4 to ϕ_6 is 1.25 ms, while the time interval between phase ϕ_3 to ϕ_4 is 3.75 ms.

Figures 4.20(a) to 4.20(b) show the formation and radial progression of the primary-secondary vortex pair at the wall as the target surface moves away from the jet exit through phases ϕ_1 to ϕ_3. The occurrence of these vortex pairs are also observed in another oscillation cycle but for phases ϕ_4 to ϕ_6, as shown in Figs. 4.21(d) to 4.21(f). The formation of the secondary vortex at these phases is not as strong as that observed for phases ϕ_1 to ϕ_3 in Fig. 4.20, because of the interaction of the target-surface with the primary vortex. When the primary vortex impinges on the surface during target-surface motion towards the jet exit, the action of the surface counteracts the vortex formation and reduces its strength, which in turn affects the formation of the secondary vortex.

The phenomenon of "jet flapping" seen in Fig. 4.19 for jet impingement on a static target surface is also observed for jet impingement on an oscillating target surface in Figs. 4.20 and 4.21. The flapping motion of the free-jet shear layer can be seen in Figs. 4.20(d) to 4.20(f) and also in Figs. 4.21(d) to 4.21(f) for target-surface oscillation at 80 Hz.

The instantaenous vector fields shown in Figs. 4.20 and 4.21 show the effect of target-surface oscillation on the ambient fluid region. The vector magnitudes in the ambient fluid region for phases ϕ_1 to ϕ_3 are greater than those for the static target surface shown in Fig. 4.19, and for phases ϕ_4 to ϕ_6 they are lower. The difference between the vectors in the ambient region for phases ϕ_1 to ϕ_3 and phases ϕ_4 to ϕ_6 is more clear when observed in Figs. 4.20 and 4.21. It is seen that the motion of the target surface away from the jet exit increases the velocity magnitude of the ambient fluid thereby increasing entrainment into the jet, whereas the motion towards the jet exit decreases the velocity magnitude of the ambient fluid.

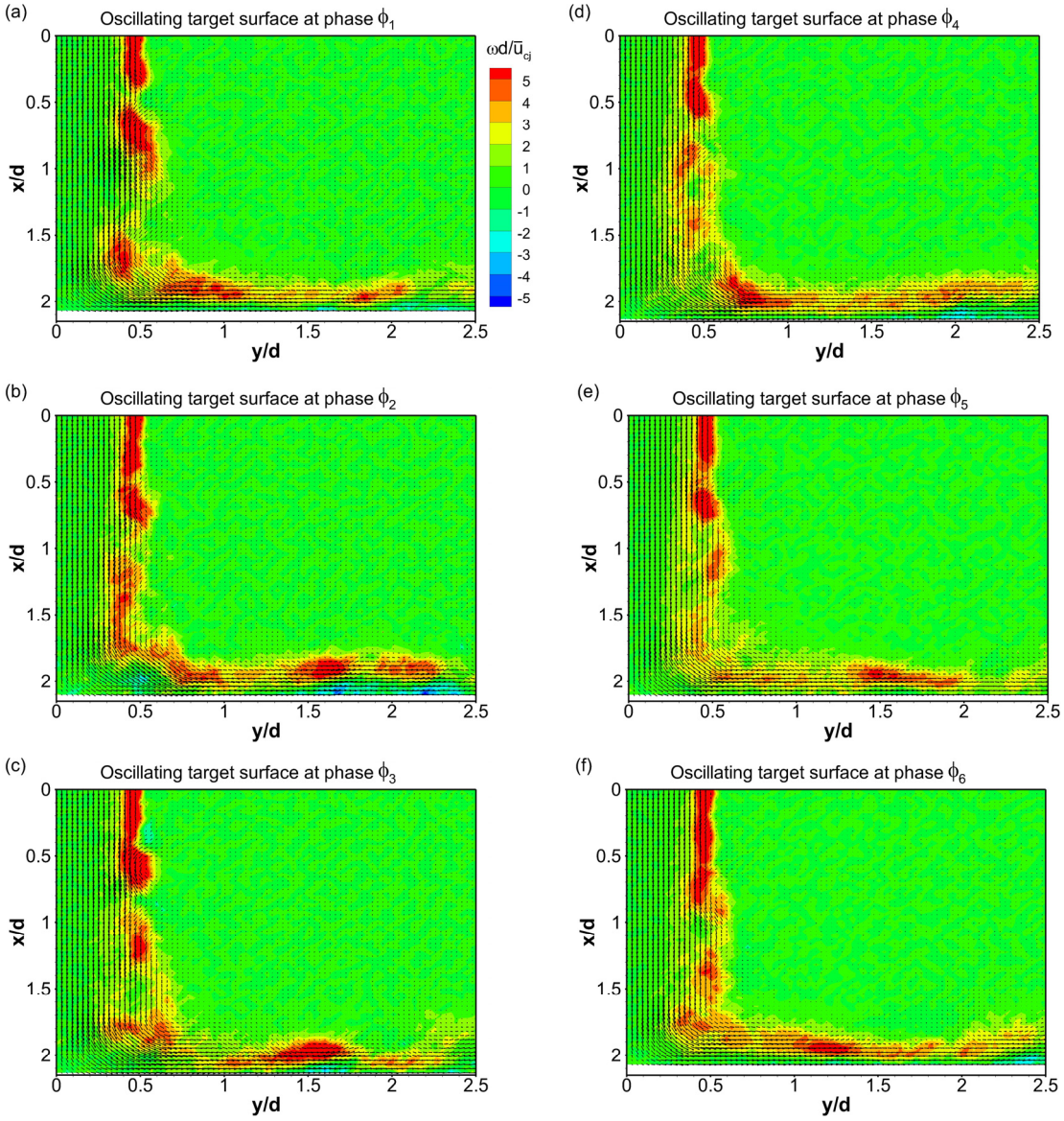

Fig. 4.22 Sequence (No. 1) of instantaneous vorticity maps of vectors reconstructed using POD modes 1 to 30 for one oscillation cycle in jet impingement on an unheated target surface oscillating at 20 Hz: (a) to (f) phases ϕ_1 to ϕ_6

The instantaneous vorticity maps in two different oscillation cycles for jet impingement on an unheated target surface oscillating at 20 Hz are shown in Figs. 4.22 and 4.23 where the vectors in each phase have been reconstructed using POD modes 1 to 30. The time interval between successive instantaneous images for phases ϕ_1 to ϕ_3 and phases ϕ_4 to ϕ_6 is 5 ms, while the time interval between phase ϕ_3 to ϕ_4 is 10 ms.

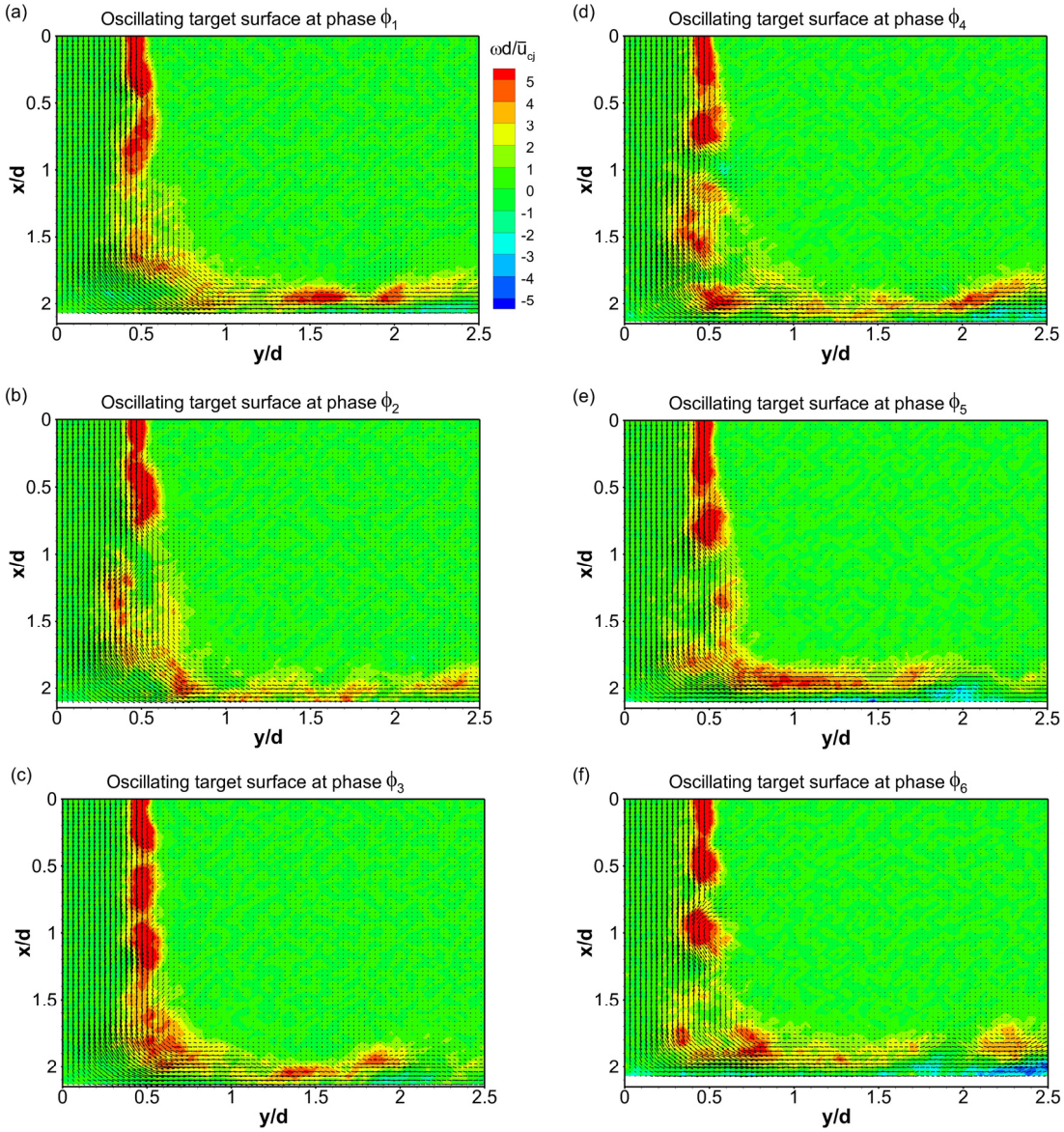

Fig. 4.23 Sequence (No. 2) of instantaneous vorticity maps of vectors reconstructed using POD modes 1 to 30 for one oscillation cycle in jet impingement on an unheated target surface oscillating at 20 Hz: (a) to (f) phases ϕ_1 to ϕ_6

The occurrence of primary-secondary vortex pairs are observed at phase ϕ_2 in Fig. 4.22(b) and at phases ϕ_5 and ϕ_6 in Figs. 4.23(e) and 4.23(f). The strength of the secondary vortices in Fig. 4.22(b) and 4.23(f) are similar to each other. However, the strength of the secondary vortex in Fig. 4.23(f) is stronger than that observed at phase ϕ_5 of target surface oscillating at 80 Hz in Fig. 4.21(e). This is due to the reduced effect of target-surface motion on the primary vortex when the target surface moves

towards the jet exit. The velocity of the target surface is lower while oscillating at 20 Hz and therefore its ability to counteract the vortex formation is reduced.

The flapping motion of the free-jet shear layer also occurs for jet impingement on an unheated target surface oscillating at 20 Hz. This is observed for phases ϕ_4 to ϕ_6 in Figs. 4.22(d) to 4.22(f) and for phases ϕ_1 to ϕ_3 in Figs. 4.23(a) to 4.23(c). The instantaneous maps in Figs. 4.22 and 4.23 show that the effect of target-surface motion on the ambient fluid region is lower than that observed in Figs. 4.20 and 4.21, for target-surface oscillation at 80 Hz. The velocity magnitudes of the vectors in the ambient fluid region for phases ϕ_1 to ϕ_3 are similar to those for phases ϕ_4 to ϕ_6 in Figs. 4.22 and 4.23. This occurs because the velocity of the target surface is lower while oscillating at 20 Hz and is not high enough to significantly accelerate or decelerate the ambient fluid during target-surface motion away from the jet exit and towards it respectively.

In summary, the instantaneous vector maps reconstructed using POD modes 1 to 30 for jet impingement on an unheated static target surface show the presence of primary-secondary vortex pairs and the flapping motion of the free-jet shear layer. These flow features are also observed in the POD reconstructed vector maps for jet impingement on an unheated target surface oscillating at both 80 Hz and 20 Hz. The formation of the secondary vortex is inhibited during target-surface motion towards the jet exit, which occurs only in target-surface oscillation at 80 Hz. At this frequency, the instantaneous vectors in the ambient fluid region attain higher velocity magnitudes than those for the static target surface, for phases during target-surface motion towards the jet exit, and lower velocity magnitudes for phases during the opposite motion. It is found that the effect of target-surface motion on the secondary vortex formation and on the ambient fluid region is insignificant for jet impingement on target-surface oscillation at 20 Hz frequency.

4.5 Turbulence statistics

4.5.1 RMS axial velocity fluctuation

Figure 4.24 shows the root-mean-square (rms) axial velocity fluctuation contours $u_{rms}/\overline{u}_{cj}$ for jet impingement on unheated, static and oscillating target surfaces. For the static target surface, the rms axial velocity fluctuation in the free-shear layer attains a maximum magnitude of 0.18 as seen in Fig. 4.24(a). The rms axial velocity fluctuations in the wall-jet do not exceed 0.12, with the maximum occurring at radial location $y/d = 2$, while the near-wall fluctuations are approximately 0.08. For phases ϕ_1 to ϕ_3, in Figs. 4.24(b) to 4.24(d), the rms axial velocity fluctuation magnitudes in the wall-jet are higher for target surface oscillating at 80 Hz, when compared with the static target surface. This is because of higher mean axial velocities and increased entrainment of the ambient fluid into the wall-jet, as shown in Fig. 4.8(c).

The rms axial velocity fluctuations in the free-jet shear layer for phases ϕ_4 to ϕ_6 in Fig. 4.24(e) to Fig. 4.24(g), are considerably higher for target-surface oscillation at 80 Hz, than those for the static target surface case. This is a result of larger shear that occurs between the decelerated ambient fluid and mean axial flow in the free-jet as shown in Fig. 4.8(g) for these phases, and also in Figs. 4.14(e) to 4.14(g). The increase in the rms axial velocity fluctuation in the free-jet shear layer can be seen to begin from phase ϕ_3, as a result of the deceleration of the ambient fluid which also begins from phase ϕ_3 as shown in Fig. 4.8(c). For target-surface oscillation at 80 Hz, it is found that the maximum rms axial velocity fluctuation in the wall-jet at radial location $y/d = 2$ for phase ϕ_2 is 15.4% greater, while that in the free-jet shear layer $y/d = 0.5$ for phase ϕ_6 is 13% greater, than that observed for the static target surface. The rms axial velocity fluctuations for target-surface oscillation at 20 Hz are similar to those for the static target surface because of the small effect of target-surface oscillation on the ambient fluid and on the mean axial jet flow as shown in Figs. 4.9(c) and 4.9(g).

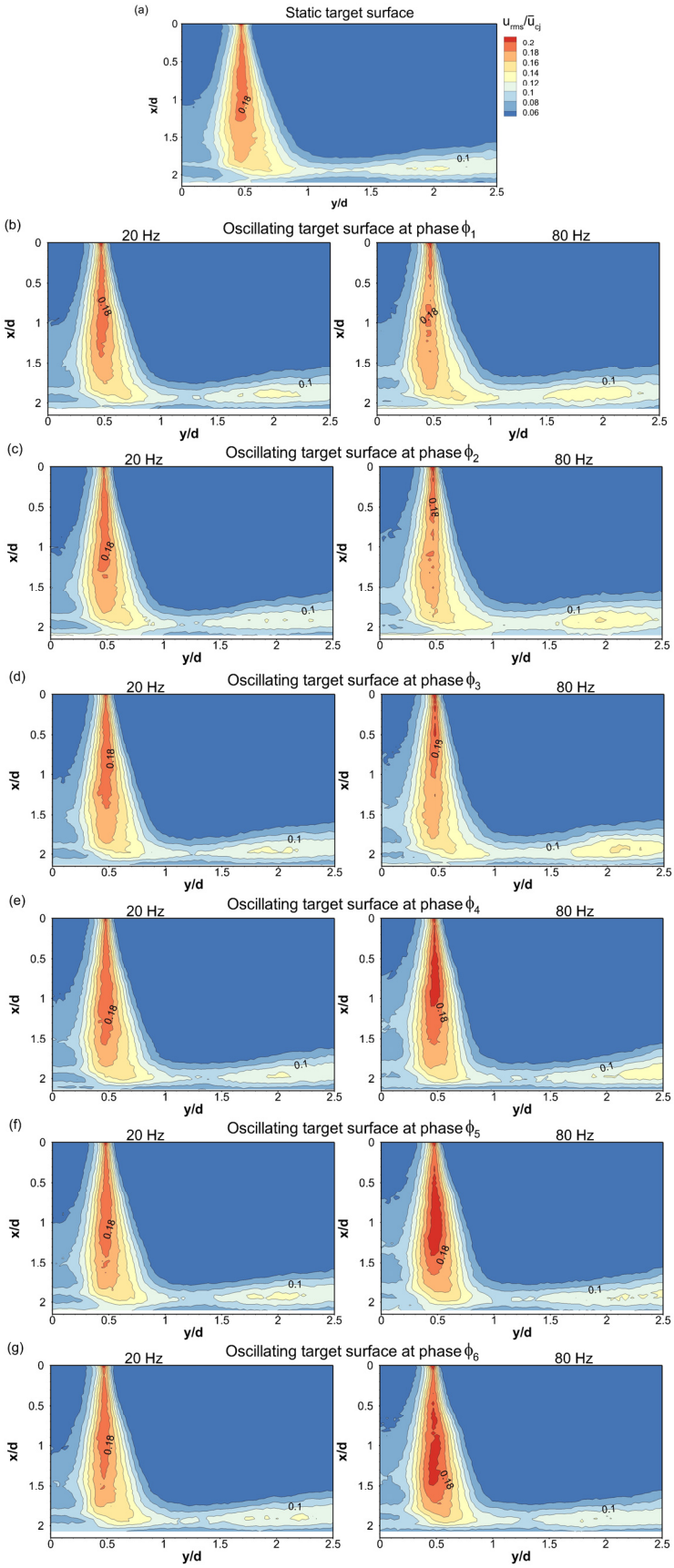

Fig. 4.24 RMS axial velocity fluctuations for jet impingement on unheated target surfaces: (a) static target surface; (b) to (g) oscillating target surface at 20 Hz and 80 Hz, at phases ϕ_1 to ϕ_6 respectively

4.5.2 RMS radial velocity fluctuation

Figure 4.25 shows the rms radial velocity fluctuation $v_{rms}/\overline{u}_{cj}$ contours for the static and oscillating target surfaces. As the wall-jet accelerates radially, it is increasingly affected by its shear due to the wall as well as the quiescent fluid above. This decelerates the wall-jet, as shown in Fig. 4.7(a), and increases the rms radial velocity fluctuations. As seen in Fig. 4.25(a) for the static target surface, the maximum rms radial velocity fluctuation in the wall-jet is 0.18, which is in the vicinity of the radial location y/d = 1.5, beyond which it decreases as the wall-jet boundary-layer thickness increases. The rms radial velocity fluctuations for target-surface oscillation at 20 Hz are higher than those observed for the static target surface, for phases ϕ_1, ϕ_2, ϕ_5 and ϕ_6. This is due to the shear between higher mean radial velocities at near-wall location and lower mean radial velocities at locations further away from the wall for these phases, as seen in Figs. 4.9(d) to 4.9(f). In addition, these 4 phases are closer to the jet exit than phases ϕ_4 and ϕ_5.

The rms radial velocity fluctuations for target-surface oscillation at 80 Hz are significantly higher than those observed for the static target surface, for phases ϕ_1, ϕ_2, ϕ_3 and ϕ_5. This is for the same reason as that for target-surface oscillation at 20 Hz, in addition to the greater effect of target-surface oscillation on the mean radial velocities as shown in Figs. 4.8(d) to 4.8(f) which gives rise to higher shear. It can also be observed that similar contour patterns occur for pairs of phases at a given target-surface oscillating frequency; phases ϕ_1 and ϕ_6, and ϕ_2 and ϕ_5 have similar patterns.

The higher fluctuations in the radial velocities for target-surface oscillation at 80 Hz are also because of entrainment of the ambient fluid into the wall-jet. This reduces the mean radial velocities near the edge of the wall-jet shear layer, as shown in Fig. 4.8(h), which in turn increases mixing and shear between the inner layers of the wall-jet and outer layers of the ambient fluid. This leads to higher radial turbulence intensities compared to that for target-surface oscillation at 20 Hz, where there is lower entrainment of the ambient fluid, as shown in Fig. 4.9(h). At a radial location y/d = 1.5 it is found that the maximum rms radial velocity fluctuation for phase ϕ_2, for target-surface oscillation at 80 Hz, is 21.8% greater than that for the static target surface.

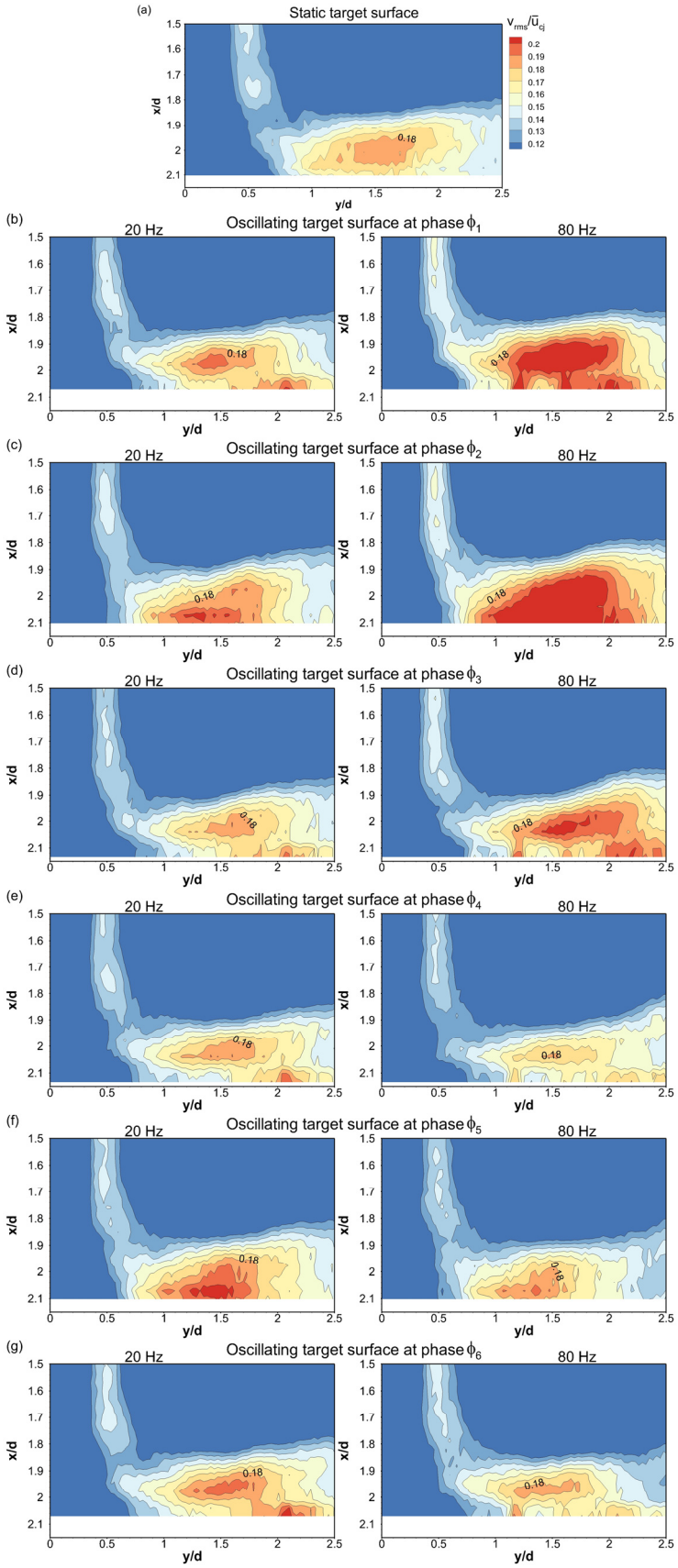

Fig. 4.25 RMS radial velocity fluctuations for jet impingement on unheated target surfaces: (a) static target surface; (b) to (g) oscillating target surface at 20 Hz and 80 Hz, at phases ϕ_1 to ϕ_6 respectively

4.5.3 Reynolds stress and turbulence kinetic energy

The non-dimensional Reynolds stress $\overline{u'v'}/\overline{u}_{cj}^2$ maps for jet impingement on unheated static and oscillating target surfaces are shown in Fig. 4.26. For the static target surface, Fig. 4.26(a) shows a maximum positive magnitude (0.012) in the free-jet shear layer, and a maximum negative magnitude (-0.008) in the wall-jet shear layer. The mean velocity gradient across the free-shear layer is negative, while the mean velocity gradient across the wall-jet shear layer is positive. The opposite signs of the Reynolds stress combined with the signs of the mean velocity gradients in these regions indicate the production of turbulence, as was also shown by Narayanan et al. (2004) and Tummers et al. (2011). The turbulence production is largest in the region where there is a change from viscous stress to turbulent stress.

The Reynolds stress in the wall-jet shear layer for phases ϕ_1 to ϕ_3 in Figs. 4.26(b) to 4.26(d), is higher for target-surface oscillation at 80 Hz than for the static target surface. The magnitude and the axial extent of the positive Reynolds stress in the free-jet shear layer for phases ϕ_5 and ϕ_6 in Figs. 4.26(f) and 4.26(g), are also higher for target-surface oscillation at 80 Hz than for the static target surface. The higher negative Reynolds stress magnitudes in the wall-jet shear layer for phases ϕ_1 to ϕ_3 signify larger production of turbulence, which is due to the combined effect of shear between the mean radial velocities in the wall-jet layers and increased entrainment of the ambient fluid, as shown in Figs. 4.8(d) to 4.8(f) and 4.8(h). The combined effect of the deceleration of the ambient fluid and the increase in the mean axial velocities in the free-jet for phases ϕ_5 and ϕ_6, as shown in Figs. 4.8(b), and 4.8(g), gives rise to higher turbulence production in the free-jet shear layer for these phases.

The Reynolds stress contours for target-surface oscillation at 20 Hz are similar to those for the static target surface because of the smaller effect of target-surface oscillation across the free-jet and wall-jet shear layers, as shown in Figs. 4.9(g) and 4.9(h). For target-surface oscillation at 80 Hz, it is found that the maximum negative Reynolds stress in the wall-jet shear layer at a radial location y/d = 2 for phase ϕ_2 is about 37% higher than that for the static target surface, while the maximum positive Reynolds stress in the free-jet shear layer y/d = 0.5 for phase ϕ_5 is about 10. 77% higher than that for the static target surface.

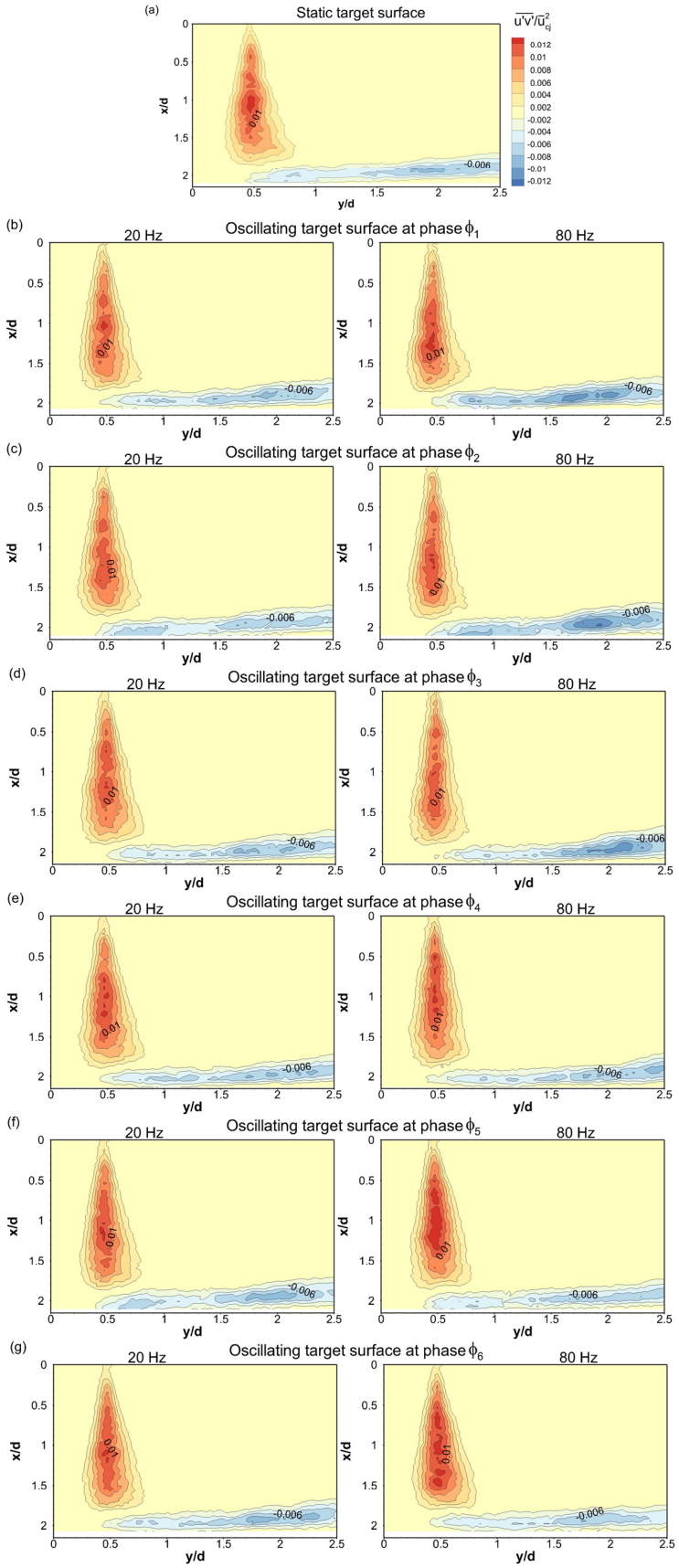

Fig. 4.26 Reynolds stress for jet impingement on unheated target surfaces: (a) static target surface; (b) to (g) oscillating target surface at 20 Hz and 80 Hz, at phases ϕ_1 to ϕ_6 respectively

Figure 4.27 shows the contours of turbulence kinetic energy, defined as $TKE = 0.5(\overline{u'^2} + \overline{v'^2})/\overline{u}_{cj}^2$, for jet impingement on static and oscillating target surfaces. For the static target surface in Fig. 4.27(a), the maximum turbulence kinetic energy in the free-jet shear layer is 0.025, while it the wall-jet shear layer it is 0.020. For target-surface oscillation at 80 Hz, phases ϕ_1 to ϕ_3 in Figs. 4.27(b) to 4.27(d), have higher turbulence kinetic energy in the wall-jet, while phases ϕ_4 to ϕ_6 in Figs. 4.27(e) to 4.27(g), have higher turbulence kinetic energy in the free-jet shear layer, when compared to that for the static target surface. These occur because of the changes in the rms axial and radial velocity fluctuations for the corresponding phases, as shown in Figs. 4.24 and 4.25, which are due to the inter-relation between the effect of target-surface oscillation on the mean axial and radial velocities in free-jet, wall-jet, and ambient regions of the impinging jet-flow, as shown in Figs. 4.8.

The action of Reynolds stress provides energy for turbulence during the static and oscillating target surface jet impingement, as can be seen upon comparing Figs. 4.26 and 4.27. Furthermore, the motion of the target surface at 80 Hz frequency of oscillation increases this supply of energy. If all the phases are considered together then the energy production in the entire flow field is significantly higher in the presence of target-surface oscillation at 80 Hz. The turbulence kinetic energy contours for target-surface oscillation at 20 Hz are similar to those of the static target surface as the oscillatory motion of target surface at this low frequency is not strong enough to affect the impinging jet-flow regions, as explained through the Reynolds stress contours shown in Fig. 4.26. For target-surface oscillation at 80 Hz, the maximum turbulence kinetic energy for phase ϕ_2 in the wall-jet is found to be 38.7% higher, while that for phase ϕ_5 in the free-jet shear layer is found to be 19.45% higher, than that for the static target surface.

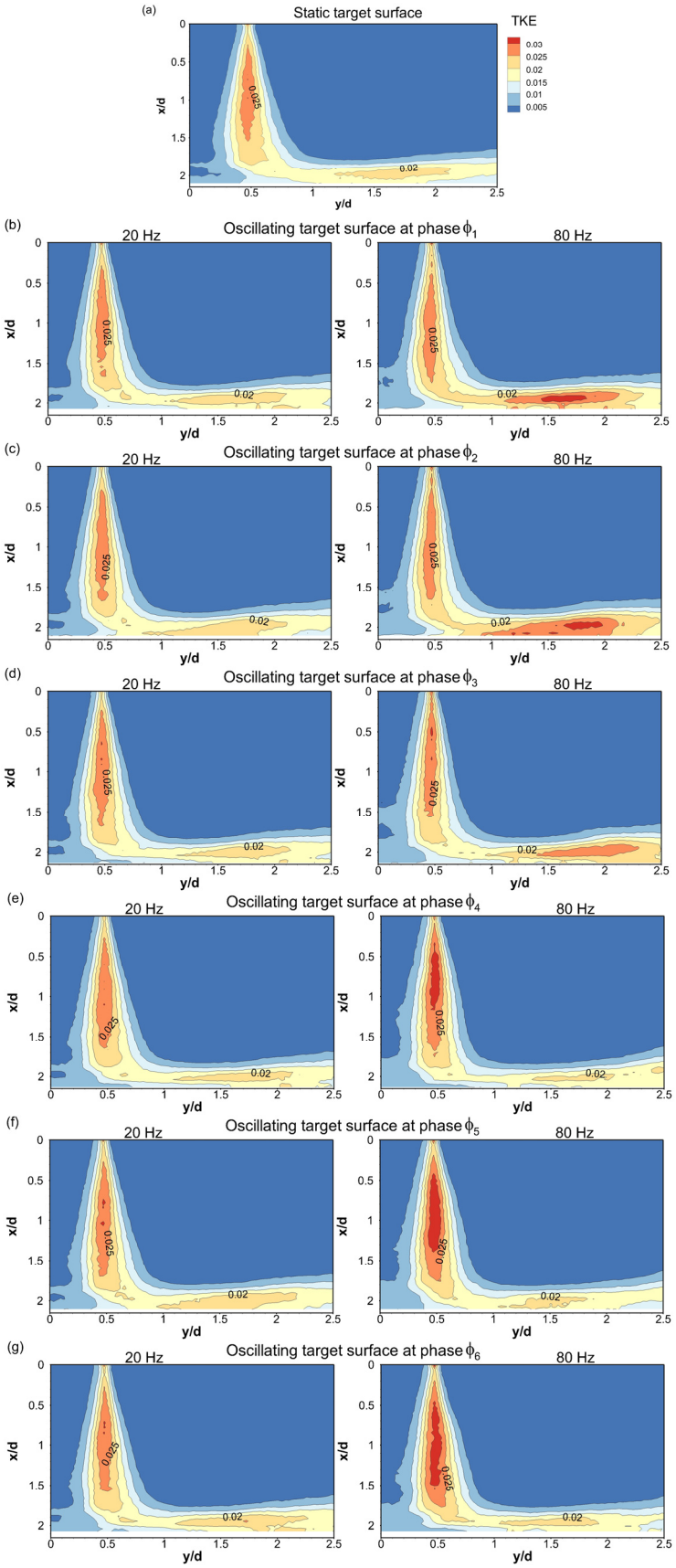

Fig. 4.27 Turbulence kinetic energy for jet impingement on unheated target surfaces: (a) static target surface; (b) to (g) oscillating target surface at 20 Hz and 80 Hz, at phases ϕ_1 to ϕ_6 respectively

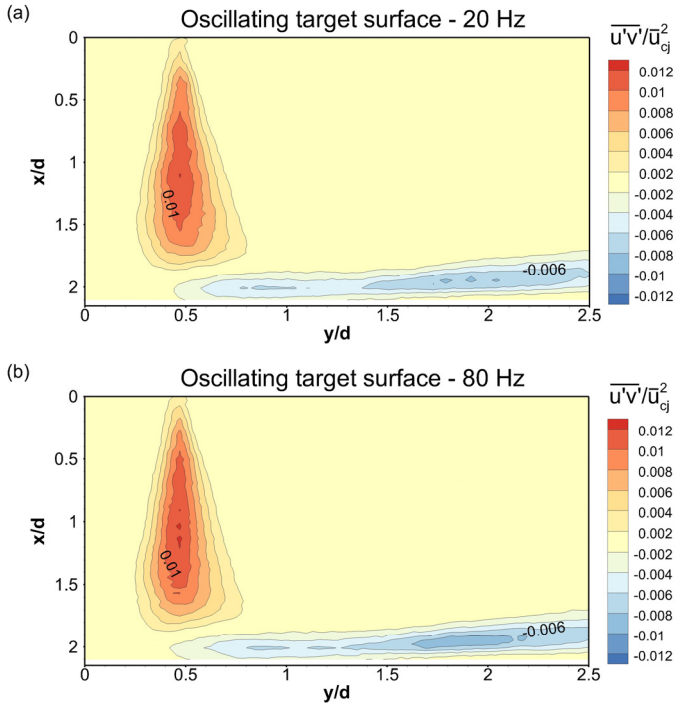

Fig. 4.28 Phase-averaged Reynolds stress for jet impingement on an unheated target surface oscillating at: (a) 20 Hz; (b) 80 Hz

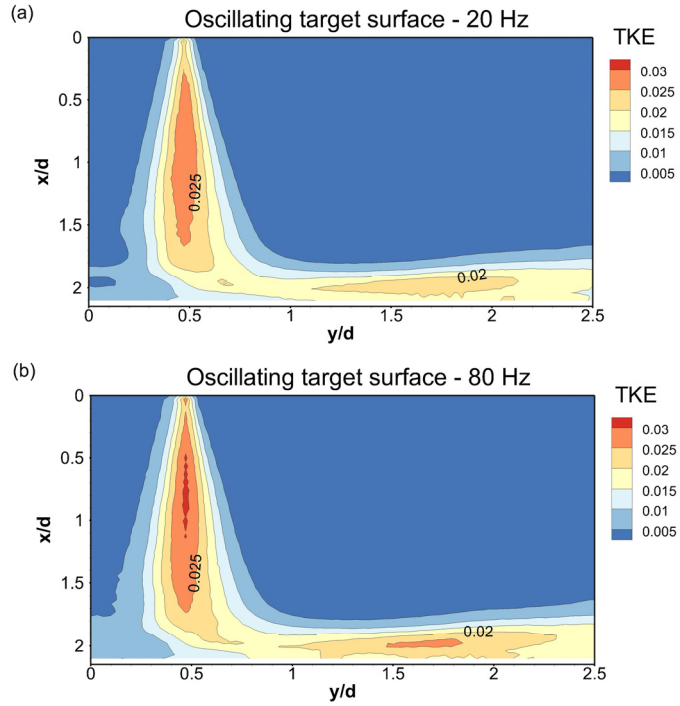

Fig. 4.29 Phase-averaged turbulence kinetic energy for jet impingement on an unheated target surface oscillating at (a) 20 Hz; (b) 80 Hz

The phase-averaged contours of Reynolds stress and turbulence kinetic energy for jet impingement on target surfaces oscillating at 20 Hz and 80 Hz are shown in Fig. 4.28 and 4.29 respectively. These maps are obtained by averaging the corresponding quantities over the 6 phases that approximately cover one cycle of oscillation of the target surface. A comparison between the phase-averaged Reynolds stress for oscillating target surfaces, in Figs. 4.28(a) and 4.28(b), and that of the Reynolds stress for the static target surface, in Fig. 4.26(a), shows that turbulence production in the impinging-jet flow due to target-surface oscillation at 80 Hz is greater than that for target-surface oscillation at 20 Hz and for the static target surface. A similar comparison of the turbulence kinetic energies shown in Figs. 4.29(a) and 4.29(b) and Fig. 4.27(a) indicates higher energy production in the entire flow field due to target-surface oscillation at 80 Hz than that at 20 Hz and the static target surface. The phase-averaged turbulence kinetic energies for target-surface oscillation at 20 Hz are similar to those for the static target surface.

4.6 Summary

The results for jet impingement on unheated static and oscillating target surfaces were presented in this chapter. The variations of the mean velocity components with target surface phases show that mean axial velocities increase during motion of the target surface away from the jet exit while the mean radial velocities decrease. The large-scale flow features of primary-secondary vortex pairs observed for jet impingement on a static target surface are also observed for jet impingement on an oscillating target surface. There is an increased entrainment of ambient fluid into the jet due to target-surface oscillation at a frequency of 80 Hz. The effect of target-surface motion while oscillating at this frequency also produces higher turbulence intensities and velocity fluctuations. These occur in the wall-jet while moving away from the jet exit, and in the free-jet shear layer while moving towards the jet exit. A similar behaviour is observed for the Reynolds stress and turbulence kinetic energies.

The next chapter presents the results for Part II of this study which involves jet impingement on heated static and oscillating target surfaces.

Part II

Jet Impingement on Heated Static and Oscillating Target Surfaces

Chapter 5

Results and Discussion: Jet Impingement on Heated Target Surfaces

The results of the second part of this study are presented in this chapter. The presentation of the results and their discussion are in the following order.

The results begin with a comparison of jet impingement on unheated and heated, static and oscillating target surfaces, in order to examine the impinging-jet flow characteristics in the presence and absence of target surface heating. The comparison is done through a presentation of the mean velocities and rms velocity fluctuations for jet impingement on unheated and heated, static and oscillating target surfaces.

The results of jet impingement on heated static and oscillating target surfaces are presented next. The fluid dynamics results from PIV measurements are presented first, followed by the heat transfer results from infrared thermography (IRT) measurements. The fluid dynamics results include the:

i. Instantaneous flow fields;
ii. Mean flow characteristics and wall-shear stress;
iii. Proper Orthogonal Decomposition (POD) analysis;
iv. RMS axial and radial velocity fluctuations; and,
v. Reynolds stress and turbulence kinetic energy.

The following heat transfer results are also presented:

i. Steady-state time-averaged spatial temperature distributions
ii. Variations of local and azimuthal Nusselt number

Following the convention adopted in Chapter 4, the spatial locations are expressed non-dimensionally based on the jet exit diameter d, while the mean velocity components and the turbulence statistics are expressed non-dimensionally based on the mean-centerline jet exit velocity ($\bar{u}_{cj}$) of jet impingement on a heated static target surface.

5.1 Comparison of jet impingement on unheated and heated, static and oscillating target surfaces

A comparative analysis of jet impingement on unheated and heated, static and oscillating target surfaces is presented below. Flow measurements were carried out for jet impingement on unheated static and oscillating target surfaces, wherein the target surface (Inconel foil) was unheated. The experimental parameters for jet impingement on the unheated static surface are the same as those for jet impingement on the heated static target surface; Re = 5000, $(h/d)_m = 1.95d$. Jet impingement on unheated and heated oscillating target surfaces is carried out at a target-surface oscillation frequency f_s = 20 Hz and peak-to-peak displacement amplitude A_s = 2.5 mm. The flow characteristics presented here are the mean axial velocity contours, the mean radial velocity profiles, and the rms axial and radial velocity fluctuations contours.

The mean axial velocity $\overline{u}/\overline{u}_{cj}$ contours for jet impingement on unheated and heated, static and oscillating target surfaces are shown in Fig. 5.1. The mean axial velocity contours for jet impingement on unheated and heated, static target surfaces in Fig. 5.1(a) shows that the axial and radial extensions of the potential-core region, marked by contour 0.97, are larger for the heated static target surface. The contours also show that the radial extension of the contour marked 0.15 is larger for the heated static target surface. These flow changes occur because the ambient fluid experiences a thermal gradient away from the wall towards the jet exit due to effect of surface heating. This increases the buoyancy of the ambient fluid which leads to lower entrainment into the jet. The reduced entrainment of the ambient fluid into the jet, when compared to that for jet impingement on an unheated static target surface, reduces mixing of the jet with the ambient fluid, and in turn reduces jet spreading.

As the target surface is vertically mounted the warmer ambient fluid experiences an induced flow in the positive y/d direction. This suggests that there is an increased entrainment into the free-jet in the negative y/d region of jet impingement on a heated static target surface. However, this region lies outside the PIV measurement region shown in Fig. 3.8(b). It should be noted that although the ambient fluid region is seeded with particles, the velocity of the buoyant ambient fluid is too small to be resolved with the PIV system and parameters used in this study.

For jet impingement on unheated and heated oscillating target surfaces, Figs. 5.1(b) to 5.1(g) show that the potential-core regions for all phases are similar in size and shape to the corresponding potential-core regions of jet impingement on both unheated and heated static target surfaces. A similar behavior can be observed for the radial extensions of the mean axial velocity contour 0.15. These observations show that the effect of target-surface oscillation at 20 Hz on the mean axial velocities is small, even in the presence of surface heating.

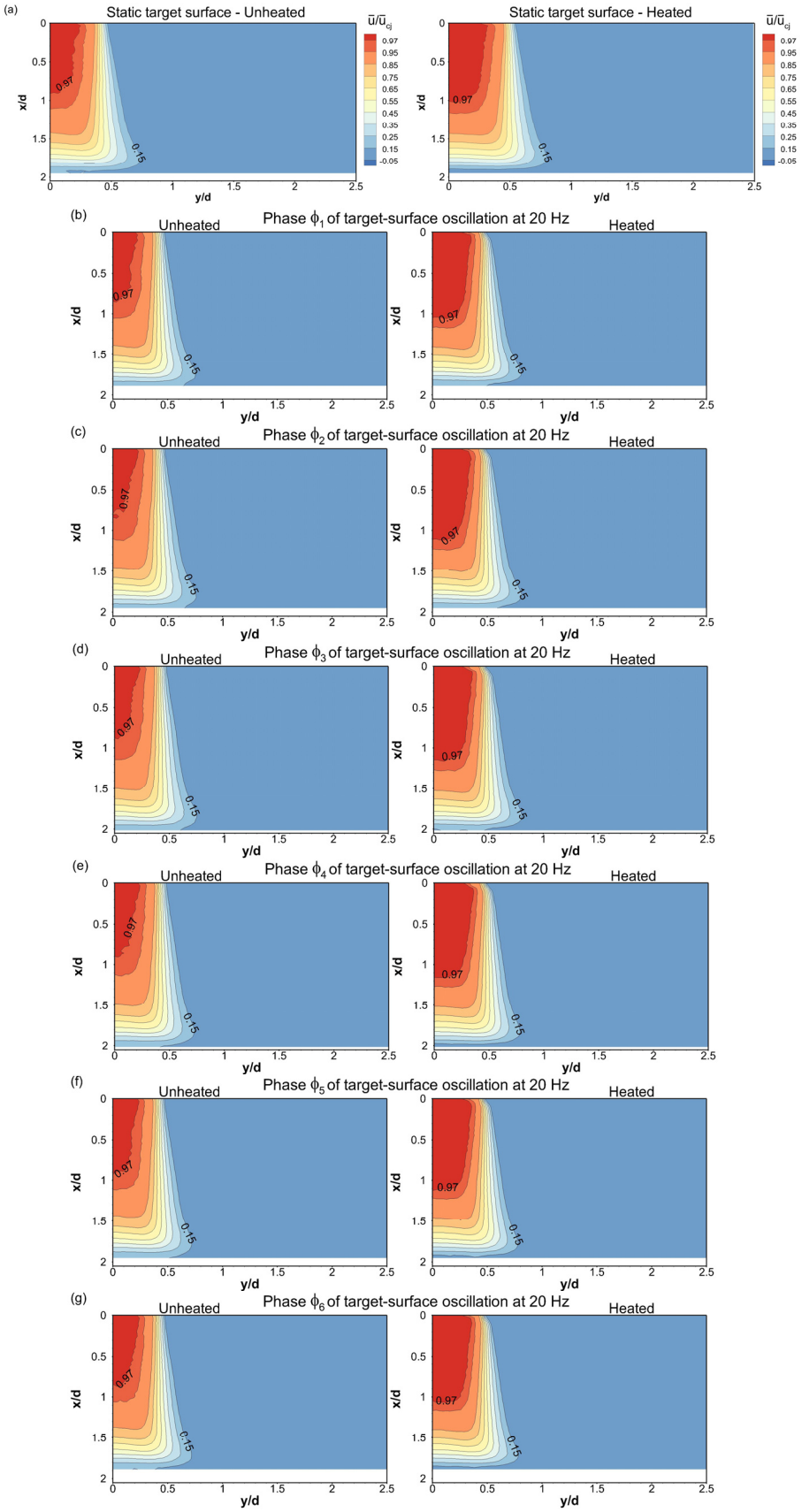

Fig. 5.1 Mean axial velocity contours for jet impingement on unheated and heated target surfaces: (a) static target surfaces; (b) to (g) oscillating target surfaces at 20 Hz, at phases ϕ_1 to ϕ_6 respectively

The mean radial velocity $\overline{v}/\overline{u}_{cj}$ profiles for jet impingement on unheated and heated static target surfaces, at y/d = 1, 1.5 and 2, are shown in Fig. 5.2. The mean radial velocities at these locations for jet impingement on a heated static target surface are observed to be greater than those for jet impingement on an unheated static target surface. Higher mean radial velocities for the heated static target occur due to higher mean axial velocities as shown in Fig. 5.1(a). At each radial location the maximum mean radial velocity for unheated and heated static target surfaces are found to occur at the same wall-normal distance. This shows that the boundary-layer thickness in the region $y/d \leq 2$ does not change due to the effect of surface heating. It is also observed that the difference between the mean radial velocities for heated and unheated static target surfaces decreases with increasing radial distance. This is due to the increased mixing effect of the warmer ambient fluid with the wall-jet as y/d increases.

The mean radial velocity profiles for jet impingement on unheated and heated oscillating target surfaces at 20 Hz, at radial locations y/d = 1, 1.5 and 2, are shown in Figs. 5.3, 5.4 and 5.5 respectively. In all these figures, it is observed that the mean radial velocities for the unheated oscillating target surface are lower than those for the heated target surface, at all phases ϕ_1 to ϕ_6. This reflects the observations between the mean radial velocities for unheated and heated static target surfaces shown in Fig. 5.1. However, in Figs. 5.3 and 5.4, at y/d = 1 and 1.5, it is observed that the maximum mean radial velocities for all phases of unheated and heated oscillating target surfaces occur adjacent to the wall, whereas the position of the maximum mean radial velocities at these radial locations for unheated and heated static target surfaces, Figs. 5.3(a) and 5.3(b), is further away in the wall-normal direction. This indicates that for both the unheated and heated oscillating target surfaces, the boundary-layer thickness decreases from that observed for the static target surfaces, which is due to the effect of target-surface oscillation. This thinning of the boundary-layer is not observed at a larger radial location, y/d = 2 in Fig. 5.5, where the boundary-layer thicknesses for unheated and heated oscillating target surfaces are found to be same as those for unheated and heated static target surfaces.

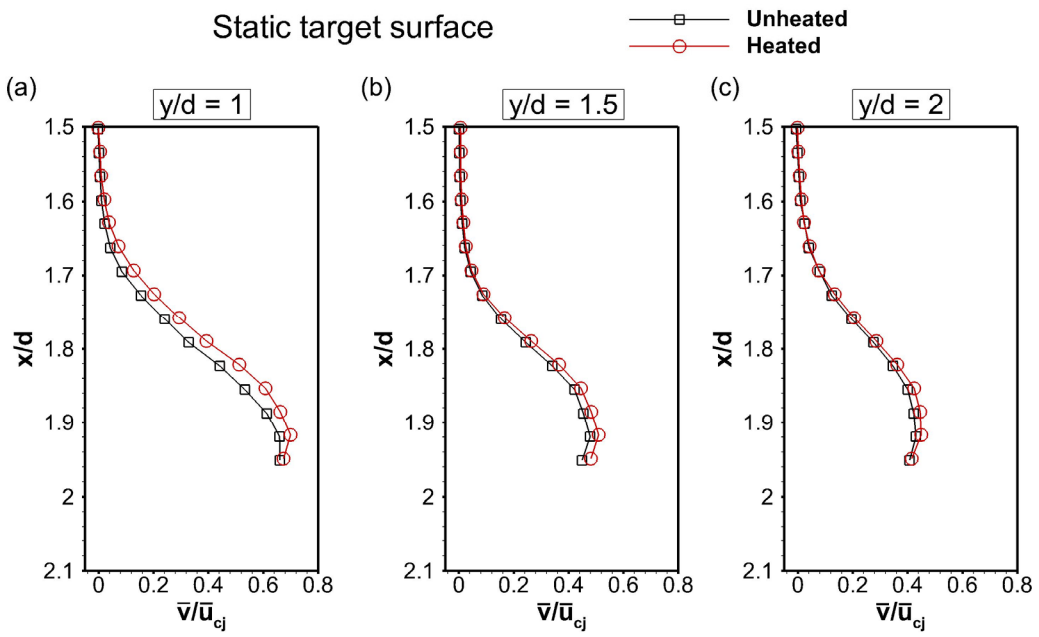

Fig. 5.2 Mean radial velocity profiles for jet impingement on unheated and heated static target surfaces at: (a) $y/d = 1$; (b) $y/d = 1.5$; (c) $y/d = 2$

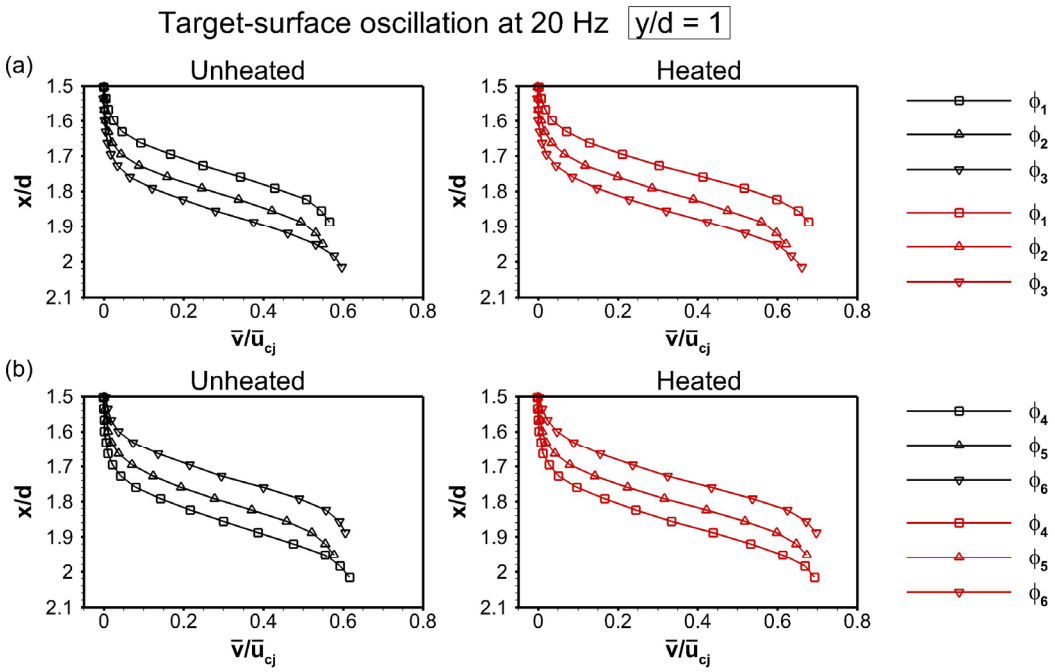

Fig. 5.3 Mean radial velocity profiles at $y/d = 1$ for jet impingement on unheated and heated oscillating target surfaces at 20 Hz, at (a) phases ϕ_1 to ϕ_3; (b) phases ϕ_4 to ϕ_6

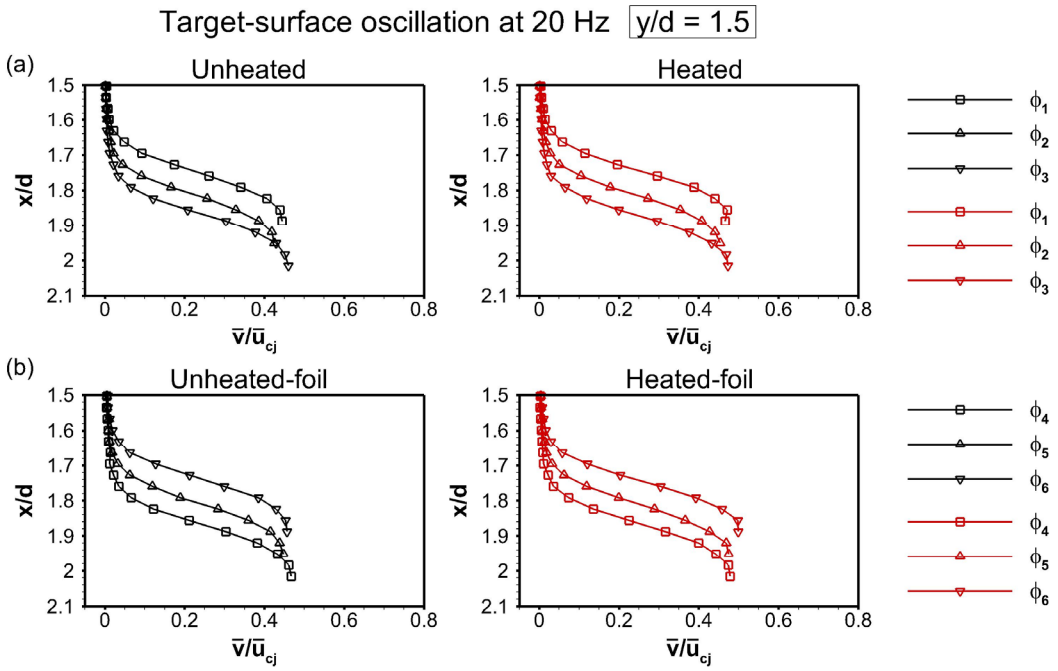

Fig. 5.4 Mean radial velocity profiles at y/d = 1.5 for jet impingement on unheated and heated oscillating target surfaces at 20 Hz, at (a) phases ϕ_1 to ϕ_3; (b) phases ϕ_4 to ϕ_6

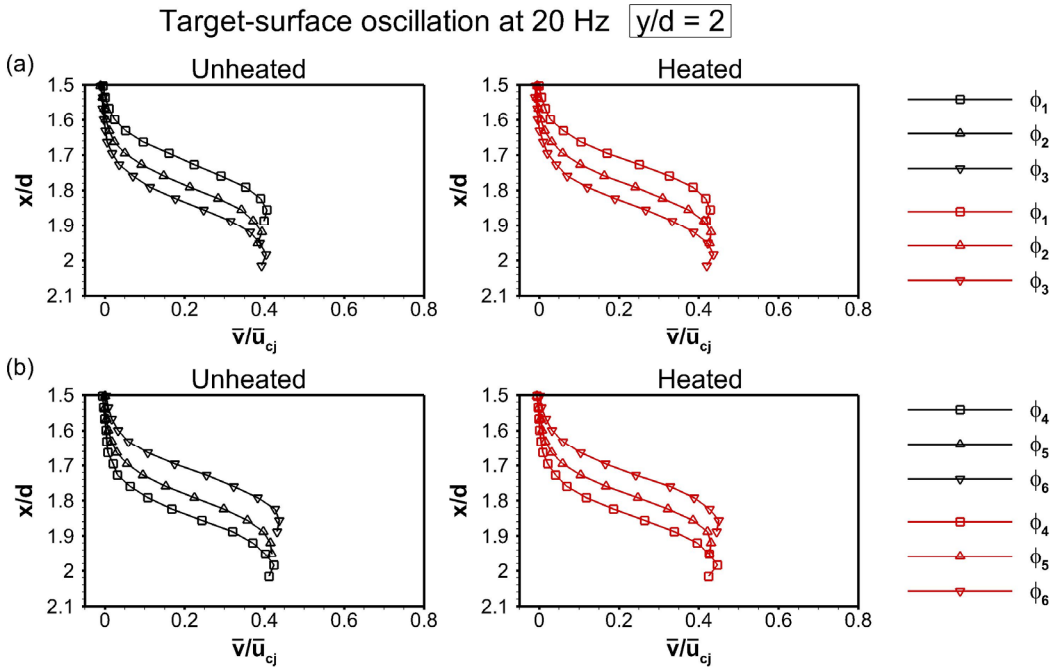

Fig. 5.5 Mean radial velocity profiles at y/d = 2 for jet impingement on unheated and heated oscillating target surfaces at 20 Hz, at (a) phases ϕ_1 to ϕ_3; (b) phases ϕ_4 to ϕ_6

The rms axial velocity fluctuation $u_{\mathrm{rms}}/\overline{u}_{cj}$ contours for jet impingement on unheated and heated, static and oscillating target surfaces are shown in Fig. 5.6. In the presence of a heated static target surface, the rms axial velocity fluctuations in the free-jet shear layer and in the wall-jet shear layer are higher than those for an unheated static target surface, as shown in Fig. 5.6(a). For the heated static target surface higher magnitudes of fluctuation in the free-jet shear layer occur due to shear interactions between higher jet axial velocities (Fig. 5.1(a)) and the buoyant ambient fluid, whereas in the wall-jet shear layer they occur due to shear interaction between the buoyant ambient fluid and the wall-jet. In Figs. 5.6(b) to 5.6(g), it is observed that the rms axial velocity fluctuations in the free-jet shear layer and in the wall-jet shear layer for each phase of heated target-surface oscillation are higher than those for the corresponding phase of unheated target-surface oscillation.

The rms radial velocity fluctuation $v_{\mathrm{rms}}/\overline{u}_{cj}$ contours in the wall-jet region are shown in Fig. 5.7. Jet impingement on a heated static surface is found to have higher magnitudes of rms fluctuations than those for jet impingement on an unheated static target surface, as shown in Fig. 5.7(a). This occurs within the wall-jet, due to higher mean radial velocities for jet impingement on a heated static target surface, and also occurs in the decelerating wall-jet shear layer, due to mixing with the buoyant ambient fluid which has a positive velocity gradient along the y/d direction. Similar characteristics also exist for jet impingement on unheated and heated, oscillating target surfaces, where the rms radial velocity fluctuations for each phase of heated target-surface oscillation are found to be significantly higher than those for the corresponding phase of unheated target-surface oscillation, as observed in Figs. 5.7(b) to 5.7(g).

Figures 5.1 to 5.7 show that target-surface heating alters the impinging-jet flow characteristics from those observed for an unheated target surface. A heated target surface is found to induce buoyancy to the ambient fluid. This lowers entrainment of the ambient fluid into the jet, which gives rise to higher mean velocities when compared to those present for jet impingement on an unheated target surface. These higher mean velocities, and the shear-layer interactions with the ambient fluid, produce higher rms velocity fluctuations in the free-jet shear layer, within the wall-jet, and in the wall-jet shear layer, for jet impingement on a heated target surface compared to that on an unheated target surface. These characteristics exist for jet impingement on both heated, static and oscillating target surfaces.

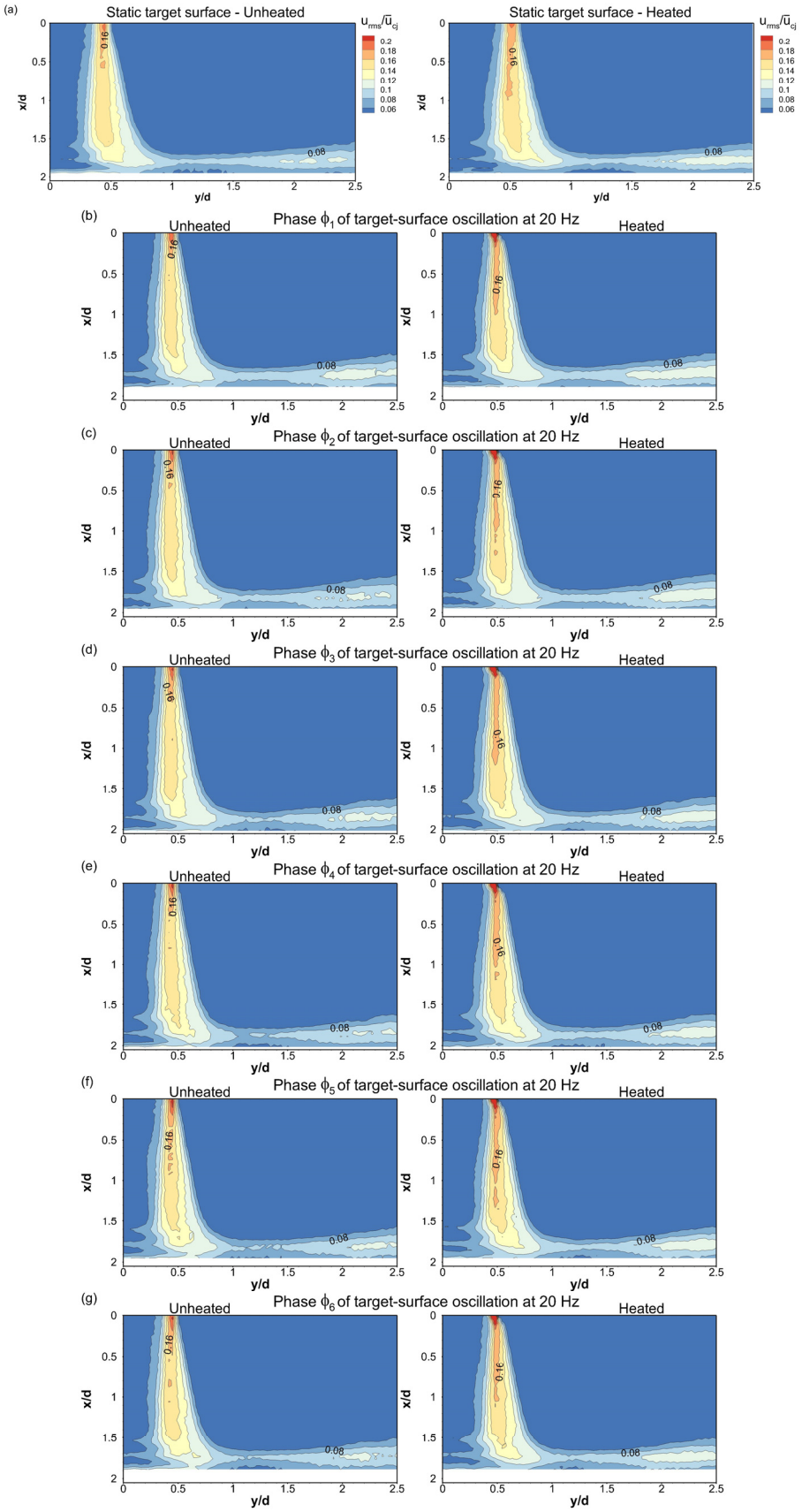

Fig. 5.6 RMS axial velocity fluctuation contours for jet impingement on unheated and heated target surfaces: (a) static target surfaces; (b) to (g) oscillating target surfaces at 20 Hz, at phases ϕ_1 to ϕ_6 respectively

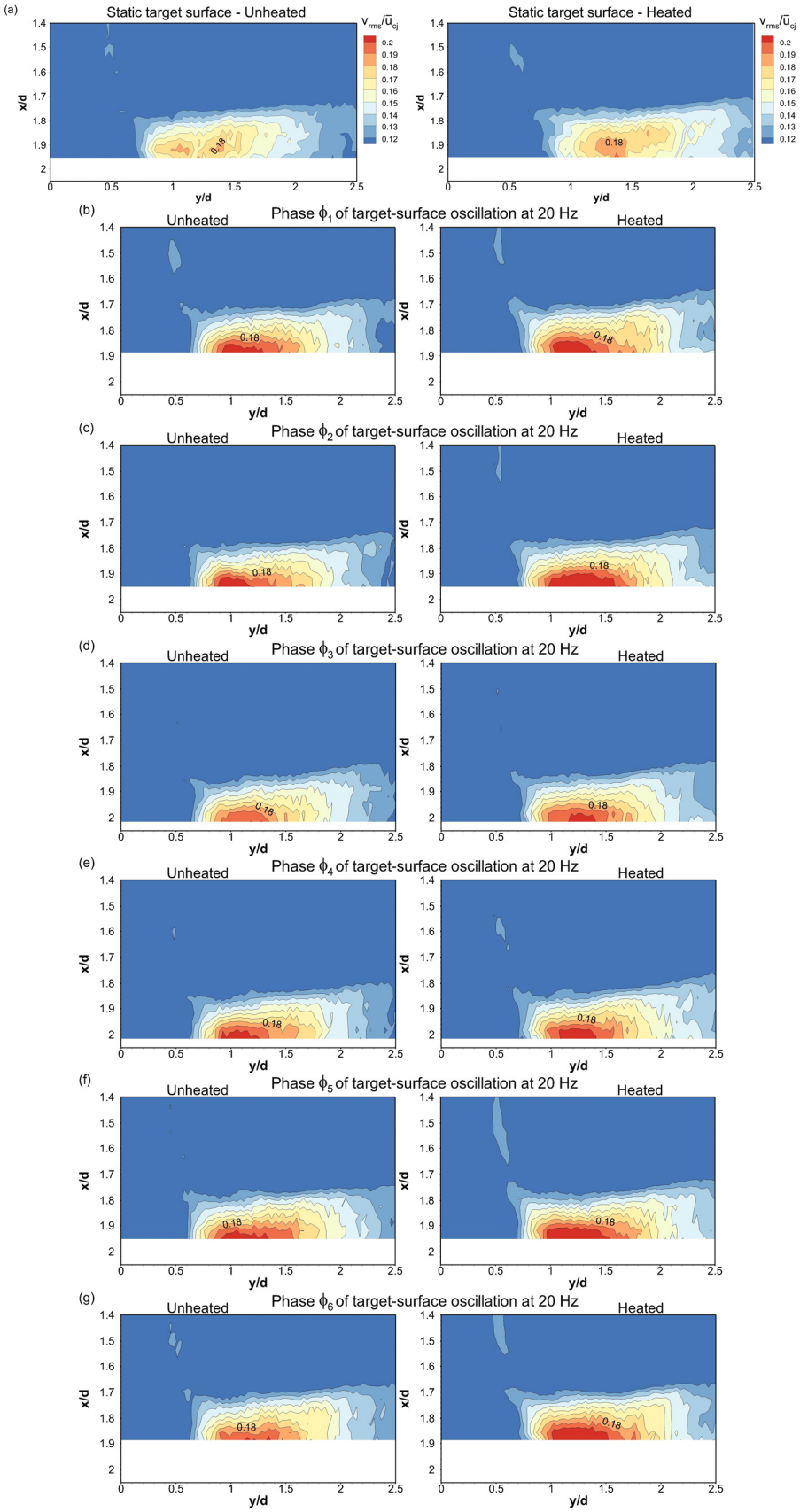

Fig. 5.7 RMS radial velocity fluctuation contours for jet impingement on unheated and heated target surfaces: (a) static target surfaces; (b) to (g) oscillating target surfaces at 20 Hz, at phases ϕ_1 to ϕ_6 respectively

5.2 Jet impingement on heated static and oscillating target surfaces: Instantaneous flow characteristics

The fluid dynamics results for jet impingement on heated static and oscillating target surfaces are presented in this, and the following sections. The relevant experimental parameters for this experimental system (No. 2) are mentioned in Chapter 3 Section 3.2.

The instantaneous velocity vector fields for jet impingement on heated static and oscillating target surfaces are shown in Fig. 5.8, where the vectors are overlaid upon the contours of velocity magnitude. To highlight flow features near the wall, the vectors are shown in a region from the impingement target surface up to a distance of $x/d = 1.4$.

The velocity magnitudes in the vicinity of the stagnation point $y/d = 0$ for phases ϕ_1 to ϕ_3 for target-surface oscillation at both 20 Hz and 50 Hz, shown in Figs. 5.8(b) to 5.8(d), are higher than those for the static target surface in Fig. 5.8(a). The near-wall velocity vectors for these phases also show a larger axial component. These occur because of target surface motion in the positive direction of the axial velocity of the jet. For these phases, higher velocity magnitudes in the vicinity of the stagnation point, as well as in the ambient region, and larger axial components of the near-wall vectors are observed for target-surface oscillation at 50 Hz, when compared to that at 20 Hz.

For phases ϕ_4 to ϕ_6 of target-surface oscillation at 20 Hz in Figs. 5.8(e) to 5.8(g), the velocity magnitude in the vicinity of the stagnation point reaches a level similar to that for the static target surface, However, for these phases of target-surface oscillation at 50 Hz, the velocity magnitude in that region is much lower because the target surface moves in an opposite direction to the axial velocity of the jet, having velocities higher than that during oscillation at 20 Hz. This results in the near-wall velocity vectors for these phases for target-surface oscillation at 50 Hz to have a lower axial component compared to those for phases ϕ_1 to ϕ_3. It is also observed that the velocity magnitude in the ambient fluid region for phases ϕ_4 to ϕ_6 of target-surface oscillation at 50 Hz is lower than that for phases ϕ_1 to ϕ_3 because of the deceleration of the ambient fluid during target-surface motion towards the jet exit.

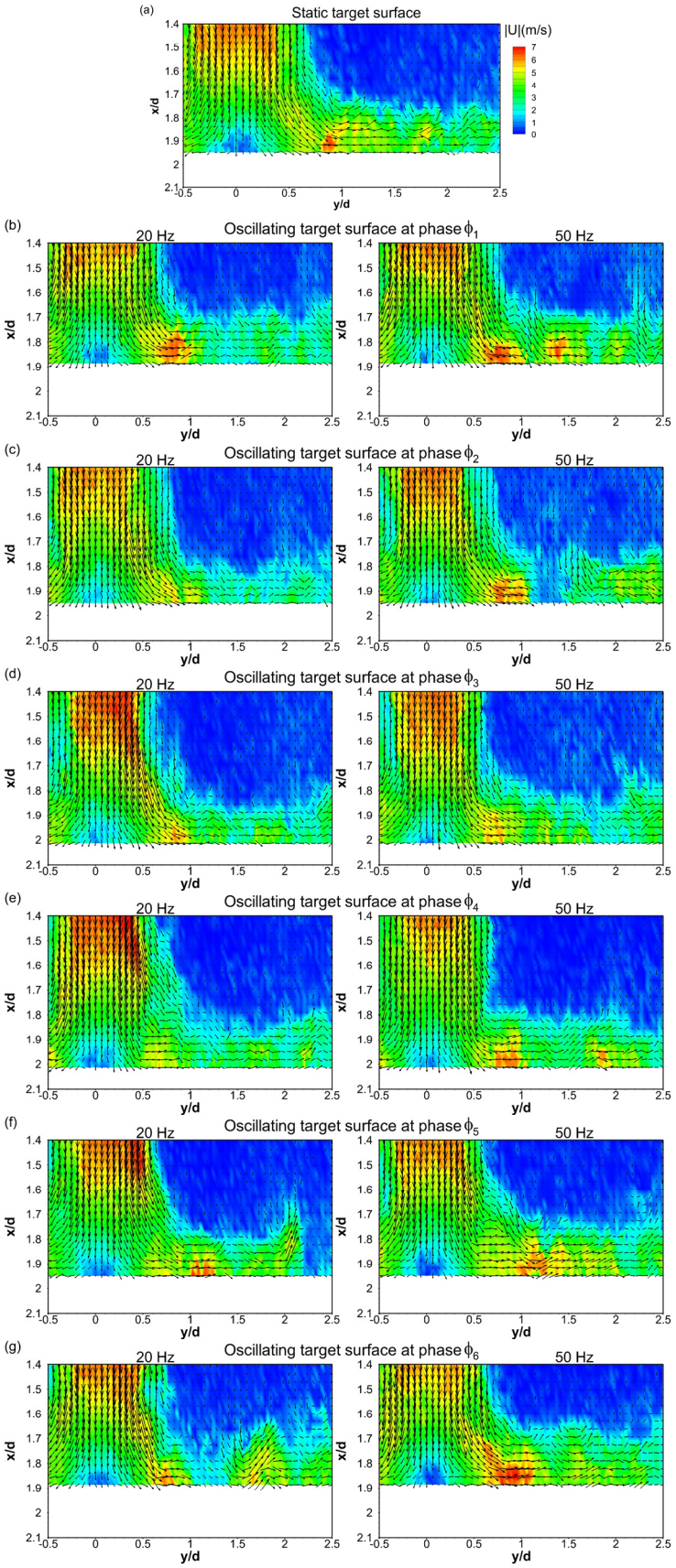

Fig. 5.8 Instantaneous velocity vector maps for jet impingement on heated target surfaces: (a) static target surface; (b) to (g) oscillating target surface at 20 Hz and 50 Hz, at phases ϕ_1 to ϕ_6 respectively

5.3 Jet impingement on heated static and oscillating target surfaces: Mean flow characteristics

5.3.1 Mean velocities

The mean axial velocity $\overline{u}/\overline{u}_{cj}$ contours for jet impingement on heated static and oscillating target surfaces are shown in Fig. 5.9. It is observed that the axial extension of the potential-core region, marked by contour level 0.97, is up to x/d = 1.1 for the static target surface, as shown in Fig. 5.9(a). For phases ϕ_3 to ϕ_6 of target-surface oscillation at 50 Hz, the axial extension of the potential-core region is shorter than that for the static target surface, as observed from Figs. 5.9(d) to 5.9(g), with the shortest potential-core length occurring at phase ϕ_3. Phases ϕ_1 and ϕ_2 for the two target-surface oscillation frequencies have the potential-core extending to the same axial distance as that for the static target surface, as shown in Figs. 5.9(b) and 5.9(c). A broadening of the jet, from that observed for the static target surface, occurs for phases ϕ_1 to ϕ_3 of target-surface oscillation at 50 Hz, as shown by the radial extent of the marked contour level 0.15. This broadening of the jet was also observed for the same phases for jet impingement on an unheated target surface oscillating at 80 Hz in Fig. 4.6.

The near-wall mean axial velocities in the impingement region are higher than those for the static target surface, for phases ϕ_1 to ϕ_3 of target-surface oscillation at both 20 Hz and 50 Hz, whereas for phase ϕ_4 to ϕ_6, during the opposite motion of the target surface, they are similar to those for the static target surface. For target-surface oscillation at 50 Hz, negative mean axial velocities, marked by contour level -0.05, are observed in the wall-jet region for phases ϕ_5 and ϕ_6 in Figs. 5.9(f) and 5.9(g). These occur because of target-surface motion in the direction opposite to the positive axial velocity of the jet and were also observed for jet impingement on unheated target-surface oscillation at 80 Hz in Fig. 4.6. The regions of negative mean axial velocities are not observed for these phases for target-surface oscillation at 20 Hz because of lower velocities of the target surface at this frequency compared to those at 50 Hz.

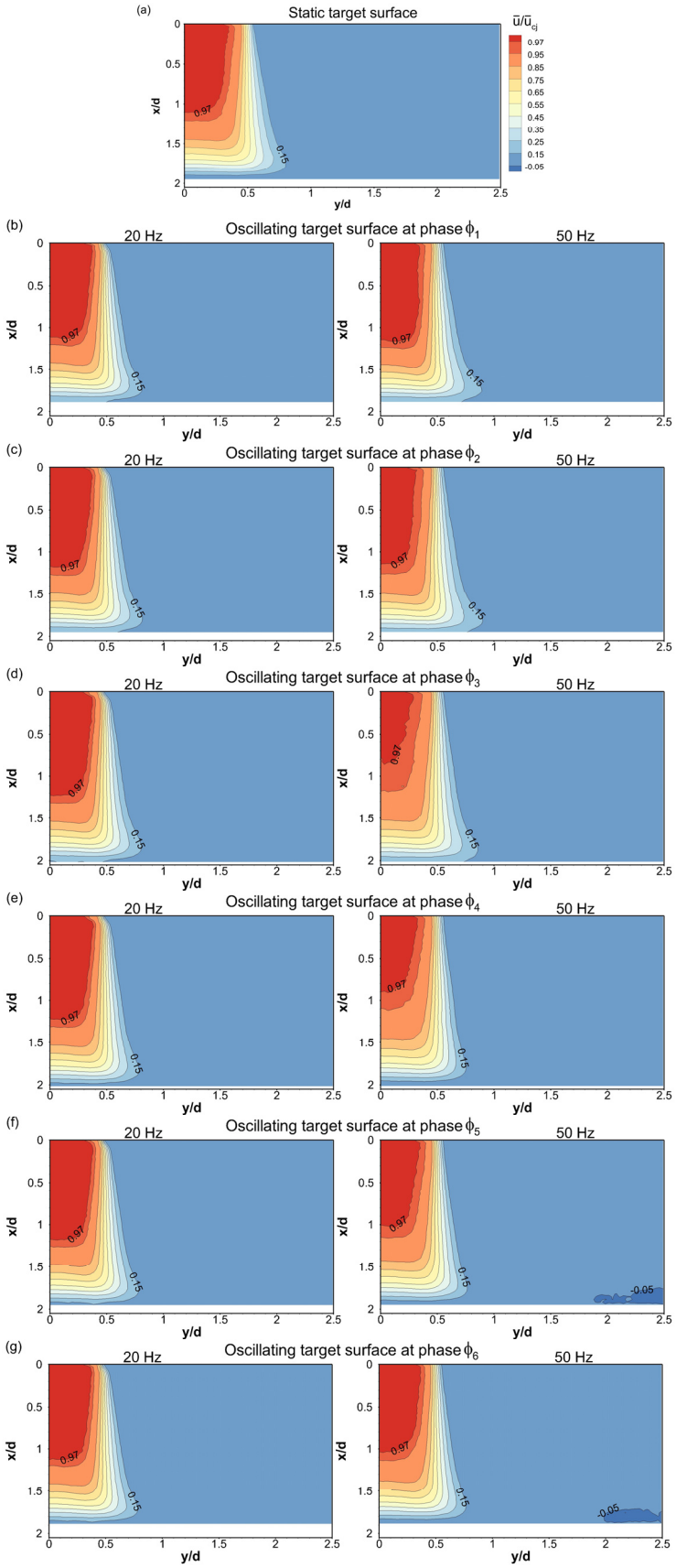

Fig. 5.9 Mean axial velocities for jet impingement on heated target surfaces: (a) static target surface; (b) to (g) oscillating target surface at 20 Hz and 50 Hz, at phases ϕ_1 to ϕ_6 respectively

The mean radial velocity $\overline{v}/\overline{u}_{cj}$ contours are shown in Fig. 5.10, where the mean radial velocity for jet impingement on a static target surface attains a maximum value of 0.8 near the wall at y/d = 0.8, as shown in Fig. 5.10(a). In the vicinity of this radial location, which marks the end of the acceleration region in the wall-jet for the static target surface, it is observed that phase ϕ_6 for target-surface oscillation at 20 Hz in Fig. 5.10(g), has higher near-wall mean radial velocities than those for the static target surface. Lower mean radial velocities than those for the static target surface are observed within this region for phases ϕ_2 and ϕ_3 of target-surface oscillation at 50 Hz, and for phase ϕ_2 of target-surface oscillation at 20 Hz, in Figs. 5.10(c) and 5.10(d). The near-wall mean radial velocities at locations $y/d > 1$ for phases ϕ_1 and ϕ_6, for both the target-surface oscillation frequencies, are found to be higher than those for the static target surface, which occur when the target surface is closest to the jet exit.

As was done in Chapter 4, to highlight the changes in the mean velocities due to target-surface oscillation, the variations of mean velocities with phases at various spatial locations for jet impingement on a heated oscillating target surface are presented. The variations for target-surface oscillation at 50 Hz are presented first as in Fig. 5.11. Shown at the bottom of each sub-figure is a representative variation of target surface velocity over two oscillation cycles. The points marked red are the mean velocities for jet impingement on a heated static target surface at the corresponding axial locations.

The variation of jet-centerline y/d = 0 mean axial velocity with phases, at various axial locations, is presented in Fig. 5.11(a). The variation of stagnation point mean axial velocity follows that of the target surface speed; with higher mean axial velocities for phases ϕ_1 to ϕ_3, when the target surface moves in a direction positive to the axial velocity of the jet, than for phases ϕ_4 to ϕ_6, when the target surface moves in the opposite direction.

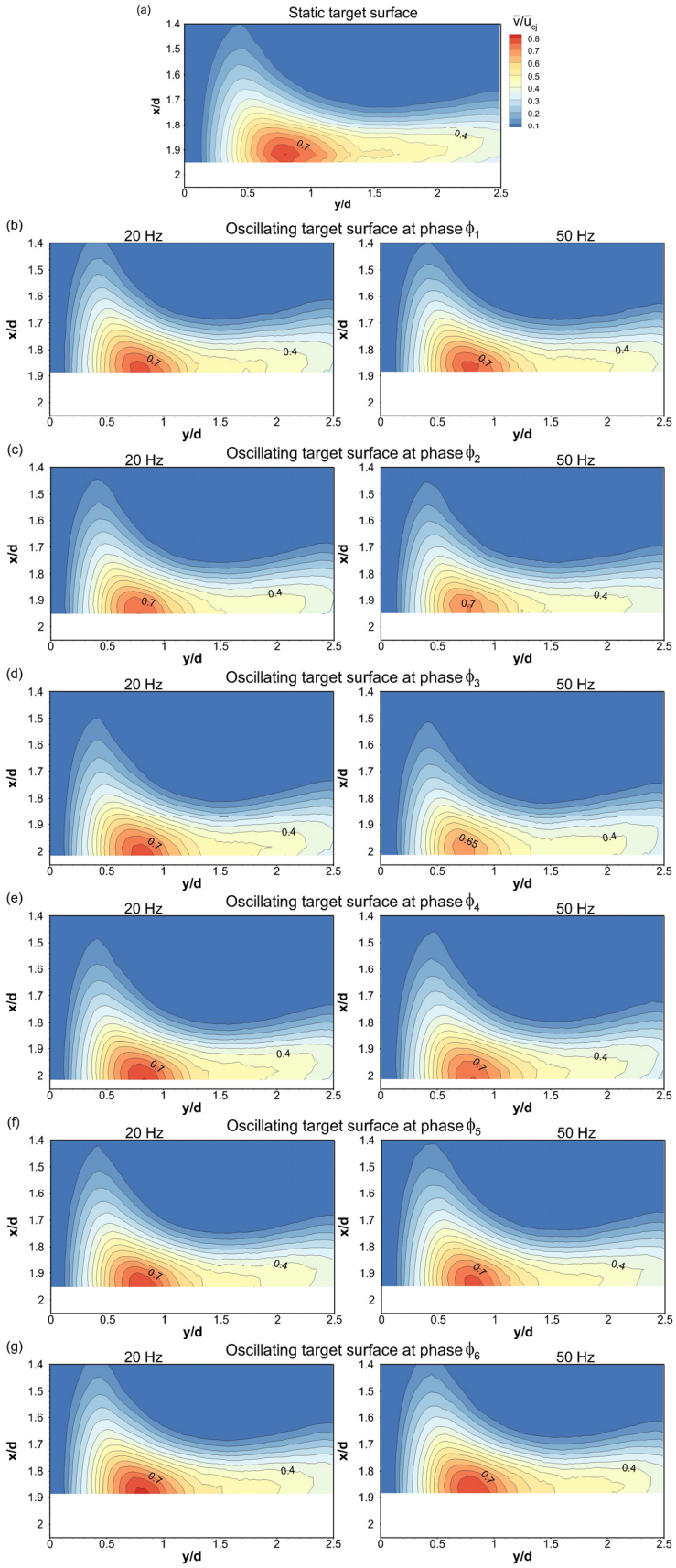

Fig. 5.10 Mean radial velocities for jet impingement on heated target surfaces: (a) static target surface; (b) to (g) oscillating target surface at 20 Hz and 50 Hz, at phases ϕ_1 to ϕ_6 respectively

The variations of jet-centerline $y/d = 0$ mean axial velocities at $x/d = 1.5$, 1.7 and 1.8 in Fig. 5.11(a) are in phase with each other, with the mean axial velocities increasing from phase ϕ_1 until phase ϕ_3, and decreasing from phase ϕ_4 until phase ϕ_6. Besides, the mean axial velocities of the jet-centerline for phases ϕ_2 to ϕ_4 are higher than that for the static target surface at these axial locations, while for phases ϕ_1 and ϕ_6 they are lower. This is expected to occur because the presence of target surface closest to the jet exit at phases ϕ_1 and ϕ_6 reduces the mean axial velocities. At an axial location $x/d = 1$ closer to the jet exit, the variation of the mean axial velocity shows a phase difference of π radians with that at a location closer to the wall $x/d = 1.8$. This means that the shortest axial extent of the potential-core region found for phase ϕ_3 of target surface oscillating at 50 Hz in Fig. 5.9(d), is due to the effect of target surface motion at an earlier phase ϕ_6.

The variation of mean axial velocities at $y/d = 0.5$ at various axial locations is shown in Fig. 5.11(b). The variations at $x/d = 1.8$ and 1.7 are in phase with each other, and also with the variations of the jet-centerline $y/d = 0$ mean axial velocities at the same axial locations as shown in Fig. 5.11(a). The variations at $x/d = 1.5$ and 1 are also in phase with each other, but their period is similar to that of the jet-centerline $y/d = 0$ mean axial velocity variation at $x/d = 1$ in Fig. 5.11(a).

The mean axial velocity variations at a farther radial location $y/d = 1.5$ from the jet-centerline are presented in Fig. 5.11(c). For points in the ambient region, $x/d = 1$ and 1.5, as well for points in the wall-jet region, $x/d = 1.7$ and 1.8, the variations show higher mean axial velocities for phases ϕ_1 to ϕ_3, and lower for phases ϕ_4 to ϕ_6, than those for the static target surface. The former indicates increased entrainment of the ambient fluid into the jet, from that for jet impingement a heated static target surface, when the target surface moves away from the jet exit during phases ϕ_1 to ϕ_3. Whereas the latter indicates deceleration of the entrained ambient fluid, from that for jet impingement a heated static target surface, when the target surface moves towards the jet exit during phases ϕ_4 to ϕ_6.

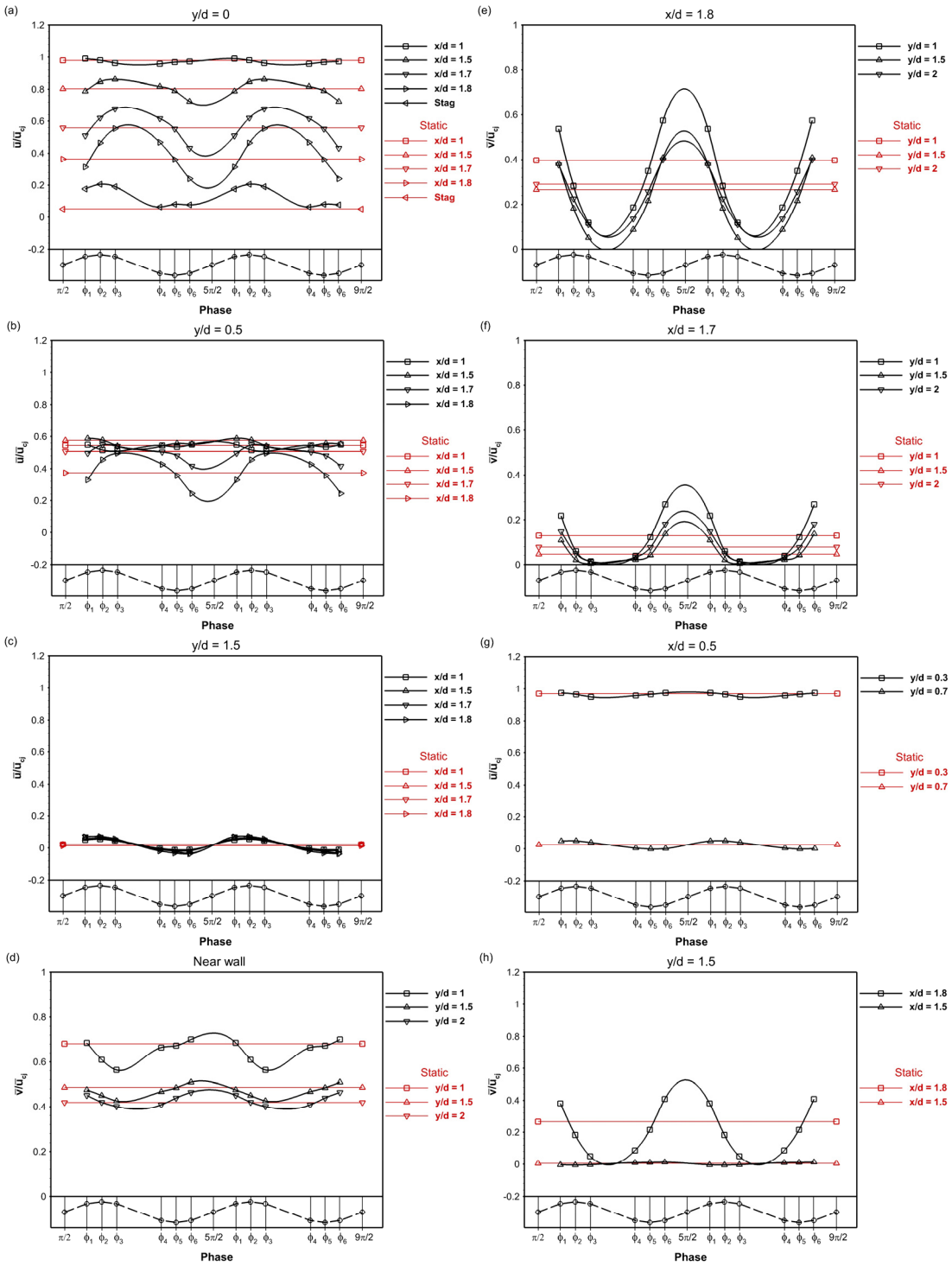

Fig. 5.11 Jet impingement on a heated target surface oscillating at 50 Hz. Variation of mean velocities with phases ϕ_1 to ϕ_6 at various spatial locations: (a) mean axial velocity at y/d = 0, x/d = 1, 1.5, 1.7, 1.8 and stagnation point (Stag); (b) mean axial velocity at y/d = 0.5, x/d = 1, 1.5, 1.7 and 1.8; (c) mean axial velocity at y/d = 1.5, x/d = 1, 1.5, 1.7 and 1.8; (d) mean radial velocity at near-wall, y/d = 1, 1.5 and 2; (e) mean radial velocity at x/d = 1.8, y/d = 1, 1.5 and 2; (f) mean radial velocity at x/d = 1.7, y/d = 1, 1.5 and 2; (g) mean axial velocity at x/d = 0.5, y/d = 0.3 and 0.7; (h) mean radial velocity at y/d = 1.5, x/d = 1.8 and 1.5. The points marked in red in each of these figures denote the corresponding values for jet impingement on heated static target surface. At the bottom of each figure is the representative variation of the target surface velocity over 2 oscillation cycles (marked as –o–).

The change in the near-wall mean radial velocities with target surface phases, at various radial locations, is shown in Fig. 5.11(d). The time periods of variations of mean radial velocities at y/d = 1, 1.5 and 2 are the same, with variations at y/d = 1.5 and 2 being more gradual than that at y/d = 1 for phases ϕ_1 to ϕ_3. The near-wall mean radial velocities for phase ϕ_6 are higher than those for the static target surface at all these radial locations, which occurs because the target surface is closest to the jet exit and moving towards it, with the highest being at y/d = 2. It is also observed that for phase ϕ_1, when the target surface is closest to the jet but moving away from the jet exit, the near-wall mean radial velocity is higher than that for the static target surface at only y/d = 2. The variations shown in Fig. 5.11(d) indicate that the effect of target-surface oscillation on the near-wall mean radial velocities is higher at lower radial distances when the target surface moves away from the jet exit. By contrast, the opposite motion of the target surface has a greater effect at farther radial distances.

The variations of mean radial velocities at locations further above the wall, at x/d = 1.8 and 1.7, at various radial locations are shown in Figs. 5.11(e) and 5.11(f). These variations are in phase with each other, wherein the mean radial velocities for phases ϕ_1 and ϕ_6, at all radial locations, are higher than those for the static target surface. In Figs. 5.11(e) and 5.11(f), the mean radial velocities at y/d = 2 are higher than those at y/d = 1.5, for both the static and oscillating target surfaces, because the wall-jet grows in width with increasing radial distance. If we compare the variation of the mean radial velocity at x/d = 1.8, y/d = 1 in Fig. 5.11(e), with the variation of the mean axial velocity at x/d = 1.8, y/d = 0.5 in Fig. 5.11(b), we observe that they are opposite to each other, which arises from mass conservation during target-surface oscillation.

The mean axial velocities at various phases that occur on either sides of the free-jet shear layer at x/d = 0.5 are shown in Fig. 5.11(g). These variations are small in magnitude compared to the corresponding magnitude of the mean axial velocity for the static target surface. Nevertheless, inside the free-jet at y/d = 0.3 the mean axial velocities decrease for phases ϕ_1 to ϕ_3 and are lower than that for the static target surface, while those outside in the ambient fluid at y/d = 0.7 also decrease for phases ϕ_1 to ϕ_3 but are higher than that for the static target surface; the latter indicates an increase of entrainment of ambient fluid into the jet. The negative velocity values for phases ϕ_4 to ϕ_6 at y/d = 0.7, show greater deceleration of the ambient fluid than that

of the jet flow at y/d = 0.3. The variations at y/d = 0.3 and y/d = 0.7 show a phase difference of π/2 radians between them.

The variation of mean radial velocities inside and outside of the wall-jet shear layer at y/d = 1.5 is shown in Fig. 5.11(h). The variation of the mean radial velocity outside the wall-jet at x/d = 1.5 is very small, however, the mean radial velocities outside the wall-jet for phases ϕ_1 to ϕ_3 are lower than that for phases ϕ_4 to ϕ_6. This indicates that there is only a minimal effect of increased entrainment of the ambient fluid into the wall-jet. Which is due to the small increment of the mean axial velocities of the ambient fluid for phases ϕ_1 to ϕ_3, from that for the static target surface, as shown in Fig. 5.11(g) at y/d = 0.7. In addition, there is buoyancy effect on the ambient fluid due to target surface heating, which lowers entrainment of the ambient fluid into the jet, as shown in Sec 5.1.

The variations of mean velocities with target surface phases for jet impingement on target-surface oscillation at 20 Hz, at various spatial locations, are shown in Fig. 5.12. Although the overall variations are similar to those for target-surface oscillation at 50 Hz shown in Fig. 5.11, some deviations from those variations do occur. These are presented in the following discussion.

The variations of jet-centerline y/d = 0 mean axial velocity at various axial locations are shown in Fig. 5.12(a). The stagnation point mean axial velocity varies similar to that shown in Fig. 5.11(a), except that the velocity values for target-surface oscillation at 20 Hz for phases ϕ_1 to ϕ_3 are lower, and for phases ϕ_4 to ϕ_6 are higher. This is because of lower target surface velocity at this oscillation frequency. The variations of jet-centerline, y/d = 0, mean axial velocities at axial locations x/d = 1.5, 1.7 and 1.8 are in phase with those shown in Fig. 5.11(a), while that at x/d = 1 is out of phase. A comparison of the magnitudes of mean axial velocities at x/d = 1 that occur for target-surface oscillation at 20 Hz and 50 Hz, in Figs. 5.12(a) and 5.11(a), show that the effect of target-surface oscillation on the potential-core of the jet is greater at 50 Hz frequency of oscillation.

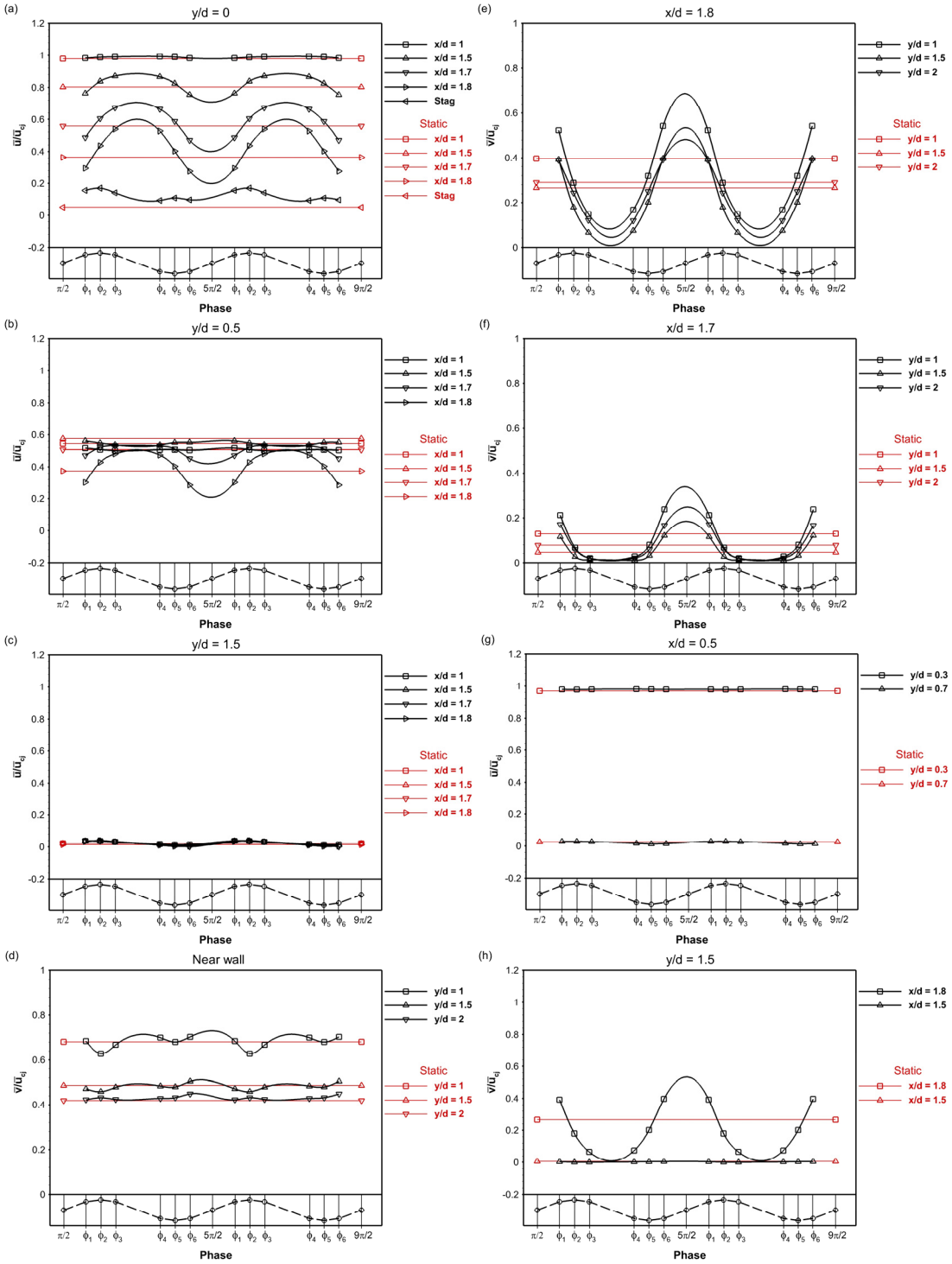

Fig. 5.12 Jet impingement on a heated target surface oscillating at 20 Hz. Variation of mean velocities with phases ϕ_1 to ϕ_6 at various spatial locations: (a) mean axial velocity at y/d = 0, x/d = 1, 1.5, 1.7, 1.8 and stagnation point (Stag); (b) mean axial velocity at y/d = 0.5, x/d = 1, 1.5, 1.7 and 1.8; (c) mean axial velocity at y/d = 1.5, x/d = 1, 1.5, 1.7 and 1.8; (d) mean radial velocity at near-wall, y/d = 1, 1.5 and 2; (e) mean radial velocity at x/d = 1.8, y/d = 1, 1.5 and 2; (f) mean radial velocity at x/d = 1.7, y/d = 1, 1.5 and 2; (g) mean axial velocity at x/d = 0.5, y/d = 0.3 and 0.7; (h) mean radial velocity at y/d = 1.5, x/d = 1.8 and 1.5. The points marked in red in each of these figures denote the corresponding values for jet impingement on heated static target surface. At the bottom of each figure is the representative variation of the target surface velocity over 2 oscillation cycles (marked as –o–).

The variations of the mean axial velocities at y/d = 0.5 and a farther radial location y/d = 1.5, shown in Figs. 5.12(b) and 5.12(c), are similar to those observed in Figs. 5.11(b) and 5.11(c), except that, the magnitudes of mean axial velocities at points in the ambient and wall-jet regions for all phases are lower for target-surface oscillation at 20 Hz. These lower values show a smaller effect of target-surface oscillation at 20 Hz on the jet and ambient fluid regions, with the latter indicating entrainment levels to be similar to those found for jet impingement on a heated static target surface.

The mean radial velocities for different phases of target-surface oscillation at 20 Hz, at locations near-wall, x/d = 1.8, and x/d = 1.7, are shown in Figs. 5.12(d), 5.12(e) and 5.12(f). The variations of near-wall mean radial velocities at y/d = 1 and 1.5 are seen to be in phase with each other. However, when compared with the variations at the same radial locations for target-surface oscillation at 50 Hz in Fig. 5.4(d), there is difference of π/5 radians. This is evident in the increase of near-wall mean radial velocities which occur from phase ϕ_2 to ϕ_3 for target-surface oscillation at 20 Hz, but occur from phase ϕ_3 to ϕ_4 for target-surface oscillation at 50 Hz. In addition to this, the magnitudes of near-wall mean radial velocities at these radial locations for target-surface oscillation at 20 Hz are lower than those for target-surface oscillation at 50 Hz.

The near-wall mean radial velocity variation at y/d = 2 in Fig. 5.12(d) for phases ϕ_1 to ϕ_3 is out of phase with those that at y/d = 1 and 1.5, and the velocity values are greater than those for the static target surface. For phase ϕ_6, at all these radial locations, the near-wall mean radial velocity is higher than that for the static target surface; this was also observed in Fig. 5.11(d) for target surface oscillating at 50 Hz. Another similar observation is that the effect of target-surface motion away from the jet exit is greater at lower radial locations.

The variations of mean radial velocities further away from the wall at x/d = 1.8 and 1.7 in Figs. 5.12(e) and 5.12(f) are similar to those observed in Figs. 5.11(e) and 5.11(f) for target-surface oscillation at 50 Hz. Besides, a comparison between the variations of mean axial velocities and radial velocities at a same axial location of x/d = 1.8 also arise from mass conservation.

The mean velocities at various phases across the free-jet and wall-jet shear layers are shown in Figs. 5.12(g) and 5.12(h). The variations in Fig. 5.12(g) show that target-surface oscillation at 20 Hz has a very small effect on the mean axial velocities inside the free-jet at y/d = 0.3 and outside at y/d = 0.7, smaller than that of target-surface oscillation at 50 Hz in Fig. 5.11(g). The variation of the mean radial velocity outside the wall-jet at x/d = 1.5 in Fig. 5.12(h) shows that the magnitudes of mean radial velocities at target surface phases are similar to those for the static target surface. This indicates that the entrainment of ambient fluid into the wall-jet for target-surface oscillation at 20 Hz is same as that for the static target surface, which is also indicated by the small variations in Fig. 5.12(c).

In summary, Figs. 5.11 and 5.12 show that the effect of target-surface oscillation on the impinging jet-flow regions is greater at a frequency of 50 Hz. The variations of near-wall mean radial velocities show a phase difference between the two target-surface oscillation frequencies. As the radial distance increases, the effect of target-surface oscillation on the near-wall mean radial velocities decreases for target-surface oscillation at 20 Hz. There is evidence of higher entrainment of the ambient fluid into the jet when the target surface oscillates at a frequency of 50 Hz.

Viewed strictly, the experimental system for jet impingement on an unheated oscillating target surface at 20 Hz (Experimental system No. 1) differs from that for jet impingement on a heated oscillating target surface at 20 Hz (Experimental system No. 2) due to the type of target surface (Chapter 3, Section 3.1). However, the experimental parameters for these two jet impingement configurations do not significantly differ (see Table 3.1 and 3.2). Thus, if a comparison is carried out, then a comparison between the variations of mean velocities for target-surface oscillation at 20 Hz that occur in these two systems, shown in Fig. 4.9 and Fig. 5.12 respectively, shows that the corresponding variations are all similar except for those of the near-wall mean radial velocities. This difference is essentially due to the difference in surface properties of the target material in these two experimental systems, and also because of the absence of target surface heating in experimental system No. 1.

A further analysis of the mean radial velocities is carried out through a presentation of the mean radial velocity profiles in order to understand the effect of target-surface oscillation on the near-wall flow. The mean radial velocity profiles for

jet impingement on heated static and oscillating target surfaces at 20 Hz and 50 Hz, at radial locations y/d = 1, 1.5 and 2, are presented in Figs. 5.13, 5.14 and 5.15 respectively. In each of these sub-figures, the mean radial velocity profile for the static target surface case, at the corresponding radial location, has been marked in red colour for ease in comparison.

The profiles at y/d = 1 in Fig. 5.13, show that the maximum mean radial velocity for all the phases of target-surface oscillation at the two frequencies is attained at the near-wall location, as opposed to the static target surface where the maximum is attained at a location further away from the wall. This means that the boundary-layer thickness reduces due to target-surface motion. As a result, the maximum mean radial velocity values for jet impingement on an oscillating target surface are lower than those for the static target surface due to their location being closer to the wall. A similar pattern is also observed in the mean radial velocity profiles at y/d = 1.5 in Fig. 5.14.

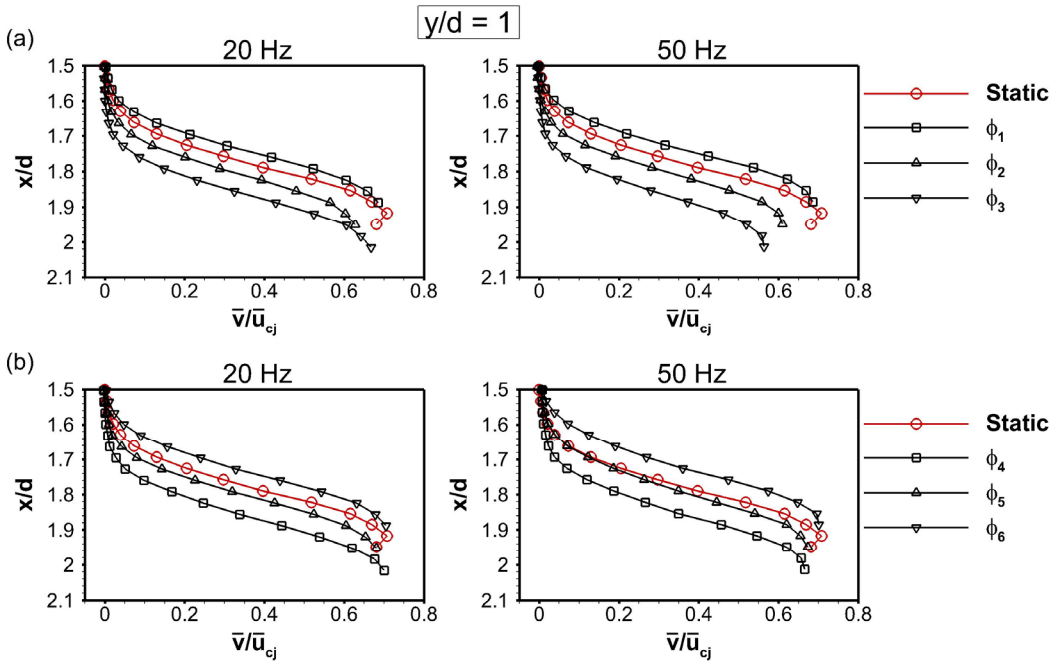

Fig. 5.13 Mean radial velocity profiles at y/d = 1 for jet impingement on heated static target surface and oscillating target surface at 20 Hz and 50 Hz, at (a) phases ϕ_1 to ϕ_3; (b) phases ϕ_4 to ϕ_6

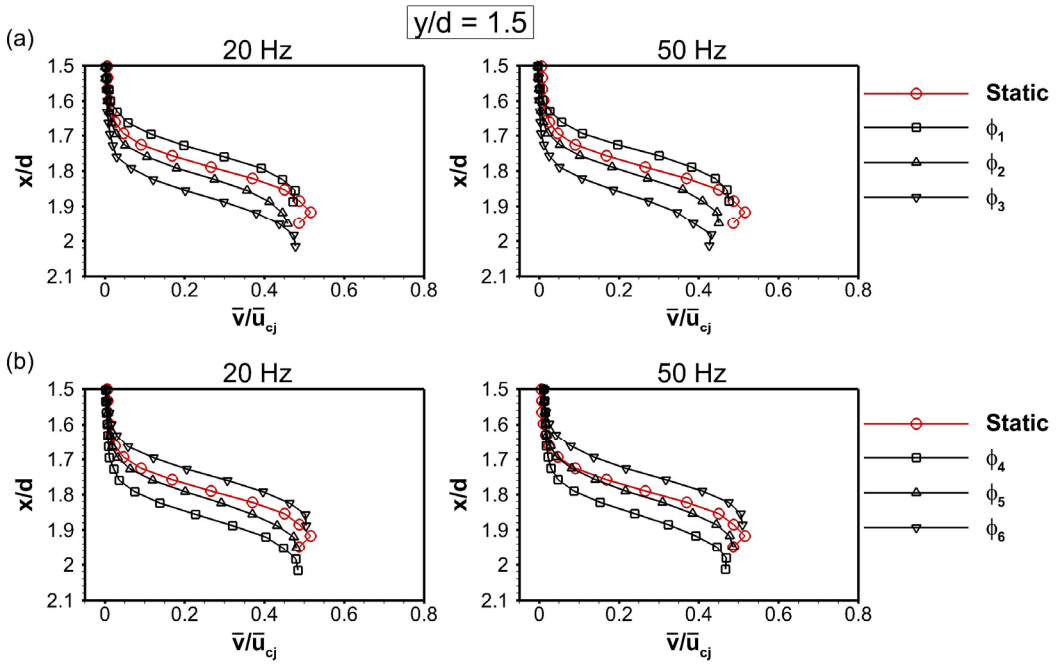

Fig. 5.14 Mean radial velocity profiles at y/d = 1.5 for jet impingement on heated static target surface and oscillating target surface at 20 Hz and 50 Hz, at (a) phases ϕ_1 to ϕ_3; (b) phases ϕ_4 to ϕ_6

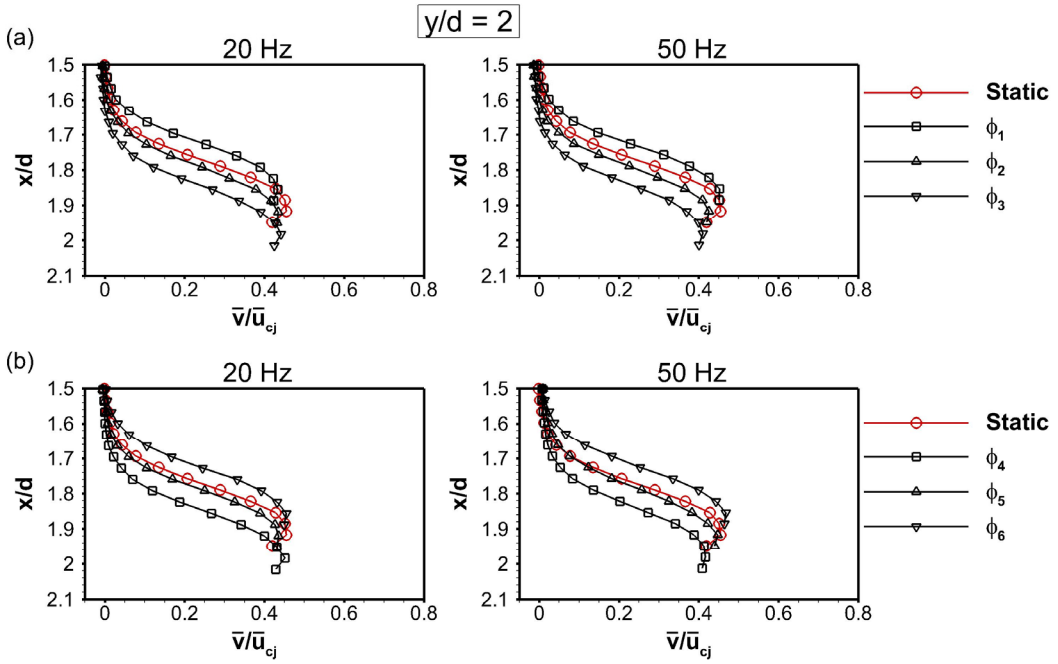

Fig. 5.15 Mean radial velocity profiles at y/d = 2 for jet impingement on heated static target surface and oscillating target surface at 20 Hz and 50 Hz, at (a) phases ϕ_1 to ϕ_3; (b) phases ϕ_4 to ϕ_6

In Figs. 5.13 and 5.14, the mean radial velocities for phases ϕ_2 and ϕ_3 of target-surface oscillation at 50 Hz are lower than those for target-surface oscillation at 20 Hz, which occurs due to higher velocity of the target surface when it moves away from the jet exit while oscillating at 50 Hz. The maximum mean radial velocity at y/d = 1.5 for phases ϕ_1 and ϕ_6 of target-surface oscillation at 50 Hz are higher those for the other phases because the target is closest to the jet exit at these two phases. The mean radial velocity profiles at y/d = 2 in Fig. 5.15, show that the boundary-layer thickness is the same for both the static and oscillating target surfaces. This indicates that the effect of target-surface oscillation on the near-wall mean radial velocities decreases with increasing radial distance, as was also shown in Figs. 5.11(d) and 5.12(d). However, for target-surface oscillation at 50 Hz we still find that the mean radial velocities for phase ϕ_6 are higher than those for the static target surface, as shown in Fig. 5.15(b).

The values of the maximum mean radial velocity as they vary with the radial coordinate for jet impingement on heated static target surface and oscillating target surfaces at 20 Hz and 50 Hz are shown in Fig. 5.16. For both the target-surface oscillation frequencies it is observed that for $y/d \geq 1$, the maximum mean radial velocities for phases ϕ_1 to ϕ_3, in Fig. 5.16(a), are lower than those for phases ϕ_4 to ϕ_6, in Fig. 5.16(b). This because of the wall-effect, as the location of the maximum mean radial velocity shifts closer to the wall than that for the static target surface as shown in Figs. 5.13 and 5.14.

The maximum mean radial velocities for target-surface oscillation at 50 Hz for phases ϕ_2 and ϕ_3 are lower than those for target-surface oscillation at 20 Hz, because of greater wall-effect at higher velocity of the target surface. The variation of the maximum mean radial velocity for the static target surface in Fig. 5.16 shows a non-monotonic decrease with the radial coordinate at $y/d > 1$. There is a local maximum at around y/d = 1.6 which indicates a region of local acceleration of the wall-jet just before this radial location. This local maximum is observed for target-surface oscillation at both the frequencies. The formation of this secondary peak in the radial variation of maximum mean radial velocity is more pronounced for phases ϕ_1 to ϕ_3, although its magnitude is lower than that for phases ϕ_4 to ϕ_6.

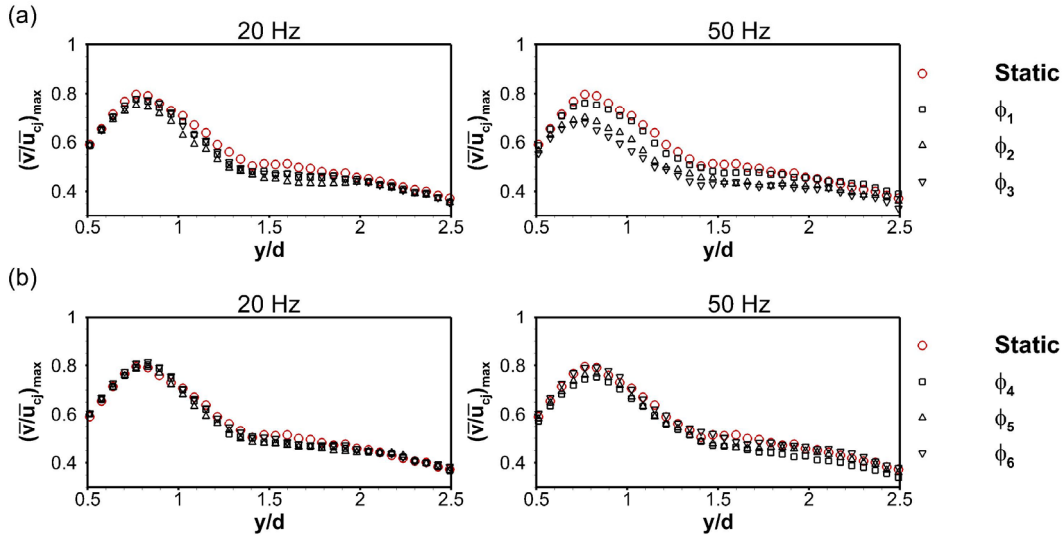

Fig. 5.16 Maximum mean radial velocity comparison for jet impingement on heated static target surface and oscillating target surface at 20 Hz and 50 Hz, at (a) phases ϕ_1 to ϕ_3; (b) phases ϕ_4 to ϕ_6

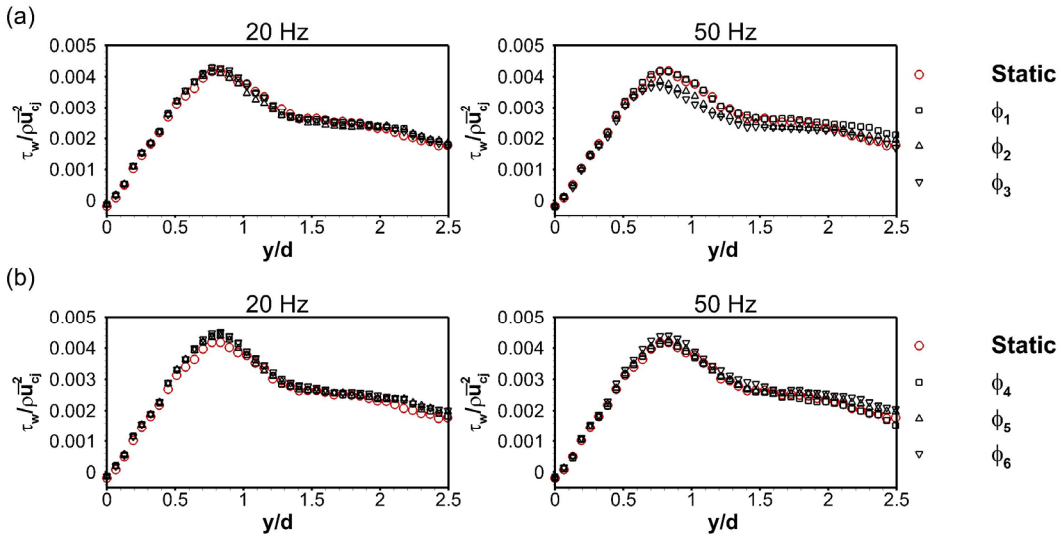

Fig. 5.17 Normalized wall-shear stress comparison for jet impingement on heated static target surface and oscillating target surface at 20 Hz and 50 Hz, at (a) phases ϕ_1 to ϕ_3; (b) phases ϕ_4 to ϕ_6

5.3.2 Wall-shear stress

The variations of normalized wall-shear stress with radial position for jet impingement on heated static and oscillating target surfaces are shown in Fig. 5.17. As done for jet impingement on unheated target surface in Chapter 4, the velocity components at the wall were taken to be zero in order to calculate the wall-shear stress, given by $\tau_w = \mu(dv/dx)_w$.

It is observed that the wall-shear stress in the region $y/d < 1$, for phases ϕ_4 to ϕ_6 of target-surface oscillation at 20 Hz in Fig. 5.17(b), is higher than that for the static target surface. In contrast, for target-surface oscillation at 50 Hz, the wall-shear stress for phase ϕ_6 is higher than that for the static target surface over the entire radial span. This is due to higher near-wall mean radial velocities produced due to target-surface oscillation at this frequency and when the target surface is at a position closest to the jet exit and moving towards it, as shown in Fig. 5.16(b). The variations of the wall-shear stress over the radial coordinate, for both the static and oscillating target surfaces, show a small secondary peak at around $y/d = 1.6$, which is similar to the location of the secondary peak seen in the variations of the maximum mean radial velocity in Fig. 5.16.

5.3.3 Mean strain rates

The mean axial strain rate $\partial\bar{u}/\partial x$ contours for jet impingement on heated static and oscillating target surfaces are shown in Fig. 5.18. The mean axial strain rates in the vicinity of the stagnation point and the near-wall locations in the impingement region for phases ϕ_1 to ϕ_3 of both target-surface oscillation frequencies, in Figs. 5.18(b) to 5.18(d), have less negative values than those for the static target surface. This occurs due to higher mean axial velocities at those phases during motion of the target surface in the positive direction of the axial velocity of the jet as shown in Fig. 5.9. The axial strain rates closer to the wall for these phases are lower for target-surface oscillation at 50 Hz than that at 20 Hz because of the effect of higher target surface velocity.

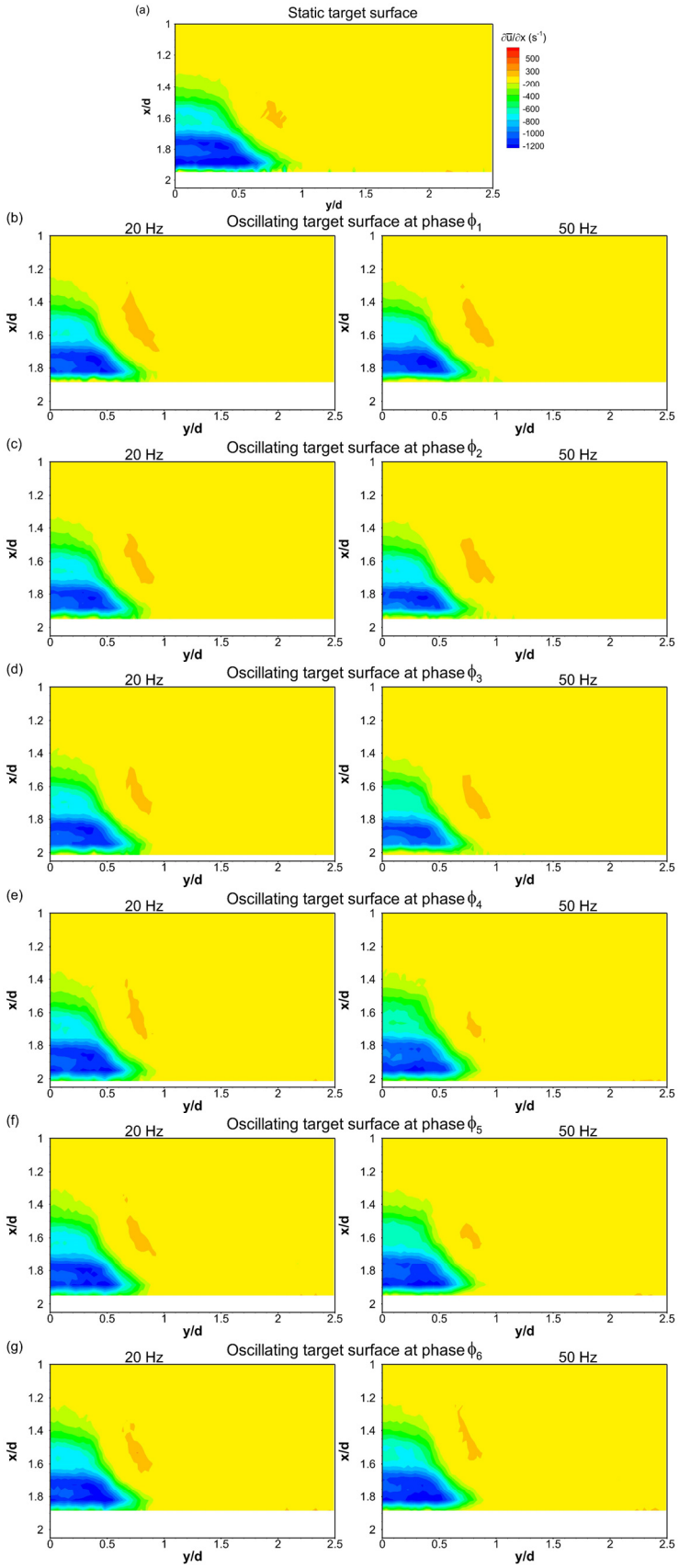

Fig. 5.18 Mean axial strain rate for jet impingement on heated target surfaces: (a) static target surface; (b) to (g) oscillating target surface at 20 Hz and 50 Hz, at phases ϕ_1 to ϕ_6 respectively

For phases ϕ_4 to ϕ_6 of target-surface oscillation at 20 Hz, in Figs. 5.18(e) to 5.18(g), the mean axial strain rates in the near-wall locations in the impingement region attain values similar to those for the static target surface. However, for these phases of target-surface oscillation at 50 Hz, the mean axial strain rates close to the wall at around y/d = 0.8 attain positive values as compared with the negative values observed for the static target surface. This occurs because of lower mean axial velocities induced by the motion of the target surface towards the jet exit as shown in Fig. 5.9.

The mean radial strain rate $\partial\bar{v}/\partial y$ contours presented in Fig. 5.19 show that the effect of target-surface oscillation on the mean radial strain rates is minimal. It is observed that the mean radial strain rates for all phases of target-surface oscillation at 20 Hz are similar to those found for the static target surface. For target-surface oscillation at 50 Hz, the mean radial strain rates for phase ϕ_3, in the region between y/d = 1 and 1.5, have less negative values than those for the static target surface in Fig. 5.19(a). For phase ϕ_6 Fig. 5.19(g), the radial strain rates in the vicinity of y/d = 1.5 have less negative values than those for static target surface, which indicates a relative local acceleration of the wall-jet.

The mean shear strain rates $(\partial\bar{u}/\partial y + \partial\bar{v}/\partial x)/2$ for jet impingement on static and oscillating target surfaces are shown in Fig. 5.20. Lower shear strain rates compared to those for the static target surface are observed in the wall-jet for phases ϕ_2 to ϕ_5 for both target-surface oscillation frequencies, whereas for phases ϕ_1 and ϕ_6 the shear strain rates are comparable to those for that static target surface. The wall-jet shear strain rates for phases ϕ_1 and ϕ_6, in Figs. 5.20 (b) and 5.20(g), for target-surface oscillation at 50 Hz are higher than those for 20 Hz.

It is observed that the shear strain rates in the free-jet shear layer for all phases of the target-surface oscillation at 20 Hz are similar to those for the static target surface. However, for phases ϕ_4 to ϕ_6 of target-surface oscillation at 50 Hz, the shear strain rates are only marginally higher than those for phases ϕ_1 to ϕ_3. This is observed by the presence of slightly longer contours of the highest negative level (marked blue) and it occurs due to the deceleration of the ambient fluid for phases ϕ_4 to ϕ_6 as shown in Fig. 5.11(c).

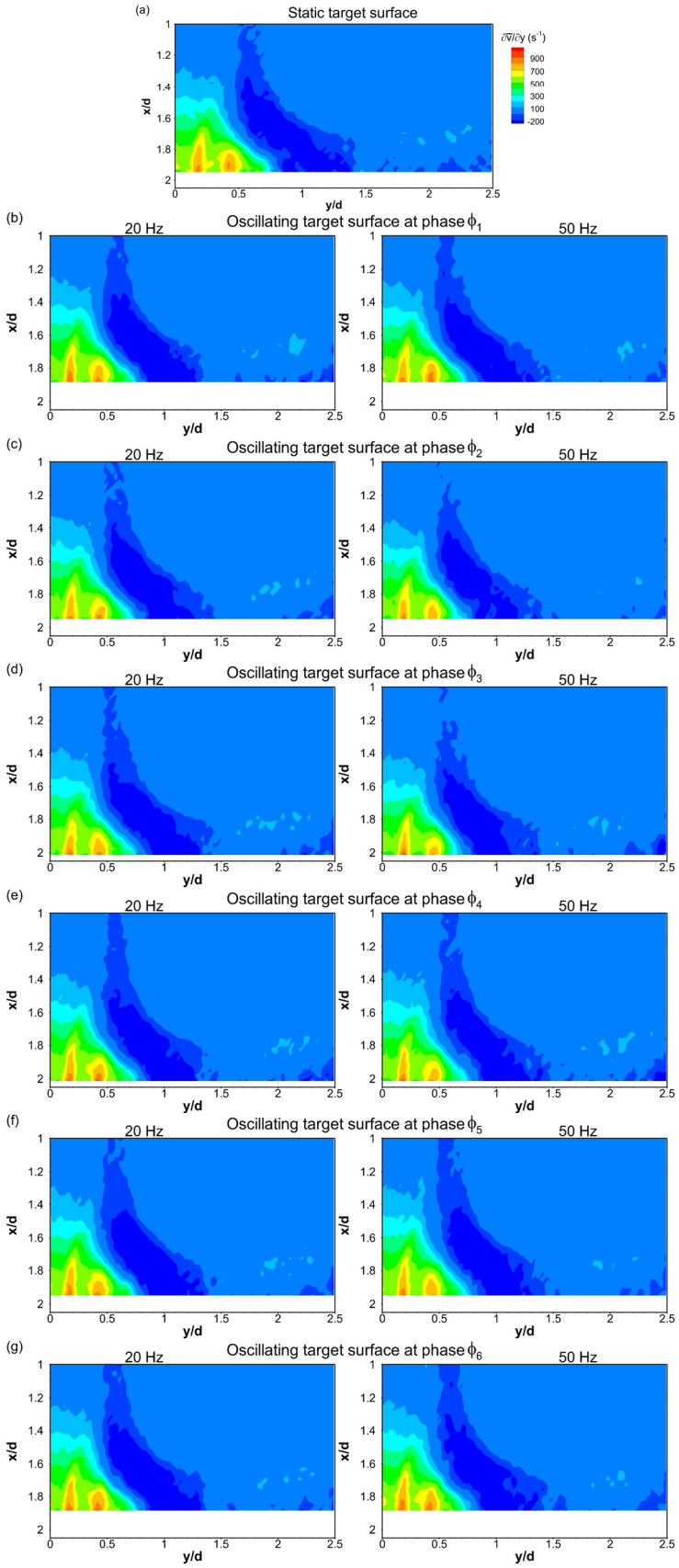

Fig. 5.19 Mean radial strain rate for jet impingement on heated target surfaces: (a) static target surface; (b) to (g) oscillating target surface at 20 Hz and 50 Hz, at phases ϕ_1 to ϕ_6 respectively

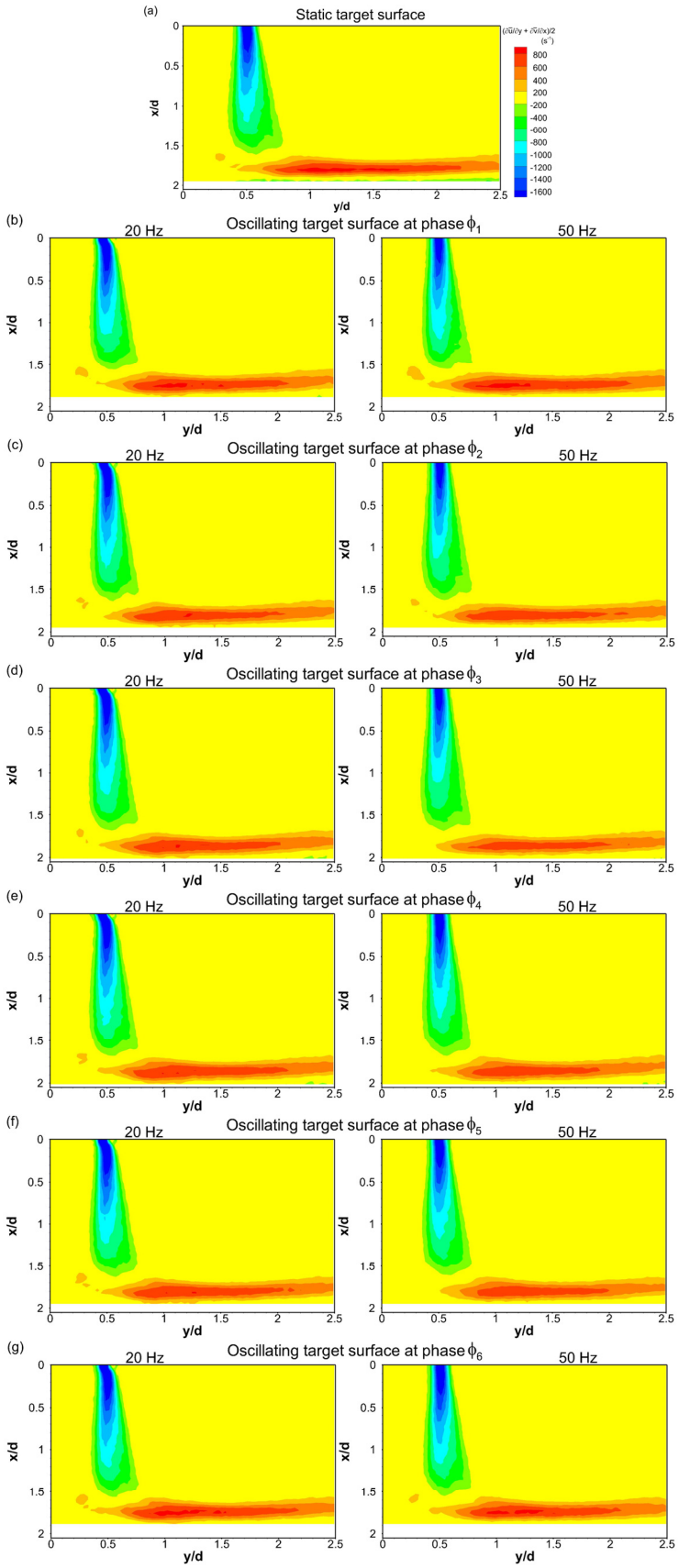

Fig. 5.20 Mean shear strain rate for jet impingement on heated target surfaces: (a) static target surface; (b) to (g) oscillating target surface at 20 Hz and 50 Hz, at phases ϕ_1 to ϕ_6 respectively

5.4 Jet impingement on heated static and oscillating target surfaces: Proper orthogonal decomposition analysis

A snapshot proper orthogonal decomposition (POD) of the flow field for jet impingement on heated static and oscillating target surfaces has been performed, using a sample size of 500 snapshots for each case. Following the POD analysis presented in Chapter 4, POD modes 2, 3 and 4 for jet impingement on heated static and oscillating target surfaces are presented first, followed by the instantaneous vector fields reconstructed using POD modes 1 to 30.

For jet impingement on heated target surfaces it is found that the first 50 modes for the static target surface contains 48.93% of the total energy, while those for target-surface oscillation at 20 Hz and 50 Hz (mean of all the phases) contain 49.20% and 49.50% of the total energies respectively. The non-dimensional vorticity $\omega d/\bar{u}_{\mathrm{cj}}$ maps for each mode with its proportion of system energy as a percentage is shown in Fig. 5.21 for target-surface oscillation at 50 Hz and in Fig. 5.22 for target-surface oscillation at 20 Hz. Each of these figures also contain the non-dimensional vorticity maps of the modes for the static target surface for comparison. As per convention, a negative vorticity region indicates a clockwise rotation.

The Mode 2 vorticity map for phase ϕ_1 of target-surface oscillation at 50 Hz in Fig. 5.21(b) shows higher vorticity in the wall-jet than that for the static target surface in Fig. 5.21 (a). This indicates higher stream-wise velocity fluctuations in the wall-jet when the target surface is closest to the jet exit. The vorticity in the free-jet shear layer of Mode 2 for phases ϕ_1 and ϕ_2 is lower than that for the static target surface, which occurs because of lower velocity fluctuation magnitudes when the mean axial velocities of both the jet and the ambient fluid increases during target-surface motion away from the jet exit. The Mode 2 maps for phases ϕ_4 and ϕ_5 in Figs. 5.21(e) and 5.21(f), have wall-jet vorticities similar to those for the static target surface but higher vorticities in the free-jet shear layer are observed for phase ϕ_4. This occurs because the target surface accelerates from phase ϕ_4 to ϕ_5 while moving towards the jet exit, thus inducing a greater shear interaction between the jet and the ambient fluid.

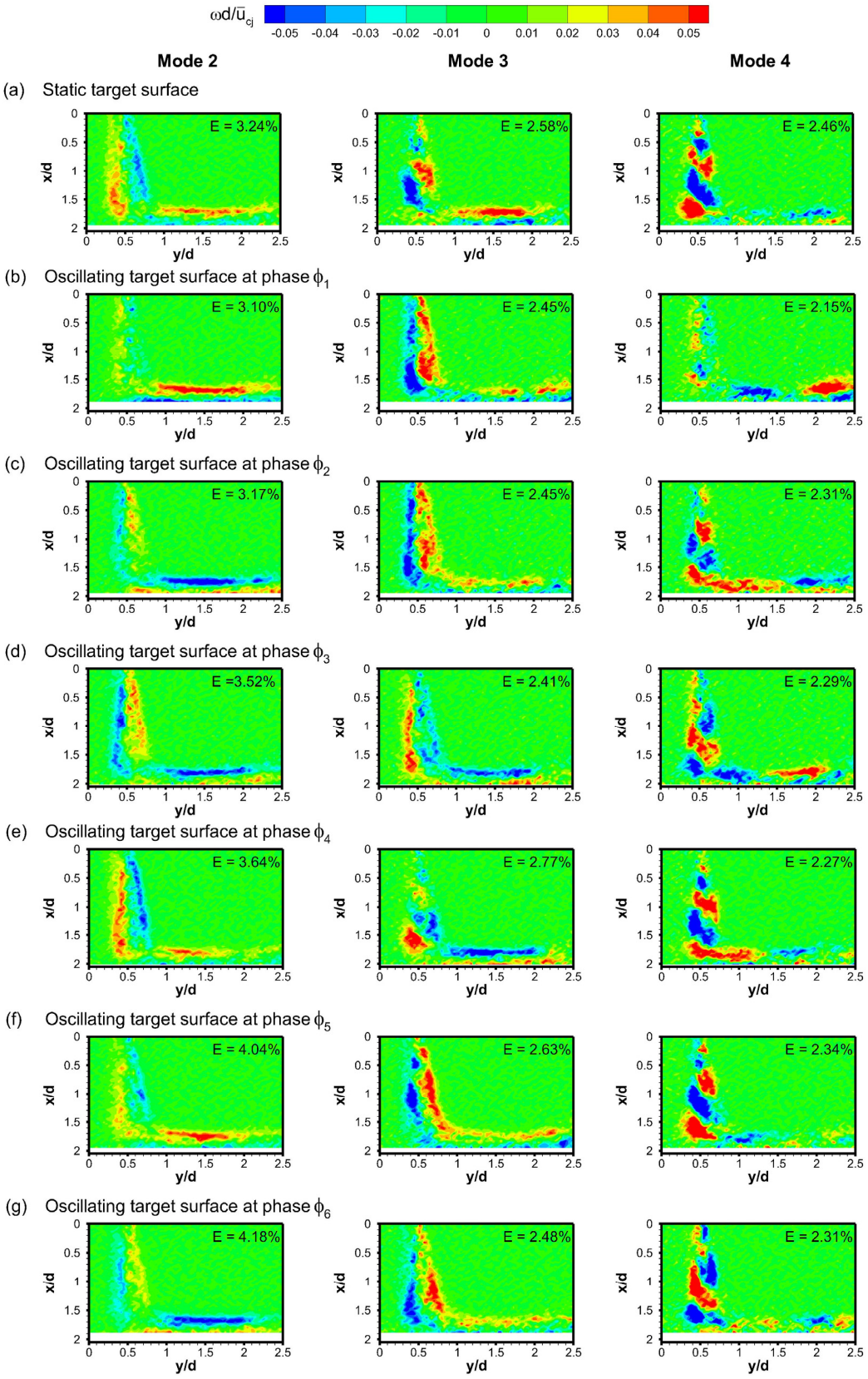

Fig. 5.21 Vorticity maps of POD modes 2 to 4 for jet impingement on heated target surfaces: (a) static target surface, (b) to (g) oscillating target surface at 50 Hz, at phases ϕ_1 to ϕ_6 respectively

The wall-jet vorticities in Mode 2 maps for phases ϕ_3 and ϕ_6, in Figs. 5.21(d) and 5.21(g), are found to be similar to each other, with the velocity fluctuations being opposite to the stream-wise direction. The Mode 3 maps for all phases except ϕ_3 and ϕ_4 are found to have comparable vorticity magnitudes. While those for phases ϕ_3 and ϕ_4 show lower vorticities than that for the static target surface, possibly due to the effect of deceleration of the target surface on the flow that occurs at these phases.

The Mode 4 map for the static target surface in Fig. 5.21(a), which shows coherent structures with alternating signs of vorticity, is found to be similar to that for phase ϕ_5 in Fig. 5.21(f), where the target surface attains its maximum velocity during oscillation and when its distance from the jet-nozzle exit is equal to that for the static target surface. The Mode 4 map for phase ϕ_1 in Fig. 5.21(b), has lower vorticity in the free-jet shear layer when compared to that for the static target surface because of lower velocity fluctuations in this region due target-surface motion away from the jet exit. It is seen that phases ϕ_2 and ϕ_4 have Mode 4 structures with same signs of vorticity, as well as phases ϕ_3 and ϕ_6 but with opposite signs of vorticity.

In the case of jet impingement on a heated target surface oscillating at 20 Hz, the Mode 2 maps for all phases in Fig. 5.22 have vorticity contours similar to that for the static target surface in Fig. 5.22(a), except for phase ϕ_6 in Fig. 5.22(g) which has lower vorticities in the free-jet shear layer and higher in the wall-jet region. The Mode 3 contours for phases ϕ_2 and ϕ_3, in Figs. 5.22(c) and 5.22(d), have structures with same vorticity signs as that for the static target surface, which indicate that the velocity fluctuations are positive in the stream-wise direction. However, phases ϕ_4 to ϕ_6 have velocity fluctuations in the opposite direction, which are similar to those found in the Mode 2 maps for these phases. These observations also match those in the Mode 3 maps for phases ϕ_4 and ϕ_6 of jet impingement on an unheated target surface oscillating at 20 Hz (Experimental system No. 1) in Figs. 4.17(e) and 4.17(g).

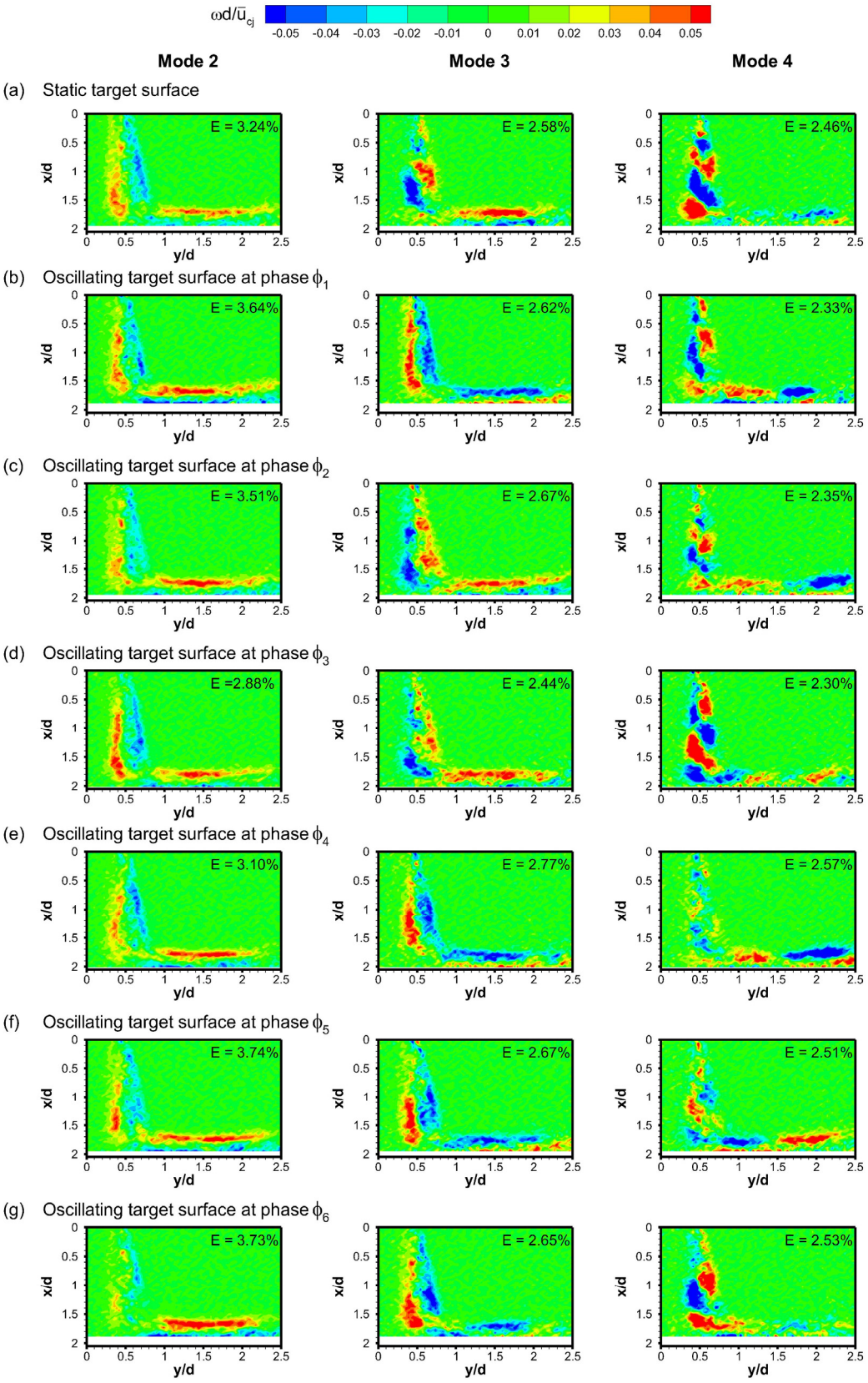

Fig. 5.22 Vorticity maps of POD modes 2 to 4 for jet impingement on heated target surfaces: (a) static target surface, (b) to (g) oscillating target surface at 20 Hz, at phases ϕ_1 to ϕ_6 respectively

The coherent structures in the Mode 4 maps for phases ϕ_1 and ϕ_2 in Figs. 5.22(b) and 5.22(c) are found to be similar to each other, whereas those for phase ϕ_6 in Fig. 5.22(g) are found to be similar to those for the static target surface. The similarities between the Mode 4 structures for phase ϕ_6 and the static target surface were also observed for jet impingement on an unheated target surface oscillating at 20 Hz in Fig. 4.17. The Mode 4 map for phases ϕ_4 in Fig. 5.22(e) show unstructured flow features in the free-jet shear layer similar to those observed in the Mode 4 map of phase ϕ_1 in Fig. 5.21(b) for target-surface oscillation at 50 Hz.

The POD modes shown in Figs. 5.21 and 5.22 show the dominant spatial features that occur in jet impingement on heated static and oscillating target surfaces. For target-surface oscillation at 50 Hz, the higher energy mode shows higher stream-wise velocity fluctuations in the wall-jet region than those for the static target surface. This occurs at the phase closest to the jet exit and moving away from it. The velocity fluctuations in the free-jet shear layer for phases during target-surface motion away from the jet exit are found to be lower in the higher energy mode for target-surface oscillation at 50 Hz. The higher energy POD modes for target-surface oscillation at 20 Hz show flow features similar to those for the static target surface, which indicates a small effect on the impinging-jet flow due to target-surface oscillation at this frequency.

5.4.1 Instantaneous vortex structures

The instantaneous vorticity maps for jet impingement on heated static and oscillating target surfaces presented in this section show flow features similar to those observed for jet impingement on unheated static and oscillating target surfaces presented in Chapter 4, Section 4.4.1. The flow features show the phenomenon of jet flapping and the occurrence of primary-secondary vortex pairs on the target surface.

The sequence of instantaneous maps for jet impingement on a heated static target surface are presented in Fig. 5.23. They show the non-dimensional vorticity contours of instantaneous vectors reconstructed using POD modes 1 to 30. Occurrence of jet flapping, in the form lateral oscillation of the free-jet shear layer can be observed in Figs. 5.23(a) through to 5.23(d), which are a result of instabilities in the free-jet shear layer.

The formation of the primary-secondary vortex pair in the wall-jet region due to interaction of the primary vortex with the surface is observed in Fig. 5.23(f). As mentioned in Chapter 4, Section 4.4.1, the formation of the secondary vortex is associated with ejection of fluid from the surface, and a local flow reversal, an event which does not occur frequently. The vectors around the secondary vortex, shown by the negative vorticity contour in Fig. 5.23(f), exhibit an ejection of fluid of the surface but no flow reversal.

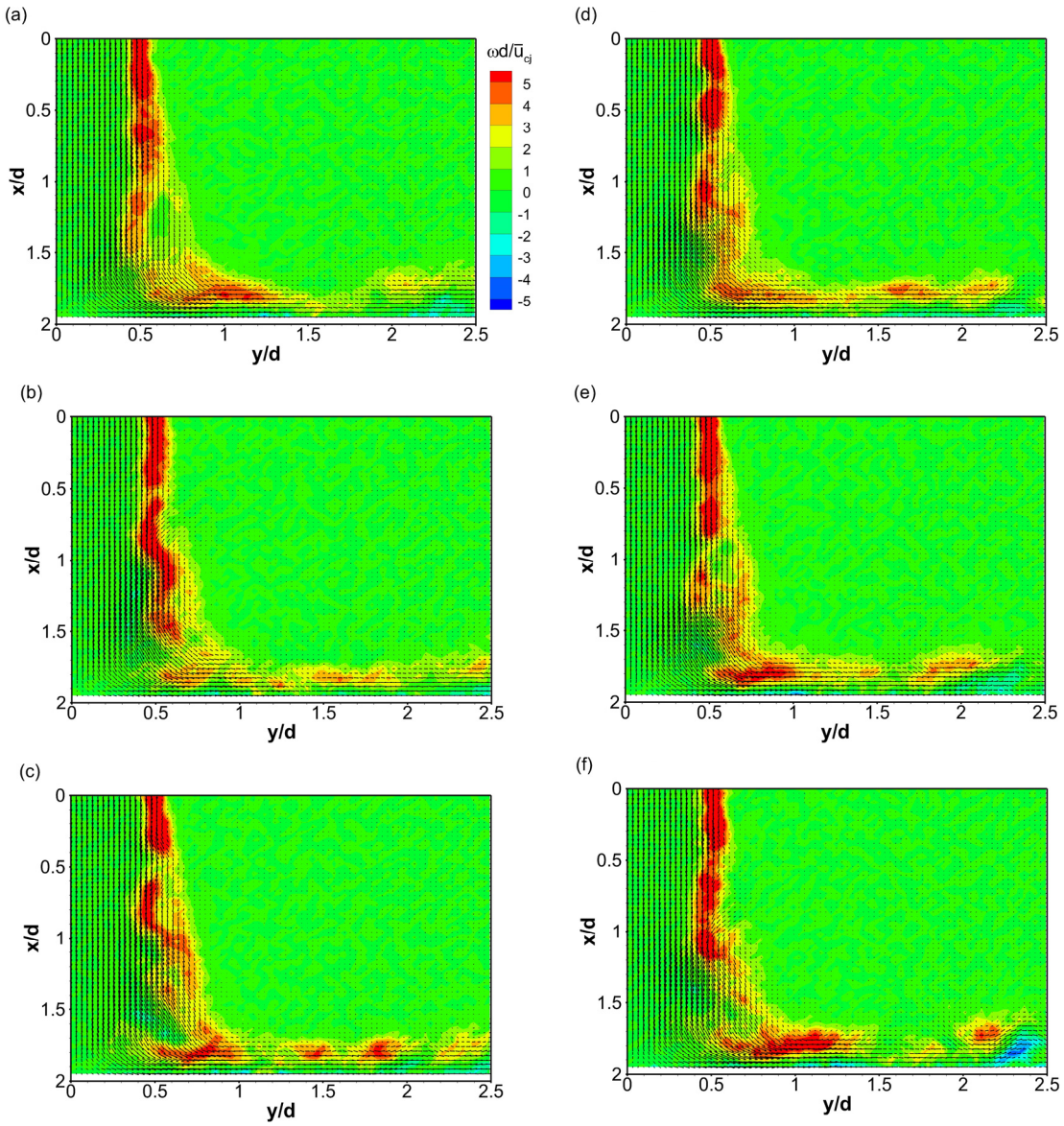

Fig. 5.23 Sequence of instantaneous vorticity maps of vectors reconstructed using POD modes 1 to 30 for jet impingement on a heated static target surface. Time between each instantaneous map is 0.01s

The instantaneous vorticity maps in two different oscillation cycles for jet impingement on a heated target surface oscillating at 50 Hz are shown in Figs. 5.24 and 5.25. The non-dimensional vorticity contours are obatined from velocity vectors reconstructed using POD modes 1 to 30. The time interval between successive instantaneous images for phases ϕ_1 to ϕ_3 and phases ϕ_4 to ϕ_6 is 2 ms, while the time interval between phase ϕ_3 to ϕ_4 is 4 ms.

The first sequence of vorticity maps in Fig. 5.24 show the formation of a primary-secondary vortex pair at phase ϕ_2 in Fig. 5.24(b) and its radial progression at the next phase ϕ_3 in Fig. 5.24(c). This also occurs in a different oscillation cycle shown in Fig. 5.25, but at phases ϕ_5 and ϕ_6 as seen in Figs. 5.25(e) and 5.25(f). It is observed that target-surface motion towards the jet exit reduces the strength of the secondary vortex, as was also found for jet impingement on an unheated target surface oscillating at 80 Hz in Fig. 4.21. The instantaneous vorticity maps in the oscillation cycles shown in Figs. 5.24 and 5.25 also show the presence of lateral oscillation in the free-jet shear layer.

The instantaneous vorticity maps in two different oscillation cycles for jet impingement on a heated target surface oscillating at 20 Hz, reconstructured using POD modes 1 to 30, are shown in Figs. 5.26 and 5.27. The time interval between successive instantaneous images in these figures for phases ϕ_1 to ϕ_3 and phases ϕ_4 to ϕ_6 is 5 ms, while the time interval between phase ϕ_3 to ϕ_4 is 10 ms.

The formation of the primary-secondary vortex pair is observed at phase ϕ_2 in Fig. 5.26(b) and at phase ϕ_5 in Fig. 5.27(e). The vorticity maps at these two phases again show that the strength of the secondary vortex is higher during target-surface motion away from the jet exit. The radial progression of the secondary vortex formed at phase ϕ_2 cannot be observed in the next phase ϕ_3 in Fig. 5.26(c), because the period of vortex motion is lower than the time between images of successive phases. As shown in Figs. 5.24 and 5.25, the flapping motion of the jet due to shear layer oscillation can also be observed in Figs. 5.26 and 5.27, when the target surface oscillates at a frequency of 20 Hz.

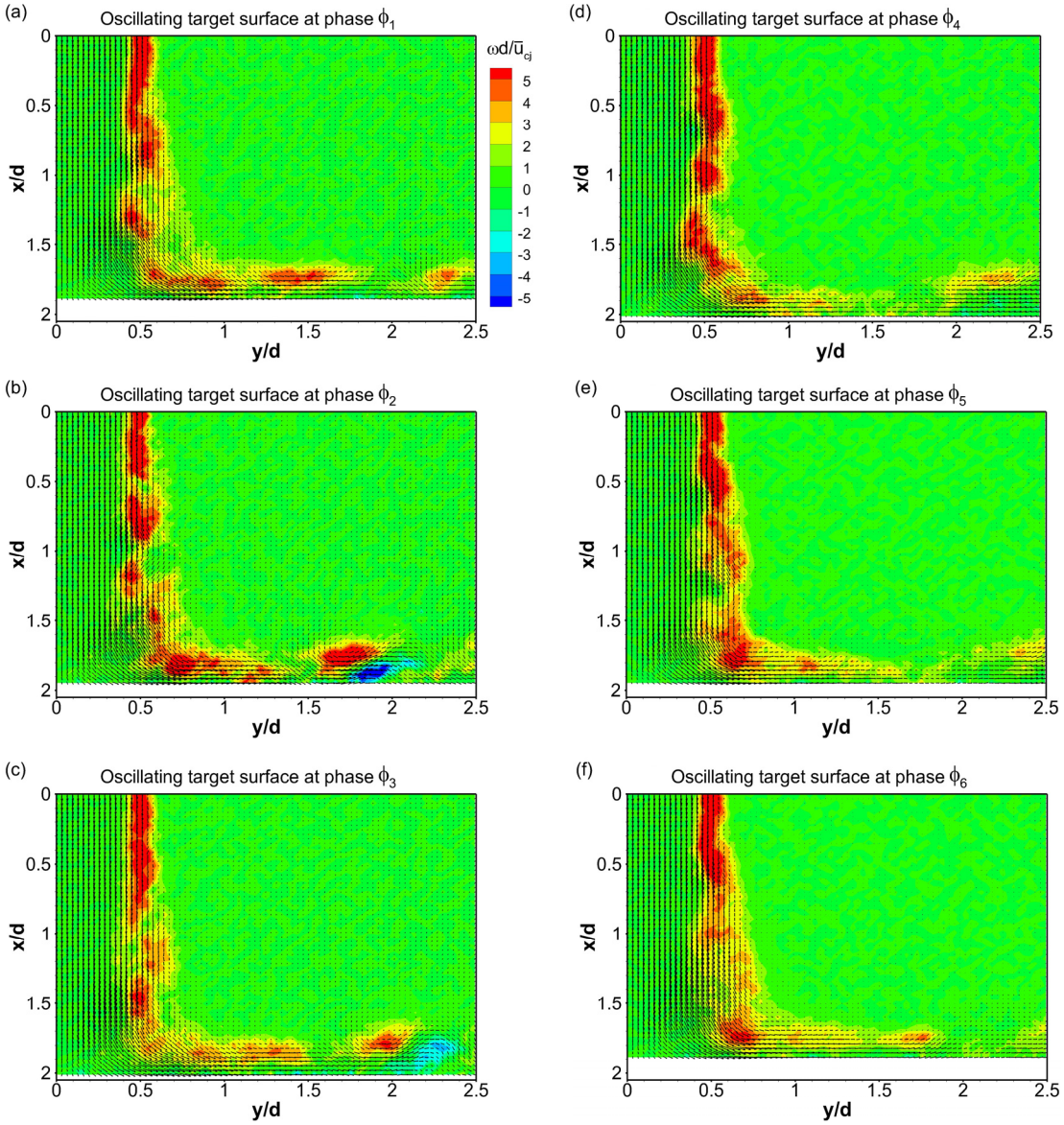

Fig. 5.24 Sequence (No. 1) of instantaneous vorticity maps of vectors reconstructed using POD modes 1 to 30 for one oscillation cycle in jet impingement on a heated target surface oscillating at 50 Hz: (a) to (f) phases ϕ_1 to ϕ_6

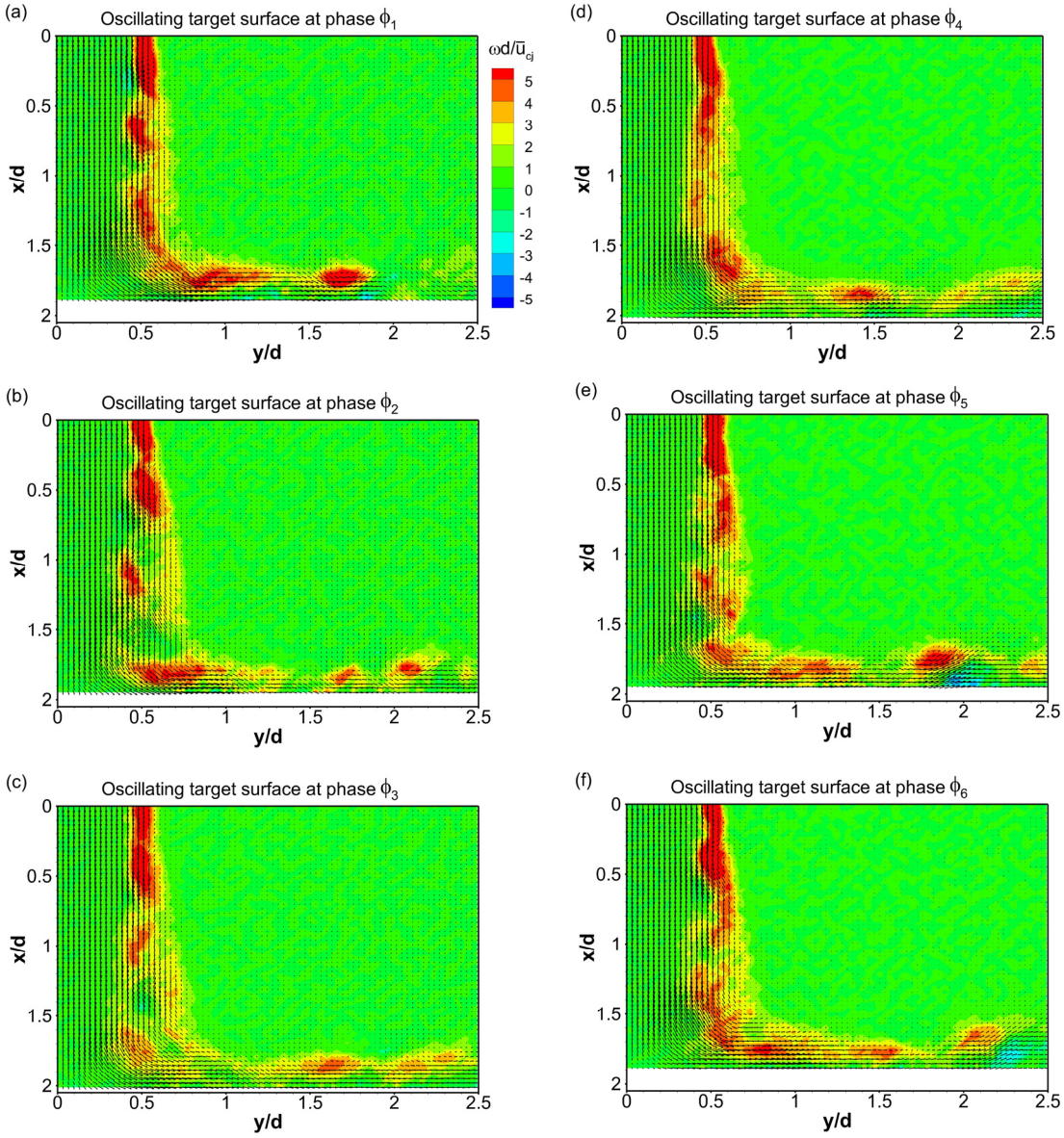

Fig. 5.25 Sequence (No. 2) of instantaneous vorticity maps of vectors reconstructed using POD modes 1 to 30 for one oscillation cycle in jet impingement on a heated target surface oscillating at 50 Hz: (a) to (f) phases ϕ_1 to ϕ_6

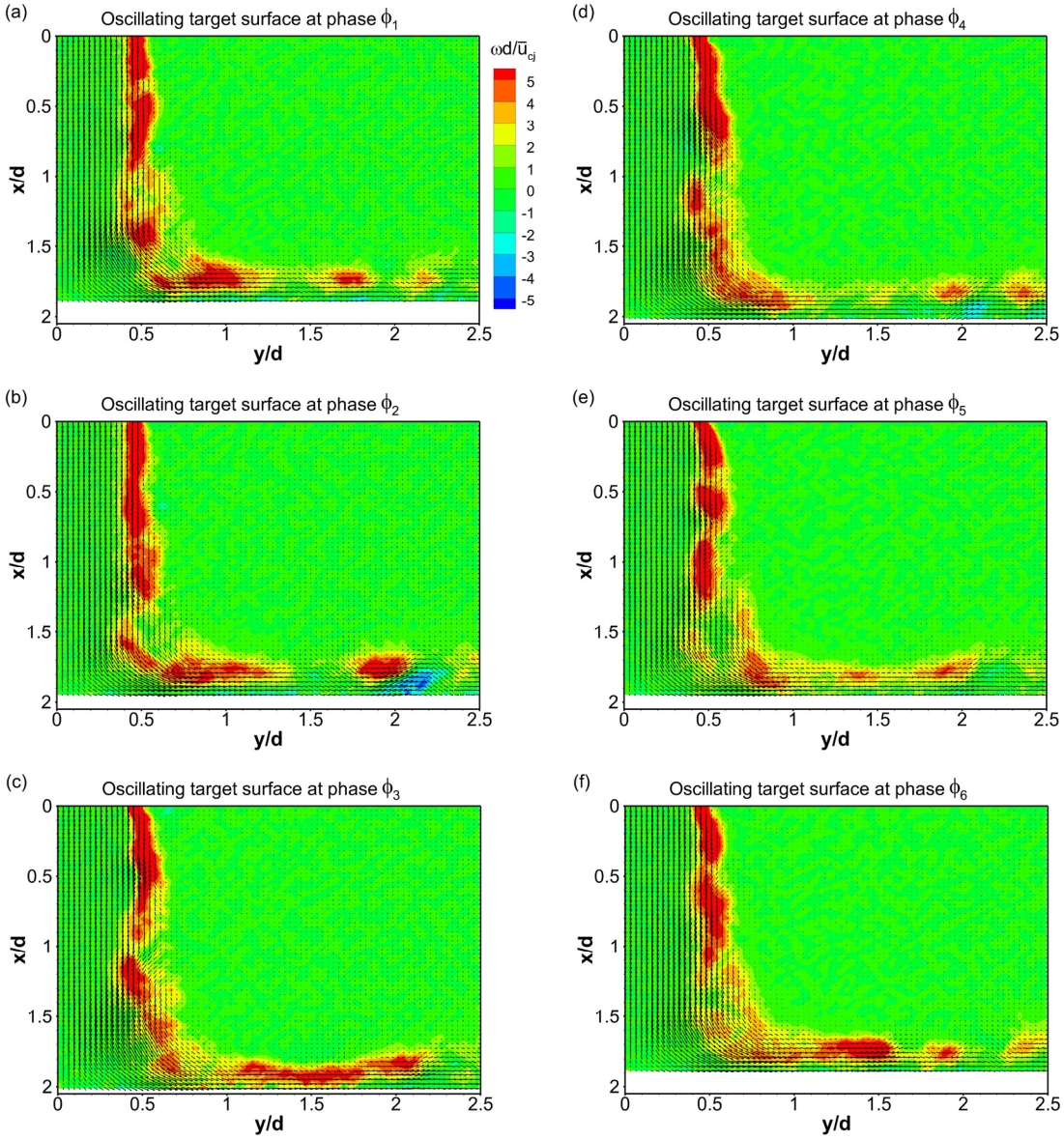

Fig. 5.26 Sequence (No. 1) of instantaneous vorticity maps of vectors reconstructed using POD modes 1 to 30 for one oscillation cycle in jet impingement on a heated target surface oscillating at 20 Hz: (a) to (f) phases ϕ_1 to ϕ_6

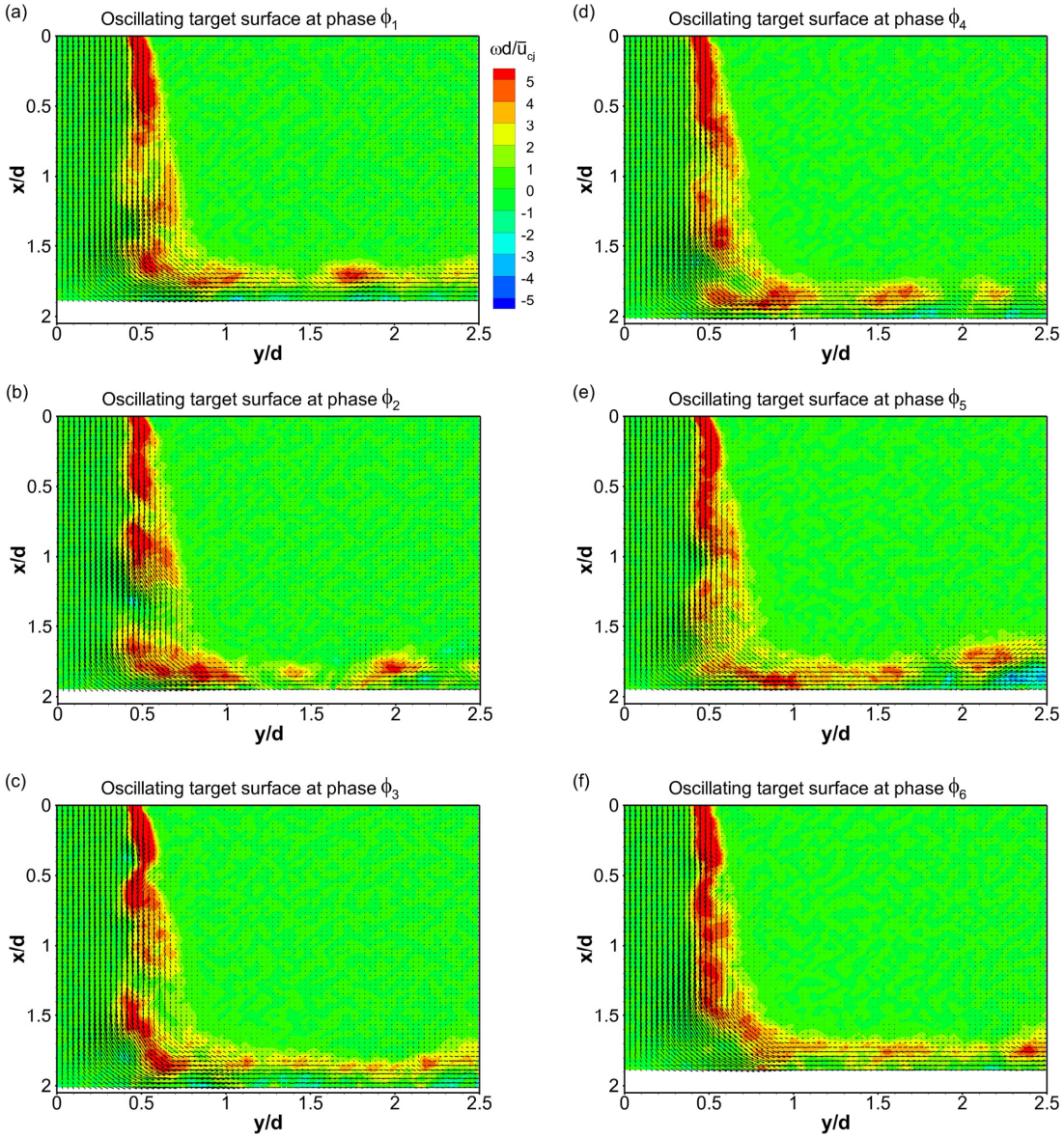

Fig. 5.27 Sequence (No. 2) of instantaneous vorticity maps of vectors reconstructed using POD modes 1 to 30 for one oscillation cycle in jet impingement on a heated target surface oscillating at 20 Hz: (a) to (f) phases ϕ_1 to ϕ_6

5.5 Jet impingement on heated static and oscillating target surfaces: Turbulence statistics

5.5.1 RMS axial velocity fluctuation

The root-mean-square (rms) axial velocity fluctuations $u_{rms}/\overline{u}_{cj}$ for jet impingement on heated static and oscillating target surfaces are shown in Fig. 5.28. For the static target surface in Fig. 5.28(a), the rms axial velocity fluctuations in the free-jet shear layer have a maximum magnitude of 0.16, while those in the wall-jet have 0.1. The rms axial velocity fluctuations in the wall-jet for phases ϕ_1 and ϕ_2, and in the free-jet shear layer for phases ϕ_5 and ϕ_6, of target-surface oscillation at 50 Hz are higher than those for the static target surface, as shown in Figs. 5.28(b) and 5.28(c), and in Figs. 5.28(f) and 5.28(g). Higher rms axial velocity fluctuations in the wall-jet region occur because of higher mean axial velocities and larger entrainment of the ambient fluid into the wall-jet, as shown in Fig. 5.11(c). However, higher rms axial fluctuation in the free-jet shear layer exists because of larger shear between decelerated ambient fluid and accelerated jet flow, as shown in Figs. 5.11(b) and 5.11(g).

The rms axial velocity fluctuations for phases of the target-surface oscillation at 20 Hz are similar to those observed for the static target surface because the effect of target-surface oscillation at this frequency on the free-jet and ambient fluid regions is very small, as shown in Fig. 5.12(g).

In Fig. 5.28, it is observed that the near-wall rms axial velocity fluctuations in the impingement region for all phases of target-surface oscillation at the two frequencies are higher than those for the static target surface. Furthermore, these fluctuations are higher for target-surface oscillation at 50 Hz. It is found that the rms axial velocity fluctuation at $x/d = 1.7$, $y/d = 2$, for phase ϕ_1 for target surface oscillating at 50 Hz, is 25.63% greater than that for the static target surface.

5.5.2 RMS radial velocity fluctuation

The rms radial velocity fluctuations $v_{rms}/\overline{u}_{cj}$ for static and oscillating target surfaces are shown in Fig. 5.29. The maximum near-wall rms radial velocity fluctuation for the static target surface attains a magnitude of 0.19 at $y/d = 1.4$ as shown in Fig. 5.29(a).

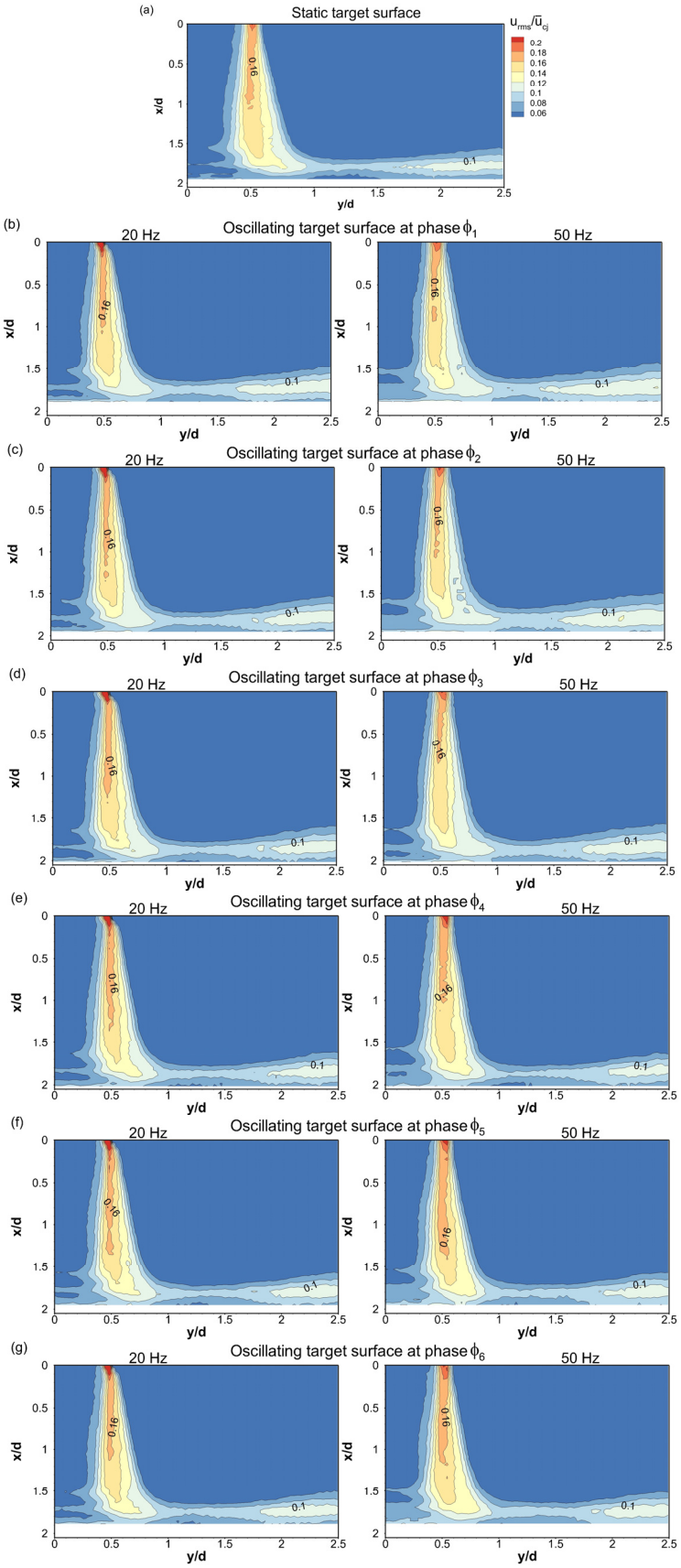

Fig. 5.28 RMS axial velocity fluctuations for jet impingement on heated target surfaces: (a) static target surface; (b) to (g) oscillating target surface at 20 Hz and 50 Hz, at phases ϕ_1 to ϕ_6 respectively

The rms radial velocity fluctuations for all phases of target-surface oscillation at both 20 Hz and 50 Hz are higher than those for the static target surface. The reason for this is attributed to higher shear between the layers of the wall-jet, as shown by the large difference in magnitudes of the mean radial velocities at near-wall locations and at x/d = 1.8, in Figs. 5.11(d) and 5.11(e), and Figs. 5.12(d) and 5.12(e).

The effect of higher entrainment of the ambient fluid into the wall-jet for phases ϕ_1 and ϕ_2 of target-surface oscillation at 50 Hz can be observed in Figs. 5.29(b) and 5.29(c), where the rms radial velocity fluctuations in the wall-jet shear layer between x/d = 1.8 and x/d = 1.7 are higher than those for target-surface oscillation at 20 Hz for these phases. At phases ϕ_3 and ϕ_4 in Figs. 5.29(d) and 5.29(e), the rms radial velocity fluctuations are found to be lower than those at the remaining phases because of lower radial velocities when the target surface is farthest away from the jet exit, as shown in Figs. 5.11(d) to 5.11(f) and Figs. 5.12(d) to 5.12(f). Phase ϕ_4 in Fig. 5.29(e) show lower rms radial velocity fluctuations in the near-wall region for 50 Hz frequency of target-surface oscillation due to lower near-wall mean radial velocities present at this phase as shown in Fig. 5.11(d). It is found that the rms radial velocity fluctuation at x/d = 1.8, y/d = 1.5, for phase ϕ_6 for target-surface oscillation at 50 Hz, is 29.90% greater than that for the static target surface.

5.5.3 Reynolds stress and turbulence kinetic energy

The Reynolds stress $\overline{u'v'}/\overline{u}_{cj}^2$ maps for jet impingement on heated static and oscillating target surfaces are shown in Fig. 5.30. The Reynolds stress for the static target surface attains a maximum positive magnitude of 0.008 in the free-jet shear layer and maximum negative magnitude of -0.004 in the wall-jet shear layer. The Reynolds stress in the wall-jet shear layer for phases ϕ_1 of target-surface oscillation at 50 Hz in Fig. 5.30(b), is higher than that for the static target surface and for target surface oscillating at 20 Hz. However, for the remaining phases of target-surface oscillation at 50 Hz and all the phases of target-surface oscillation at 20 Hz it is found to be similar to the magnitudes present the static target surface case. The Reynolds stress at x/d = 1.75, y/d = 2 for phase ϕ_1 of target surface oscillating at 50 Hz is found to be 18.37% greater than that for the static target surface.

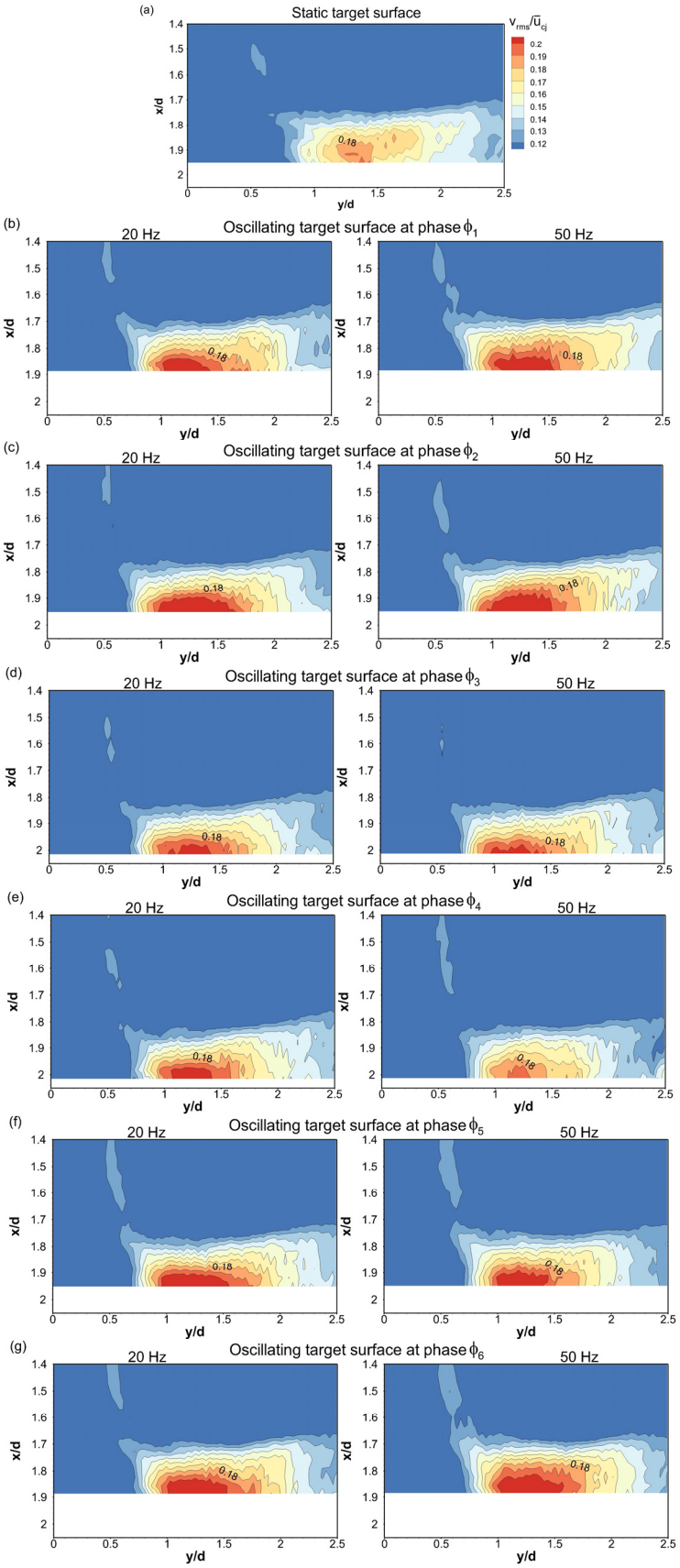

Fig. 5.29 RMS radial velocity fluctuations for jet impingement on heated target surfaces: (a) static target surface; (b) to (g) oscillating target surface at 20 Hz and 50 Hz, at phases ϕ_1 to ϕ_6 respectively

There is an increase in the near-wall Reynolds stress in the impingement region between y/d = 0.5 and 1, from that for the static target surface, which is found to occur in almost all phases of the two target-surface oscillation frequencies in Fig. 5.30. This supports the finding from the variations of mean velocities with target surface phases, in Figs. 5.11 and 5.12, that the effect of target-surface oscillation is higher at smaller radial distances from the jet centerline.

It is observed that the Reynolds stress in the free-jet shear for phases ϕ_1 to ϕ_3 of target-surface oscillation at 50 Hz, in Figs. 5.30(b) to 5.30(d), is lower than that for the static target surface. For the remaining phases of target-surface oscillation at 50 Hz and for all phases of target-surface oscillation at 20 Hz it is found that Reynolds stress in the free-jet shear layer is similar to that for the static target surface. This means that the turbulence production in the free-jet shear layer is not affected by the oscillatory motion of the target surface at these frequencies.

The turbulence kinetic energy $TKE = 0.5(\overline{u'^2} + \overline{v'^2})/\overline{u}_{cj}^2$ contours for jet impingement on heated static and oscillating target surfaces are shown in Fig. 5.31. For the static target surface in Fig. 5.31(a), it is found that the maximum TKE in the free-jet shear layer is 0.020, while that in the wall-jet is 0.015. The turbulence kinetic energies in the near-wall region are observed to be higher than those for the static target surface, for all phases of the two target-surface oscillation frequencies. The highest values attained are for phases ϕ_2 and ϕ_6, in Figs. 5.31(c) and 5.231(g), which occur because of higher near-wall rms axial and radial velocity fluctuations for these phases as shown in Figs. 5.28 and 5.29.

In Fig. 5.31, it is observed that the turbulence kinetic energy values in the free-jet shear layer for all phases of target-surface oscillation at 20 Hz do not increase from those for the static target surface. For target-surface oscillation at 50 Hz they are found to be lower than that for the static target surface for phases ϕ_1 to ϕ_3 in Figs. 5.31(b) to 5.31(d), and higher for phases ϕ_5 and ϕ_6 in Fig. 5.31(f) and 5.31(g). These occur because of the rms axial velocity fluctuations at these phases of target-surface oscillation at 50 Hz as shown in Fig. 5.28.

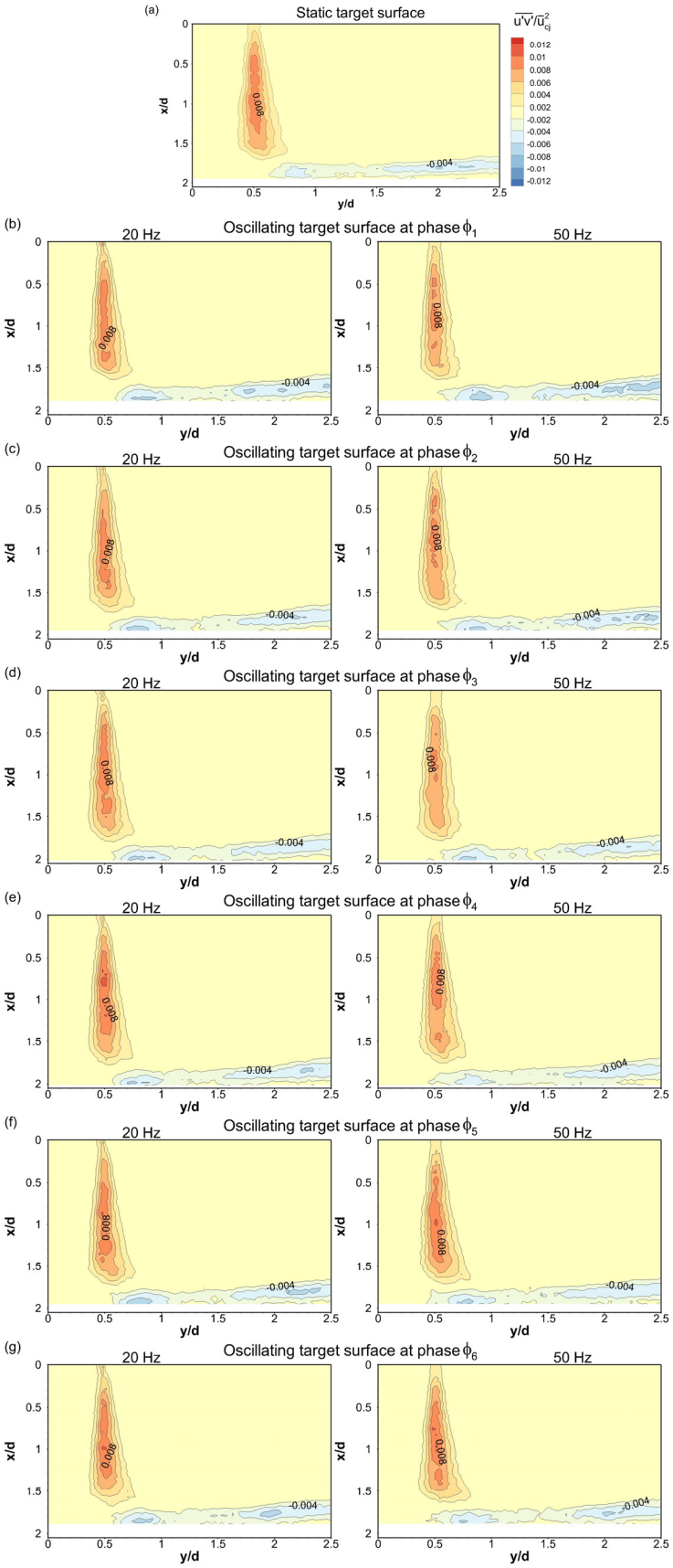

Fig. 5.30 Reynolds stress for jet impingement on heated target surfaces: (a) static target surface; (b) to (g) oscillating target surface at 20 Hz and 50 Hz, at phases ϕ_1 to ϕ_6 respectively

The phase-averaged Reynolds stress and turbulence kinetic energy contours for target-surface oscillation at 20 Hz and 50 Hz are presented in Figs. 5.32 and 5.33 respectively. These maps are obtained by averaging the corresponding quantities over the 6 phases that approximately cover one cycle of oscillation of the target surface. Figures 5.32(a) and 5.33(b) show that phase-averaged Reynolds stress in the near-wall region has higher negative values than those for the static target surface shown in Fig. 5.30(a). Although the near-wall values in the region between $y/d = 0.5$ and 1 are higher for target-surface oscillation at 20 Hz, the near-wall Reynolds stress over the entire radial span is marginally higher for target-surface oscillation at 50 Hz. However, it is found that the effect of target-surface oscillation at this frequency produces lower Reynolds stress values in the free-jet shear layer. The phase-averaged Reynolds stress contours show that the effect of target oscillation in producing higher turbulence is greater in the wall-jet region than in the free-jet shear layer.

The phase-averaged TKE contours in Fig. 5.33 show higher values in the wall-jet than those for the static target surface at both target-surface oscillation frequencies. Overall it is found that target-surface oscillation at 20 Hz gives rise to higher turbulence kinetic energies Although there is a small region of higher turbulence kinetic energy in the near-wall location between $y/d = 1$ and 1.5 for target-surface oscillation at 20 Hz in Fig. 5.33(a), the phase-averaged turbulence kinetic energies in the wall-jet region for target-surface oscillation at 50 Hz in Fig. 5.33(b) are found to be marginally higher. As observed in the phase-averaged contours of Reynolds stress in Fig. 5.32, the effect of target-surface oscillation produces higher turbulence kinetic energies in the wall-jet region than in the free-jet shear layer.

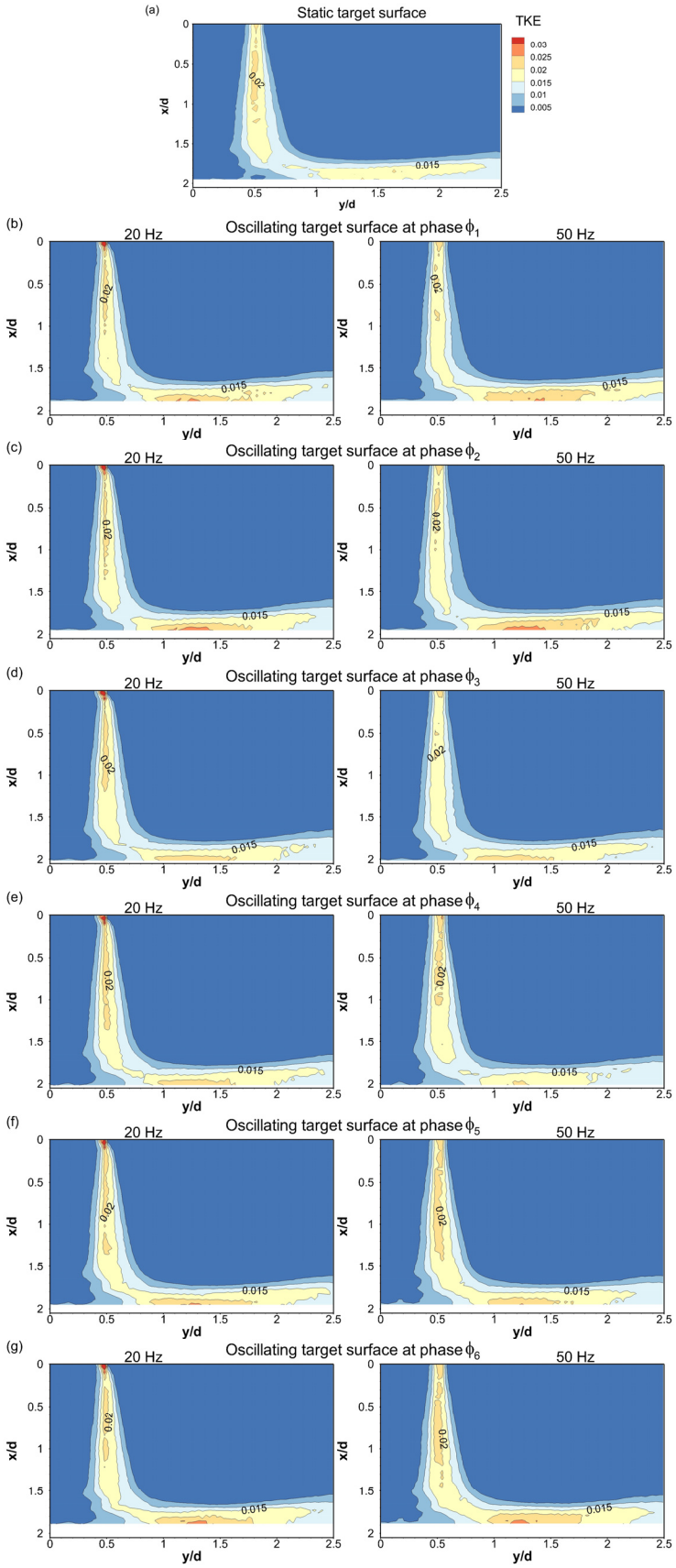

Fig. 5.31 Turbulence kinetic energy for jet impingement on heated target surfaces: (a) static target surface; (b) to (g) oscillating target surface at 20 Hz and 50 Hz, at phases ϕ_1 to ϕ_6 respectively

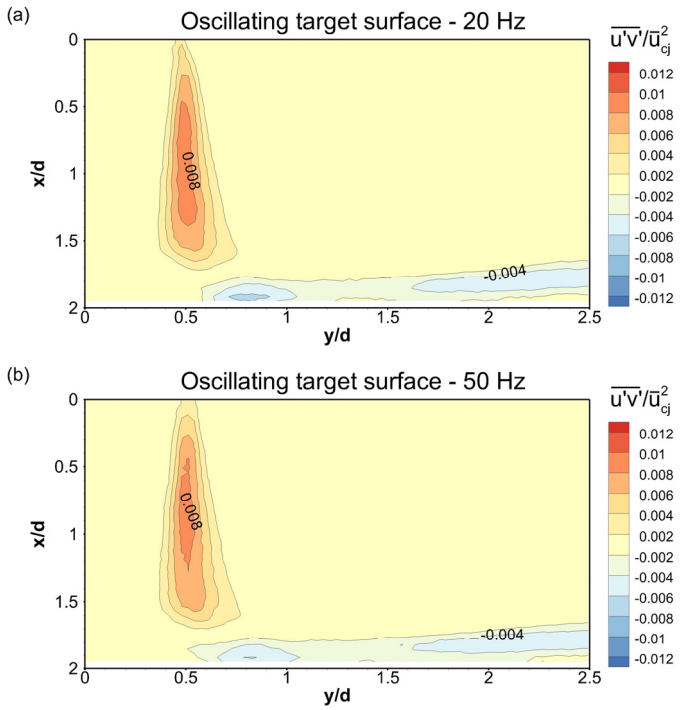

Fig. 5.32 Phase-averaged Reynolds stress for jet impingement on a heated target surface oscillating at: (a) 20 Hz; (b) 50 Hz

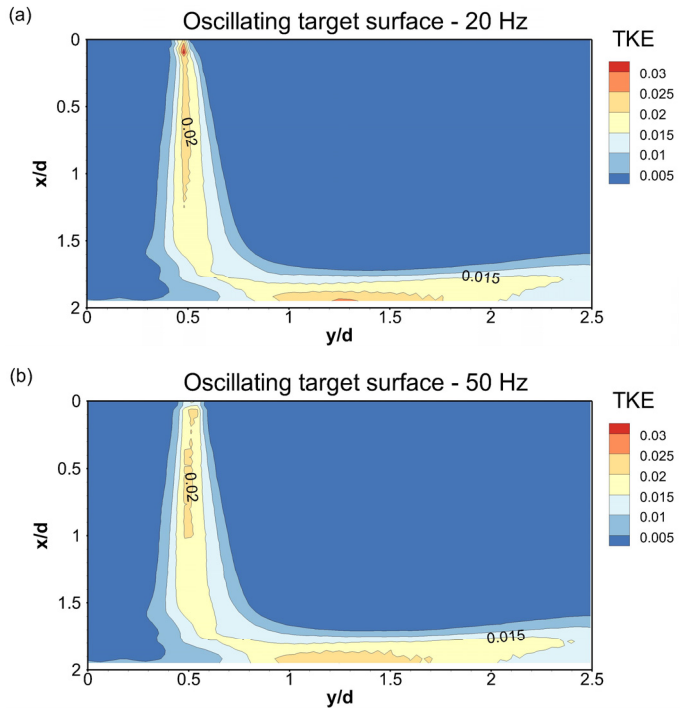

Fig. 5.33 Phase-averaged turbulence kinetic energy for jet impingement on a heated target surface oscillating at: (a) 20 Hz; (b) 50 Hz

5.6 Jet impingement on heated static and oscillating target surfaces: Heat transfer results

The results of heat transfer measurements for jet impingement on heated static and oscillating target surfaces are presented in this section. The convective heat transfer coefficients are characterized by the Nusselt number *Nu*; the process of determining *Nu* for jet impingement on a heated static target surface and heated oscillating target surface at 20 Hz and 50 Hz was presented in Chapter 3 (Section 3.5). The input heat flux for static and oscillating target surfaces was kept constant at Q_j = 680 W/m^2. This heat flux was determined to be sufficient to obtain a foil surface temperature approximately 23 ^{o}C higher with reference to the ambient temperature.

The heat transfer results presented below begin with a comparison of the Nusselt numbers obtained in this study for jet impingement on a heated static target surface with those reported previously in literature. This is followed by a presentation of the steady-state time-averaged spatial temperature distributions of the target surface obtained from infrared thermography measurements in jet impingement on heated static and oscillating target surfaces. The spatial contours of *Nu* for these two cases are provided next, followed by the local and azimuthal variations of *Nu* with the radial coordinate *y*/*d*.

5.6.1 Comparison with published studies for jet impingement on a heated static target surface

A comparison of the *Nu* values obtained in the present study of jet impingement on a heated static target surface with those reported previously by Lee and Lee (1999) and Violato et al. (2012) is shown in Fig. 5.34. The experimental parameters for jet impingement on a heated static target surface in the present study are *Re* = 5000 and *h*/*d* = 1.95, while those of Lee and Lee (1999) and Violato et al. (2012) were *Re* = 5000 and *h*/*d* = 2. Lee and Lee (1999) used air as the jet fluid and measured surface temperatures using the technique of imaging thermochromic liquid crystals coated on the heated target surface made of a gold-coated film. Violato et al. (2012) used water as the jet fluid and measured surface temperatures using infrared thermography of a thin-foil heated target surface made of constantan.

The *Nu* variations along *y*/*d* for the present work shows the occurrence of a primary peak in the vicinity of *y*/*d* = 0.5, and secondary peak in the vicinity of *y*/*d* = 2, which is consistent with that reported by Lytle and Webb (1994) in the presence of short nozzle-to-surface separation distances. Although these peaks also occur in the variations of Lee and Lee (1999) and Violato et al. (2012), their positions along the radial coordinate differs from those observed in the present work. Besides, the *Nu* values reported by Lee and Lee (1999) and Violato et al. (2012) are lower than those obtained in the present work.

The deviations are evident because of the difference in the jet exit velocity and turbulence intensity profiles in these studies with that of the present work; Lee and Lee (1999) used a fully developed jet flow coming from a straight nozzle, whereas Violato et al. (2012) used a smooth contraction nozzle that yields a laminar flow at the jet exit. Nozzle geometry has been shown to affect the velocity profile at the jet exit which in turn affects the heat transfer coefficients at the wall (Jambunathan 1992). Furthermore, the jet turbulence is also known to affect the heat transfer rates, and hence the Nusselt number (Gardon and Akfirat 1965). Although the *Nu* values obtained in the present study differ from those reported earlier, their variation along the radial coordinate are in qualitative agreement.

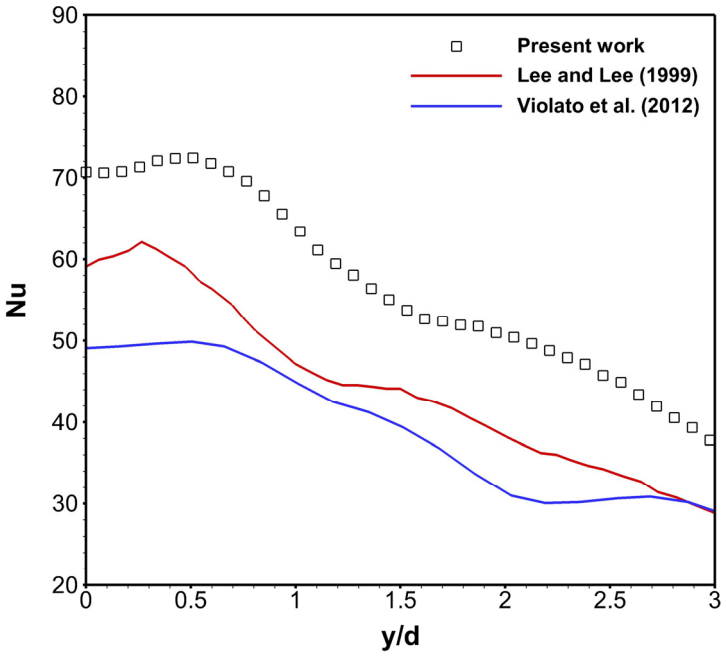

Fig. 5.34 Comparison of local Nusselt numbers *Nu* for jet impingement on a heated static target surface with those of Lee and Lee (1999) and Violato et al. (2012)

5.6.2 Steady-state heat transfer results

The steady-state time-averaged spatial temperature maps of the target surface in jet impingement on heated static and oscillating target surfaces are shown in Fig. 5.35 and 5.36. As described in Chapter 3 (Section 3.5), the target surface temperatures during jet impingement were measured with and without the input heat flux Q_j, for each of these cases. The difference of these surface temperature maps for the corresponding cases was used to determine the *Nu* values (Eqn. 3.2 and 3.8). The steady-state time-averaged surface temperatures T_w with input heat flux, for jet impingement on a static target surface and target surfaces oscillating at 20 Hz and 50 Hz are shown in Fig. 5.35, while those without T_{aw} are shown in Fig. 5.36.

The surface temperature maps with heat flux input during jet impingement on oscillating target surface at 20 Hz and 50 Hz, in Figs. 5.35(b) and 5.35(c), are similar to each other, and show higher temperatures in the impingement region y/d = -1 to 1 when compared to those for jet impingement on a static target surface in Fig. 5.35(a). When no heat flux was supplied, it is found that the surface temperatures for jet impingement on target-surface oscillation at 20 Hz and 50 Hz, in Figs. 5.36(b) and 5.36(c), are higher than those for the static target surface in Fig. 5.36(a), with surface temperatures being higher for target-surface oscillation at 50 Hz.

The surface temperature maps presented in Fig. 5.36 show that the frictional interaction between the fluid and the oscillatory target surface gives rise to an increase in surface temperatures from that present on a static target surface. And this increase in surface temperatures, induced by surface oscillation, is higher for target-surface oscillation at 50 Hz. As the surface temperatures when heat flux is applied for jet impingement on an oscillating target surface at the two frequencies, in Fig. 5.35, are similar, the difference between the corresponding temperatures in Fig. 5.35 and 5.36 is lower for target-surface oscillation at 50 Hz than at 20 Hz. The effect of target-surface oscillation on surface temperatures was not examined in previous studies by Wen (2005) and Ichimiya and Yoshida (2009) on jet impingement on oscillating target surfaces.

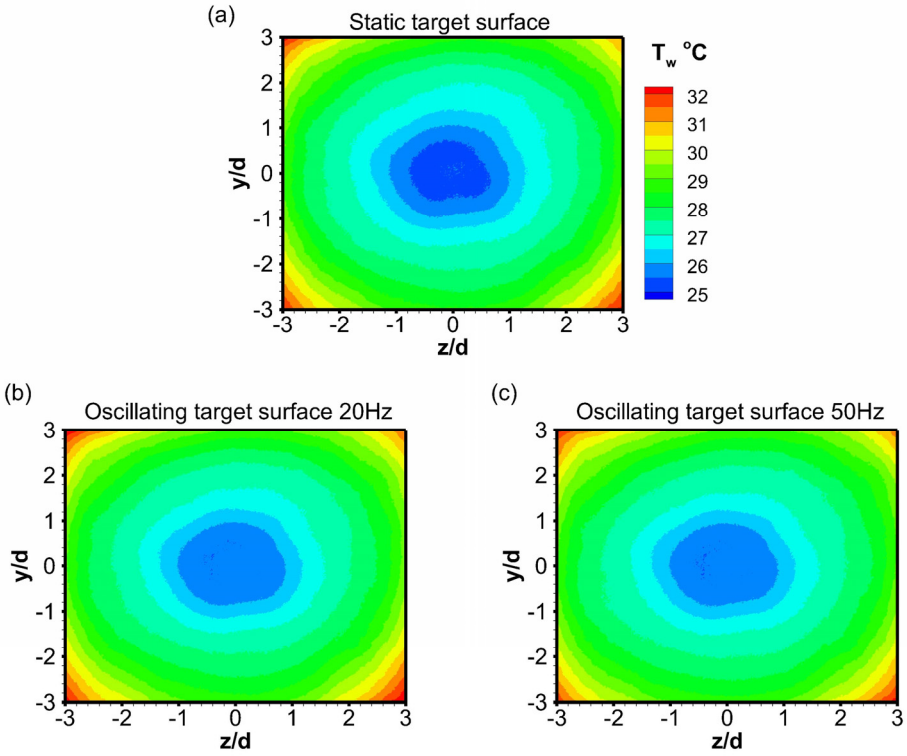

Fig. 5.35 Steady-state time-averaged temperature maps for jet impingement on target surfaces with input heat flux: (a) static target surface; (b) and (c) oscillating target surface at 20 Hz and 50 Hz respectively

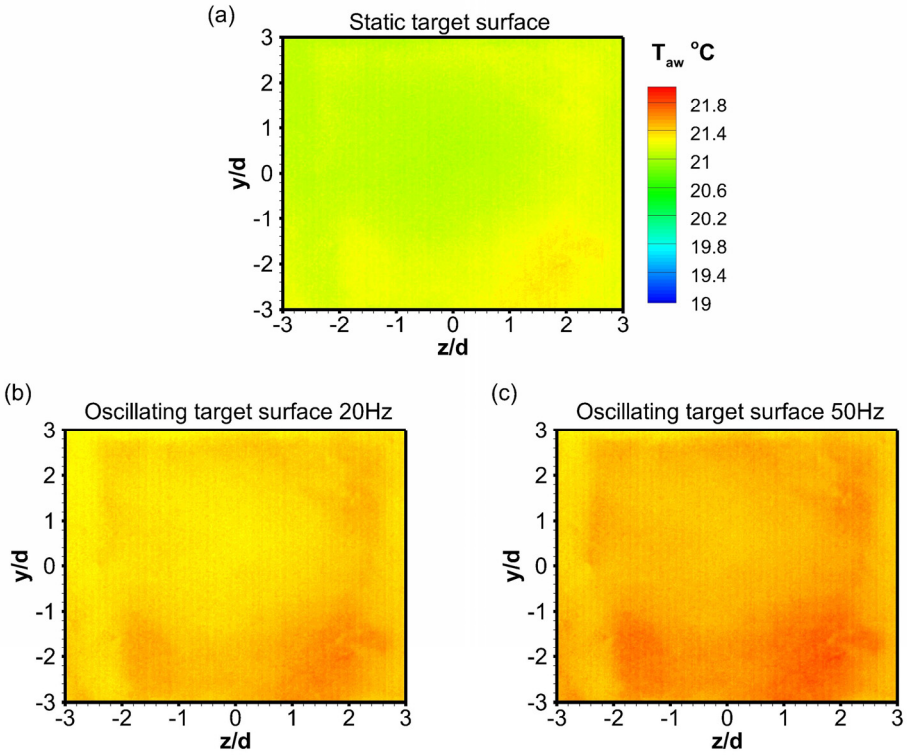

Fig. 5.36 Steady-state time-averaged temperature maps for jet impingement on target surfaces without input heat flux: (a) static target surface; (b) and (c) oscillating target surface at 20 Hz and 50 Hz respectively

Based on the above finding it is expected that *Nu* values for jet impingement on a target surface oscillating at 50 Hz are higher. The *Nu* contours for jet impingement on static and oscillating target surfaces presented in Fig. 5.37 show higher values for target-surface oscillation at 20 Hz and 50 Hz than for the static target surface, with the highest occurring for a target-surface oscillation at 50 Hz in Fig. 5.37(c). It is observed that these higher *Nu* values for the two oscillating target surfaces occur mainly in the impingement region.

Considering the temperature maps shown in Figs. 5.35 and 5.36, and the *Nu* maps in Fig. 5.37, we find that although target-surface oscillation induces higher surface temperatures, its effect on the impinging-jet flow characteristics produce higher values of *Nu*. Since the enhancement of convective heat transfer due to target-surface oscillation is observed to be significant only in the impingement region, as seen in Fig. 5.37, the underlying reason is the interaction between the axial velocity of the jet and the target surface velocity during oscillation.

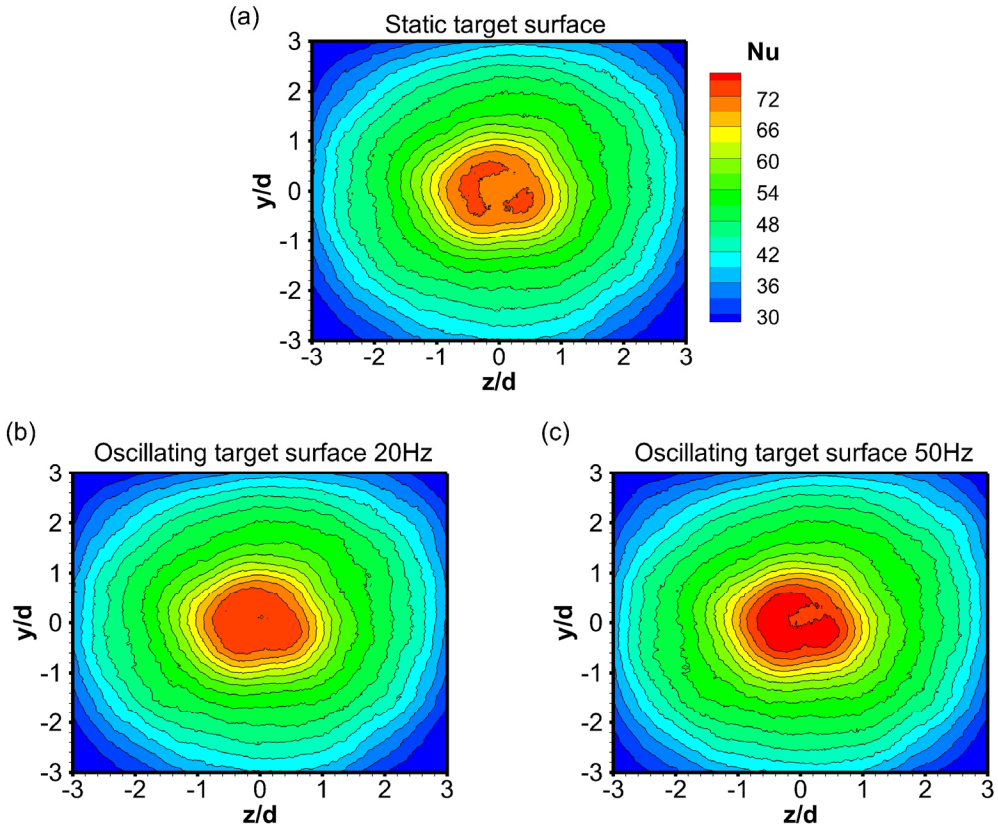

Fig. 5.37 Nusselt number *Nu* contours for jet impingement on heated target surfaces: (a) static target surface; (b) and (c) oscillating target surface at 20 Hz and 50 Hz respectively

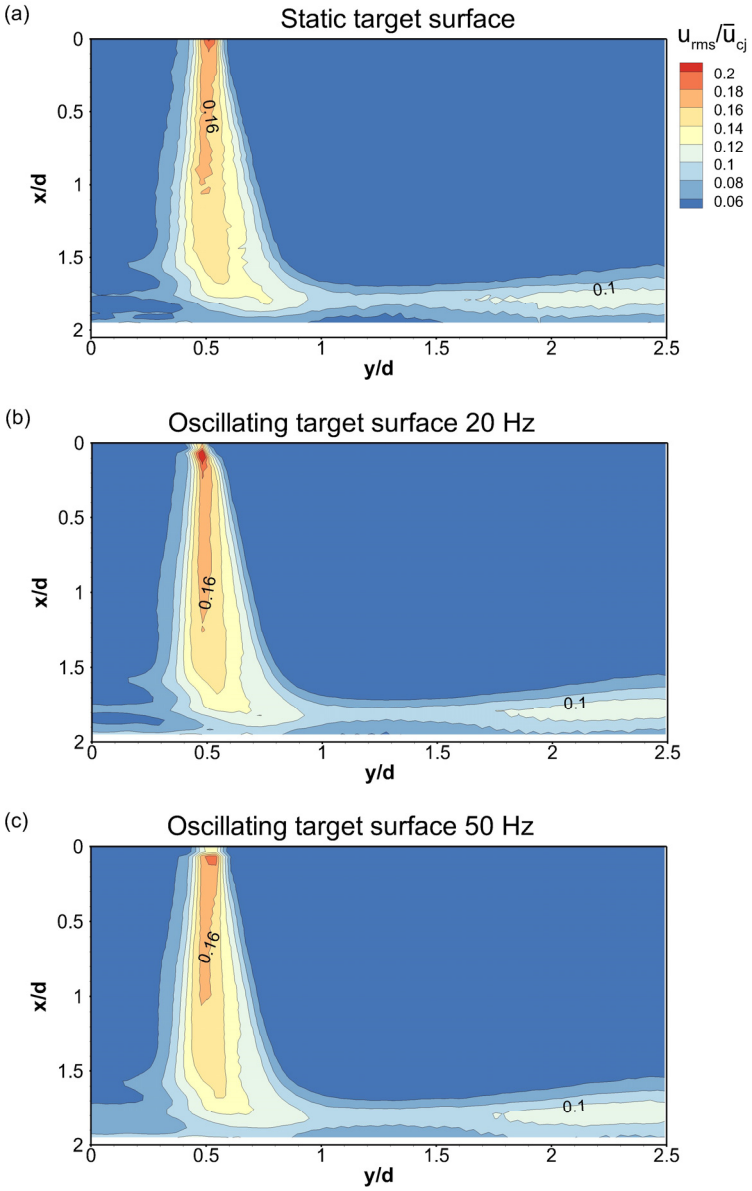

Fig. 5.38 RMS axial velocity fluctuations for jet impingement on heated target surfaces: (a) static target surface; (b) and (c) Phase-averaged RMS axial velocity fluctuations for jet impingement on oscillating target surfaces at 20 Hz and 50 Hz respectively

O'Donovan and Murray (2007) concluded that jet impingement heat transfer is dependent primarily on the magnitude of rms axial velocity fluctuations rather than that on the rms radial velocity fluctuations. In the present study, the target-surface oscillation occurs in a direction parallel to the jet axis, which means that the target-surface oscillation directly affects the axial velocities in the jet, and hence the rms axial velocity fluctuations.

In order to understand the relation between the effect of target-surface oscillation on Nusselt number and rms axial velocity fluctuation, the phase-averaged rms axial velocity fluctuations for jet impingement on a heated target surface oscillating at 20 Hz and 50 Hz are presented in Fig. 5.38(b) and 5.38(c), with the rms axial velocity fluctuations jet impingement on a heated static target surface shown in Fig. 5.38(a) for comparison. The phase-averaged quantities have been obtained by averaging the rms axial velocity fluctuations over the 6 phases that approximately cover one cycle of oscillation of the target surface, as shown in Fig. 5.28. The near-wall rms axial velocity fluctuations in the impingement region $y/d < 1$ are found to be higher for target-surface oscillation at 50 Hz in Fig. 5.38(c), compared to those for target-surface oscillation at 20 Hz in Fig. 5.38(b), and for the static target surface in Fig. 5.38(a). These higher rms axial velocity fluctuations are responsible for the increase of jet impingement heat transfer due to target-surface oscillation.

The variations of local and azimuthal averaged *Nu* with the radial coordinate, for jet impingement on static and oscillating target surfaces, are shown in Fig. 5.39. The azimuthal average is obtained by averaging all *Nu* values at a given radius around the point $y/d = 0$. These variations show that the highest *Nu* values occur for target-surface oscillation at 50 Hz, and the increase from the *Nu* values of target-surface oscillation at 20 Hz and the static target surface is higher within the region $y/d \leq 0.5$. When compared with the static target surface, the stagnation point *Nu* for target-surface oscillation at 20 Hz is 2.20% greater, while that for target-surface oscillation at 50 Hz is 5.68% greater. These values show a modest increase in jet impingement heat transfer due to target-surface oscillation, because (i) the oscillatory motion of target surface induces higher surface temperatures, as shown in Fig. 5.36, and (ii) the increase in the rms axial velocity fluctuations due to target-surface oscillation, from that for the static target surface as shown in Fig. 5.38 is not high enough to substantially increase the heat transfer rates in the impingement region.

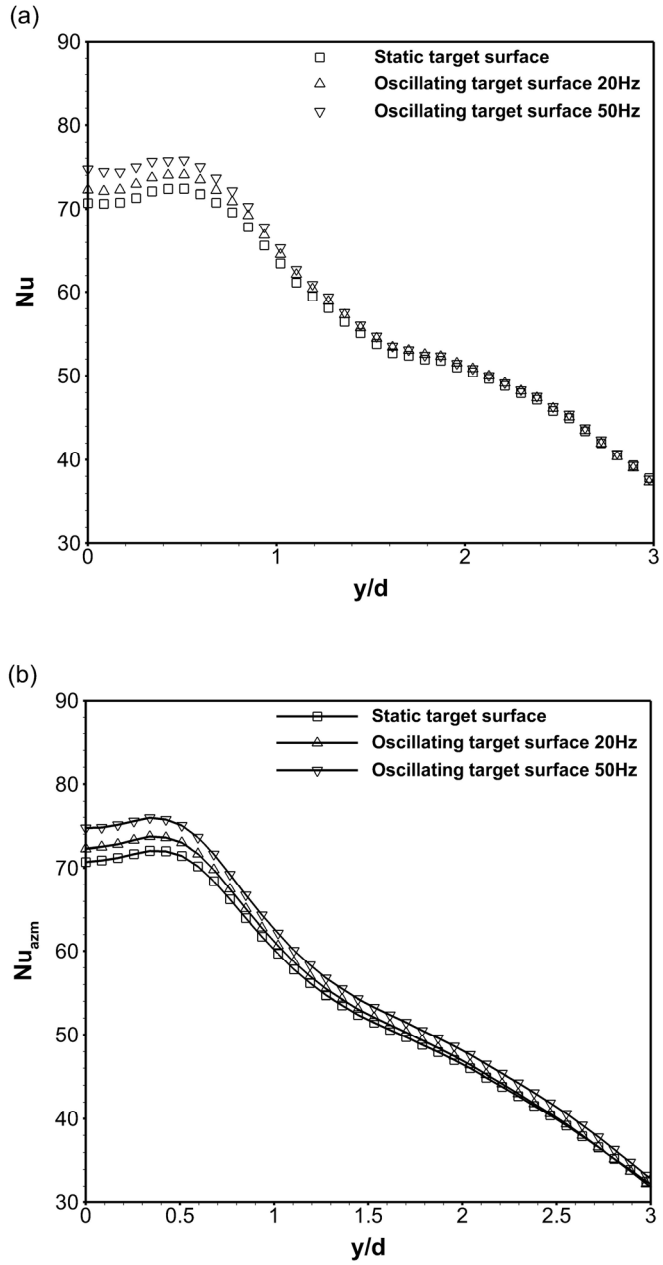

Fig. 5.39 Nusselt number *Nu* variation along the radial coordinate for jet impingement on heated static and oscillating target surfaces (a) Local *Nu* (b) Azimuthal average Nu_{azm}

In Fig. 5.39(a), the *Nu* values in the region $y/d > 2$ are similar for both static target surface and oscillating target surfaces, indicating that the effect of target-surface oscillation on heat transfer rate decreases with increasing radial distance. This occurs because the effect of target-surface oscillation on the near-wall mean radial velocities decreases with increasing radial distance as shown in Figs. 5.11(b) and 5.12(b). In addition to this, the phase-averaged Reynolds stress maps for jet impingement on a heated oscillating target surface, in Fig. 5.32, show that there is no increase in

turbulence production in the wall-jet shear layer, from that present for the static target surface in Fig. 5.30(a), as a result of target-surface oscillation.

The *Nu* variations in Fig. 5.39(a) show that the primary and secondary *Nu* peaks that exist for jet impingement on a heated static target surface also occur for jet impingement on heated oscillating target surfaces, and the radial locations of these peaks are also unaffected by target-surface oscillation. The occurrence of the secondary peak in local *Nu* at around $y/d = 1.8$ can be correlated with the local acceleration of the wall-jet and the local increase in the wall-shear stress in the neighbouring region of that location, as shown in Figs. 5.16 and 5.17. For $y/d > 1$, the azimuthal-averaged Nusselt number Nu_{azm} variation in Fig. 5.39(b) shows a small deviation from that of local Nu in Fig. 5.39(a) because of minor departures from a perfectly axisymmetric jet impingement flow. These occur due to slight misalignments of the jet nozzle exit and the target surface.

Although target-surface oscillation is found to improve jet impingement heat transfer compared to that from a static target surface, it comes at a cost of producing wall oscillation that adversely increases the temperature of the target surface. For target-surface oscillation at 50 Hz in this case, the Wormersely number is 25.56, which indicates a high level of transient inertial forces acting on the impinging-jet flow due to the target-surface motion. While these effects of target-surface oscillation on the flow produce higher turbulence intensities, their role in increasing the heat transfer rates is undermined by the negative effect of the higher surface temperatures generated by target-surface oscillation.

5.7 Summary

The fluid-dynamics characteristics for jet impingement on unheated and heated, static and oscillating target surfaces were presented in this chapter. It was found that the effect of surface heating gives rise to higher mean velocities and turbulence intensities in the impinging-jet flow when compared to an unheated target surface. The fluid dynamics and heat transfer results for jet impingement on heated static and oscillating target surfaces show that target-surface oscillation increases the heat transfer rate compared to that for a static target surface. This increase is due to higher rms axial velocity fluctuations as a result of the effect of target-surface oscillation on the impinging-jet flow. However, the enhancement of heat transfer rate

for jet impingement on an oscillating target surface is small, because the oscillatory motion of the target surface induces higher surface temperatures than those found for a static target surface.

Chapter 6

Conclusions and Directions for Future Work

6.1 Conclusions

An experimental study of turbulent jet impingement on an oscillating target surface has been conducted. This was done in two parts using two different experimental systems. In the first part, jet impingement on unheated static and oscillating target surfaces was studied, while in the second, jet impingement on heated static and oscillating target surfaces was studied. The main contribution of the entire study has been the investigation and analysis of the fluid dynamics characteristics of jet impingement for various phases of oscillation of a target surface, and its relevance to convective heat transfer.

The main conclusions of this work are presented below, in which the effects of target-surface oscillation on important flow and heat transfer quantities in the two parts of this study are presented first. These effects are described in comparison with corresponding jet impingement on a static target surface, and are presented for target-surface motion away from the jet exit and towards the jet exit, for the two target-surface oscillation frequencies in the two experimental systems. The comparison is done in a tabular form using symbols which signify a change of a given quantity due to target-surface oscillation, from that found for the corresponding static target surface.

The symbol ↑ means an increase from that for the static target surface, while the symbol ↓ means a decrease from that for the static target surface. The number of symbols of a given kind signify the magnitude of change. The symbol ↔ means no significant change in magnitude from that for the static target surface. For turbulence statistical quantities and Nusselt number, the flow region which is affected due to target-surface oscillation, is also mentioned. Table 6.1 lists the effects of target-surface oscillation on flow quantities in jet impingement on an unheated oscillating target surface in Part I of this study, and Table 6.2 lists the effects of target-surface oscillation on flow and heat transfer quantities in jet impingement on a heated oscillating target surface in Part II of this study.

Table 6.1 Effects of target-surface oscillation on flow quantities in jet impingement on an unheated oscillating target surface in Part I

	Target-surface oscillation at 20 Hz		**Target-surface oscillation at 80 Hz**	
Quantity	**Target-surface motion away from jet exit**	**Target-surface motion towards jet exit**	**Target-surface motion away from jet exit**	**Target-surface motion towards jet exit**
Mean axial velocities	↑	↓	↑↑	↓↓
Mean radial velocities	↓	↑	↓↓	↑↑
Wall-shear stress	↑	↑	↑↑	↑
RMS axial velocity fluctuations	↔	↔	↑↑ (wall-jet shear layer)	↑↑ (free-jet shear layer)
RMS radial velocity fluctuations	↑	↑	↑↑	↑↑
Reynolds stress	↔	↔	↑ (wall-jet shear layer)	↑ (free-jet shear layer)
Turbulence kinetic energy	↔	↔	↑↑ (wall-jet shear layer)	↑↑ (free-jet shear layer)

Table 6.2 Effects of target-surface oscillation on flow and heat transfer quantities in jet impingement on a heated oscillating target surface in Part II

	Target-surface oscillation at 20 Hz		**Target-surface oscillation at 50 Hz**	
Quantity	**Target-surface motion away from jet exit**	**Target-surface motion towards jet exit**	**Target-surface motion away from jet exit**	**Target-surface motion towards jet exit**
Mean axial velocities	↑	↓	↑↑	↓↓
Mean radial velocities	↓	↑	↓↓	↑↑
Wall-shear stress	↔	↑	↓	↑
RMS axial velocity fluctuations	↔	↔	↑ (wall-jet shear layer)	↑ (free-jet shear layer)
RMS radial velocity fluctuations	↑↑	↑↑	↑↑↑	↑↑↑
Reynolds stress	↔	↔	↑ (wall-jet shear layer)	↔
Turbulence kinetic energy	↑ (wall-jet shear layer)	↑ (wall-jet shear layer)	↑ (wall-jet shear layer)	↑ (free-jet shear layer)
Surface temperature	↑		↑↑	
Nusselt number	↑ (impingement region)		↑↑ (impingement region)	

The common conclusions drawn from the two parts of this study are presented below, followed by conclusions specific to Part II of this study.

6.1.1 Conclusions from Part I and II

- The effect of target-surface oscillation on the impinging-jet flow is primarily due to the interaction of target surface velocity with the mean velocities in different flow regions. The level of this effect depends on the magnitudes of the mean velocities, the spatial location from the wall, and the frequency of target-surface oscillation. The effect is higher at higher target surface velocities, which occur during 80 Hz and 50 Hz frequencies of oscillation at a given displacement amplitude.
- The mean axial velocities for jet impingement on an oscillating target surface increase from that for jet impingement on a static target surface, during target-surface motion away from the jet exit and decrease during the opposite motion. The mean radial velocities within the wall-jet have opposite variations.
- The time period of the variation of mean axial velocities with target surface phases increases as the axial distance from the target surface increases. There is a phase difference in the variations of mean axial velocities for different target-surface oscillation frequencies.
- The variations of the near-wall mean radial velocities with target surface phases have shorter time periods than those away from the wall. The effect of target-surface oscillation on the near-wall mean radial velocities decreases with increasing radial distance from the jet centreline.
- Entrainment of the ambient fluid into the jet increases from that for jet impingement on a static target surface during target-surface motion away from the jet exit. The ambient fluid undergoes deceleration during opposite target-surface motion. These are prominent only at 80 Hz and 50 Hz frequencies of target-surface oscillation.
- At target-surface oscillation frequencies of 80 Hz and 50 Hz, target-surface motion away from the jet exit lowers the mean axial strain rates in the impingement region, while the opposite motion increases the mean axial strain rates in the wall-jet region, from that for the static target surface. The mean radial strain rates are largely unaffected by target-surface oscillation.

- There is an increase in the mean shear-strain rates in the free-jet shear layer from that for the static target surface, during target-surface motion towards the jet exit at 80 Hz and 50 Hz frequencies of target-surface oscillation.
- The large-scale structures in the impinging-jet flow are not significantly altered by target-surface oscillation. However, it is observed that for 80 Hz and 50 Hz frequencies of target-surface oscillation, the target-surface motion towards the jet exit reduces the strength of the secondary vortex in the wall-jet region.
- Target-surface oscillation at 80 Hz and 50 Hz produce higher turbulence intensities than those for jet impingement on a static target surface.

6.1.2 Conclusions from Part II

- The effect of target-surface heating induces buoyancy in the ambient fluid, which lowers entrainment of the ambient fluid into the jet when compared to that for an unheated target surface. This increases the mean velocities and turbulence intensities in jet impingement on a heated target surface from those for jet impingement on an unheated target surface, and it occurs for both static and oscillating target surfaces.
- At low radial distances from the jet-centerline, the boundary-layer thickness on an oscillating target surface reduces compared to that on a static target surface. This is observed on both unheated and heated oscillating target surfaces.
- Turbulence production in the free-jet shear layer is not affected by target-surface oscillation.
- Target-surface oscillation induces higher surface temperatures, compared to those present on a static target surface, due to the frictional interaction between the fluid and the target-surface motion.
- There is an enhancement of steady-state jet impingement convective heat transfer coefficients due to target-surface oscillation. The primary cause for this is the interaction between the axial velocity of the jet and the target surface velocity, which gives rise to higher rms axial velocity fluctuations compared to that for jet impingement on a static target surface. This enhancement is observed to be higher in the impingement region than in the wall-jet region and is greater for a target surface oscillating at a frequency of 50 Hz.
- Although heat transfer rate increases in the presence of target-surface oscillation, the increment is small and it comes at the power cost of producing

high wall oscillation which in turn increases the surface temperature. This indicates that an oscillating target surface is not an efficient mechanism for jet impingement surface cooling, for the range of parameters considered in this study.

6.2 Future work

The results presented here provide a framework for future studies in which a parametric investigation of jet impingement on an oscillating target surface can be carried out. The effect of target-surface oscillation on the flow and heat transfer characteristics of jet impingement can be studied by varying parameters such as, jet Reynolds and Strouhal numbers, nozzle-to-surface separation distance, and target-surface oscillation frequency and amplitude.

The fluid dynamics and heat transfer of pulsating jets impinging on a static target surface have been the focus of several studies such as Azevedo et al. (1994), Sheriff and Zumbrunnen (1994), Hofmann et al. (2007), Janetzke et al. (2008), Xu et al. (2010) and Persoons et al. (2013). The interaction of a pulsating impinging jet with an oscillating target surface presents an unexplored yet interesting flow configuration to study unsteady jet impingement. The fluid dynamics and heat transfer characteristics of such a system can then be examined in the presence of in-phase or out-of-phase frequencies of jet pulsation and target-surface oscillation. This would determine if enhancement of jet impingement heat transfer rate can be produced by such a system.

The mechanisms of producing jet pulsation and target-surface oscillation involve additional energy costs to an unsteady jet impingement system, with the latter generating adverse effects of increasing surface temperatures as shown in the present study. Future studies can explore the possibilities of improving the efficiency of these systems, by using passive methods such as, introduction of jet swirl using angular nozzle inserts, modification of the jet nozzle design and geometry, and/or, modification of the surface geometry and characteristics by altering the shape and roughness of the target surface.

Appendix

I Dimensional analysis

The important variables which control the flow configuration in jet impingement on an oscillating target surface are the: jet-nozzle exit diameter d, jet bulk-flow speed U, fluid density ρ, fluid viscosity μ, mean nozzle-to-surface separation distance h, target-surface oscillation frequency f_s, and displacement amplitude A_s. These variables and their dimensions are listed in the table below.

Table 1. Dimensional variables for jet impingement on an oscillating target surface

d	U	ρ	μ	h	f_s	A_s
L	LT^{-1}	ML^{-3}	$ML^{-1}T^{-1}$	L	T^{-1}	L

In order to reduce the number of pertinent dimensional variables into dimensionless groups, a dimensional analysis of jet impingement on an oscillating target surface has been performed using *Buckingham Pi Theorem*. A description of this analysis is presented in here which includes the methodology and its application to derive the dimensionless groups based on a given combination of variables. The derivation of dimensionless groups formed from other combinations of variables are not presented for brevity, although expressions of these dimensionless groups have been mentioned.

Methodology

The procedure for applying the *Buckingham Pi Theorem* for dimensional analysis is as follows.

1. Identify the number of dimensional variables n which define the system. In this case $n = 7$.
2. List the dimensions of each variable, as done in the table above.
3. Find the number of dimensions j describing these variables. The dimensions for the 7 variables in this system are described by MLT, hence $j = 3$.
4. Select j variables that do not form a dimensionless group. These are called *repeating variables*. As $j = 3$, we look for 3 variables which do not form a dimensionless group.

5. Add one additional variable to the *j* repeating variables to form a power product. Then algebraically find the exponents that make the product dimensionless.
6. Do this sequentially by adding one new variable each time, to determine the corresponding dimensionless group. The number of dimensionless groups or pi products (Πs) that can be formed is given by $k = n - j$, which in this case equals 4.

Derivation of dimensionless groups

As a first choice, select d, U, ρ as the repeating variables. These do not form a Π together since only ρ has the dimension of M and only U has the dimension of T. In order to determine the first pi product we add μ to the repeating variables to form a power product as given by

$$\Pi_1 = d^a U^b \rho^c \mu^{-1}$$

The exponent of μ can be chosen arbitrarily, however in this case we select it to appear to the first power in the denominator.

The exponents a, b, c in the pi product are then found by equating the exponents of each dimension to zero and solving the equations as shown below.

$$\Pi_1 = d^a U^b \rho^c \mu^{-1} = (L)^a (LT^{-1})^b (ML^{-3})^c (ML^{-1}T^{-1})^{-1} = M^0 L^0 T^0$$

Equating the exponents gives the following equations

L: $a + b - 3c + 1 = 0$

M: $c - 1 = 0$

T: $-b + 1 = 0$

These can be solved explicitly for

$a = 1, \quad b = 1, \quad c = 1$

Therefore, the first pi product based on the repeating variables d, U, ρ is

$$\Pi_1 = \frac{\rho U d}{\mu}$$

which is the Reynolds number of the jet based on the jet-nozzle exit diameter and the jet bulk-flow speed.

The second pi product can be obtained by adding h to the repeating variables in the form of

$$\Pi_2 = d^a U^b \rho^c h$$

and solving the equations of exponents of the dimensions to get

$$\Pi_2 = \frac{h}{d}$$

Adding f_s to the repeating variables in the form of

$$\Pi_3 = d^a U^b \rho^c f_s{}^{-1}$$

gives the third pi product as,

$$\Pi_3 = \frac{U}{df}$$

while the fourth pi product is given by

$$\Pi_4 = \frac{A_s}{d}$$

which is obtained upon adding A_s to the repeating variables.

If a different combination of the repeating variables is chosen, for example the selection of d, ρ, and μ, then the dimensionless groups formed by adding the remaining variables each time are given by

$$\Pi_1 = \frac{\rho U d}{\mu} \quad \Pi_2 = \frac{h}{d} \quad \Pi_3 = \frac{\rho f_s d^2}{\mu} \quad \Pi_4 = \frac{A_s}{d}$$

Another set of repeating variables formed by the combination of u, ρ, and μ, yields the following dimensionless groups.

$$\Pi_1 = \frac{\rho U d}{\mu} \quad \Pi_2 = \frac{\rho U h}{\mu} \quad \Pi_3 = \frac{\rho U^2}{\mu f_s} \quad \Pi_4 = \frac{\rho U A_s}{\mu}$$

The combination of ρ, μ, and h as the repeating variables returns the dimensionless groups

$$\Pi_1 = \frac{h}{d} \quad \Pi_2 = \frac{\rho U h}{\mu} \quad \Pi_3 = \frac{\rho f_s h^2}{\mu} \quad \Pi_4 = \frac{A_s}{h}$$

whereas the combination of ρ, μ, and f_s gives

$$\Pi_1 = \frac{\rho f_s d^2}{\mu} \quad \Pi_2 = \frac{\rho U^2}{\mu f_s} \quad \Pi_3 = \frac{\rho f h^2}{\mu} \quad \Pi_4 = \frac{\rho f {A_s}^2}{\mu}$$

In all there are 33 different combinations of three repeating variables, including those mentioned above, that could be formed from the set of 7 dimensional variables. The different dimensionless groups formed from all these combinations of repeating variables are given in the table below.

Table 2. Dimensionless groups for jet impingement on an oscillating target surface

$\Pi_1 = \frac{h}{d}$	$\Pi_2 = \frac{A_s}{d}$	$\Pi_3 = \frac{A_s}{h}$
$\Pi_4 = \frac{U}{d f_s}$	$\Pi_5 = \frac{U}{h f_s}$	$\Pi_6 = \frac{U}{A_s f_s}$
$\Pi_7 = \frac{\rho U d}{\mu}$	$\Pi_8 = \frac{\rho U h}{\mu}$	$\Pi_9 = \frac{\rho U A_s}{\mu}$
$\Pi_{10} = \frac{\rho f_s d^2}{\mu}$	$\Pi_{11} = \frac{\rho f_s h^2}{\mu}$	$\Pi_{12} = \frac{\rho f_s {A_s}^2}{\mu}$
$\Pi_{13} = \frac{U h}{f_s d^2}$	$\Pi_{14} = \frac{U d}{f_s {A_s}^2}$	$\Pi_{15} = \frac{U A_s}{f_s h^2}$
$\Pi_{16} = \frac{\rho U^2}{\mu f_s}$		

The groups Π_1 to Π_3 are dimensionless groups based only on the length scales appearing in the system, wherein Π_1 is the nozzle-to-surface separation distance with respect to the jet-nozzle exit diameter, and, Π_2 and Π_3 are the displacement amplitude of target-surface oscillation relative to the jet-nozzle exit diameter and the nozzle-to-surface separation distance respectively.

The groups Π_4 to Π_6 represent dimensionless groups based only on the velocity scales in the system. However, Π_4 actually depicts a ratio of the target-surface oscillation time-period to the integral flow time-scale if redefined as

$$\Pi_4 = \frac{1/f_s}{d/U}$$

The group Π_6 is defined as the reciprocal of the Strouhal number based on the jet bulk-flow speed and the target-surface oscillation parameters. If the term $A_s f_s$ can be considered to represent the target-surface oscillation speed, then Π_6 can be interpreted as a ratio of the jet bulk-flow speed to the target-surface oscillation speed.

The dimensionless group Π_7 is the conventional definition of the jet Reynolds number based on the jet-nozzle exit diameter, whereas groups Π_8 and Π_9 are alternate definitions of jet Reynolds numbers based on different length scales h and A_s. The groups Π_{10} to Π_{12} can be treated as Reynolds numbers based on target-surface oscillation frequency and a given length scale, wherein Π_{12} represents a Reynolds number based on target-surface oscillation speed and displacement amplitude if re-written as

$$\Pi_{12} = \frac{\rho(A_s f_s)A_s}{\mu}$$

However, a more useful dimensionless group can be obtained using groups Π_6 and Π_7 by taking their ratio to give

$$Re_s = \frac{\rho(A_s f_s)d}{\mu}$$

which represents a Reynolds number based on the jet-nozzle exit diameter and the target-surface oscillation speed.

The pi products Π_{13} to Π_{15} represent dimensionless groups based on the jet bulk-flow speed and target-surface oscillation frequency along with various length scales present in the system. The important dimensionless group among these appears to be Π_{14} as it includes the jet bulk-flow speed and jet-nozzle exit diameter, as well as the target-surface oscillation parameters. The final group Π_{16} represents a modified Reynolds number which is based on the jet bulk-flow speed and the target-surface oscillation frequency.

The dimensionless groups mentioned in Table 2 can be used to define important characteristics of the system, for example, Π_4 characterises the time scales present in the system, while Π_6 characterises the velocity scales in the system. These

groups can also be combined in several ways to form alternate non-dimensional parameters that have certain physical significance in analysis of the system, for example Re_s, which is obtained upon dividing Π_7 by Π_6 as shown above, represents a modified Reynolds number based on the jet-nozzle exit diameter and the target-surface oscillation speed.

II PIV image processing and analysis

The image processing of the PIV images, performed before cross-correlation analysis was carried out to obtain velocity vectors, is presented below. A sample PIV image is shown in Fig. A1, which is the first frame of a double-frame single-exposure raw PIV image of jet impingement on a heated static target surface. This image shows the complete field-of-view which is $5d \times 3d$ in size. The jet nozzle is seen at the bottom left and the target surface appears as a bright vertical line across the width of the image. The ambient fluid region is the area above the top edge of the nozzle where the seeded particle density is lower than that of the jet flow. The processing involved masking the raw PIV images to remove unwanted regions upstream of the jet nozzle exit and behind the target surface, including the illuminated region along the surface. The masked PIV image is shown in Fig. A2.

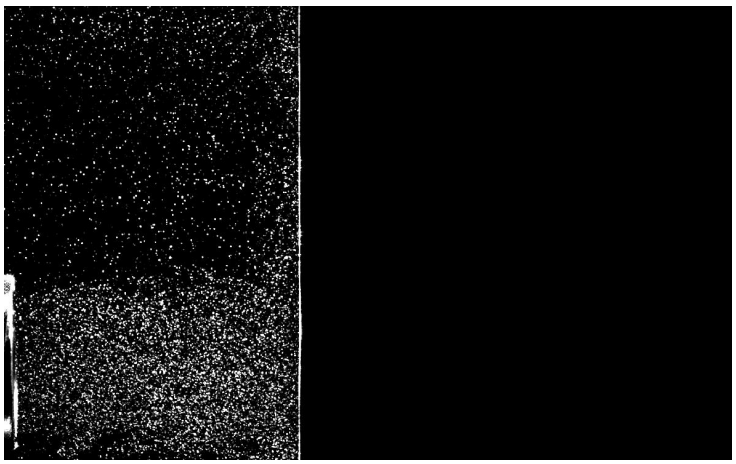

Fig. A1 Sample raw PIV image of jet impingement on a heated static target surface

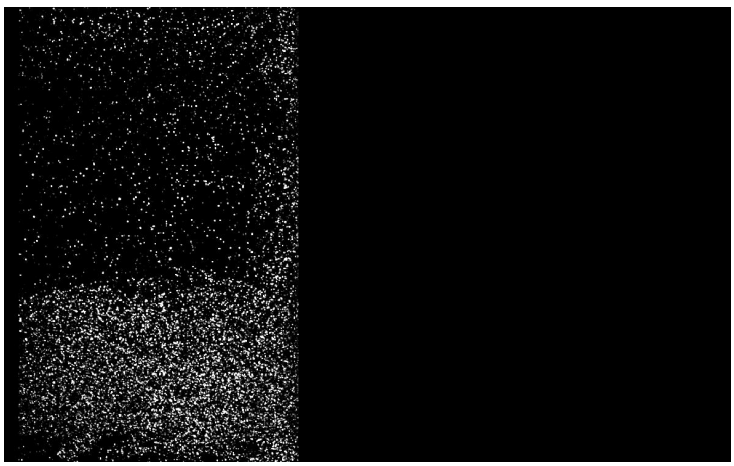

Fig. A2 Masked image of the sample raw PIV image shown in Fig. A1

Cross-correlation analysis was then performed on the masked PIV images in the region where the seeded particles were present. The vector map obtained from cross-correlation analysis of the masked PIV image of Fig. A2 is shown in Fig. A3. The vectors closest to the wall (target surface) are obtained from interrogation areas that have their centres located at the wall, i.e. at the interface between the seeded particles and the dark region in Fig. A2.

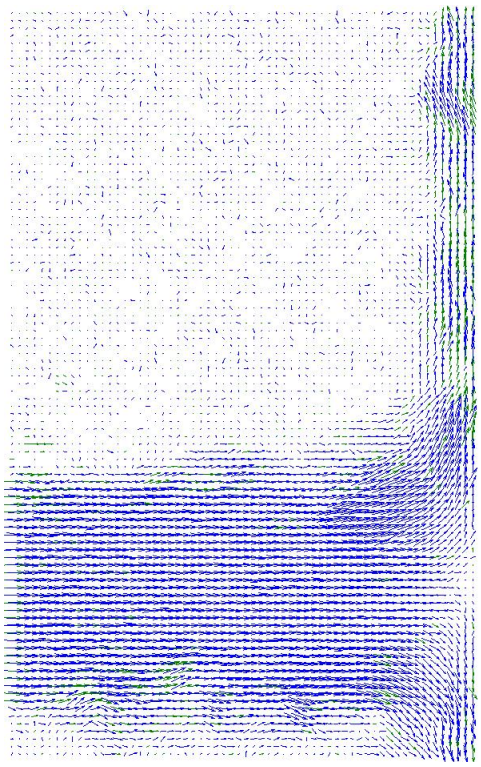

Fig. A3 Vector map obtained after cross-correlation analysis of the masked PIV image shown in Fig. A2

III Uncertainty analysis in PIV measurements

The details of estimation of uncertainties in the PIV measurements are presented in this section. These include the presentation of sample PIV images, pixel displacement histograms, and the equations used to calculate uncertainties in the measured and derived flow quantities. A sensitivity analysis on the sample-size used for proper orthogonal decomposition has also been conducted.

(a)

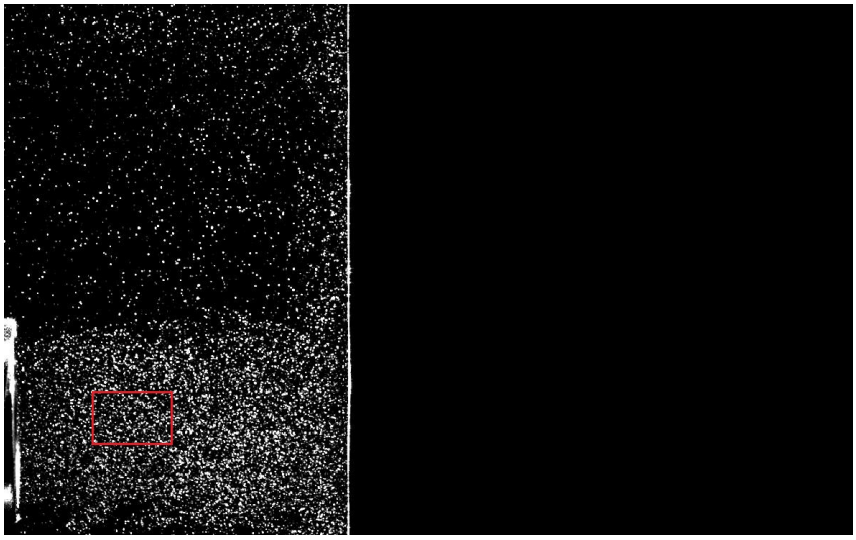

(b)

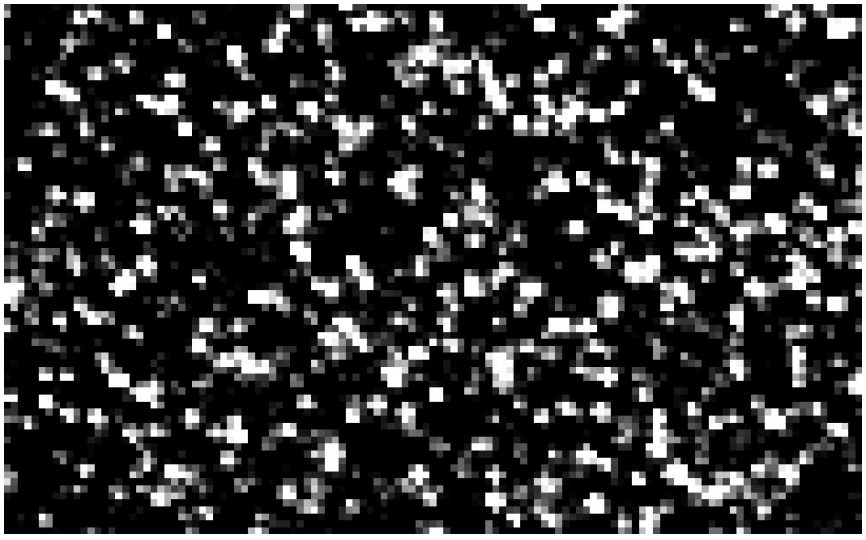

Fig. A4 Sample PIV images (a) Jet impingement on a heated static target surface (b) Enlarged image of the rectangular zone marked in red colour in (a)

The sample PIV images are shown in Fig. A4. The full field-of-view of jet impingement on a heated static target surface is shown in Fig. A4(a) with a red-coloured rectangular zone marked in the free-jet region. An enlarged image of this rectangular zone is shown in Fig. A4(b). Each square in Fig. A4(b) represents a pixel and it can be seen that most of the particle images in the flow (marked by bright and grey pixels) are atleast 2 pixels in size. This demonstrates that the Nyquist criterion for sampling was satisfied when the images were acquired.

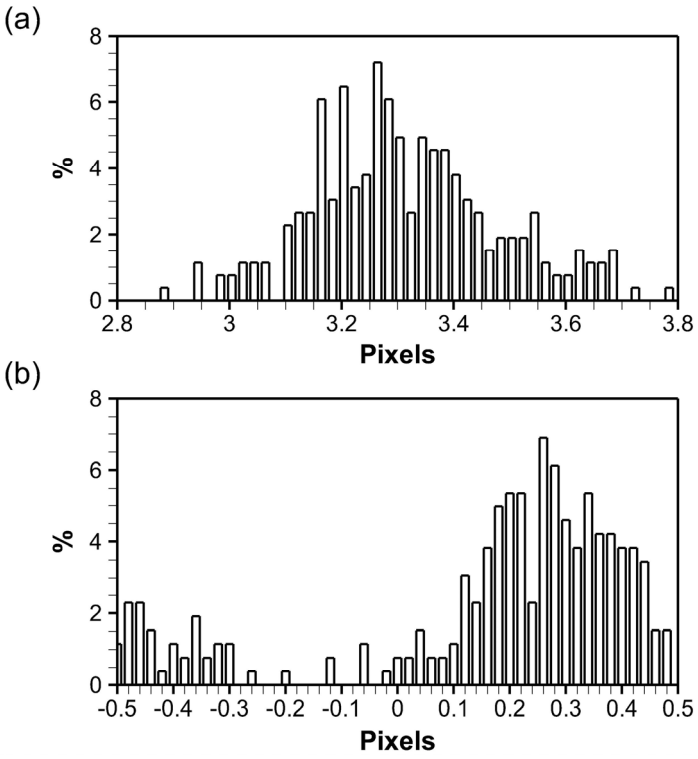

Fig. A5 Pixel displacement histograms in the flow region shown in Fig. A4(b). (a) Pixel displacement over the interrogation windows (b) Subpixel displacement

The histograms of the pixel displacement in the axial direction in the flow region shown in Fig. A4(b) are presented in Fig. A5. Figure A5(a) shows the pixel displacement over the interrogation window (16 x 16 pixels), while Fig. A5(b) shows the subpixel displacement. It is observed in Fig. A5(a) that the pixel displacement over the interrogation window is less than 4 pixels, hence ensuring that the “one-quarter rule” was satisfied during image recording.

The presence of histogram peaks near integer pixel values or a zero subpixel value indicate pixel locking in the data. However, it is observed in Fig. A5(a) that most

pixel displacements are within 3.1 and 3.6 pixels with no bias being observed towards integer pixel value of 3. The subpixel displacement histogram in Fig. A5(b) also shows no bias towards zero subpixel. These observations, as well as those from Fig. A4, establish that the PIV image recordings were free from any pixel locking effects, thereby justifying that the bias error could be neglected in the estimation of uncertainties in the measured velocities.

The details of the estimation of statistical uncertainties in the determination of respective flow quantities are provided below. These include the equations and values used for uncertainty estimation. The uncertainty equations have been derived based on the methods outlined by Benedict and Gould (1996) and Adrian and Westerweel (2011). The values used for uncertainty calculations have been taken from the data for jet impingement on an unheated static target surface. In all the following equations, the variable *N* represents the number of samples used for statistical determination and is equal to 1000.

The measured velocity $u_i(\boldsymbol{x}, t)$ is decomposed as

$$u_i(\boldsymbol{x}, t) = \overline{u_i}(\boldsymbol{x}) + u_i'(\boldsymbol{x}, t) \tag{1}$$

where $u_1 = u$, $u_2 = v$ and $\boldsymbol{x} = (x, y)$.

$\overline{u_i}$ is the mean (ensemble-average) velocity given by $\overline{u_i} = (\frac{1}{N}) \sum u_i$, and u_i' is the fluctuation of the velocity. The root-mean-square (rms) of the velocity is the square root of the variance of the velocity given by

$$u_{i_{rms}} = \sqrt{\overline{u_i'^2}} = \sqrt{(\frac{1}{N-1}) \sum (u_i - \overline{u_i})^2} \tag{2}$$

while the Reynolds stress is the covariance of the velocity components (u, v) defined as

$$\overline{u'v'} = (\frac{1}{N-1}) \sum (u - \overline{u})(v - \overline{v}) \tag{3}$$

The percentage relative uncertainty in mean velocity components is given by

$$\varepsilon_{\overline{u_i}} = \pm \frac{1.96\sigma_{u_i}}{\sqrt{N}} \left(\frac{100}{\overline{u_i}}\right) \tag{4}$$

where σ_{u_i} is the standard deviation (rms) of the velocity component. The uncertainty in the mean axial velocity $\overline{u}$ is calculated at x/d = 0.03, y/d = 0 in the free-jet region where $\sigma_u = u_{rms}$ = 0.253 m/s and $\overline{u}$ = 6.792 m/s, while that in the mean radial velocity $\overline{v}$ is calculated at x/d = 2.07, y/d = 0.8 in the wall-jet region where $\sigma_v = v_{rms}$ = 1.001 m/s and $\overline{v}$ = 5.153 m/s.

The percentage relative uncertainty in rms velocity components is given by

$$\varepsilon_{u_{i_{rms}}} = \pm \frac{1.96\sqrt{K_i - 1}}{2\sqrt{N}}(100) \tag{5}$$

where K_i is the kurtosis of velocity defined as $K_i = (\frac{1}{N})\sum(u_i - \overline{u_i})^4/(\overline{u_i'^2})^2$. The uncertainty in the rms axial velocity u_{rms} is evaluated at x/d = 0.09, y/d = 0.5 in the free-jet shear layer where K_u = 3 – 0.385, while in the rms radial velocity v_{rms} it is evaluated at x/d = 2, y/d = 1.5 in the wall-jet region where K_v = 3 + 0.213.

The percentage relative uncertainty in Reynolds stress $\overline{u'v'}$ is given by

$$\varepsilon_{\overline{u'v'}} = \pm \frac{1.96\sqrt{\overline{u'^2v'^2} - (\overline{u'v'})^2}}{\sqrt{N}}\left(\frac{100}{\overline{u'v'}}\right) \tag{6}$$

where $\overline{u'^2v'^2}$ is the covariance of (u^2, v^2). The Reynolds stress uncertainty is calculated at x/d = 1, y/d = 0.5 in the free-jet shear layer where $\overline{u'v'}$ = 0.565 (m/s)^2 and $\overline{u'^2v'^2}$ = 0.936 (m/s)^4.

The turbulence kinetic energy TKE is defined as

$$TKE = 0.5(\overline{u'^2} + \overline{v'^2}) \tag{7}$$

The uncertainty in TKE is found using the propagation of uncertainties, which in this case is given by

$$\varepsilon_{TKE} = 0.5\sqrt{(\varepsilon_{\overline{u'^2}})^2 + (\varepsilon_{\overline{v'^2}})^2} \tag{8}$$

where $\varepsilon_{\overline{u'^2}}$ is the uncertainty in $\overline{u'^2}$ and $\varepsilon_{\overline{v'^2}}$ is the uncertainty in $\overline{v'^2}$. These uncertainties are calculated using the following equation given by

$$\varepsilon_{\overline{u_i'^2}} = \pm \frac{1.96\overline{u_i'^2}\sqrt{K_i - 1}}{\sqrt{N}} \quad (9)$$

where $\overline{u_i'^2}$ is the variance of the velocity component, which is computed using Equ. (2). The percentage relative uncertainty in TKE is then equal to $\varepsilon_{TKE}(100/TKE)$. The uncertainty in TKE is calculated at $x/d = 0.75$, $y/d = 0.5$ in the free-jet shear layer where $\overline{u'^2}$ = 1.644 (m/s)^2, K_u = 3 – 0.402, $\overline{v'^2}$ = 1.000 (m/s)^2, K_v = 3 + 0.018, and TKE = 1.322 (m/s)^2.

The derived quantities such as the strain rates and vorticity have been computed using a central finite-difference formula to calculate the velocity gradients. For example, the mean axial strain rate at a point (x,y) is calculated as

$$\frac{\partial \bar{u}}{\partial x}(x,y) = \frac{\bar{u}(x+\Delta,y) - \bar{u}(x-\Delta,y)}{2\Delta} \quad (10)$$

where Δ is the displacement of the velocity sampling points, which in this case is equal in both x and y directions. The finite difference formulas for computing other derived quantities are as follows.

Mean radial strain rate

$$\frac{\partial \bar{v}}{\partial y}(x,y) = \frac{\bar{v}(x,y+\Delta) - \bar{v}(x,y-\Delta)}{2\Delta} \quad (11)$$

Mean shear strain rate

$$\frac{1}{2}\left(\frac{\partial \bar{u}}{\partial y} + \frac{\partial \bar{v}}{\partial x}\right)(x,y) = \frac{1}{2}\left(\frac{\bar{u}(x,y+\Delta) - \bar{u}(x,y-\Delta) + \bar{v}(x+\Delta,y) - \bar{v}(x-\Delta,y)}{2\Delta}\right) \quad (12)$$

Vorticity

$$\omega(x,y) = \left(\frac{\partial v}{\partial x} - \frac{\partial u}{\partial y}\right)(x,y) = \left(\frac{v(x+\Delta,y) - v(x-\Delta,y) - u(x,y+\Delta) + u(x,y-\Delta)}{2\Delta}\right) \quad (13)$$

The uncertainties in these derived quantities are calculated using a root-sum-square method (Moffat 1988) applied to their finite difference formulas. A similar approach was also adopted by Fouras and Soria (1998) to determine the accuracy of out-of-plane vorticity using in-plane velocities. The uncertainties in the derived flow quantities are given by the following expressions.

Uncertainty in mean axial strain rate

$$\varepsilon_{\overline{u}_x} = \frac{\varepsilon_u}{\sqrt{2}\Delta} \tag{14}$$

Uncertainty in mean radial strain rate

$$\varepsilon_{\overline{v}_x} = \frac{\varepsilon_v}{\sqrt{2}\Delta} \tag{15}$$

Uncertainty in mean shear strain rate

$$\varepsilon_{shear} = \frac{\sqrt{{\varepsilon_u}^2+{\varepsilon_v}^2}}{2\sqrt{2}\Delta} \tag{16}$$

Uncertainty in vorticity

$$\varepsilon_{\omega} = \frac{\sqrt{{\varepsilon_u}^2+{\varepsilon_v}^2}}{\sqrt{2}\Delta} \tag{17}$$

The uncertainties given by Equ. (14) to (17) are computed using uncertainties in the measurement of velocities, ε_u = 0.016 m/s and ε_v = 0.062 m/s, and the displacement between the vectors, Δ = 0.4 mm.

A sensitivity analysis on the effect of sample size (number of snapshots) on the proper orthogonal decomposition (POD) of the velocity field was carried out in order to check the convergence of the eigenvalues (kinetic energies). The decay of the kinetic energies with the modes *k* for various sample sizes for jet impingement on an unheated static target surface is shown in Fig. A6 on a log-log scale. The energy decay clearly shows that for all sample sizes the first 10 modes contain most of the kinetic energies and have almost the same energy values. It is also observed that the energies from modes 20 to 30 for all sample sizes do not vary significantly. Therefore, it was determined that a sample size of 500 snapshots was adequate to capture almost all of the modal energies.

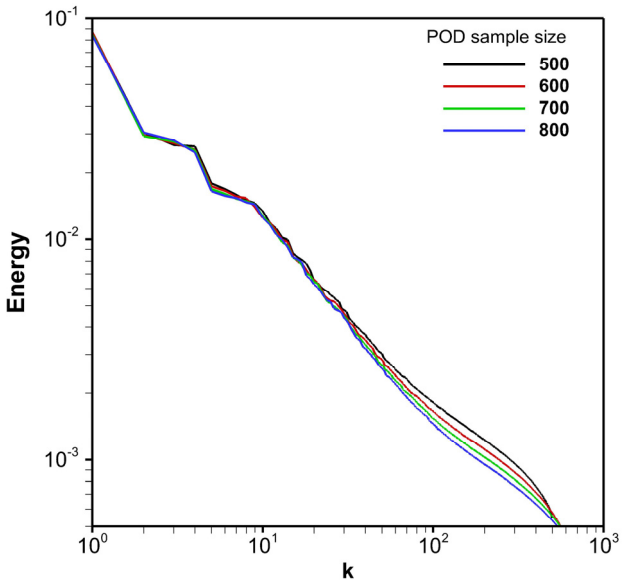

Fig. A6 Decay of kinetic energy with modes for various sample sizes for POD of the velocity field in jet impingement on an unheated static target surface

IV Uncertainty analysis in heat transfer measurements

The details of computation of uncertainty in the heat transfer quantities are presented below. The general equation for uncertainty ε_q in a quantity q estimated within a 95% confidence interval is given by

$$\varepsilon_q = \pm 1.96\sigma_q \tag{18}$$

where σ_q is the standard deviation of q. The percentage relative uncertainty in q is found by multiplying ε_q with $(100/q)$.

Repeated measurements of quantities were taken in order to determine the standard deviation of their variations and the uncertainties in them were then calculated using Equ. (18). These quantities were the electrical potential across the foil V, the current supplied to the foil I, the ambient temperature T_a, the steady-state wall temperature T_w on the foil with input heat flux, and the steady-state adiabatic wall temperature on the foil without input heat flux T_{aw}. The mean values for V and I are 0.878 V and 18.903 A, while that for T_a is 21.7 ^{0}C. The standard deviations for these are σ_V = 0.002 V, σ_I = 0.085 A, and σ_{T_a}= 0.1 ^{0}C respectively. The wall temperatures were measured at the stagnation point for jet impingement on a heated static target surface where σ_{T_w}= 0.055 ^{0}C, $\sigma_{T_{aw}}$= 0.038 ^{0}C, T_w = 25.497 ^{0}C, and T_{aw} = 21.080 ^{0}C.

The uncertainty in the heat flux quantities are also estimated at the stagnation point for jet impingement on a heated static target surface and are computed using the root-sum-square method (Moffat 1988). The relevant equations for these calculations are given as follows.

The uncertainty in the Joule heat flux Q_j is

$$\varepsilon_{Q_j} = \sqrt{{\varepsilon_V}^2 + {\varepsilon_I}^2} \tag{19}$$

The uncertainty in the radiative heat flux Q_{rad} is given by

$$\varepsilon_{Q_{rad}} = \sqrt{\left(\frac{\partial Q_{rad}}{\partial T_w}\varepsilon_{T_w}\right)^2 + \left(\frac{\partial Q_{rad}}{\partial T_a}\varepsilon_{T_a}\right)^2} \tag{20}$$

The uncertainty in the natural convection heat flux Q_{nconv} is calculated using

$$\varepsilon_{Q_{nconv}} = \sqrt{\left(\frac{\partial Q_{nconv}}{\partial T_w}\varepsilon_{T_w}\right)^2 + \left(\frac{\partial Q_{nconv}}{\partial T_a}\varepsilon_{T_a}\right)^2} \tag{21}$$

The uncertainty in the estimation of the convective heat transfer coefficient h_{conv} is given by

$$\varepsilon_{h_{conv}} = \sqrt{\left(\frac{\partial h_{conv}}{\partial Q_j}\varepsilon_{Q_j}\right)^2 + \left(\frac{\partial h_{conv}}{\partial Q_{rad}}\varepsilon_{Q_{rad}}\right)^2 + \left(\frac{\partial h_{conv}}{\partial Q_{nconv}}\varepsilon_{Q_{nconv}}\right)^2 + \left(\frac{\partial h_{conv}}{\partial T_w}\varepsilon_{T_w}\right)^2 + \left(\frac{\partial h_{conv}}{\partial T_{aw}}\varepsilon_{T_{aw}}\right)^2} \tag{22}$$

The percentage relative uncertainty in Nusselt number *Nu* is then equal to the percentage relative uncertainty in the convective heat transfer coefficient which is equal to $\varepsilon_{h_{conv}}(100/h_{conv})$.

References

Adrian RJ, Westerweel J. Particle image velocimetry. Cambridge University Press; 2011.

Aghahani M, Eslami G, Hadidi A. Heat transfer in a turbulent jet impinging on a moving plate considering high plate-to-jet velocity ratios. *J Mech Sci Technol*. 2014 Nov 1;28(11):4509-16.

Ahmed ZU, Al-Abdeli YM, Guzzomi FG. Flow field and thermal behaviour in swirling and non-swirling turbulent impinging jets. *Int J Therm Sci*. 2017 Apr 30;114:241-56.

Alimohammadi S, Murray DB, Persoons T. On the numerical–experimental analysis and scaling of convective heat transfer to pulsating impinging jets. *Int J Therm Sci*. 2015 Dec 31;98:296-311.

Amini N, Hassan YA. Measurements of jet flows impinging into a channel containing a rod bundle using dynamic PIV. *Int J Heat Mass Trans*. 2009 Nov 30;52(23):5479-95.

Arnold Charles F and Owen Webster J, inventors; Gen Motors Corp, assignee. Automotive heating, ventilating, and defrosting system. U.S. Patent 2,837,288, issued June 3, 1958.

Ashforth-Frost S, Jambunathan K, Whitney CF. Velocity and turbulence characteristics of a semiconfined orthogonally impinging slot jet. *Exp Therm Fluid Sci*. 1997 Jan 1;14(1):60-7.

Astarita T, Cardone G. Convective heat transfer on a rotating disk with a centred impinging round jet. *Int J Heat Mass Trans*. 2008 Apr 30;51(7):1562-72.

Astarita T, Carlomagno GM. Infrared thermography for thermo-fluid-dynamics. Springer Science & Business Media; 2012 Aug 4.

Azevedo LF, Webb BW, Queiroz M. Pulsed air jet impingement heat transfer. *Exp Therm Fluid Sci*. 1994 Apr 1;8(3):206-13.

Baughn JW, Hechanova AE, Yan X. An experimental study of entrainment effects on the heat transfer from a flat surface to a heated circular impinging jet. *J Heat Transf*. 1991 Nov 1;113(4):1023-5.

Baughn JW, Shimizu S. Heat transfer measurements from a surface with uniform heat flux and an impinging jet. *J Heat Transf*. 1989 Nov 1;111(4):1096-8.

Baydar E, Ozmen Y. An experimental and numerical investigation on a confined impinging air jet at high Reynolds numbers. *Appl Therm Eng*. 2005 Feb 28;25(2):409-21.

Benedict LH, Gould RD. Towards better uncertainty estimates for turbulence statistics. *Exp Fluids*. 1996 Dec 15;22(2):129-36.

Berkooz G, Holmes P, Lumley JL. The proper orthogonal decomposition in the analysis of turbulent flows. *Annu Rev Fluid Mech*. 1993 Jan;25(1):539-75.

Bradshaw P, Love EM. The normal impingement of a circular air jet on a flat surface. HM Stationery Office Report no. 3205; 1959

Brodersen S, Metzger D. Experimental investigation of the flow field resulting from the interaction between an impinging jet and a rotating disk. *Exp Therm Fluid Sci*. 1992 May 1;5(3):351-8.

Capone A, Soldati A, Romano GP. Mixing and entrainment in the near field of turbulent round jets. *Exp Fluids*. 2013 Jan 1;54(1):1434.

Carlomagno GM, Cardone G. Infrared thermography for convective heat transfer measurements. *Exp Fluids*. 2010 Dec 1;49(6):1187-218.

Carlomagno GM, Ianiro A. Thermo-fluid-dynamics of submerged jets impinging at short nozzle-to-plate distance: a review. *Exp Therm Fluid Sci*. 2014 Oct 31;58:15-35.

Chang SW, Su LM, Zheng Y. Reciprocating impingement jet heat transfer with surface ribs. *Exp Heat Transfer*. 2000 Oct 1;13(4):275-97.

Chattopadhyay H, Saha SK. Turbulent flow and heat transfer from a slot jet impinging on a moving plate. *Int J Heat Fluid Fl*. 2003 Oct 31;24(5):685-97.

Chen SJ, Tseng AA. Spray and jet cooling in steel rolling. *Int J Heat Fluid Fl*. 1992 Dec 1;13(4):358-69.

Chong MS, Perry AE, Cantwell BJ. A general classification of three-dimensional flow fields. *Phys Fluids A: Fluid Dynamics*. 1990 May;2(5):765-77.

Choo KS, Kim SJ. Comparison of thermal characteristics of confined and unconfined impinging jets. *Int J Heat Mass Trans*. 2010 Jul 31;53(15):3366-71.

Cirillo F, Isopi GM. Glass tempering heat transfer coefficient evaluation and air jets parameter optimization. *Appl Therm Eng*. 2009 Apr 30;29(5):1173-9.

Cooper D, Jackson DC, Launder BE, Liao GX. Impinging jet studies for turbulence model assessment—I. Flow-field experiments. *Int J Heat Mass Trans*. 1993 Jul 1;36(10):2675-84.

Dantec Dynamics 2D-PIV reference manual. Dantec Dynamics 2005

Dano BP, Liburdy JA. Structure detection and analysis of non-circular impinging jets in a semi-confined array configuration. *Exp Therm Fluid Sci*. 2007 August;31(8):991-1003

De Bonis MV, Ruocco G. An experimental study of the local evolution of moist substrates under jet impingement drying. *Int J Therm Sci*. 2011 Jan 31;50(1):81-7.

Didden N, Ho CM. Unsteady separation in a boundary layer produced by an impinging jet. *J Fluid Mech*. 1985 Nov 1;160:235-56.

Donatti CN, Silveira RA, Bridi G, Maliska CR, da Silva AF. Ice accretion simulation in presence of a hot air anti-icing system. In 19th International Congress of Mechanical Engineering (COBEM) 2007 Nov.

Ekkad SV, Kontrovitz D. Jet impingement heat transfer on dimpled target surfaces. *Int J Heat Fluid Fl*. 2002 Feb 28;23(1):22-8.

El Hassan M, Assoum HH, Sobolik V, Vétel J, Abed-Meraim K, Garon A, Sakout A. Experimental investigation of the wall shear stress and the vortex dynamics in a circular impinging jet. *Exp Fluids*. 2012 Jun 1;52(6):1475-89.

El Hassan M, Assoum HH, Martinuzzi R, Sobolik V, Abed-Meraim K, Sakout A. Experimental investigation of the wall shear stress in a circular impinging jet. *Phys Fluids*. 2013 Jul;25(7):077101.

Esfahanian V, Javaheri A, Ghaffarpour M. Thermal analysis of an SI engine piston using different combustion boundary condition treatments. *Appl Therm Eng*. 2006 Feb 28;26(2):277-87.

Fairweather M, Hargrave G. Experimental investigation of an axisymmetric, impinging turbulent jet. 1. Velocity field. *Exp Fluids*. 2002 Sep 1;33(3):464-71.

Fénot M, Dorignac E, Lalizel G. Heat transfer and flow structure of a multichannel impinging jet. *Int J Therm Sci*. 2015 Apr 30;90:323-38.

Fitzgerald JA, Garimella SV. A study of the flow field of a confined and submerged impinging jet. *Int J Heat Mass Trans*. 1998 Apr 1;41(8-9):1025-34.

Fouras A, Soria J. Accuracy of out-of-plane vorticity measurements derived from in-plane velocity field data. *Exp Fluids*. 1998 Oct 15;25(5):409-30.

Fujii T, Imura H. Natural-convection heat transfer from a plate with arbitrary inclination. *Int J Heat Mass Trans*. 1972 Apr 1;15(4):755-767.

Gardon R, Akfirat JC. The role of turbulence in determining the heat-transfer characteristics of impinging jets. *Int J Heat Mass Trans*. 1965 Oct 1;8(10):1261-72.

Gardon R, Akfirat JC. Heat transfer characteristics of impinging two-dimensional air jets. *J Heat Transf*. 1966 Feb 101:107.

Gau C, Chung CM. Surface curvature effect on slot-air-jet impingement cooling flow and heat transfer process. *ASME, Transactions, J Heat Transf*. 1991 Nov 1;113:858-64.

Gauntner JW, Livingood J, Hrycak P. Survey of literature on flow characteristics of a single turbulent jet impinging on a flat plate. NASA TN D-5652. 1970 Feb 1:19.

Geers LF, Tummers MJ, Hanjalić K. Experimental investigation of impinging jet arrays. *Exp Fluids*. 2004 Jun 1;36(6):946-58.

Geers LF, Tummers MJ, Hanjalić K. Particle imaging velocimetry-based identification of coherent structures in normally impinging multiple jets. *Phys Fluids*. 2005 May;17(5):055105.

Geers LF, Tummers MJ, Bueninck TJ, Hanjalić K. Heat transfer correlation for hexagonal and in-line arrays of impinging jets. *Int J Heat Mass Trans*. 2008 Oct 31;51(21):5389-99.

Goldstein RJ, Behbahani AI, Heppelmann KK. Streamwise distribution of the recovery factor and the local heat transfer coefficient to an impinging circular air jet. *Int J Heat Mass Trans*. 1986 Aug 1;29(8):1227-35.

Goldstein RJ, Sobolik KA, Seol WS. Effect of entrainment on the heat transfer to a heated circular air jet impinging on a flat surface. *J Heat Transfer*. 1990;112:608-11.

Hall JW, Ewing D. On the dynamics of the large-scale structures in round impinging jets. *J Fluid Mech*. 2006 May 25;555:439-58.

Hammad KJ, Milanovic I. Flow structure in the near-wall region of a submerged impinging jet. *J Fluids Eng-T ASME*. 2011 Sep 1;133(9):091205.

Harmand S, Pellé J, Poncet S, Shevchuk IV. Review of fluid flow and convective heat transfer within rotating disk cavities with impinging jet. *Int J Therm Sci*. 2013 May 31;67:1-30.

Han JC, Dutta S, Ekkad S. Gas turbine heat transfer and cooling technology. CRC Press; 2012 Nov 27.

Han B, Goldstein RJ. Jet-Impingement Heat Transfer in Gas Turbine Systems. *Ann NY Acad Sci*. 2001 May 1;934(1):147-61.

Ho CM, Nosseir NS. Dynamics of an impinging jet. Part 1. The feedback phenomenon. *J Fluid Mech*. 1981 Apr 1;105:119-42.

Hofmann HM, Kaiser R, Kind M, Martin H. Calculations of steady and pulsating impinging jets—an assessment of 13 widely used turbulence models. *Numer Heat Transfer Part B: Fundamentals*. 2007 Apr 30;51(6):565-83.

Hollworth BR, Wilson SI. Entrainment effects on impingement heat-transfer: Part 1 – Measurements of heated jet velocity and temperature distributions and recovery temperatures on target surface. *J Heat Transf*. 1984 Jan 1;106(4):797-803.

Hoogendoorn CJ. The effect of turbulence on heat transfer at a stagnation point. *Int J Heat Mass Trans*. 1977 Dec 1;20(12):1333-8.

Howe H, inventor; Kloeckner Humboldt Deutz Ag, assignee. Piston cooling arrangement for a reciprocating piston internal combustion engine with an injection nozzle. United States patent US 3,709,109. 1973 Jan 9.

Hrycak P. Heat transfer from impinging jets. A literature review. AFWAL-TR-81-3054. 1981 Jun.

Hrycak P. Heat transfer from round impinging jets to a flat plate. *Int J Heat Mass Trans*. 1983 Dec 1;26(12):1857-65.

Huang L, El-Genk MS. Heat transfer of an impinging jet on a flat surface. *Int J Heat Mass Trans*. 1994 Sep 30;37(13):1915-23.

Hunt JC, Wray AA, Moin P. Eddies, streams, and convergence zones in turbulent flows. In Studying turbulence using numerical simulation databases, 2. Proceedings of the 1988 Summer Program p 193-208 (SEE N89-24538 18-34).

Hussain AK, Reynolds WC. The mechanics of an organized wave in turbulent shear flow. *J Fluid Mech*. 1970 Apr;41(2):241-58.

Hwang SD, Cho HH. Effects of acoustic excitation positions on heat transfer and flow in axisymmetric impinging jet: main jet excitation and shear layer excitation. *Int J Heat Fluid Fl*. 2003 Apr 30;24(2):199-209.

Hwang TG, Doh DH, Okamoto K. 4D-PTV Measurements of an impinged jet with a dynamic 3D-PTV. *J Visual-Japan*. 2005 Jan 1;8(3):245-52.

Ichimiya K, Yoshida Y. Oscillation effect of impingement surface on two-dimensional impingement heat transfer. *J Heat Transf*. 2009 Jan 1;131(1):011701.

Ihli T, Ilić M. Efficient helium cooling methods for nuclear fusion devices: Status and prospects. *Fusion Eng Des*. 2009 Jun 30;84(2):964-8.

Jainski C, Lu L, Sick V, Dreizler A. Laser imaging investigation of transient heat transfer processes in turbulent nitrogen jets impinging on a heated wall. *Int J Heat Mass Trans*. 2014 Jul 31;74:101-12.

Jambunathan K, Lai E, Moss MA, Button BL. A review of heat transfer data for single circular jet impingement. *Int J Heat Fluid Fl*. 1992 Jun 1;13(2):106-15.

Janetzke T, Nitsche W, Täge J. Experimental investigations of flow field and heat transfer characteristics due to periodically pulsating impinging air jets. *Heat Mass Transfer*. 2008 Dec 1;45(2):193-206.

Jeffers N, Stafford J, Conway C, Punch J, Walsh E. The influence of the stagnation zone on the fluid dynamics at the nozzle exit of a confined and submerged impinging jet. *Exp Fluids*. 2016 Feb 1;57(2):1-5.

Jeong J, Hussain F. On the identification of a vortex. *J Fluid Mech*. 1995 Feb;285:69-94.

Jha JM, Ravikumar SV, Sarkar I, Pal SK, Chakraborty S. Ultrafast cooling processes with surfactant additive for hot moving steel plate. *Exp Therm Fluid Sci*. 2015 Nov 30;68:135-44.

Kataoka K, Sahara R, Ase H, HARADA T. Role of large-scale coherent structures in impinging jet heat transfer. *J Chem Eng Jpn*. 1987a Feb 20;20(1):71-6.

Kataoka K, Suguro M, Degawa H, Maruo K, Mihata I. The effect of surface renewal due to largescale eddies on jet impingement heat transfer. *Int J Heat Mass Trans*. 1987b Mar 31;30(3):559-67.

Katti V, Prabhu SV. Experimental study and theoretical analysis of local heat transfer distribution between smooth flat surface and impinging air jet from a circular straight pipe nozzle. *Int J Heat Mass Trans*. 2008 Aug 31;51(17):4480-95.

Kim KC, Min YU, Oh SJ, An NH, Seoudi B, Chun HH, Lee I. Time-resolved PIV investigation on the unsteadiness of a low Reynolds number confined impinging jet. *J Visual-Japan*. 2007 Jan 1;10(4):367-79.

Klein D, Hetsroni G. Enhancement of heat transfer coefficients by actuation against an impinging jet. *Int J Heat Mass Trans*. 2012 Jul 31;55(15):4183-94.

Koseoglu MF, Baskaya S. The effect of flow field and turbulence on heat transfer characteristics of confined circular and elliptic impinging jets. *Int J Therm Sci*. 2008 Oct 1;47(10):1332-46.

Landreth CC, Adrian RJ. Impingement of a low Reynolds number turbulent circular jet onto a flat plate at normal incidence. *Exp Fluids*. 1990 Jan 1;9(1):74-84.

Launder BE, Rodi W. The turbulent wall jet measurements and modeling. *Annu Rev Fluid Mech*. 1983 Jan;15(1):429-59.

Lee J, Lee S-J. Stagnation region heat transfer of a turbulent axisymmetric jet impingement. *Exp Heat Transfer*. 1999 Apr 1;12(2):137-56.

Lee J, Lee SJ. The effect of nozzle aspect ratio on stagnation region heat transfer characteristics of elliptic impinging jet. *Int J Heat Mass Trans*. 2000 Feb 29;43(4):555-75.

Lee RC, Sahm MK, inventors; The BOC Group, Inc., assignee. Impingement jet freezer and method. United States patent US 5,740,678. 1998 Apr 21.

Lin J, Russell H, inventors; Logetronics Inc, assignee. Dryer for photographic film. United States patent US 3,834,040. 1974 Sep 10.

Liu Z, Reitz RD. Modeling fuel spray impingement and heat transfer between spray and wall in direct injection diesel engines. *Numer Heat Transfer Part A: Applications*. 1995 Nov 1;28(5):515-29.

Liu T, Nink J, Merati P, Tian T, Li Y, Shieh T. Deposition of micron liquid droplets on wall in impinging turbulent air jet. *Exp Fluids*. 2010 Jun 1;48(6):1037-57.

Livingood JN, Hrycak P. Impingement heat transfer from turbulent air jets to flat plates: a literature survey. NASA TM X-2778. 1973 May

Lumley JL. The structure of inhomogeneous turbulent flows. Atmospheric Turbulence and Radio Wave Propagation. Nauka, Moscow, 1967

Lytle D, Webb BW. Air jet impingement heat transfer at low nozzle-plate spacings. *Int J Heat Mass Trans*. 1994 Aug 1;37(12):1687-97.

Martin H. Heat and mass transfer between impinging gas jets and solid surfaces. *Adv Heat Transf*. 1977 Dec 31;13:1-60.

Matsuda S, Saji N, Yaga M, Ishikawa M, Oyakawa K. Synchronal measurement of flow structure and heat transfer of impingement jet. *J Therm Sci*. 2010 Jun 1;19(3):228-33.

McLaren D, Orr WW, inventors; The Boeing Company, assignee. Thermal anti-icing system for aircraft. United States patent US 5,011,098. 1991 Apr 30.

Meola C, de Luca L, Carlomagno GM. Influence of shear layer dynamics on impingement heat transfer. *Exp Therm Fluid Sci*. 1996 Jul 1;13(1):29-37.

Meslem A, Sobolik V, Bode F, Sodjavi K, Zaouali Y, Nastase I, Croitoru C. Flow dynamics and mass transfer in impinging circular jet at low Reynolds number. Comparison of convergent and orifice nozzles. *Int J Heat Mass Trans*. 2013 Dec 31;67:25-45.

Metzger DE, Grochowsky LD. Heat transfer between an impinging jet and a rotating disk. *J Heat Transf*. 1977 Nov;99:663.

Meyers JJ, Leighton RG, Api DM, Domoto GA, Panides E, Deshpande NV, Hays AW, Lohr SW, Taylor TN, inventors; Xerox Corporation, assignee. Hot air impingement drying system for inkjet images. United States patent US 6,463,674. 2002 Oct 15.

Middelberg G, Herwig H. Convective heat transfer under unsteady impinging jets: the effect of the shape of the unsteadiness. *Heat Mass Transfer*. 2009 Oct 1;45(12):1519-32.

Mobtil M, Bougeard D, Solliec C. Inverse determination of convective heat transfer between an impinging jet and a continuously moving flat surface. *Int J Heat Fluid Fl*. 2014 Dec 31;50:83-94.

Moffat RJ. Describing the uncertainties in experimental results. Exp Therm Fluid Sci. 1988 Jan 1;1(1):3-17.

Montagné B, Sodjavi K, Bragança P, Meslem A, Kristiawan M. Experimental investigation of nozzle shape effect on wall shear stress beneath impinging round jet. International Conference on Mechanics, Fluid Mechanics, Heat and Mass Transfer (MFMHMT 2014), Feb 2014, Interlaken, Switzerland.

Morris G, Acton E, inventors; Morris George J., assignee. Methods and apparatus for freezing tissue. United States patent application US 10/297,754. 2001 Jun 7.

Mozumder AK, Monde M, Woodfield PL. Delay of wetting propagation during jet impingement quenching for a high temperature surface. *Int J Heat Mass Trans*. 2005 Dec 31;48(25):5395-407.

Naber J, Enright B, Farrell P. Fuel impingement in a direct injection diesel engine. WISCONSIN UNIV-MADISON; 1988 Sep 15.

Naguib AM, Jiang W, Zhang K. Source advection effects on unsteady-surface-pressure asymmetry in oblique impinging jets. *AIAA J*. 2012 Jul;50(7):1634-8.

Narayanan V, Seyed-Yagoobi J, Page RH. An experimental study of fluid mechanics and heat transfer in an impinging slot jet flow. *Int J Heat Mass Trans*. 2004 Apr 30;47(8):1827-45.

Nasif G, Barron RM, Balachandar R. Simulation of jet impingement heat transfer onto a moving disc. *Int J Heat Mass Trans*. 2015 Jan 31;80:539-50.

Nishino K, Samada M, Kasuya K, Torii K. Turbulence statistics in the stagnation region of an axisymmetric impinging jet flow. *Int J Heat Fluid Fl*. 1996 Jun 1;17(3):193-201.

Nguyen TD, Pellé J, Harmand S, Poncet S. PIV measurements of an air jet impinging on an open rotor-stator system. *Exp Fluids*. 2012 Aug 1;53(2):401-12.

Norajitra P, Abdel-Khalik SI, Giancarli LM, Ihli T, Janeschitz G, Malang S, Mazul IV, Sardain P. Divertor conceptual designs for a fusion power plant. *Fusion Eng Des*. 2008 Dec 31;83(7):893-902.

O'Donovan TS, Murray DB. Jet impingement heat transfer–Part I: Mean and root-mean-square heat transfer and velocity distributions. *Int J Heat Mass Trans*. 2007 Aug 31;50(17):3291-301.

Pavlova A, Amitay M. Electronic cooling using synthetic jet impingement. *J Heat Transf*. 2006 Sep 1;128(9):897-907.

Persoons T, McGuinn A, Murray DB. A general correlation for the stagnation point Nusselt number of an axisymmetric impinging synthetic jet. *Int J Heat Mass Trans*. 2011 Aug 31;54(17):3900-8.

Persoons T, Balgazin K, Brown K, Murray DB. Scaling of convective heat transfer enhancement due to flow pulsation in an axisymmetric impinging jet. *J Heat Transf*. 2013 Nov 1;135(11):111012.

Polat S. Heat and mass transfer in impingement drying. *Dry Technol*. 1993 Jan 1;11(6):1147-76.

Bro CO, Boguslawski L. Local heat transfer from a rotating disk in an impinging round jet. *J Heat Transf*. 1986 May 1;108(2):357-64.

Popiel CO, Trass O. Visualization of a free and impinging round jet. *Exp Therm Fluid Sci*. 1991 May 1;4(3):253-64.

Raffel M, Willert CE, Wereley S, Kompenhans J. Particle image velocimetry: a practical guide. Springer; 2013 Dec 19.

Roux S, Fénot M, Lalizel G, Brizzi LE, Dorignac E. Experimental investigation of the flow and heat transfer of an impinging jet under acoustic excitation. *Int J Heat Mass Trans.* 2011 Jul 31;54(15):3277-90.

Roy S, Nasr K, Patel P, AbdulNour B. An experimental and numerical study of heat transfer off an inclined surface subject to an impinging airflow. *Int J Heat Mass Trans.* 2002 Apr 30;45(8):1615-29.

Sagot B, Antonini G, Christgen A, Buron F. Jet impingement heat transfer on a flat plate at a constant wall temperature. *Int J Therm Sci*. 2008 Dec 1;47(12):1610-9.

Sakakibara J, Hishida K, Maeda M. Vortex structure and heat transfer in the stagnation region of an impinging plane jet (simultaneous measurements of velocity and temperature fields by digital particle image velocimetry and laser-induced fluorescence). *Int J Heat Mass Trans.* 1997 Sep 1;40(13):3163-76.

Salvadori VO, Mascheroni RH. Analysis of impingement freezers performance. *J Food Eng*. 2002 Sep 30;54(2):133-40.

Sarkar A, Nitin N, Karwe MV, Singh RP. Fluid flow and heat transfer in air jet impingement in food processing. *J Food Sci*. 2004 May 1;69(4):CRH113-22.

Scarano F. Iterative image deformation methods in PIV. *Meas Sci Technol*. 2001 Nov 23;13(1):R1.

Senter J, Solliec C. Flow field analysis of a turbulent slot air jet impinging on a moving flat surface. *Int J Heat Fluid Fl*. 2007 Aug 31;28(4):708-19.

Sharif MA, Banerjee A. Numerical analysis of heat transfer due to confined slot-jet impingement on a moving plate. *Appl Therm Eng*. 2009 Feb 28;29(2):532-40.

Sheriff HS, Zumbrunnen DA. Effect of flow pulsations on the cooling effectiveness of an impinging jet. *J Heat Transf* 1994 November;116(4):886-95.

Shukla V, Elliott GS, Kear BH. Nanopowder deposition by supersonic rectangular jet impingement. *J Therm Spray Techn*. 2000 Sep 1;9(3):394-8.

Sirovich L. Turbulence and the dynamics of coherent structures. I. Coherent structures. *Q Appl Math*. 1987;45(3):561-71.

Smedley GT, Phares DJ, Flagan RC. Entrainment of fine particles from surfaces by gas jets impinging at normal incidence. *Exp Fluids*. 1999 Mar 15;26(4):324-34.

Soria J. An investigation of the near wake of a circular cylinder using a video-based digital cross-correlation particle image velocimetry technique. *Exp Therm Fluid Sci*. 1996 Feb 1;12(2):221-33.

Soria J. Experimental studies of the near-field spatio-temporal evolution of zero-net-mass-flux (ZNMF) jets. In Vortex Rings and Jets 2015 (pp. 61-92). Springer Singapore.

Sozbir N, Yao SC. Experimental investigation of water mist cooling for glass tempering. *Atomization Spray*. 2004;14(3).

Stevens J, Webb BW. Measurements of the free surface flow structure under an impinging, free liquid jet. *J Heat Transf*. 1992 Feb 1;114(1):79-84.

Stevens J, Webb BW. Measurements of flow structure in the radial layer of impinging free-surface liquid jets. *Int J Heat Mass Trans*. 1993 Oct 1;36(15):3751-8.

Striegl SA, Diller TE. The effect of entrainment temperature on jet impingement heat transfer. *J Heat Transf*. 1984 Feb;106:27.

Terzis A, Ott P, von Wolfersdorf J, Weigand B, Cochet M. Detailed Heat Transfer Distributions of Narrow Impingement Channels for Cast-In Turbine Airfoils. *J Turbomach*. 2014 Sep 1;136(9):091011.

Tesař V. Characterisation of subsonic axisymmetric nozzles. *Chem Eng Res Des*. 2008 Nov 30;86(11):1253-62.

Tu CV, Wood DH. Wall pressure and shear stress measurements beneath an impinging jet. *Exp Therm Fluid Sci*. 1996 Nov 1;13(4):364-73.

Tummers MJ, Jacobse J, Voorbrood SG. Turbulent flow in the near field of a round impinging jet. *Int J Heat Mass Trans*. 2011 Nov 30;54(23):4939-48.

Violato D, Ianiro A, Cardone G, Scarano F. Three-dimensional vortex dynamics and convective heat transfer in circular and chevron impinging jets. *Int J Heat Fluid Fl*. 2012 Oct 31;37:22-36.

Viskanta R. Heat transfer to impinging isothermal gas and flame jets. *Exp Therm Fluid Sci*. 1993 Feb 1;6(2):111-34.

Volkner W, Schmedemann H, inventors; Licentia Patent-Verwaltungs-GMBH, assignee. Aircraft de-icing. United States patent US 4,036,457. 1977 Jul 19.

Wannassi M, Monnoyer F. Fluid flow and convective heat transfer of combined swirling and straight impinging jet arrays. *Appl Therm Eng*. 2015 Mar 5;78:62-73.

Wang H, Yu W, Cai Q. Experimental study of heat transfer coefficient on hot steel plate during water jet impingement cooling. *J Mater Process Tech*. 2012 Sep 30;212(9):1825-31.

Weigand B, Spring S. Multiple jet impingement− a review. *Heat Transf Res*. 2011;42(2).

Wen MY. Flow structures and heat transfer of swirling jet impinging on a flat surface with micro-vibrations. *Int J Heat Mass Trans*. 2005 Feb 28;48(3):545-60.

Westerweel J, Scarano F. Universal outlier detection for PIV data. *Exp Fluids*. 2005 Dec 1;39(6):1096-100.

Willert CE, Gharib M. Digital particle image velocimetry. *Exp Fluids*. 1991 Jan 1;10(4):181-93.

Xu P, Yu B, Qiu S, Poh HJ, Mujumdar AS. Turbulent impinging jet heat transfer enhancement due to intermittent pulsation. *Int J Therm Sci*. 2010 Jul 31;49(7):1247-52.

Yang HQ, Kim T, Lu TJ, Ichimiya K. Flow structure, wall pressure and heat transfer characteristics of impinging annular jet with/without steady swirling. *Int J Heat Mass Trans*. 2010 Sep 30;53(19):4092-100.

Yang TL, Chang SW, Su LM, Hwang CC. Heat transfer of confined impinging jet onto spherically concave surface with piston cooling application. *JSME Int J B-Fluid T*. 1999 May 15;42(2):238-48.

Yao S, Guo Y, Jiang N, Liu J. An experimental study of a turbulent jet impinging on a flat surface. *Int J Heat Mass Trans*. 2015 Apr 30;83:820-32.

Young RM, Hargather MJ, Settles GS. Shear stress and particle removal measurements of a round turbulent air jet impinging normally upon a planar wall. *J Aerosol Sci*. 2013 Aug 31;62:15-25

Zuckerman N, Lior N. Jet impingement heat transfer: physics, correlations, and numerical modeling. *Adv Heat Transf*. 2006 Dec 31;39:565-631.

Zumbrunnen DA. Convective heat and mass transfer in the stagnation region of a laminar planar jet impinging on a moving surface. *J Heat Transf*. 1991 Aug;113:563-570.